E-260

UICC/HEP-80-01
FERMILAB-THESIS-1980-25

CORRELATIONS BETWEEN HIGH TRANSVERSE MOMENTUM HADRONS IN $\pi^{\pm}p$, $K^{-}p$ and pp COLLISIONS AT 200 GeV/c

BY

ROBERT WALTER STANEK
B.S., University of Illinois at Chicago Circle, 1970
M.S., University of Illinois at Chicago Circle, 1971

THESIS

Submitted in partial fulfillment of the requirements
for the degree of Doctor of Philosophy in Physics
in the Graduate College of the
University of Illinois at Chicago Circle, 1980

Chicago, Illinois

CORRELATIONS BETWEEN HIGH TRANSVERSE MOMENTUM HADRONS IN $\pi^{\pm}p$, $K^{-}p$ and pp COLLISIONS AT 200 GeV/c

Robert Walter Stanek, Ph.D.
Department of Physics
University of Illinois, Chicago, 1980

ABSTRACT

This thesis presents a study of the quantum number correlations between secondary hadrons produced in a high transverse momentum reaction involving proton and meson beams incident on hydrogen at 200 GeV/c.

Events with a single trigger particle having p_T in the range between 1.5 GeV/c and 4.5 GeV/c and produced between $67^{\circ} \lesssim \theta^{*} \lesssim 104^{\circ}$ are investigated using information from a multiparticle spectrometer at Fermilab. These trigger particles are identified as either a $\pi^{\pm}$, $K^{\pm}$ or $p^{\pm}$. Ratios of the cross sections for producing these various triggers are found and compared to several hard scattering models. We also look in a $\pm 45^{\circ}$ azimuthal wedge 180° opposite the trigger particle and study the ratio of relatively fast positive hadrons to negative hadrons for different trigger types.

For various triggers, h and h', excellent agreement with the Chicago-Princeton data for pp collisions is found in the trigger production ratios $\frac{d\sigma}{dp_T}(pp \to hX)/\frac{d\sigma}{dp_T}(pp \to h'X)$. We present data here for the first time for $\pi^{\pm}$ and K^{-} induced reations. For any type charged trigger, $h^{\pm}$, there is a remarkable similarity between $\frac{d\sigma}{dp_T}(pp \to h^{+}X)/\frac{d\sigma}{dp_T}(pp \to h^{-}X)$ and $\frac{d\sigma}{dp_T}(\pi^{+}p \to h^{+}X)/\frac{d\sigma}{dp_T}(\pi^{+}p \to h^{-}X)$ where these ratios are $\simeq 2$ and increase rapidly at large p_T. In contrast, the ratio $\frac{d\sigma}{dp_T}(\pi^{-}p \to h^{+}X)/\frac{d\sigma}{dp_T}(\pi^{-}p \to h^{-}X)$ is $\simeq 1$ throughout the p_T

range. With limited statistics, we show that this is also true for K^- induced events.

Predictions from a CIM - QF parameterization by Chase and Stirling and from QCD are shown to agree reasonably well with all the proton induced ratios within our p_T region. The same is true for the π^- induced ratios but Chase and Stirling fail to explain the π^+ induced ratios.

On the away side, we calculate $R_a(h)$ which is the ratio of positive to negative hadrons produced in the reaction $ap \rightarrow hX$. The excess of positive hadrons opposite a K^- or $\bar{p}$ trigger in pp collisions reported by the British-French-Scandinavian group at the ISR is not seen. We do see, however, a charge dependent effect for all beams - $R(h^-) > R(h^+)$. In agreement with QCD, $R_a(h)$ is not strongly dependent on particle types h having identical charge. When x_e of the away hadrons becomes small, we show that charge conservation may explain our away ratios. We construct naive models in CIM and QCD to predict the away ratios for particles with $x_e \geq 0.4$. There are features of either model which explain the general trends of our data.

ACKNOWLEDGEMENT

In creating this vast experiment, thanks are due to people at all levels. I mention here those people who have greatly contributed to my education and well being over those long years.

Above all, I thank Professor H. Goldberg, my thesis advisor, for his encouragement, perseverance and many helpful discussions. I also wish to thank Professor A. Pagnamenta for teaching me the most important aspects of high energy physics that I know.

I have enjoyed working with most of the MPS collaborators and wish to express my appreciation to them for creating an exciting atmosphere. Professor R. Gomez has my thanks for many useful discussions and his friendship. Professor E. Malamud and Professor V. Ashford are also fondly remembered as people who helped me along in the analysis at very crucial times.

The following are individuals who deserve to be acknowledged, but who probably never will be other than here.

The author is grateful to Mr. W. Cramer and Mr. D. Williams for teaching him most of his electronics techniques. Stanley Pogorzelski cannot be forgotten for taking the time to teach, advise, and talk about machine shop techniques and general lessons in life. Ray and Nancy Krass, Lt. Frank Eng and Dr. Leonard Winchester will also be warmly remembered for their role in constructing proportional chambers and associated equipment.

Finally, to my sweetheart, Mary, thank you for showing me that I had to stop and smell the roses before I pass them by.

TABLE OF CONTENTS

Page

ACKNOWLEDGEMENT iii

CHAPTER I - INTRODUCTION 1

CHAPTER II - EXPERIMENTAL APPARATUS AND TECHNIQUES 12

2.1 Overview 12

2.2 Experimental Technique 14

a. Beam and Beam Cerenkov Counters 14

b. Target 19

c. Detectors 19

Scintillation Counters 19

Proportional Chambers - Overview 23

Proportional Chambers - Construction 24

Spark Chambers 32

d. Analysis Magnet 33

e. Calorimeters 33

Construction 36

Calibration 39

f. Cerenkov Counter 39

2.3 Trigger Electronics and Data Acquisition System 48

a. Trigger System 48

b. Data Acquisition System Overview 53

c. ADC and Jorway Scaler Data Transfer 57

d. PWC Data Transfer 58

e. WSC Data Transfer 59

f. LeCroy Scaler Data Transfer 60

CHAPTER III - DATA ANALYSIS 61

TABLE OF CONTENTS (Continued)

Page

3.1 Overview 61

3.2 Track Finding and Data Summary Tapes 61

3.3 Calorimeter Responses 65

a. Calibration 65

b. Triggering Biases 69

3.4 Cerenkov Counter Photoelectrons and Gains ... 80

3.5 Particle Identification 86

3.6 Single Particle Trigger 104

3.7 Corrections to the Trigger Particle 114

a. Beam Cerenkov Efficiency 116

b. Target Attenuation 116

c. Acceptance 116

d. Track Finding Efficiency 117

e. Calorimeter Responses 117

f. Cl Efficiency, π-K Contamination, δ-Rays 120

3.8 The Ratio $\frac{d\sigma}{dp_T}(pp \to h^+X)/\frac{d\sigma}{dp_T}(pp \to h^-X)$ 125

3.9 Cl Identified Trigger Particles Ratios in pp Collisions 130

CHAPTER IV - DATA ANALYSIS RESULTS 139

4.1 Cross Section Ratios for $\pi^{\pm}$ and K^- Beams 139

4.2 Away Side Acceptances 145

4.3 Away Side - Trigger Particle Correlations ... 154

CHAPTER V - CONCLUSIONS 176

5.1 High p_T Scattering and the QCD Model 177

5.2 High p_T Scattering and the CIM Model 186

TABLE OF CONTENTS (Continued)

Page

5.3 Model Predictions 187

a. QCD and the Trigger Side 187

b. CIM and the Trigger Side 194

c. QCD and the Away Side 200

d. CIM and the Away Side 209

5.4 Summary 214

REFERENCES 216

APPENDIX A 219

VITA 229

LIST OF TABLES

Table		Page
1.1	Kinematic regions of Fermilab and ISR experiments that measure correlations in high p_T events	10
2.1	M6 West beamline parameters	15
2.2	Parameters of M6 beam Cerenkov counters	17
2.3	Hadron beam composition in M6 West	18
2.4	Definition of triggers and biases used	54
3.1	Summary of LH_2 data input into this analysis	62
3.2	Some important parameters kept in various stages of the data summary	66
3.3	Results of the beam calibration of calorimeter modules with hadrons and electrons	68
3.4	C1 threshold momenta for air and the He-air mixture	81
3.5a	C1 photoelectron yield for air	83
3.5b	C1 photoelectron yield for the He-air mixture	84
3.6	The average number of particles contributing Cerenkov light to a given cell	88
3.7	The fraction of ON signals that a pulse height of "1" occurs in any cell of C1	97
3.8	Fraction of C1 tagged particles that are in the various ID classes defined in the text	105
3.9	Fraction of particular C1 tagged particles found in the different cells of C1	106
3.10	Fraction of the C1 tagged particles that contribute light to a given number of mirrors	107
3.11	The pion and kaon detection efficiency in C1 as a function of their p_T	123
3.12	Ratios of positive charge to negative charge production cross sections for pp collisions calculated for three methods for combining left and right triggers	129

LIST OF TABLES (Continued)

Table		Page
4.1	A summary of the kinematic regions explored in this analysis	155
5.1	The valence quark content of various initial states	182
5.2	The away side ratio prediction of the naive QCD model opposite charged triggers	207
5.3	The away side ratio prediction of QF and CIM opposite specific trigger particles	213

LIST OF FIGURES

Figure		Page
1.1	The transverse momentum dependence of the invariant cross section for inclusive π^0 production at various center of mass energies	3
1.2	The expected dynamics of the inclusive reation AB → CX at high p_T	4
1.3	Center of mass kinematic variables and regions associated with high p_T events	6
2.1	A plan view of the MPS as used in the present experiment (E260)	13
2.2	The calculated efficiencies for detection of pions, kaons and protons for run numbers 393 - 505	21
2.3	Schematic diagram of cylindrical hydrogen target	22
2.4	PWC wire winding apparatus	26
2.5	PWC wire tensioning apparatus	29
2.6	Schematic drawing of the general contruction features of the UICC PWC's	31
2.7	Spark chamber pulsing system	34
2.8	Typical single event display picture	35
2.9	Calorimeter structure	37
2.10	p_T and Feynman x regions covered by the calorimeter modules	38
2.11a	Plan view of spectrometer Cerenkov counter (C1)	41
2.11b	Elevation view of spectrometer Cerenkov counter	42
2.11c	Mirror sampling of spectrometer Cerenkov counter	43
2.12	p_T and Feynman x regions covered by C1 mirrors	46
2.13a	Schematic of trigger electronics; derivation of the spark chamber trigger from beam counters and logical requirements	50
2.13b	Resets and the ADC load signal	51

LIST OF FIGURES (Continued)

Figure		Page
2.14	An overview of the PDP11 - MPS hardware interaction	55
3.1	Schematic drawing showing the calorimeter response to particles with incident momentum (a) less than the bias and (b) far above the bias	71
3.2	The apparent p_T seen by a calorimeter module when a particle is bent into it by the magnet	72
3.3	The average charged multiplicity into a single calorimeter module with a HIPT trigger	76
3.4a,b	A Monte Carlo calculation of the trigger rate difference between pions and protons assuming the response is to kinetic energy. (a) Only one incident particle; (b) incident trigger and one additional pion	78
3.4c,d	(c) The trigger and two additional pions; (d) the trigger and three additional pions	79
3.4e	(e) An average of 0 to 3 pions accompanying the trigger	79
3.5	The expected average efficiency of the C1 mirrors in front of the calorimeters	91
3.6a	The number of effective photoelectrons for a π tag	93
3.6b	The same as Figure 3.6a but for a πK tag	94
3.7a	The number of effective photoelectrons for a Kp tag	95
3.7b	The number of effective photoelectrons for particles judged too close to threshold	96
3.8	A plot of the probability that a πK could be a π vs. the probability that it could be a K from a pulse height analysis	101
3.9	Schematic of the reclassification of πK's into π's and K's from a pulse height analysis	102
3.10	Pulse height distribution of Cell 4 with incident particles having momentum between (a) 10 and 20 GeV/c and (b) 20 and 30 GeV/c	103

LIST OF FIGURES (Continued)

Figure		Page
3.11	Number of particles entering the trigger module with the HIPT trigger	109
3.12	A plot of E_{mod}/p vs. p_T for all particles entering the trigger module	111
3.13	Rapidity distribution of particles with $2.0 \leq p_T < 3.0$ GeV/c into the trigger module	112
3.14	Transverse momentum distributions for particles chosen according to the (a) HIPT and (b) LOPT triggers	113
3.15	Azimuthal angle distribution of trigger particles	118
3.16	Sketch of bend-in particles and bend-out particles	121
3.17	The ratio $\frac{d\sigma}{dp_T}(pp \to h^+X)/\frac{d\sigma}{dp_T}(pp \to h^-X)$ for left and right side triggers and low and high bias triggers separately	128
3.18	Our charge production ratio from pp collisions compared to data from the Chicago-Princeton group	131
3.19a,b	The ratios $\frac{d\sigma}{dp_T}(pp \to hX)/\frac{d\sigma}{dp_T}(pp \to h'X)$ uncorrected for calorimeter response or Cl efficiency. The hadrons h/h' have been tagged by Cl as (a) π^+/π^-; (b) π^+/Kp^+	134
3.19c,d	Same as Figure 3.19a but for h/h' as (c) π^-/Kp^-; (d) Kp^+/Kp^-	135
3.20a,b	The ratios $\frac{d\sigma}{dp_T}(pp \to hX)/\frac{d\sigma}{dp_T}(pp \to h'X)$ which have been corrected for efficiencies of both the calorimeter and Cl. h/h' is tagged as (a) π^+/π^-; (b) π^+/Kp^-	137
3.20c,d	Same as Figure 3.20a but for h/h' as (c) π^-/Kp^-; (d) Kp^+/Kp^-	138
4.1	Ratios of positive charge to negative charge production cross sections for (a) π^+p, (b) π^-p and (c) K^-p collisions	141

LIST OF FIGURES (Continued)

Figure		Page
4.2a,b	The ratios $\frac{d\sigma}{dp_T}(\pi^- p \to hX)/\frac{d\sigma}{dp_T}(\pi^- p \to h'X)$ which have been corrected for Cl efficiency. The hadrons h/h' have been tagged by Cl as (a) π^+/π^-; (b) π^+/Kp^+	143
4.2c,d	Same as Figure 4.2a but for h/h' as (c) π^-/Kp^-; (d) Kp^+/Kp^-	144
4.3	(a) A sketch of the effect of the magnet aperture on the acceptance. (b) A qualitative expectation of the acceptance as a function of θ	147
4.4	Charge dependent limitations of the magnet aperture	149
4.5a	A θ distribution of away side particles having $0.3 \leq p_T < 1.0$ GeV/c	150
4.5b	Same as Figure 4.5a but the away particles are in the region $1.0 \leq p_T < 2.0$ GeV/c	151
4.6a	A θ distrubition of bend-in particles on the away side having $p_T \geq 0.3$ GeV/c	152
4.6b	Same as Figure 4.6a but for away side bend-outs	153
4.7	Fractional amount of background above a given p_T. The background is assumed to follow an $\exp(-6p_T)$ spectrum	156
4.8a	The p_T spectra of the trigger particles used in the away side analysis for the reactions $pp \to h^+X$ and $pp \to h^-X$	159
4.8b	Same as Figure 4.8a but for the reactions $\pi^- p \to h^+X$ and $\pi^- p \to h^-X$	160
4.8c	Same as Figure 4.8a but for the reactions $pp \to \pi^+X$ and $pp \to Kp^+X$	161
4.8d	Same as Figure 4.8a but for the reactions $\pi^- p \to \pi^+X$ and $\pi^- p \to Kp^+X$	162
4.9a-d	The away side ratio of positive hadrons to negative hadrons opposite a charged trigger; (a) $\pi^+ p \to h^+X$; (b) $\pi^+ p \to h^-X$; (c) $pp \to h^+X$ (d) $pp \to h^-X$	165
4.9e,f	Same as Figure 4.9a but for (e) $\pi^- p \to h^+X$; (f) $\pi^- p \to h^-X$	167

LIST OF FIGURES (Continued)

Figure		Page
4.10	A comparison of the E260 p induced away side ratios with other Fermilab and ISR experiments	170
4.11	The away side ratio of positives to negatives opposite a trigger tagged by Cl as a π or Kp for (a) π^+p, (b) pp and (c) π^-p collisions	174
5.1	Schematic of the underlying structure of high p_T scattering for AB → CX	178
5.2	(a) Quark distributions within the proton and (b) quark distributions within the pion	183
5.3	Decay functions for quarks into mesons and for gluons into π^0's	185
5.4	The elementary subprocesses for the CIM models	188
5.5	The charged and π production ratios compared to the QCD model and CIM models for pp collisions	190
5.6	(a) The charged and π production ratios for π^-p collisions compared to the FF and CS parameterizations; (b) The charged production ratios for π^+p collisions compared to FF and CS	193
5.7a	The lowest order QF and CIM subprocesses for pp collisions producting π or K triggers	196
5.7b	Same as Figure 5.7a but for π^-p collisions	197
5.7c	Same as Figure 5.7a but for π^+p collisions	198
5.8	(a) A sketch of the underlying scattering in the cd center of mass and (b) with quarks a and b with a transverse momentum in the trigger direction	201
5.9	The possible scattering diagrams in QCD for (a) pp collisions, (b) π^+p collisions and (c) π^-p collisions	204
5.10	QCD predictions for the away side data of (a) E494 and (b) BFS	206
5.11	The same as 4.11 but we now compare various Fermilab and ISR data to our p induced data	211

CHAPTER I

INTRODUCTION

Since the beginning of modern physics, science has probed deeper and deeper into matter to determine its ultimate characteristics. It is interesting to recall some history. At the end of the nineteenth century when clues as to what might explain the structure of the atom were sought, J. J. Thomson proposed that the atom was essentially negative point charges interspersed in a continuous positively charge medium. This model, of course, was succssful at interpreting the periodicity found in Mendeleev's atomic table. However, in the early part of the twentieth century, Rutherford noticed a strange anomaly in scattering α particles off gold atoms. The angular distribution of scattered particles could not be accounted for by using the Thomso model. In particular, Rutherford noticed relatively large yields of scattered α particles at large angles, or equivalently, at large momenta transverse to the incident particle direction. Indeed, it was postulated that if the atom contained just a pointlike charged mass at its center, then the scattered α particles correctly followed the observed center-of-mass distribution

$$\frac{d\sigma}{d\Omega^*} \sim \frac{1}{\sin^4\theta^*/2} \sim \frac{1}{p_T^4} \tag{1.1}$$

where p_T, the transverse momentum of the scattered α particles relative to the incident direction, is $p_{lab}\sin\theta p^*=\sin\theta^*/2$. Rutherford then proposed the current notion of the atom consisting of a hard-core nucleus at the center with the electrons orbiting about this center.

In the same spirit as Rutherford, physics in the 1960's had consisted of scattering experiments searching for clues as to what

the basic constituents of the nucleon may be. The early notion of the proton being a gray sphere Lorentz contracted in the direction of its motion was certainly applicable to diffractive type scattering. In the 1970's when accelerators at Fermilab and the ISR came into operation, the push deeper into the proton continued. Again another unexpected anomaly arose. As seen in Figure 1.1, the cross section for the inclusive reaction $pp \rightarrow \pi^0 X$ at large transverse momentum departed from the e^{-6p_T} behavior seen at low p_T to a form easily parameterized by[1]

$$E\frac{d^3\sigma}{dp^3} \simeq \frac{120}{(1+p_T^2)^4} e^{-13x_T} \text{ mbarns/GeV}^2 \qquad (1.2)$$

where $x_T = 2p_T/\sqrt{s}$ and s is the center of mass energy. Once again the large yield of particles at high p_T and the form of Eq. 1.2 may lead us into postulating that our spherical proton really consists of pointlike entities somehow bound together.

Recent interpretations of deep inelastic lepton scattering in terms of the Quark-Parton model[2,3,4,5] give support to the notion that when two hadrons collide to produce a hadron at large p_T, constituents of the initial hadrons may scatter at large angles and then themselves fragment into the observed high p_T secondaries. Figure 1.2 shows that under this assumption there may be four "jets" produced by this mechanism. Two quarks, c and d, are scattered at wide angles and subsequently fragment into either a group of low momentum particles summing to the original quark momentum (Jet), or into one particle which takes a large fraction of the momentum (Single Particle) plus a few additional slow hadrons. The remaining beam (target) constituents will then fragment into hadrons in the forward (backward) direction.

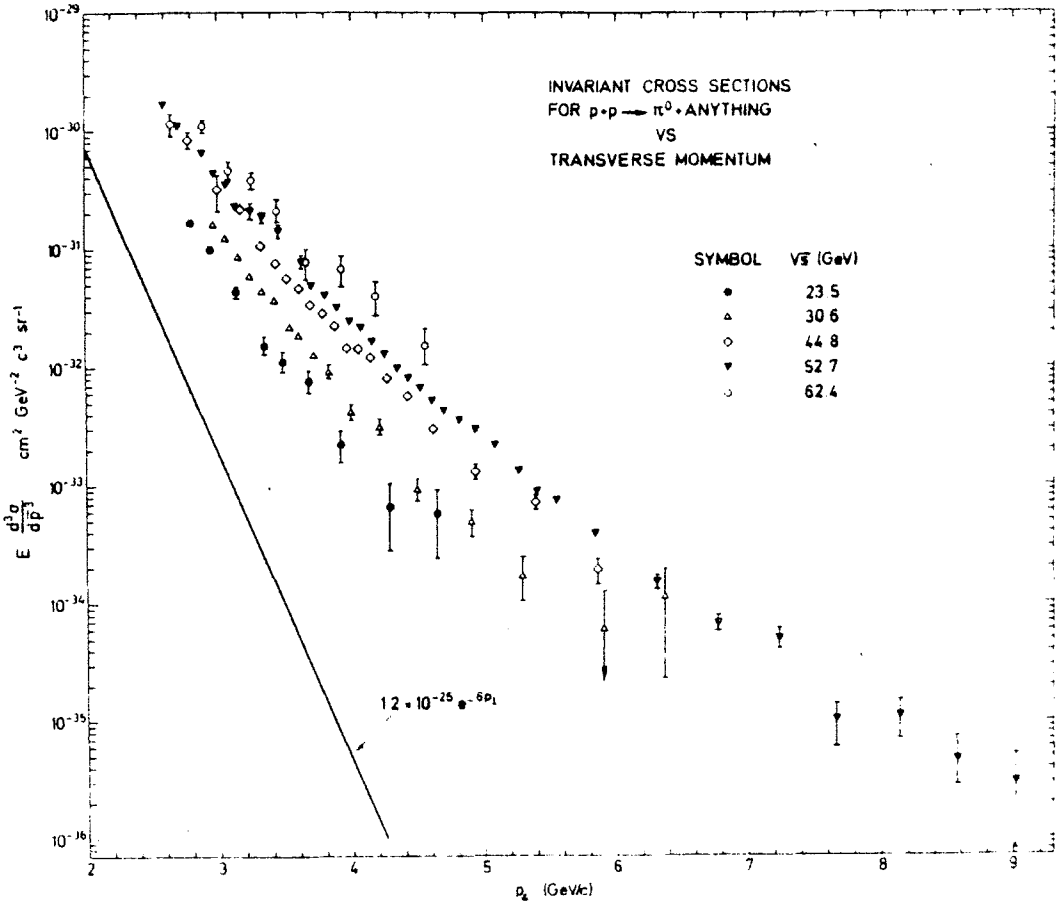

Figure 1.1 The transverse momentum dependence of the invariant cross section for inclusive π^0 production at various center of mass energies. The solid line is the extrapolation of the exponential fall-off at low p_T.

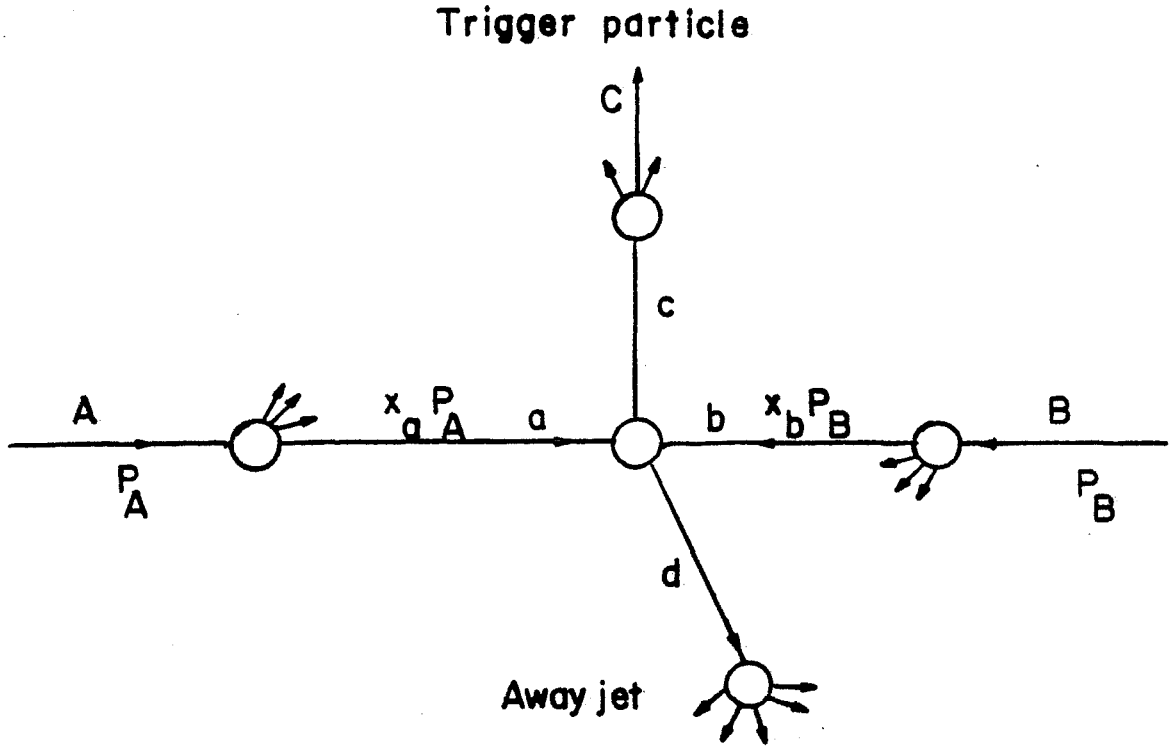

Figure 1.2 The expected dynamics of the inclusive reaction $AB \rightarrow CX$ at high p_T. Scattered constituent c fragments into the trigger particle and constituent d fragments into the away jet.

At the present time, most high p_T experiments have been performed with the single particle trigger. Theoretical biases have prompted a study of the region around the trigger particle - the trigger side - and in the hemisphere 180^o in azimuth opposite the trigger particle - the away side. Figure 1.3 shows the relevant center of mass kinematic regions and variables associated with a single particle trigger. Note that the trigger and and away sides are not rigorously defined but are chosen according to a particular experiment or experimenter's intuition.

Early investigations of high p_T events starting in 1973 tried to answer the question of how the structure of associated hadrons was changed relative to that of typical inelastic events if one required the presence of a particle of large p_T. At the ISR, the Pisa - Stony Brook group[6] measured the multiplicity of charged hadron associated with a high p_T photon and found a dramatic enhancement ove the inelastic events. The increase of the away side multiplicity became very dramatic as one selected associated hadrons of higher p_T. The distribution in polar angle of away particles was found to be approximately constant over the range $40^o \lesssim \theta^* \lesssim 140^o$ while the distribution in azimuthal angle peaked at 180^o opposite the trigger. This broad enhancement was suggestive of a "jet" or "fan" of particle opposite the high p_T photon. Similar distributions were later reported opposite a π^o trigger by the Aachen-CERN-Heidelberg-Munich[7] (ACHM) and CERN-Columbia-Rockefeller[8] (CCR) groups at the ISR. The latter showed the away side multiplicities were not inconsistent with a momentum conservation model but that the trigger side multiplicities could not be explained by the same model. Later groups at the ISR, CERN-Columbia-Rockefeller-Saclay[9] (CCRS), CERN-Collége de France

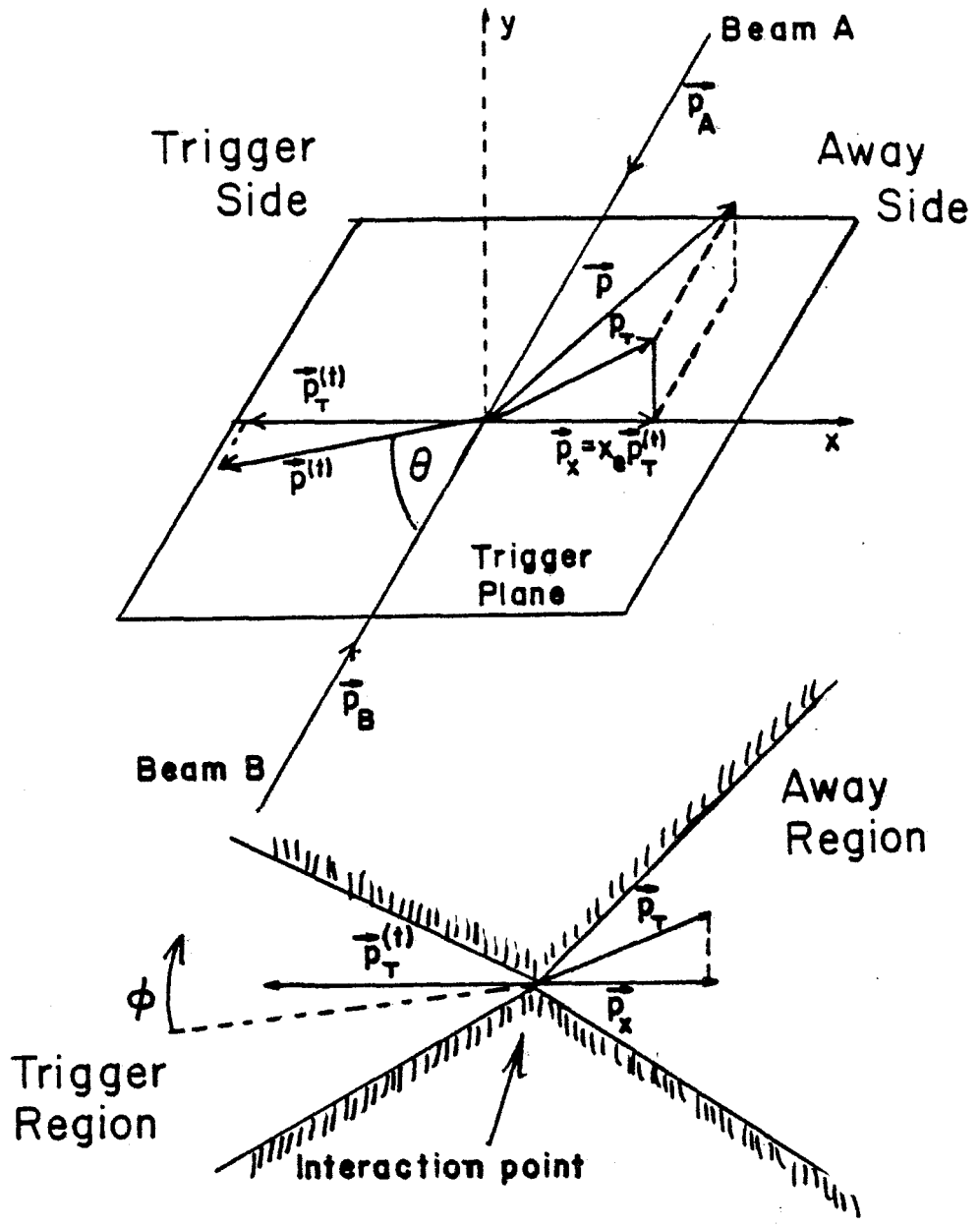

Figure 1.3 Center of mass kinematic variables and regions associated with high p_T events.

Heidelberg-Karlsruhe[10] (CCHK) and British-French-Scandinavian[11] (BFS have investigated the two particle correlation function between a charged trigger particle or π^0 and associated trigger side and away side hadrons. To gain further insight into events that have the trigger particle produced at angles other than 90°, the polar angle of the trigger was chosen as far forward as 17° in the center of mas. They showed that as the p_T of the associated hadron increases, the correlation function with either side particles becomes several orde: of magnitude larger than for inelastic events. The probability of finding a second particle of high p_T on the same side as the trigger is greatest when the associated particle is within ~ 1 unit of rapidity and ~ 35° of azimuth of the trigger. Similar to the Pisa - Ston; Brook result, the away side hadrons were found to be spread out uniformly into about 2 units of rapidity and, if the trigger p_T is relatively large or the event multiplicity high, are independent of the rapidity of the trigger particle. Momentum conservation alone is not sufficient to explain all the observed distributions and correlations

By the end of 1976 it became clear from correlation measurements in rapidity, ϕ and p_T that, consistent with all notions of the hard collisions of two proton constituents, a two-jet structure probably existed in high p_T events. CCHK, Daresbury-Illinois-Liverpool-Rutherford[12] (DILR) and BFS[13,14,15] at the ISR and a Columbia-Fermila Stony Brook group[16] (E494) at Fermilab turned to quantum number correlations in high p_T single particle events. The CCHK group, using a positively charged trigger, measured the ratio of away side positive hadrons to away side negative hadrons for various intervals of associated hadron rapidities. Identifying the trigger as π, K or p, the DILR group studied the away multiplicites as a function of

trigger type in pp collisions. For 90° triggers, no effect was seen for different types of triggers. But as the trigger went forward, a dependence on trigger type was noticed in the multiplicities as well as the rapidity spectra. Along the same lines as the CCHK group, the BFS collaboration looked at the correlation function with an identified trigger and associated secondaries on the away and trigger sides. No quantum number dependence was seen for associated hadrons with $p_T \leq 0.6$ GeV/c. With associated hadrons of larger p_T, both trigger and away sides showed charge dependent effects along with a slight dependence on the triggering particle's type. Furthermore, an early result reported by BFS[14] showed that for away hadrons with $p_T \geq 1.5$ GeV/c and triggers between 3 GeV/c and 4.5 GeV/c, there was a dramatic depletion of the number of negative hadrons opposite a K^- or $\bar{p}$ trigger. This effect seemed to be a strong function of the kinematic regions chosen in the away-side definition. As the p_T of the trigger went down, this depletion of negatives with $p_T \geq 1.5$ GeV/c became less striking. In a later analysis using slower particles on the away-side and carefully selecting the kinematic cuts, BFS[15] report that there is only a charge dependent effect and not an away-side dependence on particle type.

The early BFS results are inconsistent with some popular theoretical models[5,17,18] and are not confirmed at Fermilab by E494. Here the number of particular hadrons (π, K or p) with $p_T \geq 2.25$ GeV/c opposite an identified trigger with p_T between 3 GeV/c and 4 GeV/c in 400 GeV pBe collisions shows no drastic effect for triggers other than $\bar{p}$ for which a depletion of positives occurs. There is, as noted by BFS, a slight excess of positive particles on the away-side if the trigger is negative.

To gain further insight into the mechanisms responsible for the correlations reported above it will be the purpose of this work to present additional correlation studies involving baryon number, charge and strangeness obtained in events with a high p_T particle. These events were obtained from a Fermilab experiment using a multi-celled gas Cerenkov counter to identify final state particles in a calorimeter triggered multiparticle spectrometer (E260). Besides the advantage of being able to study all secondaries in the forward direction with almost full acceptance, this experiment has the unique feature of being able to select π, K or p beams of both polarity. Quarkologists will argue that the correlations measured will be a strong function of the types of quarks in the initial state. Data with various beams are invaluable in determining the parameters of models trying to explain high p_T phenomena or determining their worth.

A verification of the BFS or E494 results will be attempted here using incident protons. However, the comparison of our results to these experiments may be complicated by the fact that each experiment explores different kinematic regions. The most important variables here may be the center of mass energy $\sqrt{s}$, the trigger angle, and the variables relating to the severity of the collisions - x_T and x_e. x_T is the fraction of the available incident momentum that the trigger particle takes in the transverse direction, i.e., $x_T = 2p_T/\sqrt{s}$. x_e is a measure of how fast the away particles are going compared to the trigger particle. $x_e = \vec{p}_{Ta} \cdot \vec{p}_T / |\vec{p}_T|^2$, where $\vec{p}_{Ta}$ is the transverse component of momentum of the away particle. As shown by CCHK, the away side particles are dependent on their rapidity and therefore the away side rapidity, y, may be an important variable. For comparison, Table 1.1 lists the kinematic regions spanned by the ISR experi-

Experiment	X_T	Trigger θ	x_e	Away y	$\sqrt{s}$(GeV)	Ref
E260	$0.15 \leq X_T \leq 0.5$	$104^o \leq \theta \leq 67^o$	Xe $\geq$ 0.4	$0 \leq y \leq 0.88$	19.4	present work
E494	$0.22 \leq X_T \leq 0.29$	90^o	Xe $\geq$ 0.75	$\|y\| \leq 0.32$	27.4	16
CCHK	$0.06 \leq X_T \leq 0.19$	$9^o \leq \theta \leq 21^o$	Xe $\geq$ 0.1	$\|y\| \leq 1$	53	10
DILR	$X_T \geq 0.05$	90^o, 62.5^o, 45^o	Xe $\geq$ 0.2	$\|y\| \leq 0.5$	45	12
BFS-Early	$0.11 \leq X_T \leq 0.17$	90^o	Xe $\geq$ 0.33	$\|y\| \leq 1$	53	14
BFS-Recent		90^o	*	*	53	15

* This analysis constructs a jet of particles opposite the trigger by adding all particles with $p_T > 0.36$ GeV/c. It then required that $p_T^J > 1.5$ GeV/c, $|y^J| < 2$ and $|\phi^J| < 30^o$ where these variables refer to the constructed jet.

TABLE 1.1 Kinematic regions of Fermilab and ISR experiments that measure correlations in high p_T events.

ments - CCHK, DILR and BFS - and the Fermilab experiments - E494 and this experiment E260 - as used in their results.

In Chapter II of this report we will detail the experimental apparatus including the calorimeter and Cerenkov counter, and the manner in which data were taken. A summary of the construction techniques for the Proportional Wire Chambers will also be given. Chapter III describes the data sample, data reduction techniques, trigger definitions and the procedure for Cerenkov identification of the secondary hadrons. We will compare some of our data with existing data to show that our analysis techniques are correct. Our analysis will be of events where the trigger is formed by requiring only one particle of high transverse momentum, and using the methods described in Chapter III we will then present correlation data in Chapter IV for these single particle triggers. Finally, in Chapter V, we will discuss hard scattering model predictions and make corresponding comparisons with our data.

CHAPTER II

EXPERIMENTAL APPARATUS AND TECHNIQUES

2.1 Overview

Experiment 260 was performed in the Meson Lab at the Fermi National Accelerator Laboratory (Fermilab) by a collaboration between the following institutions: Caltech, Fermilab, Indiana University, UCLA and UICC. These institutions were responsible for the design and construction in 1975 of the Multiparticle Spectrometer[21] (MPS), on which the jet experiment, E260, was performed. The major goals of the experiment were:

a) the comparison of the jet cross section to the single particle cross section at high p_T using both meson and proton beams[20];

b) to determine whether hadron induced jets were identical to lepton induced jets[19]; and

c) the determination of quantum number flow in high p_T events between the initial state, the trigger and all associated hadrons.[44]

A plan view of the spectrometer as used for E260 is shown in Figure 2.1. A positive or negative 200 GeV/c beam was incident on a 12 inch by 2 inch cylindrical liquid hydrogen (LH_2) target. Large transverse momentum events were selected by triggering on energy deposited in Pb-Fe-scintillator calorimeters situated at 102 ± 39 mrad on either side of the beam. The mean triggering angle is then equivalent to 90° in the center of mass (CMS) at 200 GeV/c. All accompanying particles between 0° and ~130° in the CMS were then able to have their momentum reconstructed from 18

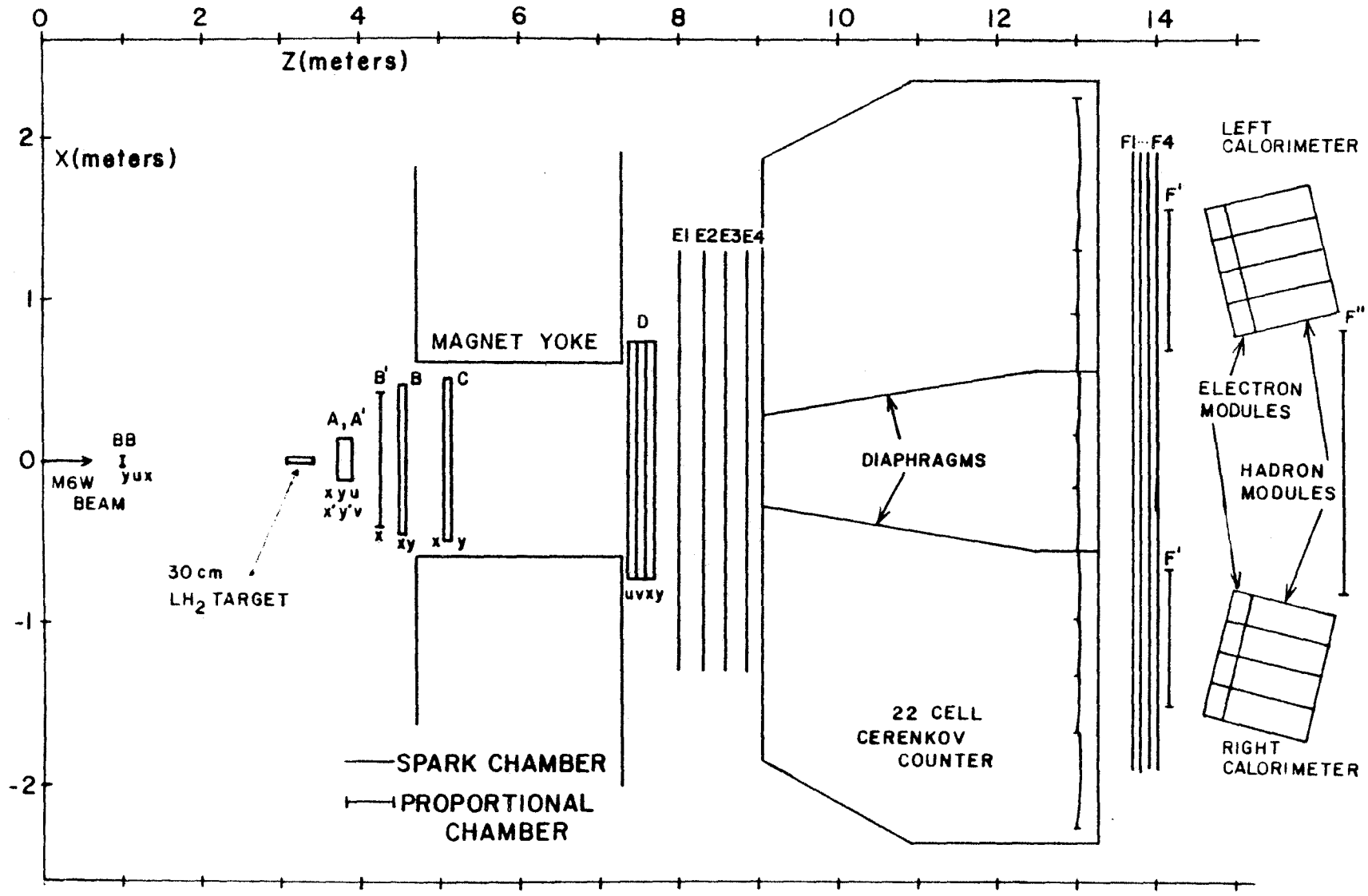

Figure 2.1 A plan view of the MPS as used in the present experiment (E260)

proportional chamber planes and 16 spark chamber gaps and, in most cases, identified as a π, K or p from a 22 cell Cerenkov counter.

A test run of the jet experiment beginning in December, 1975, enabled the spectrometer to be thoroughly debugged and provided useful preliminary data from a berryllium target[20]. The present analysis has a total of 938,000 triggers available from the 200 GeV beam on the hydrogen target obtained during the summer of 1976.

2.2 Experimental Technique

a. Beam and Beam Cerenkov Counters

The M6 west beam incident on the MPS is a high resolution, unseparated, positive or negative beam, with reasonable flux from 10 GeV/c to 200 GeV/c. For 10^{13} 400 GeV protons per spill onto an 8" Be meson target, a positive flux of 5×10^6/spill and a negative flux of 2×10^6/spill at 200 GeV were easily obtained with momentum resolution still better than 1%. Table 2.1 lists the major beam parameters[21]. The spill time (ramp flat-top) was 1.75 seconds and the main ring repetition rate was normally about 15 seconds.

The momentum, flux and beam sizes at any of the four foci were all adjustable by the experimenters via Fermilab's remote console to a MAC 16 computer monitoring and controlling magnet currents, voltages and collimator openings. The beam sizes at each focus were monitored by Fermilab Segmented Wire Ionizing Chambers (SWIC's) with resolutions of 1 mm. The currents in the momentum selecting magnet string were monitored at the MAC console and were not allowed to vary by more than about 5 amps out of 5000. The field in this magnet string was known at any time by checking the output of an NMR probe placed inside an identical bending magnet whose coils were connected in series with the momentum selecting string. Hysteresis

Target Size for Listed Properties			
Width		±0.02	inch
Height		±0.02	inch
Length		8.00	inch (Be)
Production Angle	θ_p	3.0	mr
Lab Angle	θ_v	0.7	mr
	θ_h	2.5	mr
Momentum Range			
Minimum	$P_{o_{min}}$	10	GeV/c
Maximum	$P_{o_{max}}$	200	GeV/c
Solid Angle	$\Delta\Omega$	1.34	μst
Angular Acceptance			
Horizontal	$\Delta\theta_h$	± .56	mr
	$\Delta\theta_v$	± .76	mr
Momentum Bite			
Minimum	$\Delta p/p$	±0.014	%
Maximum	$\Delta p/p$	1.0	%
Dispersion At Mom. Slit	$\frac{\Delta X}{\Delta p/p}$	2.48	inch/%
Properties at Experiment	($\Delta p/p$ = ±0.014%)		
Horizontal Width		±0.031	inch
Horizontal Divergence		±0.36	mr
Vertical Height		±0.026	inch
Vertical Divergence		±0.67	mr

Table 2.1 M6 West beamline parameters.

was only about 10 gauss out of 18 Kgauss at 200 GeV beam. Therefore, the absolute beam momentum was known very accurately under the assumption that the series reference magnet had the exact field as the actual beamline magnets. The average beam operating conditions during the experiment were:

Intensity

Positive: 4.5×10^6/spill

Negative: 2.5×10^6/spill

Beam size at LH_2 target

Horizontal: 9 ± 2 mm

Vertical: 7 ± 2 mm

In addition to the standard Fermilab SWIC's, the experimenters inserted 8 proportional wire chamber (PWC) planes in the beam to aid in the reconstruction of 2 or more beam particles within the resolution time of the PWC's, or 2 or more particles in an RF bucket. The beam size was measured in the beam chambers and SWIC's at the fourth focus and we estimate the maximum error in size determination throughout the entire experiment as 2 mm.

Further, the incident beam particle was tagged by four beam Cerenkov counters. Table 2.2 lists their properties and Table 2.3 lists the expected yields of π, K and p beam particles for 190 and 200 GeV/c beams with the main ring targeting at 400 GeV. Under normal operation PRUSS and CO were set at the π threshold, BDIFF was set on the proton peak and DISC was set on the kaon peak with a K signal defined as a 6-fold coincidence of any of the 8 photomultipliers. For low beam intensity ($\lesssim 10^5$/spill) the Cerenkov counters operated at $\gtrsim$ 95% efficiency. However, due to beam divergence in high intensity operation, the threshold counters operated

Name	Type	Z Position (center)	Length	Number & Type of Phototubes	Annulus Angle	Max Gas Pressure
Pruss	Threshold (but has anti so can be used as differential)	911 ft	96 ft	2-RCA^{C}31000M	5 mr	15 psiq
CO	Threshold	1079 ft	60 ft	1-RCA^{C}31000M	-	60 psiq
BDIFF	Differential	1245 ft	45 ft	3-Phillips	10 mr	15 atm
DISC	Differential	1322 ft	19 ft	8-RCA^{C}31000M	24.5 mr	20 atm

Table 2.2 Parameters of M6 beam Cerenkov counters.

Momentum	Positive Beam			Negative Beam		
(GeV/c)	π^+	K^+	P	π^-	K^-	$\bar{P}$
190	.206 ± .020	.026 ± .003	.768 ± .020	.946	.044 ± .004	.010 ± .001
200	.180 ± .020	.023 ± .002	.797 ± .020	.949	.043 ± .004	.008 ± .001

Table 2.3 Hadron beam composition in M6 obtained from 300 GeV on target measurements and then scaled to 400 GeV on target. Fluxes have been corrected for decay from the third to fourth focus.

at $\lesssim$ 85% efficiency. The DISC counter frequently failed due to bad electronics and leaks in the counter. Using the methods described in Section 2b of Appendix A, in Figure 2.2 we plot the efficiencies for detecting a π, K and p using these counters. The low π efficiency is due to pions firing the BDIFF counter and not inefficiencies

b. Target

A schematic diagram of the liquid hydrogen target is shown in Figure 2.3. The hydrogen itself is a cylindrical cell 30.5 cm long by 4.8 cm. in diameter enclosed in a spun aluminum vacuum jacket. The center of the entrance flange was determined by sweeping the beam across the target and measuring the interaction rate as a function of beam position in a downstream PWC. After initially bringing the beam up it was always first checked that the beam was through the target's center.

c. Detectors

Properties of all the PWC's and wire spark chambers (WSC's) can be found in the MPS Workshop[21]. Here we just summarize and point out important points of the spark chambers and detail the construction of the PWC's made at Chicago Circle.

Scintillation Counters

Just upstream of the LH_2 target were two 1" x 1" x ¼" scintillation counters, SA and SB, used to define a beam particle. A third counter, SC, having a $\frac{3}{4}$" diameter hole, vetoes halo particles. About 11 meters downstream of the target was a 2" x 2" x ¼" scintillation counter, the "2X2", positioned to signal an interaction in or after the target. A pretrigger strobe, or interacting beam trigger, was formed by requiring $SA \cdot SB \cdot \overline{SC} \cdot \overline{2X2}$. The interacting beam rate was about 5%.

Figure 2.2 The calculated efficiencies for the detection of pions, kaons and protons, ε_C^{π}, ε_C^{K} and ε_C^{P}, as defined by Eq. A.10 of the appendix. Plotted in the figure are the efficiencies for runs 393 through 505. We indicate in the figure positive and negative beams. Arrows indicate calculated efficiencies which are off scale.

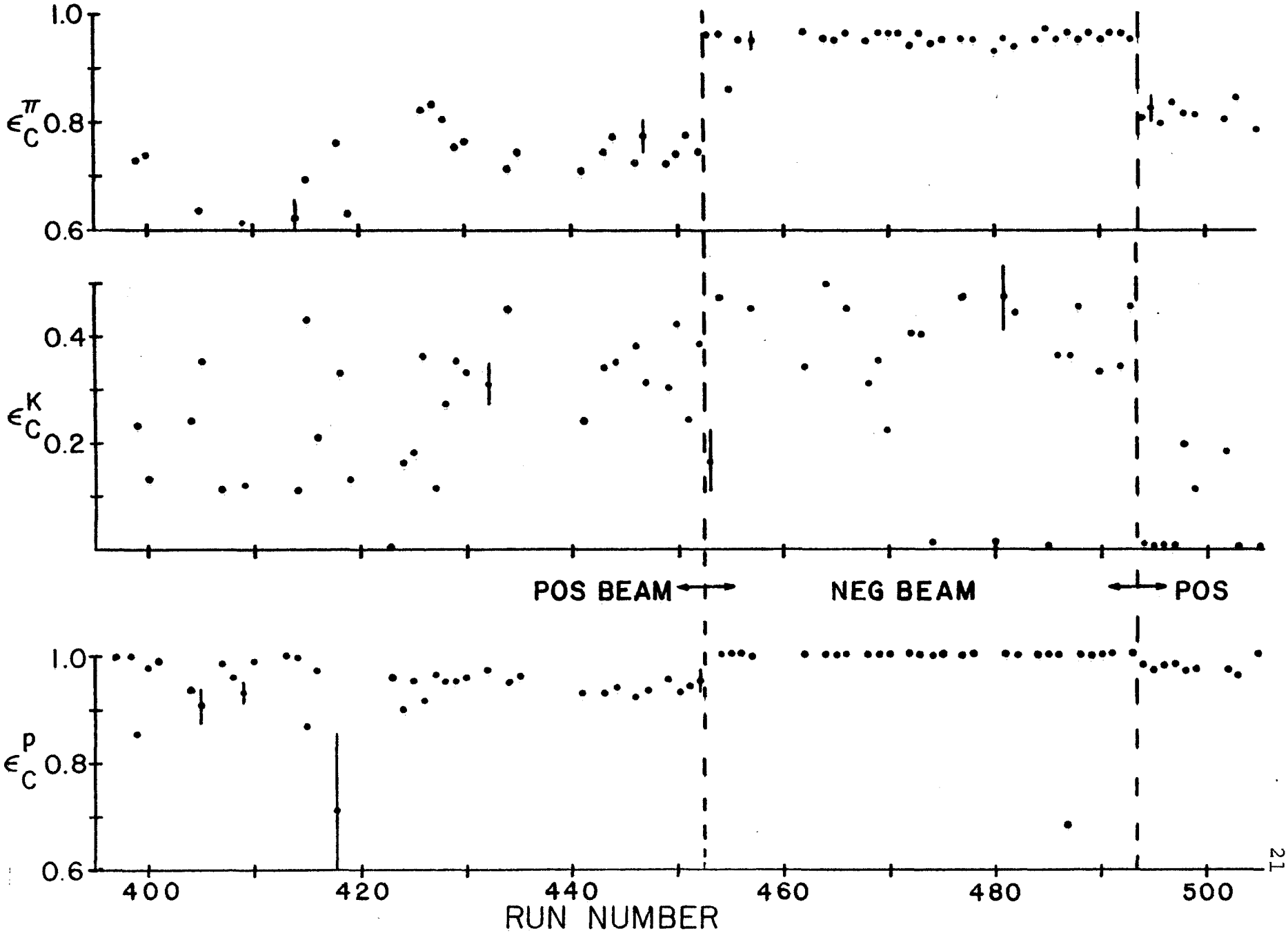
1.0
0.8
0.6
ϵ_C^π
0.4
0.2
ϵ_C^K
POS BEAM
NEG BEAM
POS
1.0
0.8
0.6
ϵ_C^P
400
420
440
460
480
500
RUN NUMBER

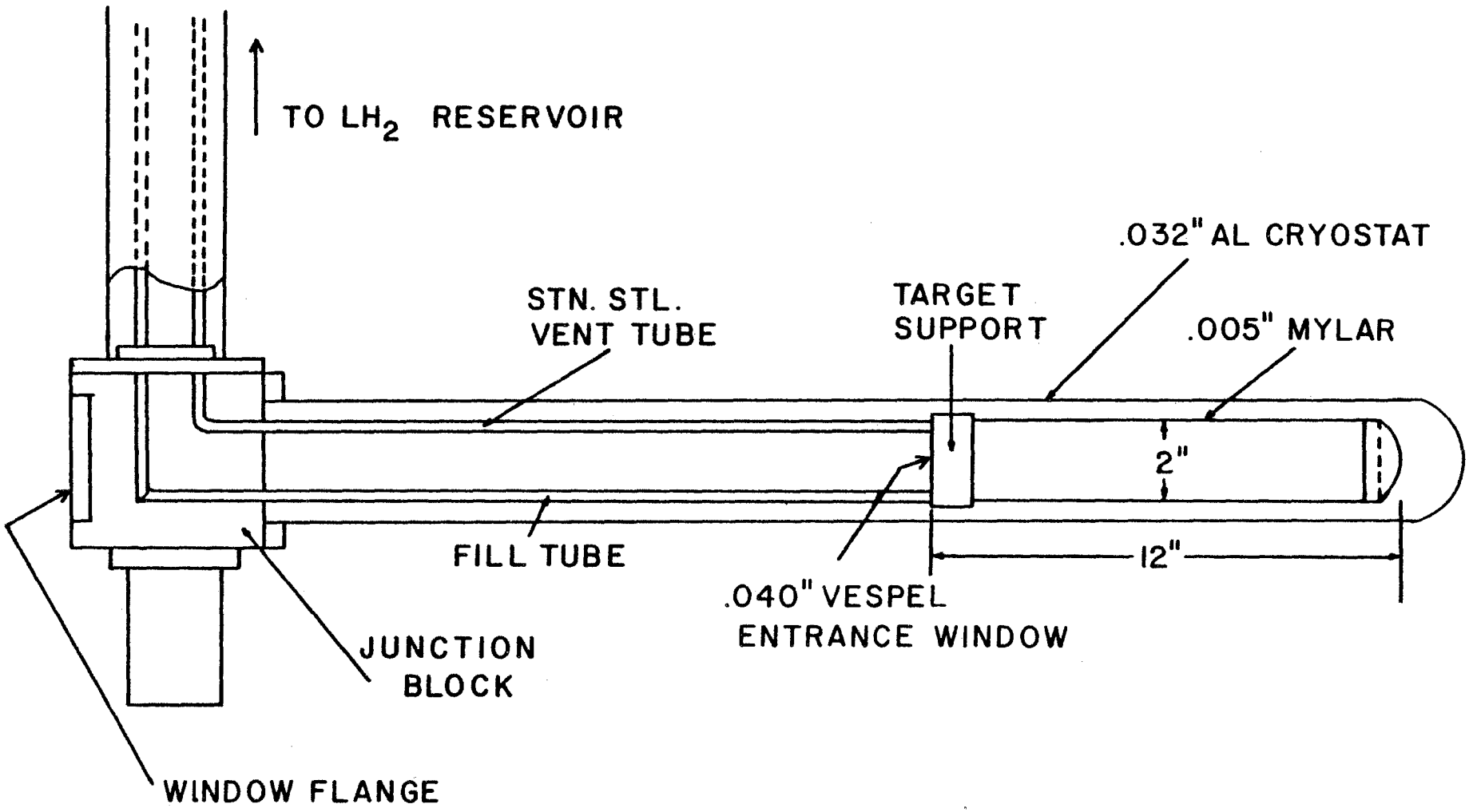

Figure 2.3 Schematic diagram of cylindrical hydrogen target.

Proportional Chambers - Overview

The entire front end of the spectrometer consits of PWC's - stations BB, A, A', B', B and C in Figure 2.1. The BB chambers were just upstream of the target giving the beam position to $\pm \frac{1}{2}$ mm. Slant BB chambers were installed to aid in reconstructing the interacting beam particle if there were more than one beam track found in the event. For high intensity running, as noted in Section 2.2a, multiple beam hits occurred in approximately 30% of the triggers.

Just downstream of the target were the A and A' PWC's, each plane of which had 256 wires. The A station consisted of planes with 1 mm wire spacing staggered by 0.5 mm with respect to the identically contructed A' chambers. A and A' both contained x and y coordinate planes. (We use a right hand coordinate system with z in the beam direction and y up. Particles bend in the x-z plane.) The only stereo chambers in front of the magnet were AU and, perpendicular to it, AV. These 1 mm planes were placed at an angle of 45° in the x-y plane. Essentially identical in construction were chambers B', B and C with a 13 wire/inch spacing and 512 wires in x and 320 wires in y. Chamber B', consisting of only an x plane, was situated 0.5 m downstream of the A chambers. Chambers B and C both measured x and y coordinates. B was located against the face of the analysis magnet while C was 25 cm into the magnet and thus slightly felt the effect of the magnet's fringe field.

In back of the magnet, PWC stations D, F' and F" were used essentially to make roads for the offline track finding. Except for the amplifiers used, all D chambers and the F" were of the same construction: 320 wires spaced at 5.5 wires/inch. DU and DV were

mutually perpendicular planes tilted at 15^{0} in the x-y plane. The D station occupied about 60 cm immediately after the magnet. Directly in front of the calorimeters were chambers F' with 130 wires each spaced at 4/inch. F" spanned the central region between the two calorimeters. Both F' and F" measured the x coordinate.

As detailed in the MPS Workshop[21], PWC signals were suitably amplified, delayed and placed at the inputs of parallel in serial out shift registers (SN7496). The pretrigger strobe loaded the shift registers.

All PWC's were plateaued using low intensity beam particles after long shutdowns or after a possible change in gas composition. After plateauing a check for dead wires was made by triggering on an interacting beam and fully illuminating the chambers. No thoroug study of chamber efficiency as a function of position has yet been made.

Proportional Chambers - Construction

Construction of chambers B, B', C, D, F' and F" followed a University of Chicago procedure[22]. Essential in the construction were a wire-winding apparatus, a wire stretching jig and a flat table.

Figure 2.4 shows the wire-winding setup. A piece of ¼" aluminum was rolled into a cylinder of approximately 30" height by 90" circumference and welded at the seam and to a ½" aluminum base. This drum was turned about its axis and the base machined round to provide a lip of about ½". An overall epoxy[23] casting enabled the originally out-of-round drum to be then machined concentrically with the previously machined base without measurable distortion due to machining stress relief. This resulted in a drum with a circum-

Figure 2.4 PWC wire winding apparatus. Wire from the spool is fed through the tensioning device mounted on the tool rest and is wound around the epoxy coated drum. Wire spacing is selected by appropriate settings of the lead-screw gear box.

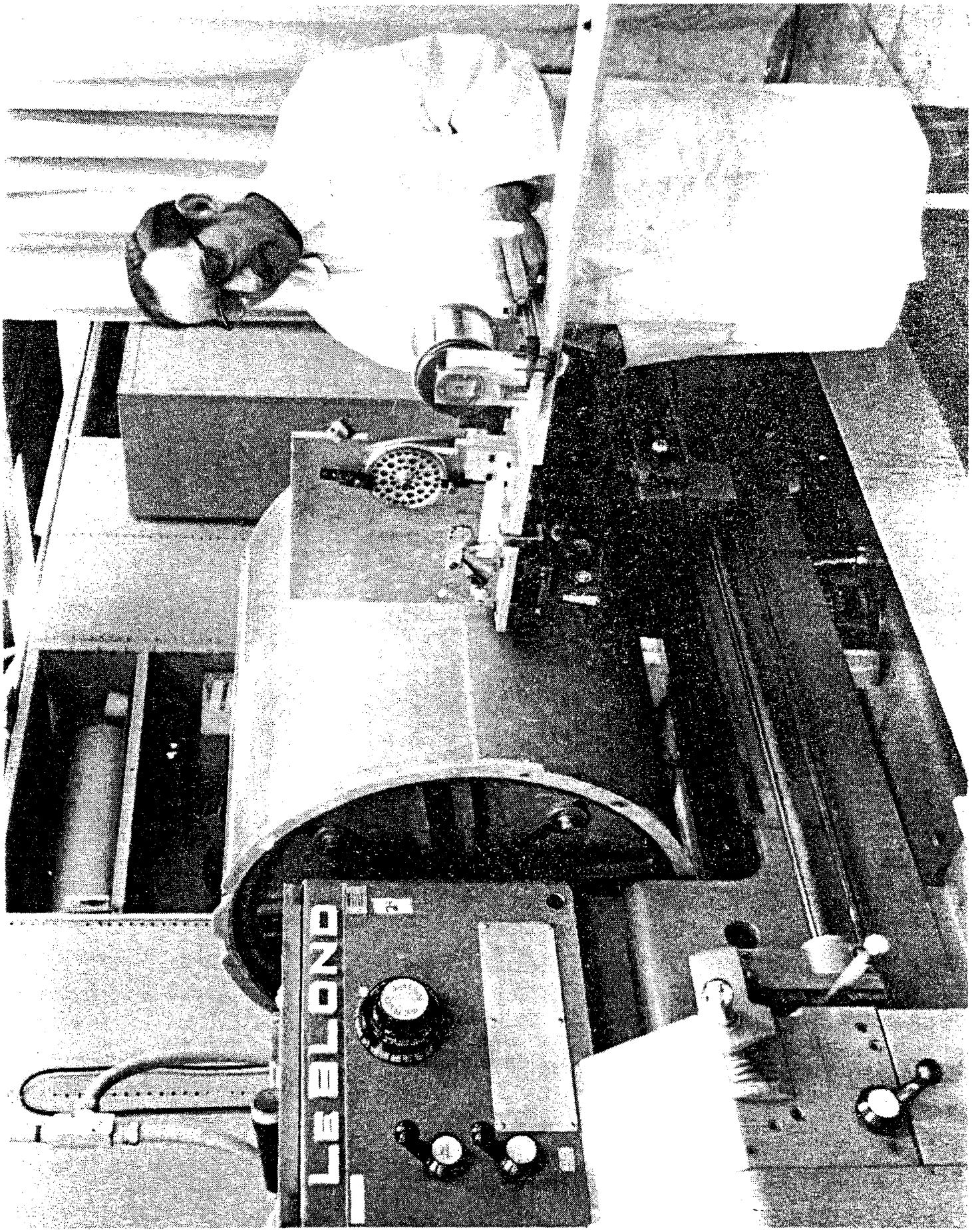
LELAND

ference of 94" and an effective length of 28½" with a radius variation of less than 0.003". The drum was mounted onto the chuck of a large LeBlond split-bed lathe. A wire feed mechanism with a slight frictional drag for tensioning was mounted on the tool rest. The last feed pulley of this device was carefully made to reduce the lateral play which might affect the wire spacing. Wire spacings were measured with a travelling microscope and found to be constant within $\pm$ 2%.

Two steel bars, 1" x 1/8", separated by about 4" were fastened axially to the drum and wires were then wound onto the drum, over the bars, at the required wire spacing. The wires were epoxied to the bars and later cut between the two bars and removed to the stretching jig as shown in Figure 2.5. Both tungsten and Be-Cu wires were wound in this manner. For sets of shorter wires, 4 bars were placed diametrically opposed on the drum.

Once on the stretcher the tension on the wires was roughly adjusted to the desired value by hanging a small weight at the center of one of the wires and measuring its deflection. Electrostatic resonance was used to fine tune the tension. A 2" wide aluminum bar connected to a high voltage sine-wave generator was placed ~1 cm under the stretched wire plane. A 1/16" piece of G10 was used between the bar and the wires to prevent arcing. The high voltage generator simply consisted of a laboratory sine-wave generator whose output was boosted by a 40 watt audio amplifier. This signal was fed into a step-up transformer and the "audio" turned up to just before the point where corona discharge was heard. The frequency of the generator was tuned to one of the resonant frequencies given a particular length wire and tension. The stretching jig then ad-

Figure 2.5 Apparatus for tensioning one set of wires removed from the wire winding drum. The fixtures which hold the ends of the wires are clamped to a lab table and can be levelled and positioned for the long or short wires. Also shown is the high voltage oscillator and heat lamps used to speed the setting of epoxy.

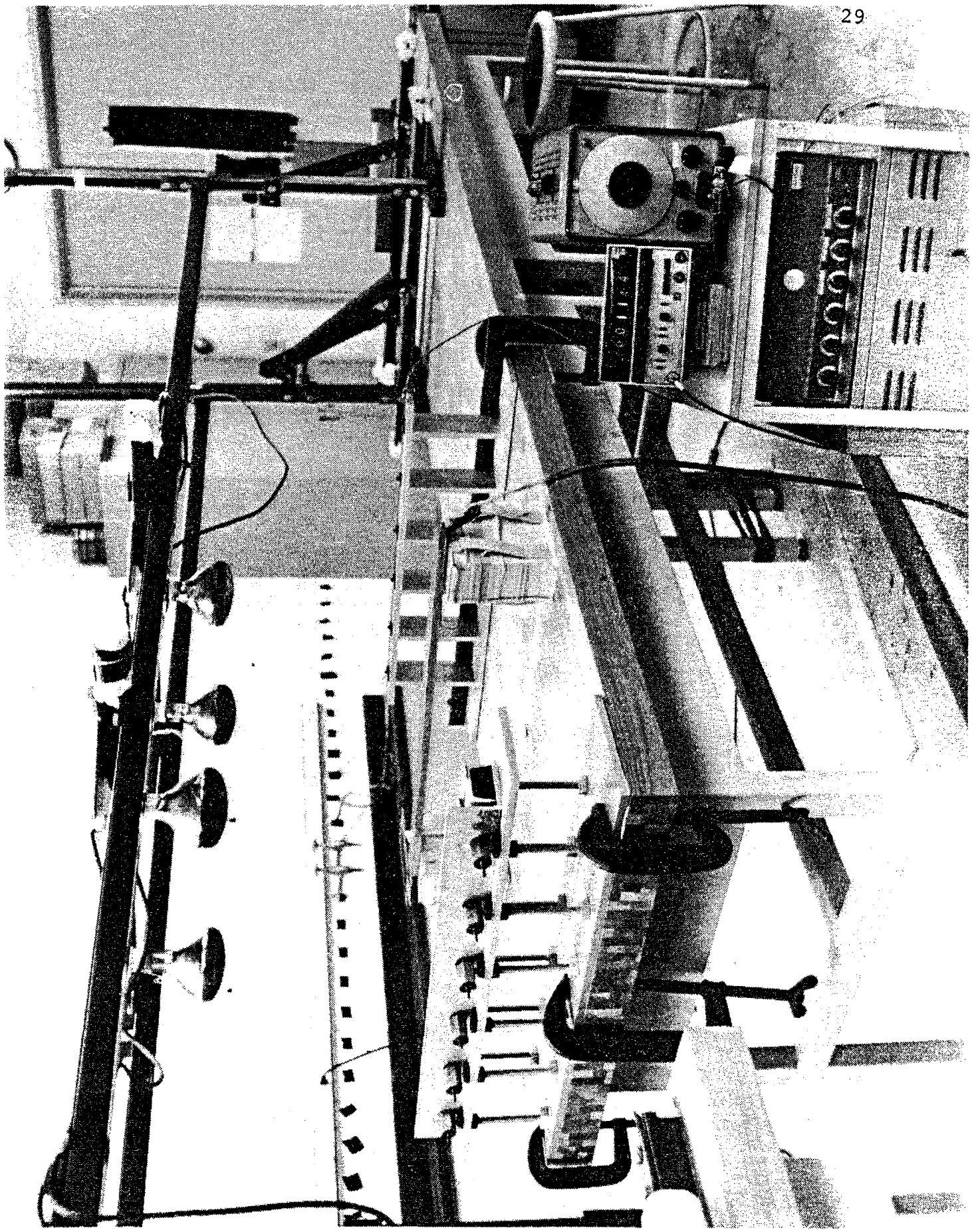

justed to get uniform tension across the 38" wide wire section. Using this method we were able to obtain tension uniformity to bette: than ~4%. The major cause of the variation is thought to be nonuniform drag from the wire unwinding itself from the spool onto the drum.

Figure 2.6 shows the general construction features of all the PWC's. For each plane of wires two aluminum frames were welded from rectangular box tubing of dimensions 3" x 2" x 1/8" wall. All G10 pieces needed to make the required gap were first saw cut and then ground to uniform thicknesses. Assembly began as the cathode suppor pieces were positioned and firmly clamped to a steel table that was measured to be flat to within 0.006". Epoxy thickened with diatomaceous earth was spread on the G10 pieces and the roughened Al frame placed on top of them. Due to the rigidity of the frame this procedure forced the wire plane to take the shape of the flat surface. Similarly, the anode mother board or dummy spacer was clamped down, spread with epoxy, and a frame with the cathode support already in place was placed onto these pieces. The gap was maintained by precision shims placed between the flat table and the cathode. The G10 extended over the inside edge of the frame by $\frac{1}{4}$" - $\frac{1}{2}$" to prevent high voltage breakdown to the frame and to provide a support for the gas window. We found that to reduce high voltage breakdown problems all sharp G10 edges had to be rounded and the G10 surfaces well cleaned with acetone.

Tension on the cathode wires was large - $\geq$ 500 grams/wire. For a wire spacing of 1/16" or less, considerable force is exerted on the chamber frames thus necessitating their prestressing. It was calculated that a single prestressing load placed at the center of

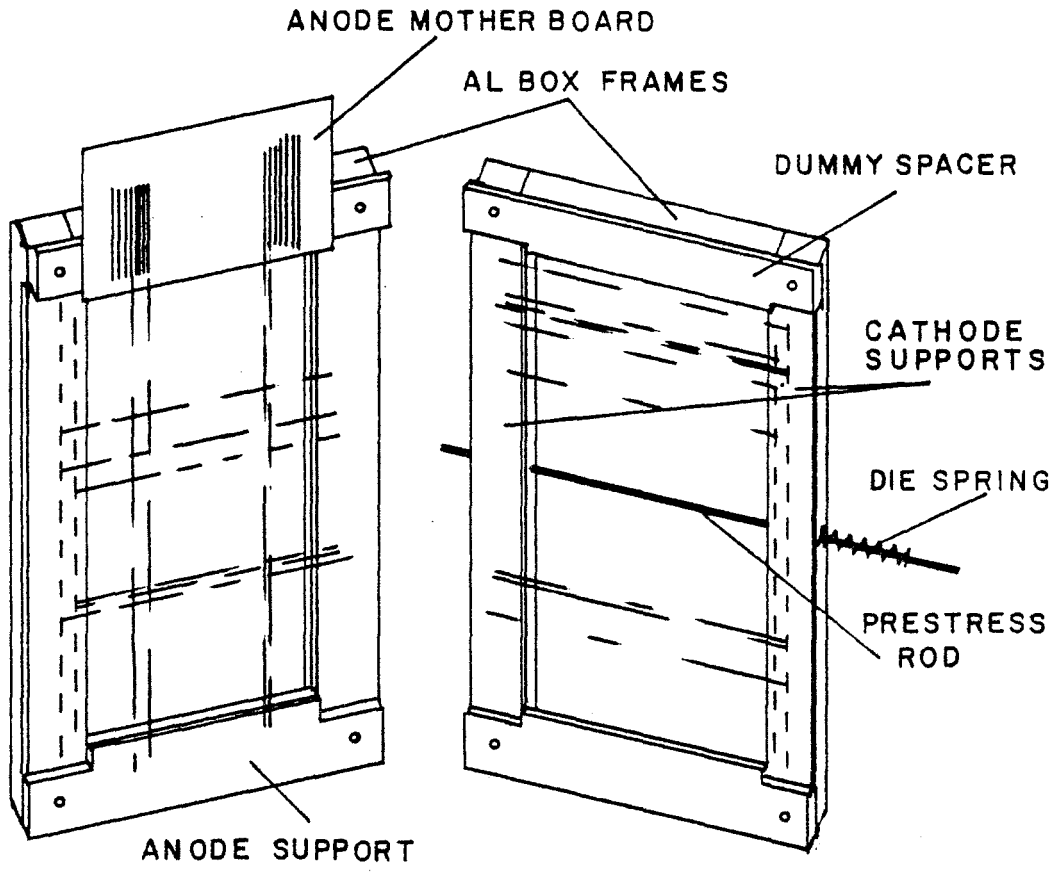

Figure 2.6 A schematic drawing of the general construction features of the UICC proportional wire chambers.

the frame equal to 52% of the uniformly loaded frame was necessary. The loads involved in the B and C chambers were ~40 lb/inch and in the D chambers ~20 lb/inch. Heavy-duty die springs were purchased and incorporated into the prestressing system as shown in Figure 2.6 Measuring the compression of the spring with calipers enabled us to know the force applied. Once prestressed, the frames were brought up under the wires, carefully positioned and the wires epoxied down to the frames. Since only 28" sections went on at a time, adjacent groups were positioned carefully using a travelling microscope. Sharp ends in the cathode wires were either buried in epoxy or silicone rubber (RTV 21). Once the chamber wires were complete, the two frames were joined and the chamber cleaned by blowing away dust with a strong jet of air. Two 1 mil sheets of Mylar were stretched and placed over the G10 lips to act as gas windows and heavy Mylar or lucite sealed the edges. Before the chamber was sealed with RTV 21, it was ascertained that no high voltage problems existed and that, with a β (Sr^{90}) source, proportional signals $\geq$ 1 mV into 1KΩ impedance could be seen. Finally, Al foil covered the faces of the chamber for r.f. shielding.

There is a certain amount of "black magic" involved in the construction and operation of PWC's, but we have found that, except for gross errors, these proportional chambers, coupled with sensitive amplifiers (threshold $\leq$ 1 mV into 100Ω) operated very well independent of the carefulness (or carelessness) with which they were built. As noted in the MPS Workshop[21], plateaus of up to 300 volts were common with a gas mixture of 80% Argon and 20% CO_2.

Spark Chambers

Stations E and F were magnetostrictive wire chambers with aluminum wires spaced at 0.032". A gas mixture of 90% neon and 10% heliu

bubbled through ethyl alcohol, was recirculated and purified using a commercial system. Each station had 4 modules, each consisting of a gap of y-y wires and a gap of u (or v) -x wires. Therefore, each module had 3 readouts: x, y, u or v. The magnetostrictive wand was read out at both ends. The signal at each end was then discriminated and shaped and fed into "Anna"[24] type time digitizers (MTD's). Each plane was able to record up to 28 sparks plus fiducials.

The high voltage pulse was applied by one thyratron (Wagner Electric-Tungsol Division) per module. A charge-line setup[25] using RG 59 coaxial cable was used to store the charge. The pulsing system is shown in Figure 2.7. In addition, the chambers had pulsed clearing fields and dc clearing fields on each module nominally set to about 55 volts/cm. Dead time after pulsing was 50 msec. Chamber performance during the run was monitored online by visually inspecting Single Event Displays. A typical event display is shown in Figure 2.8. If it seemed that a spark chamber had low efficiency or spurious sparks, suitable adjustments were made to the high voltage or clearing field.

d. Analysis Magnet

The MPS magnet is a superconducting ferrite magnet with a maximum $\int Bdl$ = 25 kGm. To diminish the magnet transverse momentum kick, this experiment ran at half field corresponding to a p_T kick to each particle of 0.375 GeV/c. The magnet has 1.22 m long poles with an aperture of 1.22 m width by 0.61 m height. Although a detailed field map was made, this analysis used a simple square-field approximation for momentum determination.

e. Calorimeters

Although the E260 calorimeters are discussed in detail elsewhere[20,26,27] it is useful to summarize some important points.

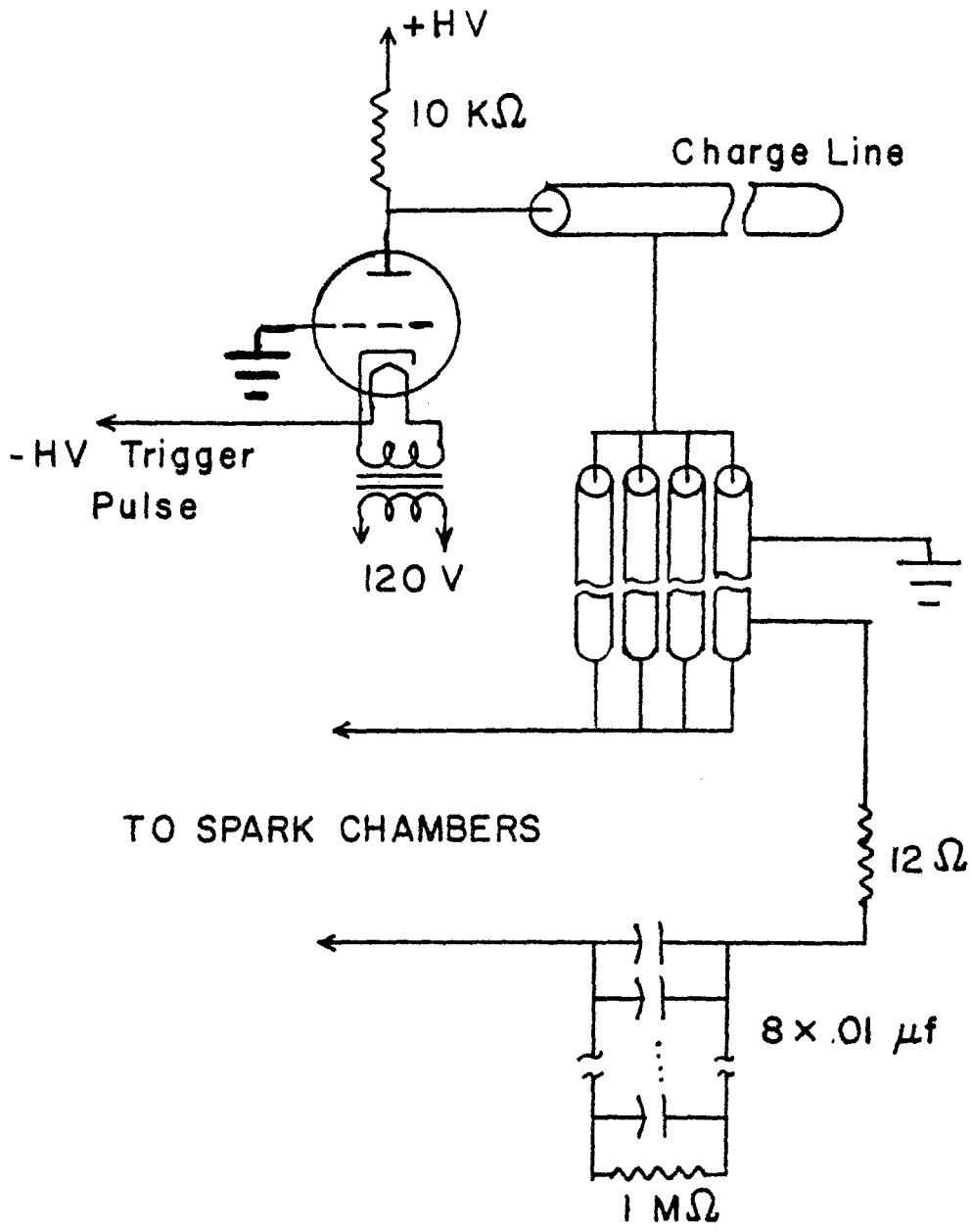

Figure 2.7 Spark chamber pulsing system .

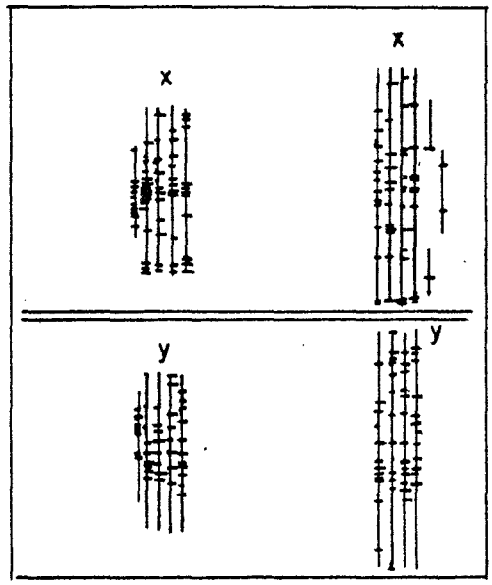

Figure 2.8 A typical single event display picture obtained on-line. Vertical lines represent both PWC's and WSC's. Sparks in these chambers are shown as tic marks on these lines. Only the chambers downstream of the magnet are shown with the x-view in the top region and the y-view below it.

Construction

To provide for fast, simultaneous jet and single-particle triggers in the range $2 \lesssim p_T \lesssim 8$ GeV/c, the MPS used two segmented calorimeters centered at 90° in the CMS and subtending the region $60^\circ \lesssim \theta^* \lesssim 110^\circ$. Figure 2.9 shows the calorimeter construction.

Each calorimeter consists of two parts - a front electromagnetic section and a rear hadron section. Each part was further horizontally segmented into four modules 0.21 m wide by 1.6 m high. A module, therefore, consists of an electromagnetic part with 13.6 radiation lengths of Pb measuring electron and photon energies, and a hadron part with 4.5 absorption lengths of steel measuring hadron energies. The hadronic shower is sampled 15 times and the electromagnetic shower sampled 6 times, both with ¼" NE102 plastic scintillator. RCA 6655A phototubes are attached to the tops and bottoms of the scintillators in each part as shown in Figure 2.9. The entire calorimeter structure was surrounded by a light-tight plywood box through which bulkhead mounts permitted HV and signal cables to be attached. Zener diode regulated bases, which were affected by temperature changes, were used on the phototubes. In an attempt to keep the temperature swings of the bases to a minimum, a 5000 BTU air conditioner was attached to the calorimeter boxes. This, however did not eliminate the gain variation completely. Figure 2.10 shows the kinematic regions accepted by each calorimeter module. Moving outward from the beam, the calorimeter modules are labelled L1H to L4H (L1E to L4E) for hadron (electron) modules on the left looking downstream and, similarly, R1 to R4 for modules on the right.

The signals from all the phototubes of a given module (electron + hadron) were summed to generate a signal proportional to the energy

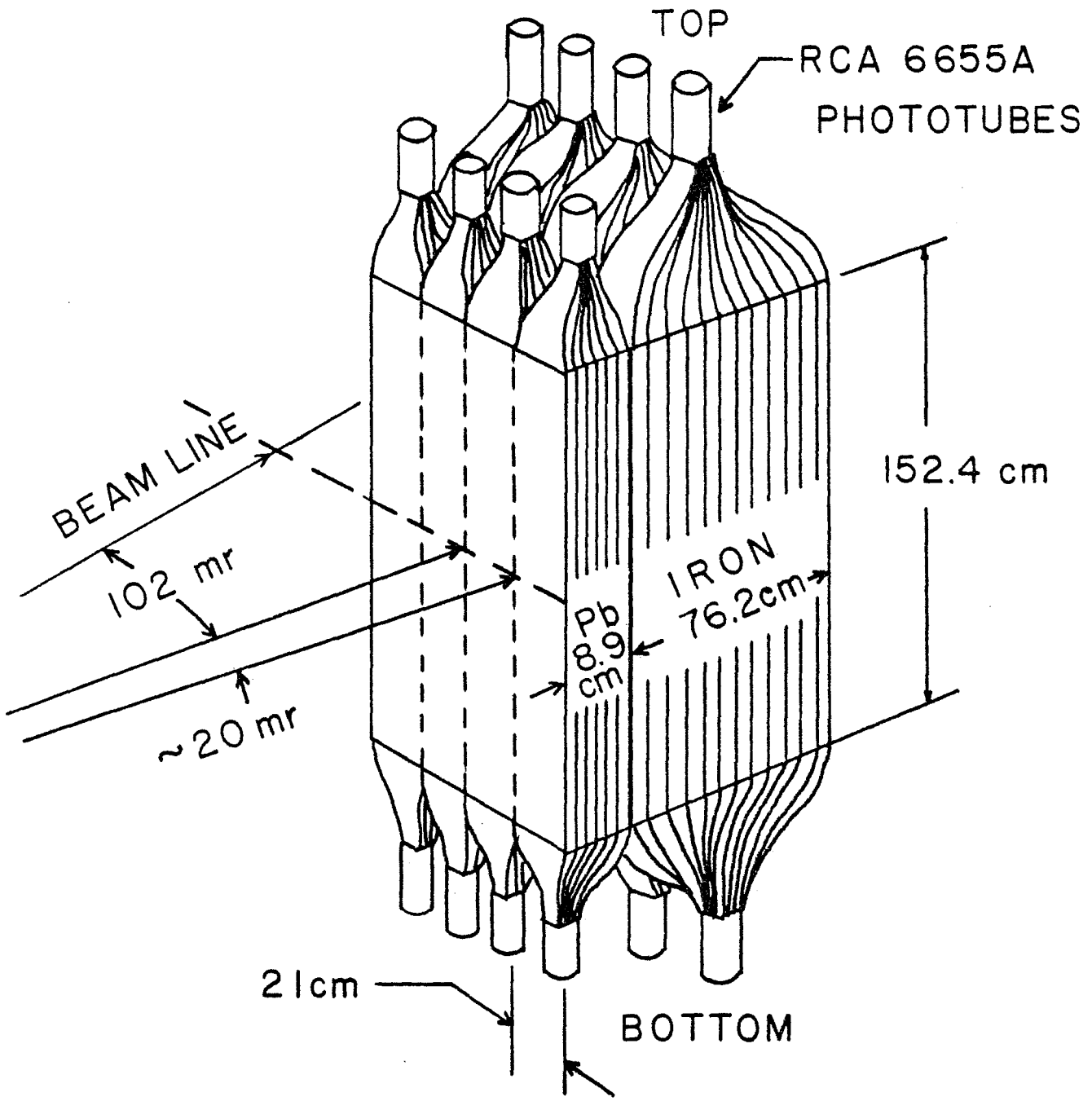

Figure 2.9 Calorimeter structure.

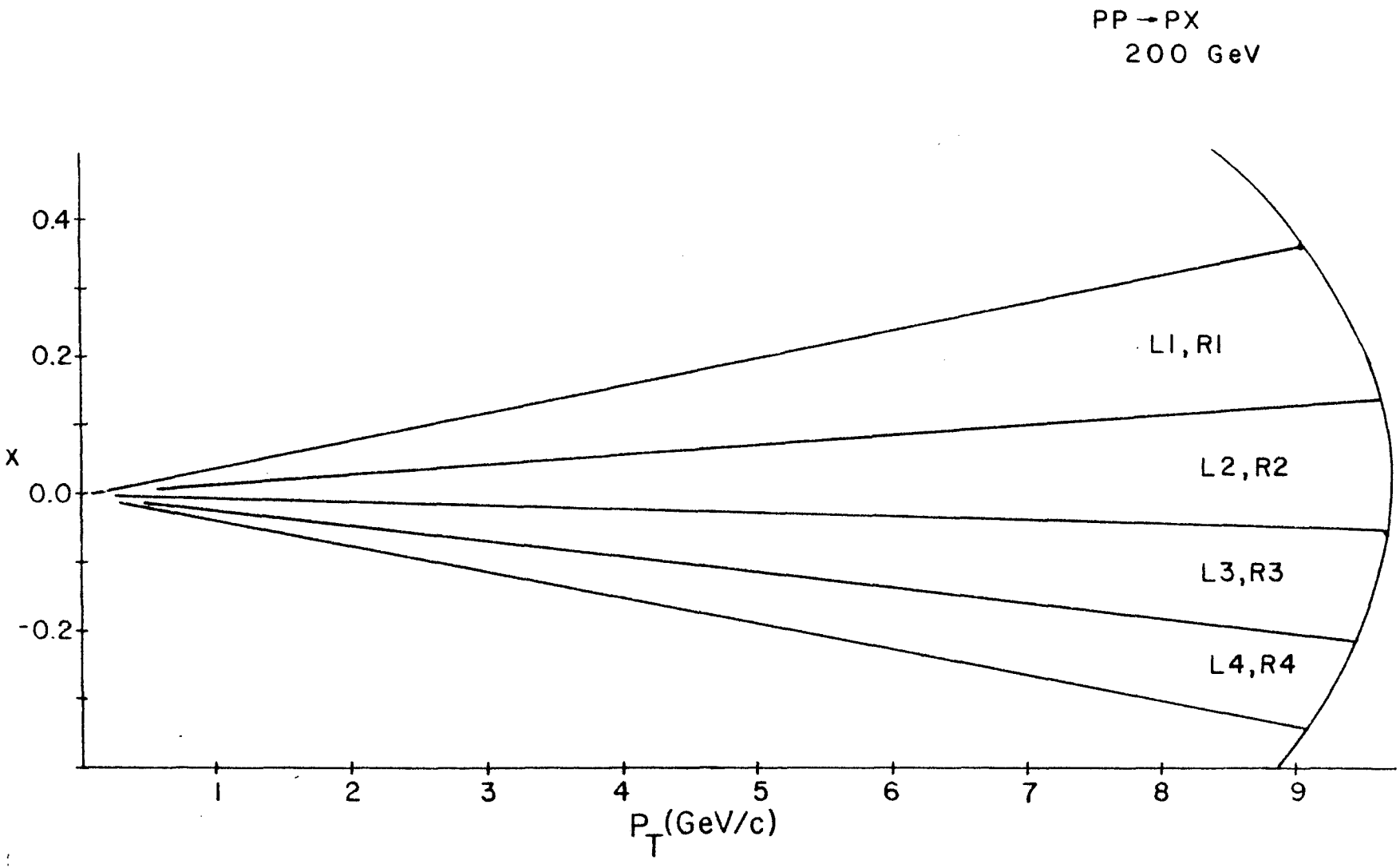

Figure 2.10 p_T and Feynman x regions covered by calorimeter modules. These boundaries are plotted for R1E - R4E but the corresponding modules (LH, LE and RH) cover essentially the same

deposited in the module. The trigger will be discussed further in Section 2.3a and in Chapter III.

Calibration

To calibrate each calorimeter a beam of 10, 25, 40 and 100 GeV/c negative particles was directed into the center of each module. The high voltage for each tube was then adjusted so that the gains were approximately such that 17 GeV/c particles gave pulse height in channel 100 of a 10-bit ADC (LRS Model 2249). The beam was moved vertically in each module to calibrate the vertical position determination. The pulse height information was written onto tape and calibration constants later determined by offline analysis. This will be discussed in Chapter III. The gain calibration was maintained by means of Bi^{207} sources and scintillators glued to the light pipes near each phototube and source calibration checks were done each week.

f. Cerenkov Counter

A large multi-celled atmospheric threshold Cerenkov counter (C1) was situated immediately after the E station spark chambers. The main frame of the counter was a large rectangular steel box designed to withstand pressures slightly above atmospheric (Figure 2.11). The size of C1 was determined primarily by the desire to match its solid angle acceptance to that of the rest of the spectrometer system. The entrance window, which is a laminate of 250 μ Mylar and 150 μ black polyethylene, is 3.6 m wide by 1.5 m high. Separating the counter into three sections are two opaque diaphragms made of the Mylar-polyetylene laminate. For particles not traversing these diaphragms, the minimum radiator length is 4.1 m. At the downstream end of the counter is a plane of 22 mirrors placed edge to edge and covering an area of 4.5 x 1.4 m^2. Each of the upper 11 mirrors is inclined at

Figure 2.11 Schematic drawing of spectrometer Cerenkov counter (C1). (a) Plan view. (b) Elevation view. (c) Mirror sampling. Note that mirror 1 is defined as top left hand side looking downstream.

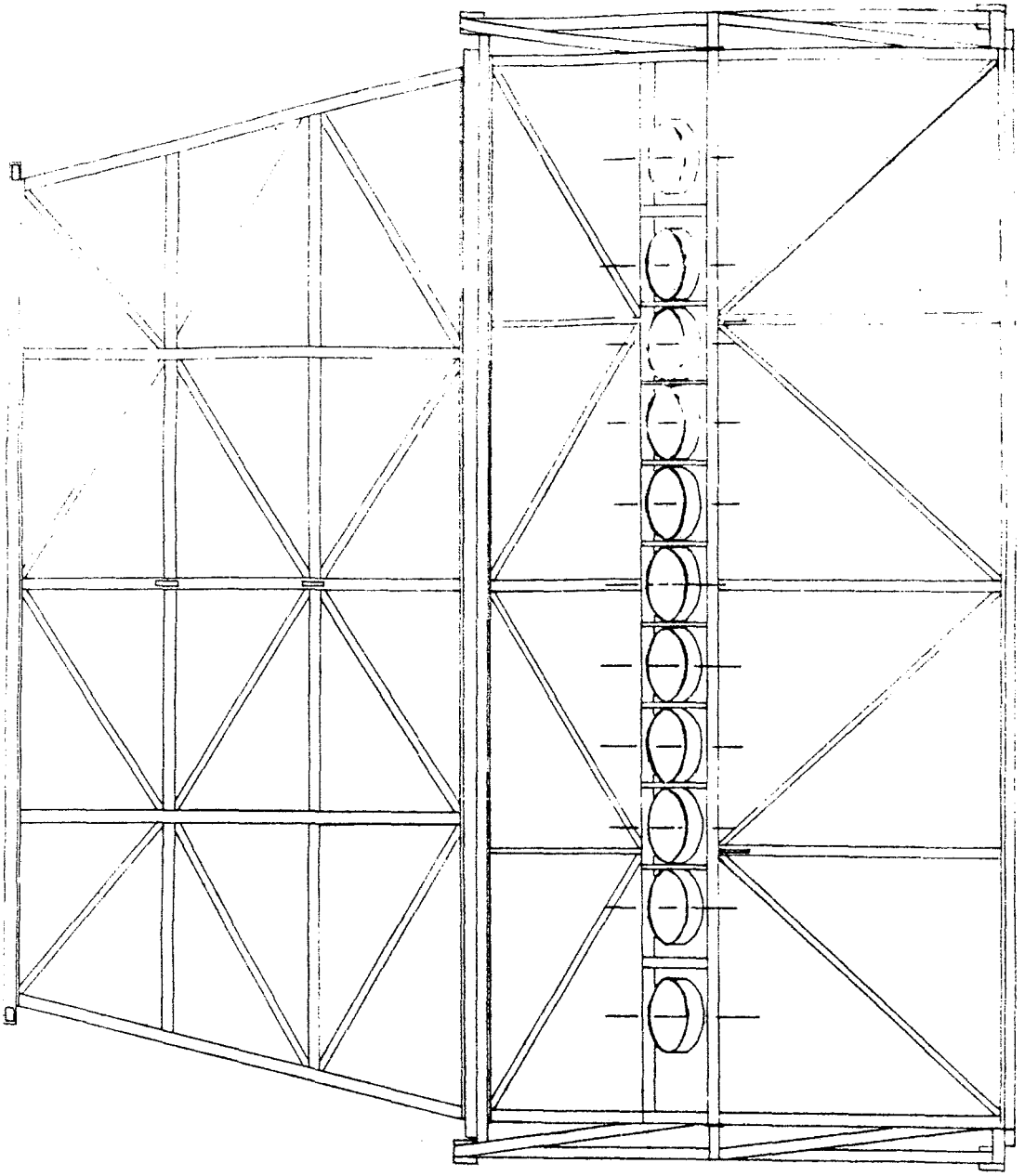

(a)

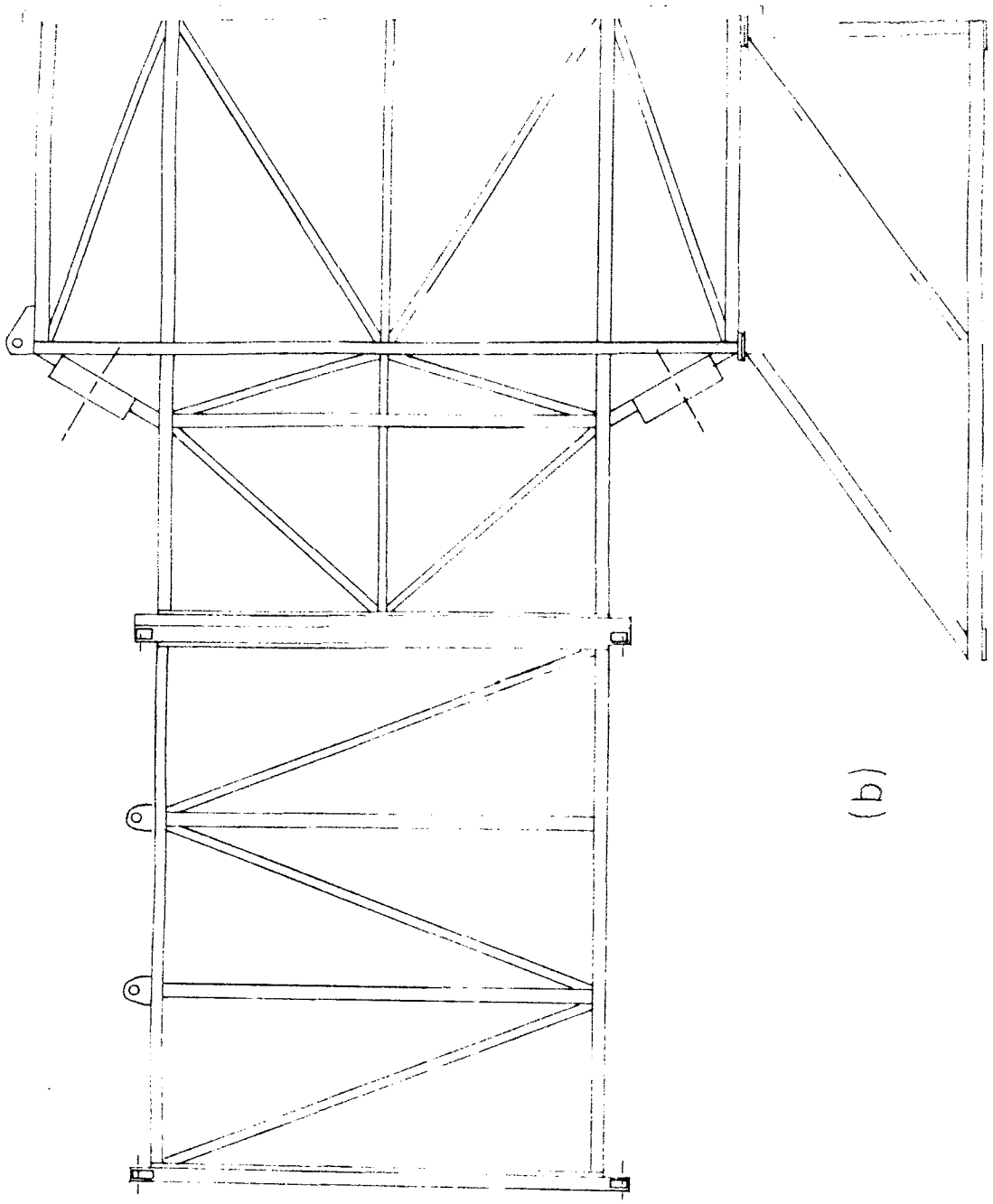

(b)

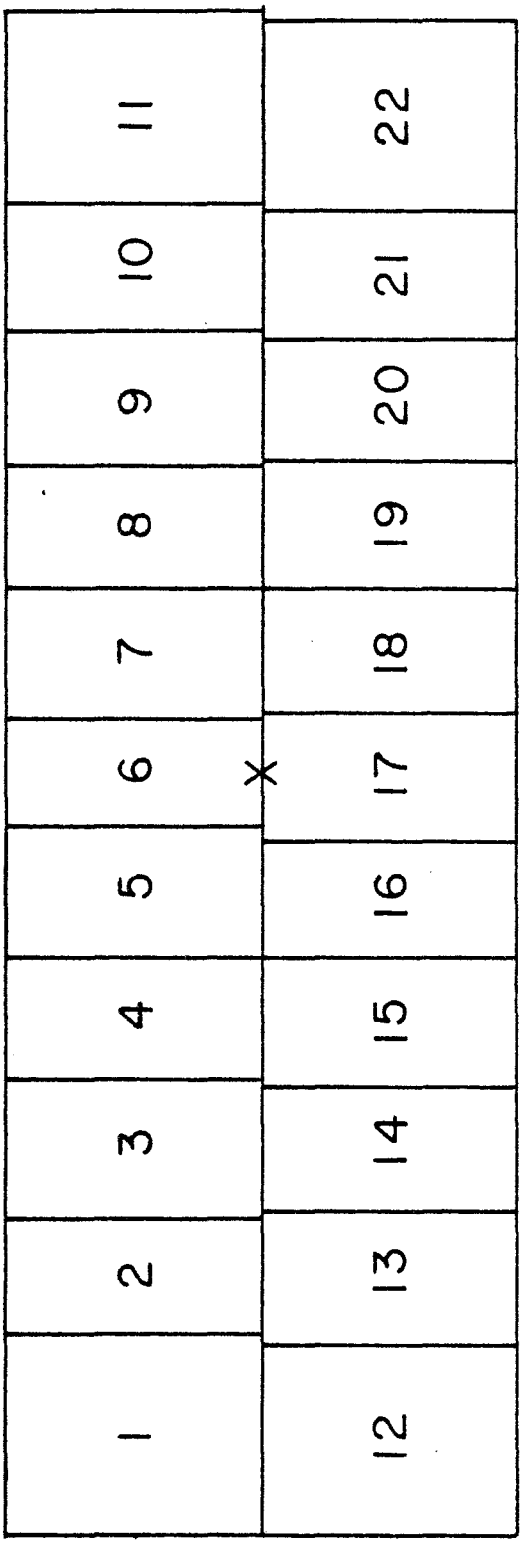

(c)

about 15° from the vertical so that it reflects light into one of th 11 upper light cone/phototube assemblies. The lower mirrors were similarly adjusted to shine light into the lower cones. The light cones were designed to accept all Cerenkov light incident at less than a maximum cutoff angle of about 25° to the axis of the cone[28]. The light thus collected was then detected by 5" RCA 4522 photomulti pliers. Figure 2.12 shows the kinematic regions each mirror accepts Notice that mirror 1 is in the top left hand corner (looking down-stream) and mirror 12 is directly below it.

Quartz windows were used to seal the light cones from the rest of the C1 gas system. Because C1 was not the last element in the spectrometer, the mirrors were necessarily made of low mass material to reduce multiple scattering and δ-ray production. They were constructed of aluminized Mylar with a styrofoam backing. The reflectivity was measured to be 85% at best at 300 nm wavelength. The siz of the cones was fixed by the diameters of the phototubes and the radius of curvature of the mirrors was determined by ray tracing techniques. A radius of curvature of 1.0 m was judged to give uniform optical response for a variety of particle trajectories. With the front entrance window removed and ordinary incandescent light bulbs replacing the phototubes, the mirrors were aligned by simply viewing the light intensity patterns across the face of the mirrors at a distance of about 75 feet from the counter.

C1 was run with two types of radiator - air ($n = 1.000293$) and a mixture of 2/3 He and 1/3 air ($n = 1.000122$). Approximately 30% of the data is with the helium filling. Once filled with the He mixtur the gas composition was checked and monitored by comparing the filli with air using a laser refractometer. There is a negligible error

Figure 2.12 p_T and Feynman x regions covered by C1 mirrors. This figure was made using top right hand mirrors - 6, 7, 8, 9, 10, and 11 - but the corresponding cells have essentially the same boundaries.

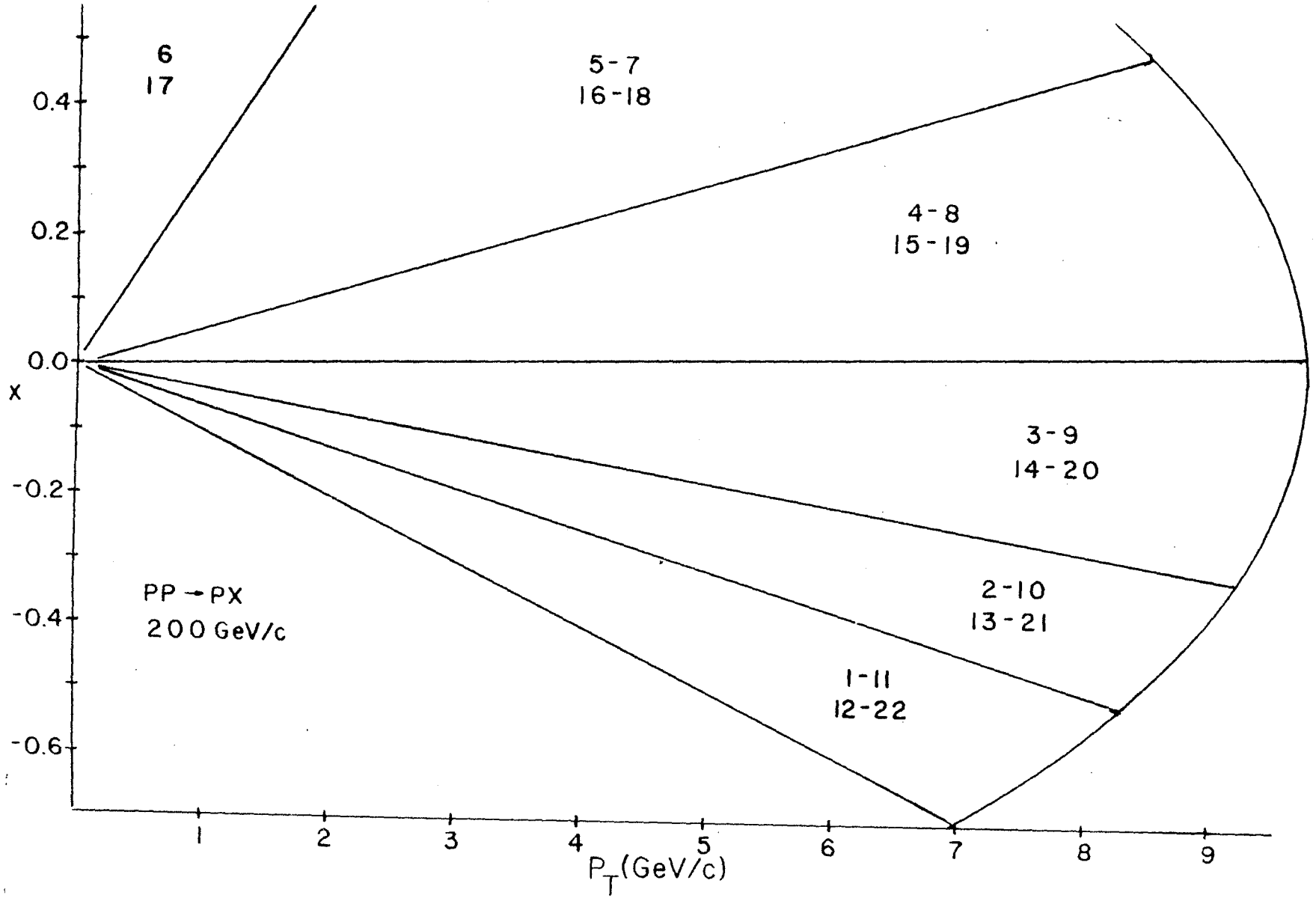
6
17
5-7
16-18
4-8
15-19
3-9
14-20
2-10
13-21
1-11
12-22
PP → PX
200 GeV/c
0.4
0.2
0.0
-0.2
-0.4
-0.6
x
1
2
3
4
5
6
7
8
9
P_T(GeV/c)

in the indeces of refraction due to humidity variations in the atmos phere while a ~5% error each can be attributed to: (a) temperature variation, (b) barometric changes and (c) the wavelength dependence of n between 3000 Å and 5000 Å.

For the above configuration we can calculate the expected photoelectron yield for $\beta = 1$ particles. The number of photoelectrons a the first dynode, assuming one reflection in the light cone, is give by

$$N_{\gamma e} \simeq 500 \sin^2 \theta_C \cdot L_R \cdot R_M \cdot T_W \cdot R_L \cdot T_P \cdot \varepsilon_c \cdot \varepsilon_Q \qquad (2.$$

where

$\sin^2\theta_C = 1-1/\beta^2 n^2 \simeq 2(n-1)$

L_R = Radiator length in cm

$R_{M,L}$ = Reflectivity of mirrors, light cones

$T_{W,P}$ = Transmissivity through quartz window of Cl, phototube

ε_Q = Quantum efficiency of phototube

ε_c = Overall light collection efficiency

We assume a reflectivity of 85% for both cones and mirrors and a tran missivity of 90% for both Cl windows and RCA 4522 windows. The quan tum efficiency for this tube is approximately 27%. For a radiator length of 4.1 m and an overall collection efficiency of 90%, we calculate for $\beta = 1$ particles

$$N_{\gamma e,Air} = 16$$
$$N_{\gamma e,He} = 6.6$$

The anode signal of each phototube was capacitively coupled to the input of a 10 bit ADC to obtain pulse height information for eac

cell. Pedestals were adjusted to fall roughly in channel 10. The ac coupling caused some concern for cells 6 and 17 directly in the beam region; the high rate often caused the levels at the input of the ADC's to be positive, causing a pulse height of 1. Due to the large size of the counter it was virtually impossible to direct a beam into any one cell to calibrate it. It was therefore important to have the phototubes at a high gain to be efficient especially for the He running.

If we write the number of photoelectrons as $N_{\gamma e} = AL_R \sin^2\theta_C$, then A is a quality factor which characterizes the counter taking into account the Cerenkov light spectrum and the counter optics. A can be calculated for C1 using the variables in Eq. 2.1. We find for C1, at best, $A \simeq 66\ cm^{-1}$. The best photomultipliers today can provide A from about 100 - 200 cm^{-1}. In section 3.4 we will show that, in practice, A can be considerably lower for C1. This is probably not due to any one factor in Eq. 2.1 but most likely is due to the light collection efficiency, the spectral response of the phototube and the reflectivity of the mirrors and light cones.

2.3 Trigger Electronics and Data Acquisition System

a. Trigger System

An overall view of the triggering system is shown in Figure 2.13. An interacting beam particle signals a pretrigger as defined in Section 2.2c. If the online computer, a PDP 11/45 is ready to process data then the pretrigger forms a latch, PRETRIGLTCH, that prevents taking another interacting beam particle before the logging of the event is complete. The PRETRIGLTCH has two primary functions. First of all, it is clipped to 126 nsec and becomes the load pulse for the PWC shift registers. Any PWC information obtained during this 126 nsec

Figure 2.13 Schematic diagram of trigger electronics; (a) derivation of spark chamber trigger from beam counters and trigger logical requirements; (b) schematic diagram of resets and ADC load signals.

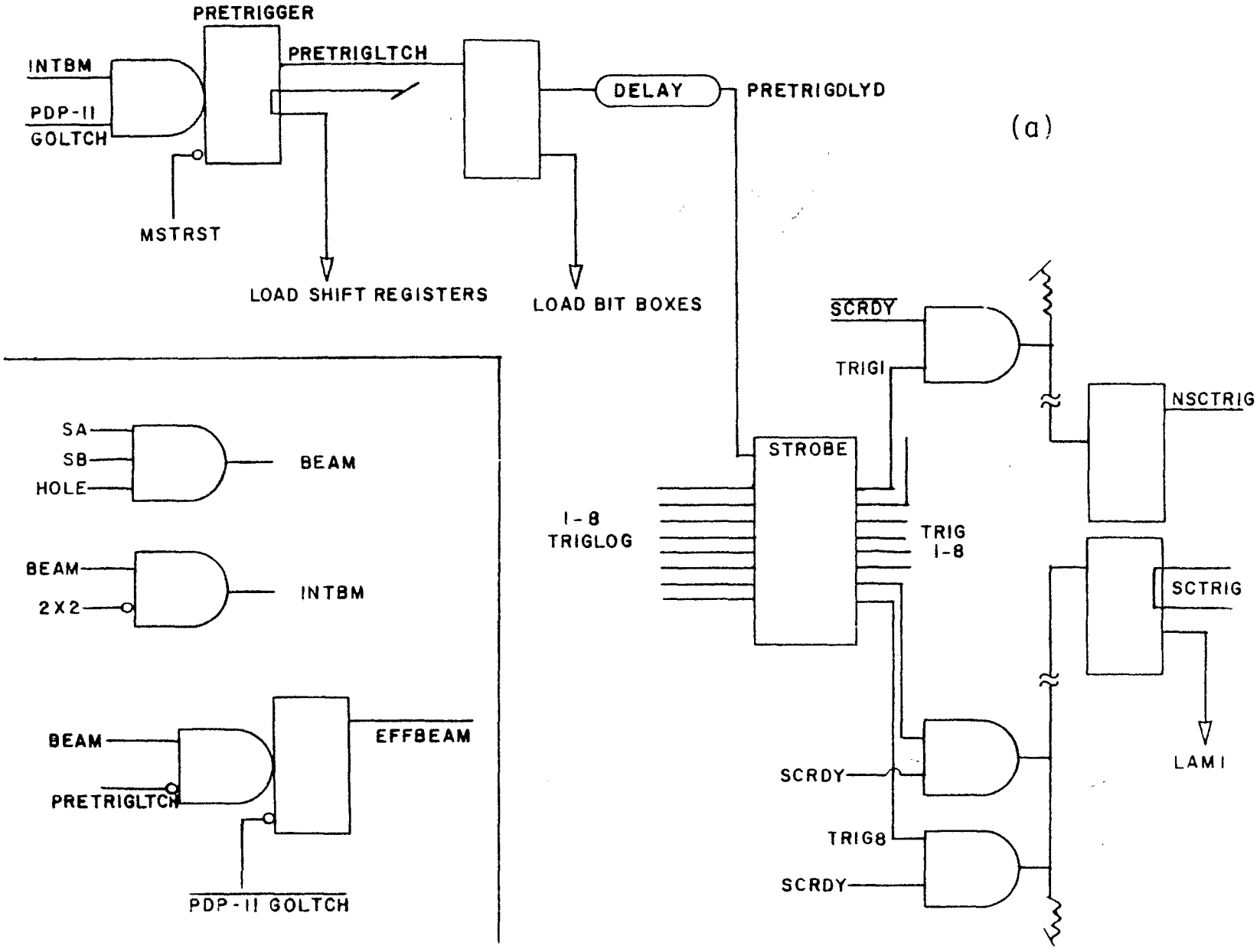
PRETRIGGER
INTBM
PDP-11
GOLTCH
PRETRIGLTCH
MSTRST
LOAD SHIFT REGISTERS
DELAY
PRETRIGDLYD
LOAD BIT BOXES
(a)
SCRDY
TRIGI
NSCTRIG
STROBE
1-8
TRIGLOG
TRIG
1-8
SCTRIG
LAMI
SCRDY
TRIG8
SCRDY
SA
SB
HOLE
BEAM
BEAM
2X2
INTBM
BEAM
PRETRIGLTCH
EFFBEAM
PDP-11 GOLTCH

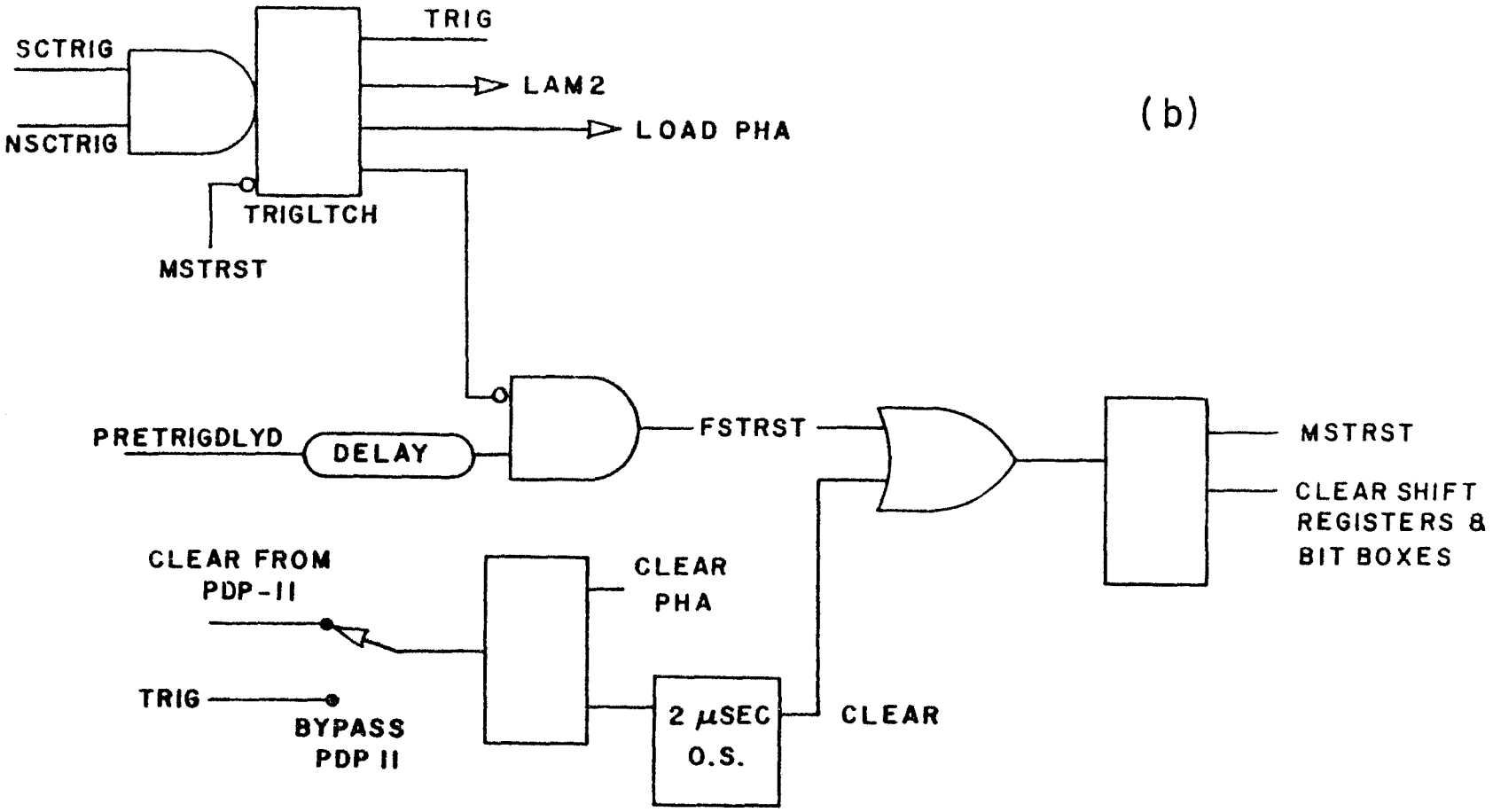
SCTRIG
NSCTRIG
TRIG
LAM2
LOAD PHA
TRIGLTCH
MSTRST
(b)
PRETRIGDLYD
DELAY
FSTRST
MSTRST
CLEAR SHIFT
REGISTERS &
BIT BOXES
CLEAR FROM
PDP-11
CLEAR
PHA
TRIG
BYPASS
PDP 11
2 μSEC
O.S.
CLEAR

gate will be loaded into the shift register. The PRETRIGLTCH, suitably delayed, also strobes up to eight main trigger logic requirements, the TRIGLOGs. The output of the TRIGLOG strobes are put into coincidence with the Spark Chamber Ready signal to finally fire the spark chambers and to form the trigger latch, TRIG. If, however, a TRIG does not occur, then the pretrigger resets itself and clears the shift registers, ready to start the cycle over. Notice here, however, that we still scale the TRIGLOGs and the amount of effective beam taken even though the experiment may not have been triggered because the spark chambers were not ready. The effective beam is just the amount of beam when the PDP 11 is in the ready mode. This is typically 80% of the beam onto the target.

Having formed a trigger, TRIG now goes on to fire a gate generator to load pulse height information into the ADC's. Therefore, if no trigger is generated the ADC's do not get loaded. This is important due to the fact that they need $\geq$ 2 μsec to settle after being cleared. The PDP 11 is signalled that it should begin reading in shift register, ADC and MTD information. TRIG signals a CAMAC LAM/LATCH[29] and, through CAMAC, the PDP 11 begins to process the event. We will discuss this further in Sections 2.3b through 2.3e. After logging the event, the computer sends out a CLEAR which clears the ADC's and, 2 μsec later, resets the pretrigger latch and the trigger latch to accept another event. To bypass the computer, a toggle switch enables the TRIG signal to be delayed and finally reset the system.

For E260 five simultaneous TRIGLOGs were implemented. Four were derived from the calorimeters while the fifth was simply an interacting beam trigger which was defined as a signal in the beam defining hodoscope and none in the 2 x 2 counter. The 2 x 2 veto covers approxi-

mately 7 msr about the forward direction in the CMS. The possible calorimeter triggers were generated as follows. The anode signals o all four phototubes in a module - electron, hadron/top, bottom - wer added by directly mixing with a LRS 428 to generate a signal proportional to the total energy deposited in the module. For each module this signal was attenuated in proportion to the mean lab angle of th module. The module signals thus become proportional to the average transverse momentum of the particles entering it. Two basic types o triggers were formed:

JET - the sum of all four modules in the right or left calorimeter is required to be above a preset "jet" bias, and

SINGLE PARTICLE - the signal from any one module is required to be greater than a preset "single particle" bias.

Two sets of bias levels for each trigger existed. A lower bias was set approximately 1 GeV/c less in p_T for each trigger type. Since t p_T spectrum is steeply falling, we divided, or counted down, the low bias data to avoid being swamped by the higher trigger rate. The dividing factors were picked such as to have about equal low bias and high bias trigger rates. An interacting beam trigger was recorded a every tenth trigger. Table 2.4 summarizes the trigger types, biases and divisions used.

b. Data Acquisition System Overview

Figure 2.14 shows a schematic diagram of the ties between the M hardware and the PDP 11 with its peripheral equipment. The basic pu pose of the data acquisition system (DAS) was to obtain the ADC, MTD

Trigger		Biases (Gev/c)	Division
Jet	HIJET	4.0	1
		3.5	1
	LOJET	3.0	30,37
		2.5	37
Single Particle	HIPT	3.0	1
		2.7	1
	LOPT	2.0	30,80
		1.7	80
Interacting Beam		$\theta^* \gtrsim 3^\circ$	1 Every 10 Triggers

Table 2.4 Definition and biases of triggers used. Also shown are the division factors for the low bias triggers. Each trigger has two slightly different thresholds since the biases were changed about half way through the experiment.

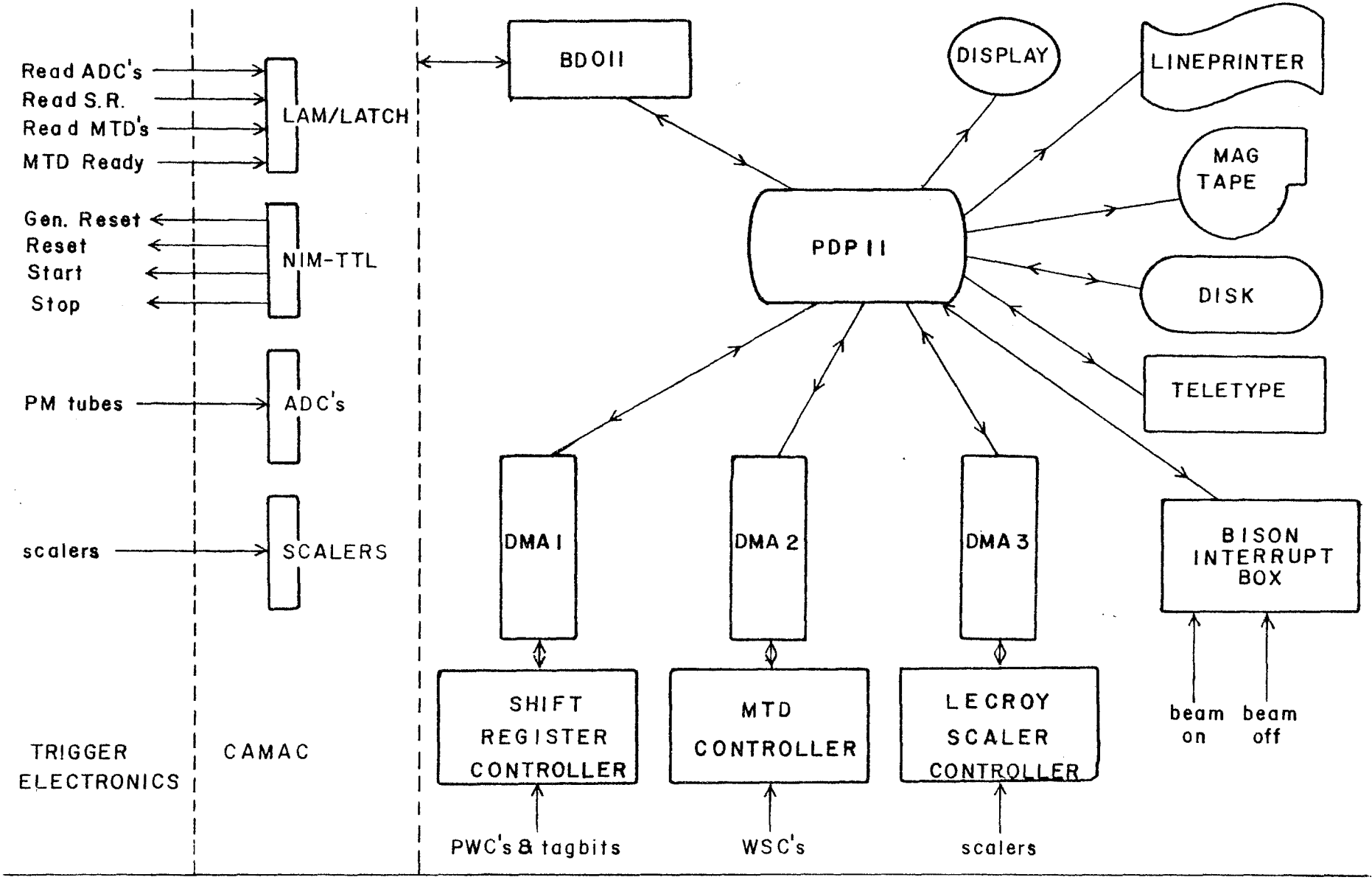

Figure 2.14 An overview of the PDP11 - MPS Hardware Interaction

PWC and scaler information from the hardware and record these onto magnetic tape in a quick and efficient manner.

The PDP 11 communicated with the experiment through both CAMAC and Direct Memory Access (DMA). The experimenters communicated with the computer through its peripherals and the Bison Interrupt Box[30].

The Beam On interrupt is supplied to the Bison Interrupt Box from an external signal synchronized with the main ring cycle and signals the computer to stop any analysis and get ready to take in events from the upcoming beam spill. This requires the swapping of histograms, etc. from core to disk and data input routines from disk back to core. The PDPGO latch (Figure 2.13) is turned on. In one of the CAMAC crates is contained the LAM/LATCH which interrupts the PDP 11 at the beginning of an event when the trigger electronics indicates that a trigger has been satisfied. The value of this LAM/LATCH word specifies the type of data the hardware will contain. Pulse height information from the Lecroy ADC's and the contents of 24 bit scalers (Jorway Model 84 and 85) are transferred to the PDP 11 via CAMAC. This CAMAC unit communicates with the computer through an EG&G BD011 interface. The LAM/LATCH also signals through the BD011 that shift register data and MTD data are to be read in. But the data here is transferred directly into regions of core by the DMA's whose transmission is initiated by the online software. For each DMA a controller organizes the particular data into 16-bit words of known format. This will be described below. After all the data has been read, an end-of-event software flag is set and the computer generates a reset to the trigger electronics and reinitializes the PWC DMA.

Finally, the Beam Off interrupt signals the computer that input

data has been temporarily suspended. The PDPGO latch is turned off, the data accumulated on disk is written onto tape and the software proceeds to do simple analysis. A version of MULTI[31] adapted to the MPS allows for histogramming event attributes and graphically displaying individual events on the CRT. The data collection was limited by the MTD read-in speed and the maximum event rate, limited by spark chamber dead time, was about 20 events/sec. On the average, 1,000 words of data per event were read into the PDP 11. At the end of a run MULTI neatly summarizes PWC operation, Cerenkov counter and calorimeter pulse heights and any hardware or software errors occurring.

c. ADC and Jorway Scaler Data Transfer

Both the LeCroy ADC and Jorway (CAMAC) 24-bit scaler data are transferred to the PDP 11 through the BD011 interface. All scalers are read at the beginning of a beam spill and at the end of a beam spill signalled by the Beam On/Off interrupts. The software, at the appropriate times, sends out commands to the BD011 to read each of the 12 CAMAC scalers through the CAMAC Branch Highway under the DMA mode where the data transfer is under control of the BD011. Each of the CAMAC scalers reads into two 16-bit words: the high order 8 bit followed by the low order 16 bits. The scaler redundancy - two readings per spill of CAMAC and LeCroy scalers and also visual scale at the end of a run - was added to eliminate errors in cross section determinations.

If the first bit of the LAM/LATCH word is on, then the outline software is instructed to address the BD011 to read the ADC's, again in the DMA mode. Each of the 75 channels of ADC read into one

16-bit word. When done reading the ADC's, data control passes to MULTI and we proceed to read other hardware.

d. PWC Data Transfer

When the LAM/LATCH has the second bit on shift register data is present and is to be read into the PDP 11. Before describing this procedure, we will first need to describe the shift registers and the shift register controller further.

As mentioned in Sections 2.2c and 2.3a, all PWC information is loaded into 5-bit shift registers which have their serial output all connected to produce a string of bits that can grow to an indefinite length. At the beginning of the shift register chain are the Bit Boxes. These are also shift registers that accept 16 individual NIM logic signals per unit. The output of these contain 32 bits, but every other input of the shift registers is grounded to force a zero between adjacent input signals. There are two such units that record the trigger type (HIJET, LOJET, HIPT, LOPT), beam Cerenkov counters and calorimeter trigger module. The bit boxes are loaded by the pre-trigger just as the other shift registers. Thus the length of the shift register word was no bigger than the maximum number of proportional wires + Tagbits + 1, or 5506 bits long.

The controller, upon receipt of a software signal, sends clock pulses out to the shift registers to now shift the contents into the serial output chain and into the controller. Once the sequence is initiated the software proceeds to gather other data. The controller has two counters - the edge counter and the width counter. When scanning the shift register chain, the width counter records the number of contiguous bits that are on up to a total of 8 and the edge counter records the address of the last bit that was on in this group. A

16-bit word is constructed from the edge address and the width, and this word is passed via DMA to the PDP 11. The first 13 bits contai the address and the last 3 bits the width.

Data transmission is stopped when the controller transfers a wo with all bits on or when the controller reaches a preset address. A all-bits-on word is formed simply by grounding the end of the shift register chain. A bit is set in the shift register DMA to signal th software that PWC transfer is complete.

e. WSC Data Transfer

In a similar fashion to the PWC transfer, the spark chamber MTD transfer is controlled by a DMA device and initiated by the software when the third bit of the LAM/LATCH is on. The readout was done in this manner rather than the original CAMAC readout of the ANNA modul to increase readout speed.

Each WSC plane has two wand outputs. The sparks were detected by zero-crossing discriminators and converted to TTL logic levels. The two signals were read into two inputs of an MTD. Each MTD has four inputs that have a 15-word capacity (each word 16 bits). There fore, each plane can record up to 30 sparks not counting fiducials. If there are $\leq$ 14 sparks then the coordinate for each spark is measured twice, once from each end of the wand. A 16-bit counter counts 20 MI clock pulses between sparks and this work gets strobed into sequenti memory locations. When this counter overflows a "0" is read into th next available location. Also associated with each input is a 4-bit address counter which counts the number of wand pulses at the input. The four 4-bit counters are packed into one 16-bit address word per module.

The MTD controller operates in two cycles in transferring data via the MTD DMA unit. In the address register cycle the controller

reads the 16-bit address words into the computer. The DMA is reset after all the MTD modules are read in and in the data cycle the MTD digitizations, including the "0" word, are transferred through the DMA. While the wand digitizations are read into core the software remains busy unpacking the addresses. A check that the data is monotonically increasing and that the addresses agree with the number of digitizations in each input is done after all the data is read in. Bit 9 of the LAM/LATCH is turned on to signal that the MTD's are ready to accept more information. Appropriate error flags are set and summarized at the end of a run.

f. LeCroy Scaler Data Transfer

Besides the Jorway scalers mentioned in Section 2.3c the experiment also recorded information from 24-bit LeCroy scalers (LeCroy Model 850A). Data transfer for these scalers proceeds via DMA unlike the Jorway scalers. The LeCroy Scaler Controller formats the 24-bit word into two 16 bit words: the first word contains bits 1 through 16 and the second word contains bits 9 through 24. The software, after the DMA transfer, changes the format to agree with the CAMAC format for 24-bit scalers.

CHAPTER III

DATA ANALYSIS

3.1 Overview

The data reduction starts along the standard line of making Dat Summary Tapes (DST's) from the raw data tapes. Proceeding further, Condensed Summary Tapes (CST's) were written because the DST's contained too much information to conveniently facilitate tape handling A further condensed tape (CCST) was made to make tape jobs on Fermilab's CDC6600 run smoother. A total of about 950 K triggers were recorded on 165 raw data tapes. The final physics analysis proceede from three 1600 BPI CCST's. All the physics analysis was done on Fermilab's 6600. Table 3.1 gives a summary of the data taken from the hydrogen target that is used in this analysis.

As a check of our analysis the HIPT trigger was investigated an simple charge ratios were compared with the Chicago-Princeton group[3] (CP) for p beams. Particle identification using Cl was attempted an particular ratios such as $\frac{\sigma(pp\to\pi^+X)}{\sigma(pp\to\pi^-X)}$, $\frac{\sigma(pp\to K^+X)}{\sigma(pp\to K^-X)}$, etc. for the triggering particle were compared with the CP results.

3.2 Track Finding and Data Summary Tapes

The first step in the analysis consisted of finding tracks through the spectrometer. All the chambers were first aligned using beam particles. Using the measured chamber positions along the beam direction (z-coordinate) the relative x and y coordinates were found by using "straight throughs" - beam with the magnet off - and "curve throughs" - beam with the magnet at full or half field.

The z-coordinates of the chambers were known from careful measurement of chamber positions. Straight throughs had, by definition (x,y) coordinates = (0,0). By analyzing the straight throughs each

Beam - Polarity	HIJET Bias	HIPT Bias	C1 Filling	Triggers
190 - POS	4	3	Air	98 K
			He	0
190 - NEG	4	3	Air	29 K
			He	25 K
200 - POS	4	3	Air	102 K
			He	56 K
200 - NEG	4	3	Air	50 K
			He	0
200 - POS	3.5	2.7	Air	95 K
			He	74 K
200 - NEG	3.5	2.7	Air	243 K
			He	113 K

Table 3.1 Summary of data (liquid hydrogen target) input into this analysis. Triggers refer to all types of triggers written onto tape. Another 53 K triggers were not acceptable.

chamber was given an x and y translation such that the calculated average (x,y) coordinate was (0,0). The positions of the chambers i back of the magnet relative to those in front of the magnet were adjusted by using curved throughs. Knowing the magnetic field and the beam momentum the x displacement at any chamber can be calculated ar the chambers then adjusted to give the correct momentum. Furthermor from solidly determined wide angle interacting beam tracks rotations of the chambers were detected and physically corrected and the alignment parameters then turned more finely. The spectrometer momentum resolution was thus found to be $\frac{\Delta p}{p} = 0.07 \cdot p\%$.

Since the track finding algorithms were not necessarily optimiz the first time data was processed, the philosophy for the DST's was taken that one should include the raw data from the event should one want to look for further tracks. Therefore the DST's contained both the raw data plus the reconstructed track information. The track finding algorithm follows a standard technique of deciding whether o not enough spark* information exists within a road - a region around the line joining two sparks which are at the beginning and at the en of a group of chambers. The requirement that a track exists was set essentially by the minimum number of sparks in the road and the χ^2 of the best straight-line fit through these sparks. This algorithm was used in the following fashion in the high multiplicity events in E260:

a) The primary interaction vertex is determined by the beam tracks, solidly determined y tracks (non-bending) and x tracks before the magnet. The minimum number of

---

* A spark is defined as either a hit in a PWC or a spark in a WSC.

non-beam tracks required in the vertex determination is three.

b) From this vertex position determine all y tracks.

c) Find all x tracks after the magnet.

d) Match the x tracks after the magnet with the y tracks found in (b).

e) Project these matched after tracks to the center of the magnet and match them to any x tracks found before the magnet.

Note that this method of track finding only allows tracks to come from the primary interaction vertex. Thus neutral V's or interactions downstream of the target are not recorded as real tracks. However, since the DST contains the track information as well as the raw data it is relatively simple to go back and reconstruct these. A detailed discussion of the track finding algorithm can be found in our beryllium papers and our current preprint[20], and a discussion of the criteria for defining tracks will be found in the thesis by K. Yung.[33] Here it is sufficient to mention that the track finding efficiency is estimated at 90-95% with no spurious high p_T tracks.

For the purpose of this analysis we decided to use only particles associated with the primary vertex. As a result, strangeness correlations between $K^{\pm}$'s and K^{o}'s which are important will be neglected. Our DST's were thus reduced to CST's by deleting all raw data and keeping only some select information from the DST's. Since the track finding criteria were very loose many overlapping, but possibly real, tracks were still contained on the CST's. For example if two tracks share the same sparks in the x-view and use different sparks in the y-view, then, depending on how reliable the fits to these sparks are, both or

only one track may be real. Due to the large number of tapes yet at this stage a further condensation of the data into CCST's was made b saving only hydrogen target associated events and not recording "unnecessary" information. "Unnecessary" applies to this analysis only and, in fact, what was once deemed unnecessary was often found throu trial and error to be really useful. We exclude from the CCST bad tracks, corrected pulse heights that are ≤ 0 or very small, the various track and event quality factors and the beam Cerenkov tagbits an pulse heights. In constructing the CCST from the CST the beam particle is identified using the beam Cerenkovs and the secondaries are identified using Cl pulse height information. Tracks are determined to be good if they satisfy certain quality criteria. These include minimum number of sparks on a track and a χ^2 cut for overlapping tracks. A detailed discussion can be found in Reference 33. Table 3. summarizes the various stages of data storage.

3.3 Calorimeter Response

a. Calibration

The energy response from the calorimeter can be parameterized as

$$P^h_{inc} = L^h_h g^h_h \sqrt{T_h B_h} + L^h_e g^h_e \sqrt{T_e B_e} \qquad (31.a)$$

for incident hadrons, and

$$P^e_{inc} = L^e_h g^e_h \sqrt{T_h B_h} + L^e_e g^e_e \sqrt{T_e B_e} \qquad (3.1b)$$

for incident electrons, where

$P^{e,h}_{inc}$ = incident electron, hadron momentum

$T_{e,h}(B_{e,h})$ = pedestal corrected pulse heights for electron, hadron top (bottom) tube.

g^p_c = pulse height to energy proportionality constant.

CONTENTS	INCLUDED ON			
	DATA TAPES	DST	CST	CCST
RAW DATA	X	X		
RUN, EVENT NO.	X	X	X	X
TRIGGER TAGBITS	X	X	X	X
CHAMBER POSITIONS AND PARAMETERS		X		
BEAM CHAMBER HITS COORDINATES			X	
OVERLAPPING TRACKS		X	X	
HIGH QUALITY TRACKS		X	X	X
VERTEX COORDS.		X	X	LH_2
VERTEX ERROR, χ^2		X	X	
BEAM, MAGNET PARAMETERS		X	X	X
BEAM CERENKOV INFORMATION	X	X	X	
BEAM 4-VECTOR				X
TRACK FIT PARAMETERS		X	X	
CERENKOV, CALOR. PULSE HEIGHT	X	X	X	NON ZERO
TRACK MOMENTA		X	X	
4-MOMENTA				X
Y SLOPE, INTERCEPT		X	X	
X SLOPE, INTERCEPT BEFORE MAGNET		X	X	
X SLOPE, INTERCEPT AFTER MAGNET		X	X	X

Table 3.2 Some important parameters kept in various stages of data summary.

p = particle type, electron or hadron and

c = calorimeter module type, electron or hadron.

L_c^p = transverse leakage into neighboring modules.

c and p are defined as above.

Due to the attenuation in the scintillator the vertical position in module c, y_c, can be written as

$$y_c = y_{0c} + \frac{\bar{\lambda}_c}{2} \ln \frac{T_c}{B_c} \qquad (3.2)$$

where $\bar{\lambda}_c$ is the average top and bottom attenuation length and y_{0c} is the y = 0 offset of the calorimeter module.

Using the beam calibration data described in Section 2.2e the above parameters were found for each calorimeter module. Table 3.3 lists the results of that analysis. Transverse leakage is about 10 20% in the hadron modules and the energy-to-pulse height factor is adjusted accordingly when calculating the expected energy from the calorimeter pulse heights. The leakage correction is used in the je trigger also and therefore the jet energy as calculated directly fro the calorimeter will be too high by 10 - 20%. However this analysis will not depend on this point.

The energy resolution for both electrons and hadrons varies as $1/\sqrt{E}$. We find from the calibration data

$$\frac{\sigma}{E}\Big|\text{electrons} = 0.33/\sqrt{E}$$

$$\frac{\sigma}{E}\Big|\text{hadrons} = 1.08/\sqrt{E}$$

The y-coordinate resolution, also determined from the beam calibrati was found to be about $\pm$ 10 cm.

This analysis will not rely heavily on the absolute energy cali bration of the calorimeters. We will mainly be interested in ratios

Module	$L_h^h g_h^h$	$L_e^h g_e^h$	$L_e^e g_e^e$	y_o (m)	$\bar{\lambda}$ (m)
L1H	.188			-.021	1.73
L2H	.171			-.016	2.09
L3H	.176			-.011	1.92
L4H	.175			-.056	1.74
R1H	.165			-.112	1.44
R2H	.165			.021	1.65
R3H	.168			-.067	1.60
R4H	.177			-.013	1.79
L1E	.6	.226	.172	.058	1.45
L2E		.204	.161	-.008	1.17
L3E		.213	.166	-0.56	1.77
L4E		.208	.167	0.35	1.27
R1E		.203	.176	-.038	1.45
R2E		.198	.170	.045	2.02
R3E		.237	.178	-.077	1.65
R4E		.246	.165	.045	1.51

Table 3.3 Results of beam calibration of calorimeter modules with hadrons and electrons. These parameters relate the calorimeter's response to the incident energy as given by Eq. 3.1.

of triggering particles so that we will be more interested in the triggering efficiency.

If there is a signal in both the top and bottom tubes of a module then we calculate for either electron or hadron module c

$$y_{mod,c} = y_{0c} + \frac{\bar{\lambda}_c}{2} \ln \frac{T_c}{B_c} \tag{3.3a}$$

$$E_{mod,c} = g'_c \sqrt{T_c B_c} \tag{3.3b}$$

$$P_{Tmod,c} = E_{mod,c} \sqrt{\frac{x^2_{mod,c} + y^2_{mod,c}}{(z_{mod,c} - z_{t0})^2 + x^2_{mod,c} + y^2_{mod,c}}} \tag{3.3c}$$

where $g'_c = g^h_c L^h_c$. $x_{mod,c}$ and $z_{mod,c}$ are the x and z coordinates of the center of the front face of calorimeter module c. z_{t0} is the z-coordinate of the center of the LH_2 target. If only one phototube in a module fires we set $y_{mod,c} = \pm$ 0.8 m (half the calorimeter height) and calculate $E_{mod,c}$ as

$$E_{mod,c} = g'_c R e^{-0.8/\bar{\lambda}_c} \tag{3.3d}$$

where R is the non-zero phototube response. We will refer to only one tube firing as a module with a "bad-y". The calorimeter response to a particle traversing the electron and hadron modeuls will be denoted as p_{Tmod} and is the sum of electron and hadron p_T's.

$$p_{Tmod} = p_{Tmod,e} + p_{Tmod,h} \tag{3.3e}$$

b. Triggering Biases

A single particle trigger can be generated by particles that have momenta less than the thresholds required by the calorimeters. This can occur in several ways: (i) the calorimeter responds with an upward fluctuation due to finite resolution, (ii) the magnet imparts a p_T kick to charged particles, (iii) several other particles

may add additional energy to the triggering module, and (iv) the trigger may be a function of the particles' masses. All these effects become negligible for p_T's far above threshold.

The resolution of the calorimeter implies that the calorimeter will respond with momentum p_o to a particle having incident momentum p_{in}. This response, $R(p_{in},p_o)$, is an approximate Gaussian about p_{in} with $\sigma \propto \sqrt{p_{in}}$. As shown in Figure 3.1, particles with momenta less than the bias will have a small probability of triggering the experiment when p_o is above the threshold. Thus triggering efficiency is small for incident momenta below bias, becomes ~50% at threshold and is essentially 100% and independent of the calorimeters far above bias.

For triggering on charged particles with steep momentum spectra, the effect of the magnet on particles below threshold is substantial. Figure 3.2 depicts how the calorimeter, responding to an energy E, sees an apparent p_T. From the figure, the apparent p_T is $E\,\frac{x+\Delta x}{z_1+z_2}$ while the real p_T is $E\,\frac{x}{z_1+z_2}$. The magnet therefore adds a p_T contribution to the trigger of magnitude

$$E\,\frac{\Delta x}{z_1+z_2} \simeq p_{Tk}\,\frac{z_1}{z_1+z_2} \qquad (3.4)$$

where p_{Tk} is the magnet p_T kick (0.375 GeV/c). The more abundant lower p_T particles will be given this added kick so that, in essence, the magnet lowers the calorimeter threshold. Note that this is only true for particles which bend outwards while those that bend inwards effectively raise the threshold.

Since the direction of the magnet kick depends on the charge of the particle and the direction of the magnetic field, for any particular magnet setting then, the right side calorimeter prefer-

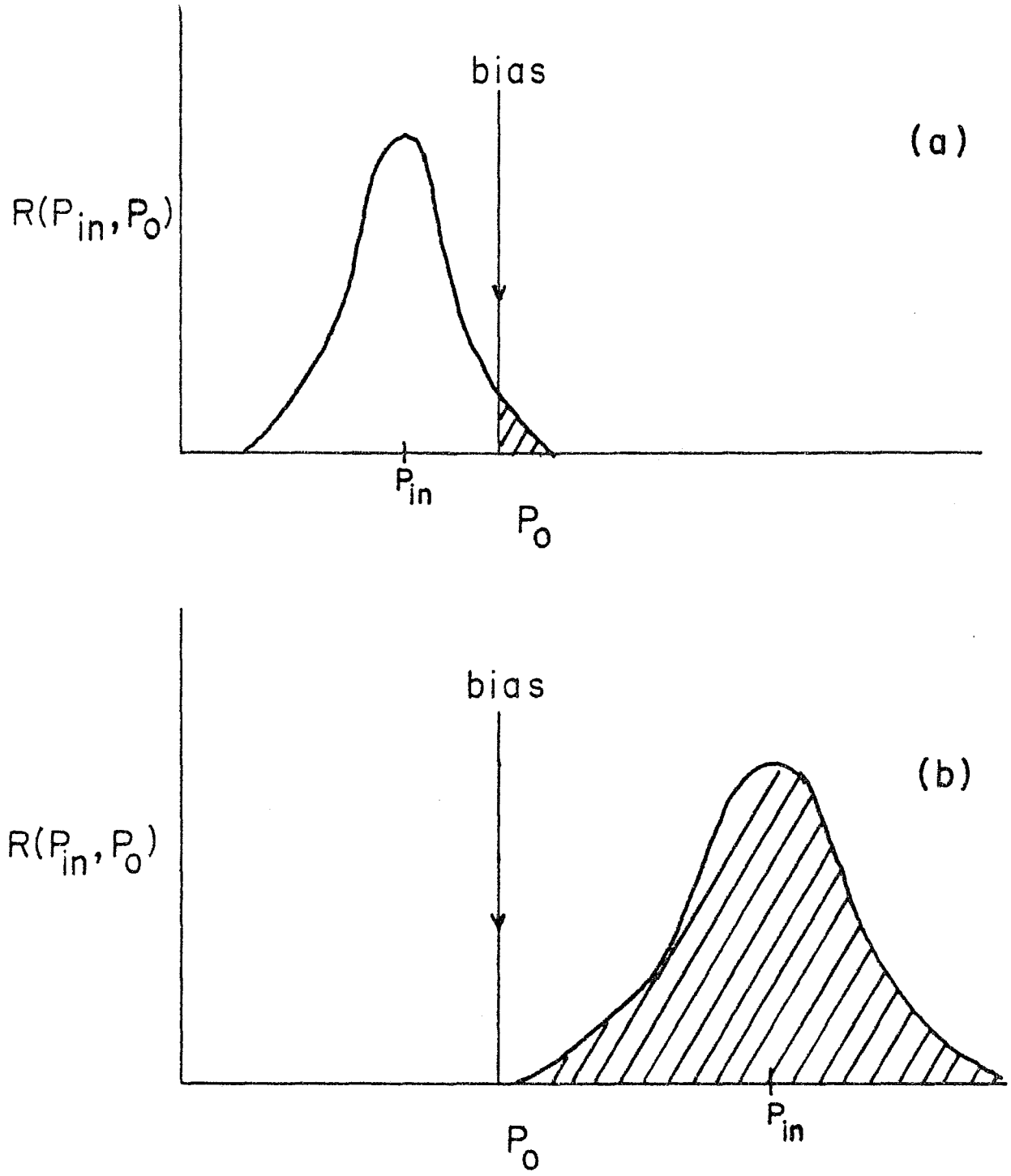

Figure 3.1 Schematic drawing showing the response of the calorimeter to particles of incident momentum, p_{in}, (a) less than the bias and (b) far above the bias. A trigger occurs whenever the calorimeter response, p_o, is above the bias (shaded regions).

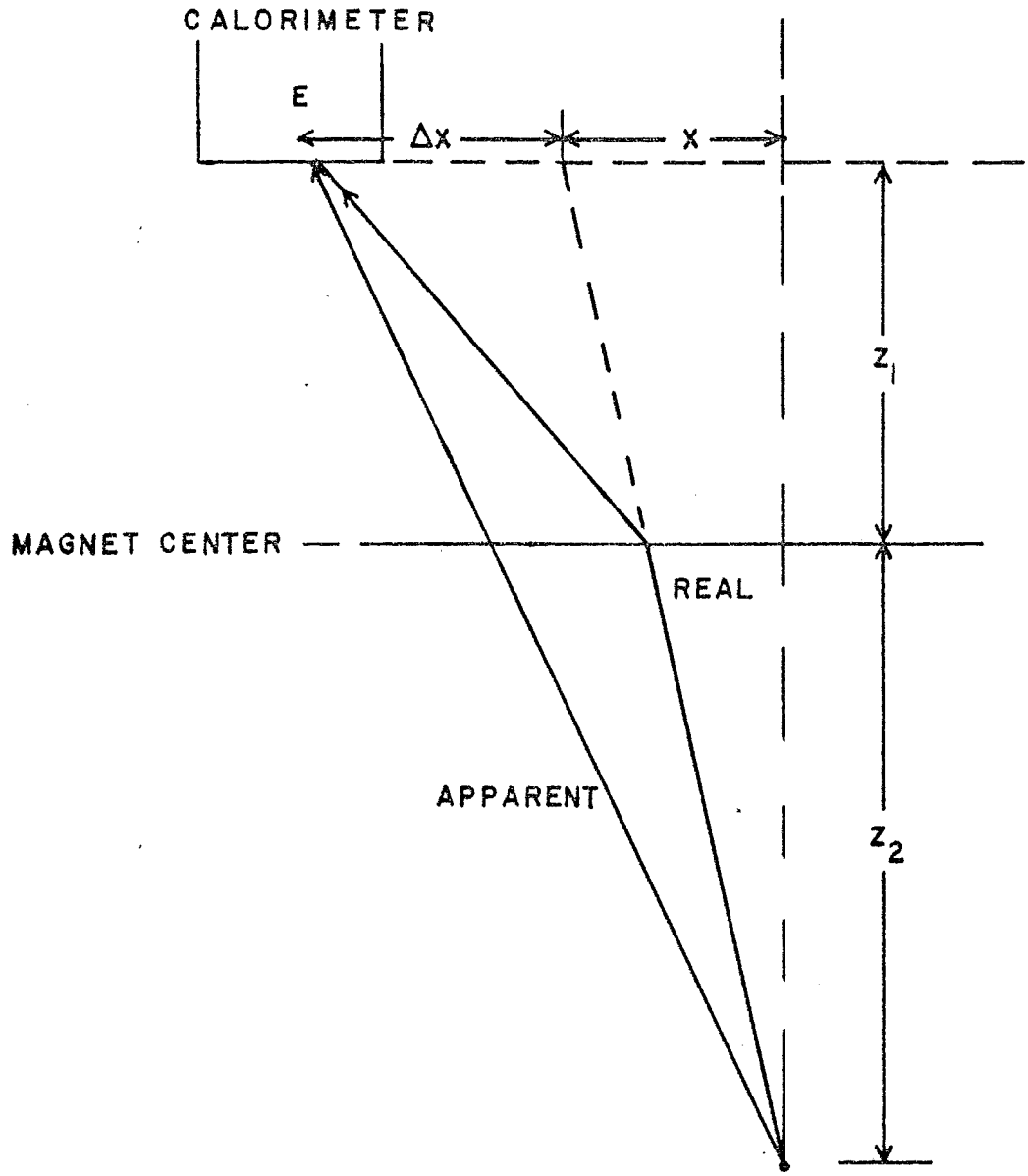

Figure 3.2 A sketch of how an apparent p_T is seen by a calorimeter module when a particle is bent into it by the magnet. The calorimeter measures an energy E but the p_T it sees is proportional to the mean lab angle which is not the same as the production angle of the particle.

entially triggers on one sign of charge and the left side on the opposite charge. Because the thresholds and responses of the left and right calorimeters may be slightly different, points (i) and (ii above imply that it is important to take equal amounts of both polarity magnetic fields. We show in Section A.2c of the Appendix how to make corrections for the left-right triggers if we know how much effective beam there is for a particular magnet setting.

Besides the resolution and the magnet effect we need to next ask how often will the calorimeter trigger on many low p_T particles thus signalling an event with high p_T. Especially for the single particle trigger where we would like to see only one particle of hig p_T into a calorimeter module the magnet can pick several of the abun dant like-charge, low p_T particles and sweep them into a particular module and bring the response above bias. However, competing with the sharp p_T spectrum is the probability that a small region of phas space will be occupied by two or more hadrons. Therefore the single particle trigger rate for this mechanism is proportional to the prob ability of seeing two particles entering a single module. We can estimate this process for, say, magnet off and uncorrelated inelastic events and compare to the similar one-particle events. The rati of two-particle rate to one-particle rate is given by

$$\frac{C_2(p_{Tcal})}{C_1(p_{Tcal})} = \frac{P(2)}{P(1)}\, f(0)\, \frac{\int_0^\infty dp_{T1} \int_{p_{T1}}^\infty f(p_T) R(p_T, p_{Tcal})\, dp_T}{\int_0^\infty dp_T f(p_T) R(p_T, p_{Tcal})} \qquad (3.5)$$

where P(2) is the probability of getting two particles into the calo remeter and P(1) is the probability of getting one particle. $f(p_T)$ is the true p_T spectrum of particles but such that $f(x)f(y) \propto f(x+y)$.

It is obvious that the ratio of the two integrals in Eq. 3.5 is greater than 1 since we include the denominator in the integral over p_{T1}. If $f(0)P(2)/P(1) \geq 1$ then the two particle process may well dominate the single particle process. Inelastic events are characterized by a central rapidity plateau and using this information we can calculate the mean number, ΔN, of particles within a rapidity interval, Δy, around $y = 0$ (90^{o} in CMS).

$$\Delta N = \frac{1}{\sigma_{tot}} \sum_{i} \frac{d\sigma^{i}}{dy} \Delta y \tag{3.6}$$

where σ_{tot} is the total cross section for, say, $pp \rightarrow X$ and $\frac{d\sigma^{i}}{dy}$ is the cross section producing hadron i in rapidity interval between y and y+dy. If ΔN is the mean number of particles produced, the probability of obtaining m particles follows a Poisson distribution. Therefore,

$$\frac{P(2)}{P(1)} = \frac{e^{-\Delta N}\Delta N^{2}}{2!} \cdot \frac{1!}{e^{-\Delta N}\Delta N} = \frac{\Delta N}{2} \tag{3.7}$$

For π^{+} and π^{-} production by protons $\frac{d\sigma}{dy} \simeq 35$ mb in the central region[34]. A calorimeter module subtends $\Delta y \simeq 0.20$ and at 200 GeV, $\sigma_{tot} \simeq 40$ mb. Then the average number of π's from pp collisions in this rapidity interval is

$$\Delta N \simeq 2.35/40 \cdot 0.20 = 0.35$$

For a very rough idea of the magnitude of this effect we can look at an ideal detector with $R(p_{Tinc}, p_{Tcal}) = p_{Tcal}\delta(p_{Tinc} - p_{Tcal})$, and a distribution of particles that follow $f(p_T) = e^{-bp_T}/b$, we calculate

$$\frac{C_2(p_{Tcal})}{C1(p_{Tcal})} = \frac{P(2)}{P(1)} p_{Tcal}^{b} \tag{3.8}$$

If we parameterize the high-p_T spectrum, Eq. 1.2, as e^{-bp_T} we find that at any value of p_T that $b = 7/p_T$. Therefore our two-particle

rate for an ideal detector according to Eq. 3.8 is about 20% greater than the single particle rate. It is not hard to imagine that with the added p_T kick of the magnet and the calorimeter with a poor resolution that the multiparticle trigger may be non-negligible when supposedly dealing with the single particle trigger. With the jet trigger where the rapidity acceptance is larger, we expect this prob lem to be even more severe. Figure 3.3 shows the average charged multiplicity, ΔN, in a single calorimeter module when there is a hig p_T particle having the largest p_T of all incident particles, $p_{Tin,ma}$ We see that at lower values of transverse momentum, the multiplicity is not too different than that calculated above. There is an extra particle into the trigger module about 40% of the time.

Still another effect which may become important later in the analysis is the fact that the calorimeter response is an approximate function of the incident kinetic energy, not momentum[35]. For a fixe momentum, a proton has less kinetic energy than a pion and therefore should trigger less efficiently. Using a Monte Carlo that approximates the E260 calorimeters in resolution and shower shapes, Figure 3.4 gives the triggering rate difference between high p_T π's and p's as a function of their p_T and the multiplicity of accompanying particles. One high p_T particle (π or p) with a spectrum of e^{-3p_T} is accompanied by from 0 - 3 low p_T π's with spectra of e^{-3p_T} hitting the calorimeter. A single particle trigger is demanded ($p_{Tmod} \geq$ 3.0 GeV/c). On the average, π's trigger about 20% of the time more frequently than protons below bias. This is a strong function of the multiplicity in the trigger module where the effect is very large for only one π or p incident. The added energy of the accompanying π's tend to wash the effect out. In the actual triggers we

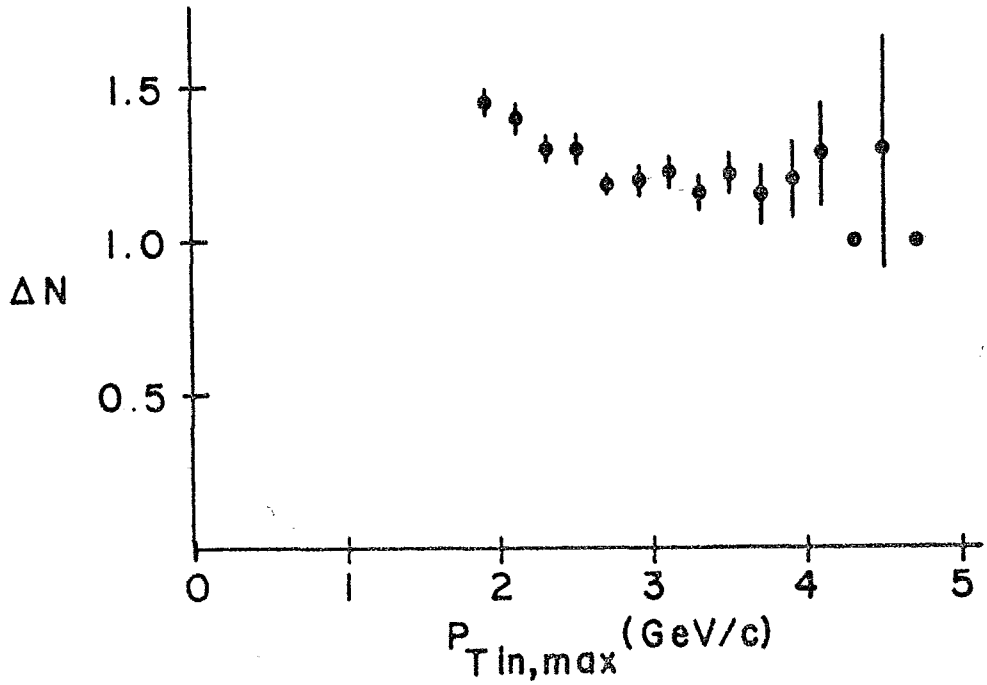

Figure 3.3 The average multiplicity of charged particles into a single calorimeter module with a HIPT trigger. It is plotted against the transverse momentum of the fastest particle into the module.

Figure 3.4 A Monte Carlo calculation of the difference in trigger rates for pions and protons normalized to the pion trigger rate. We assume that the calorimeter responds to kinetic energy and not momentum. The rate differences are shown in the figure for: (a) 1-particle trigger, (b) 2-particle trigger, (c) 3-particle trigger, and (d) 4-particle trigger. (e) averages over (a) through (d).

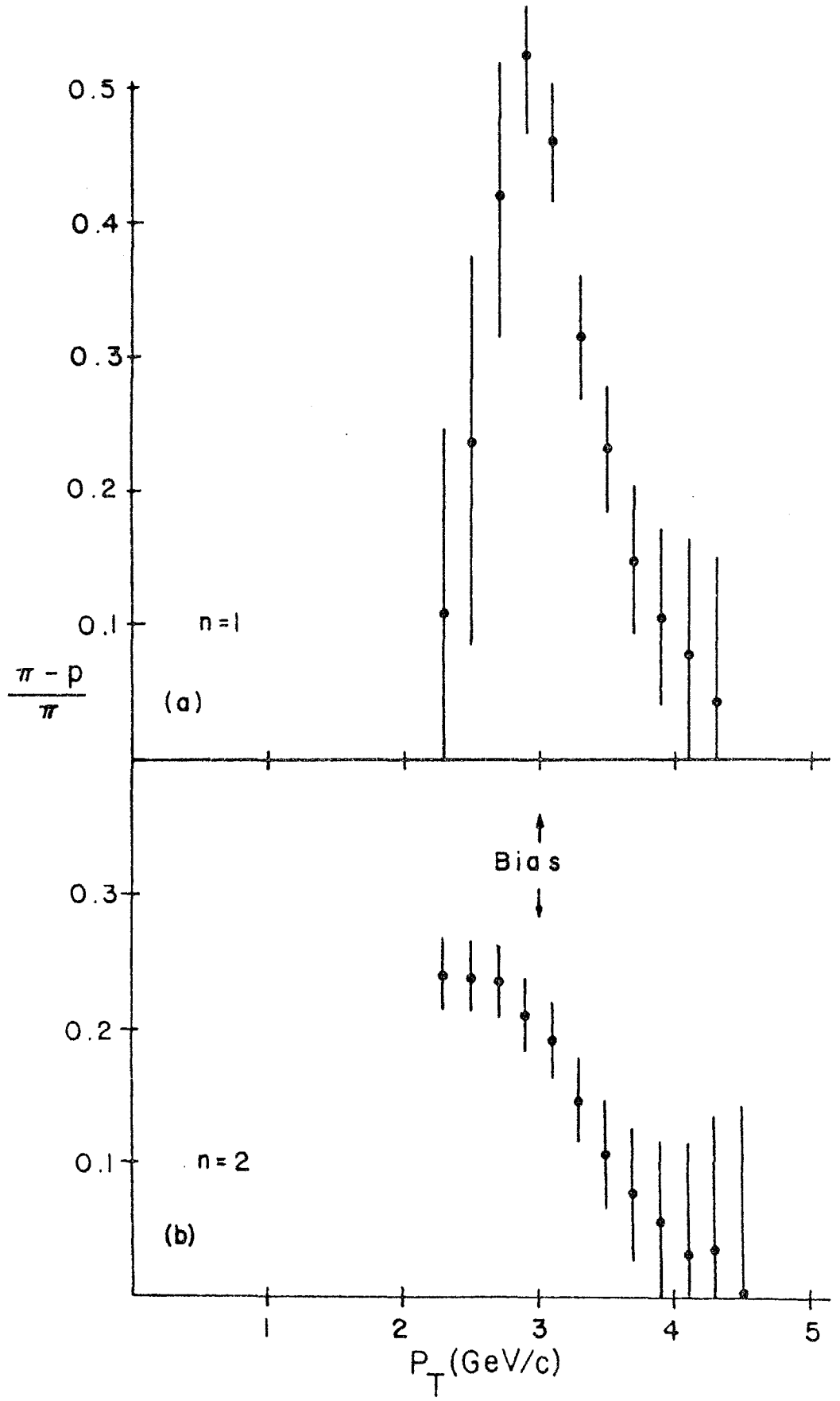
0.5
0.4
0.3
0.2
0.1
n=1
$\frac{\pi - p}{\pi}$
(a)
Bias
0.3
0.2
0.1
n=2
(b)
1
2
3
4
5
P_T (GeV/c)

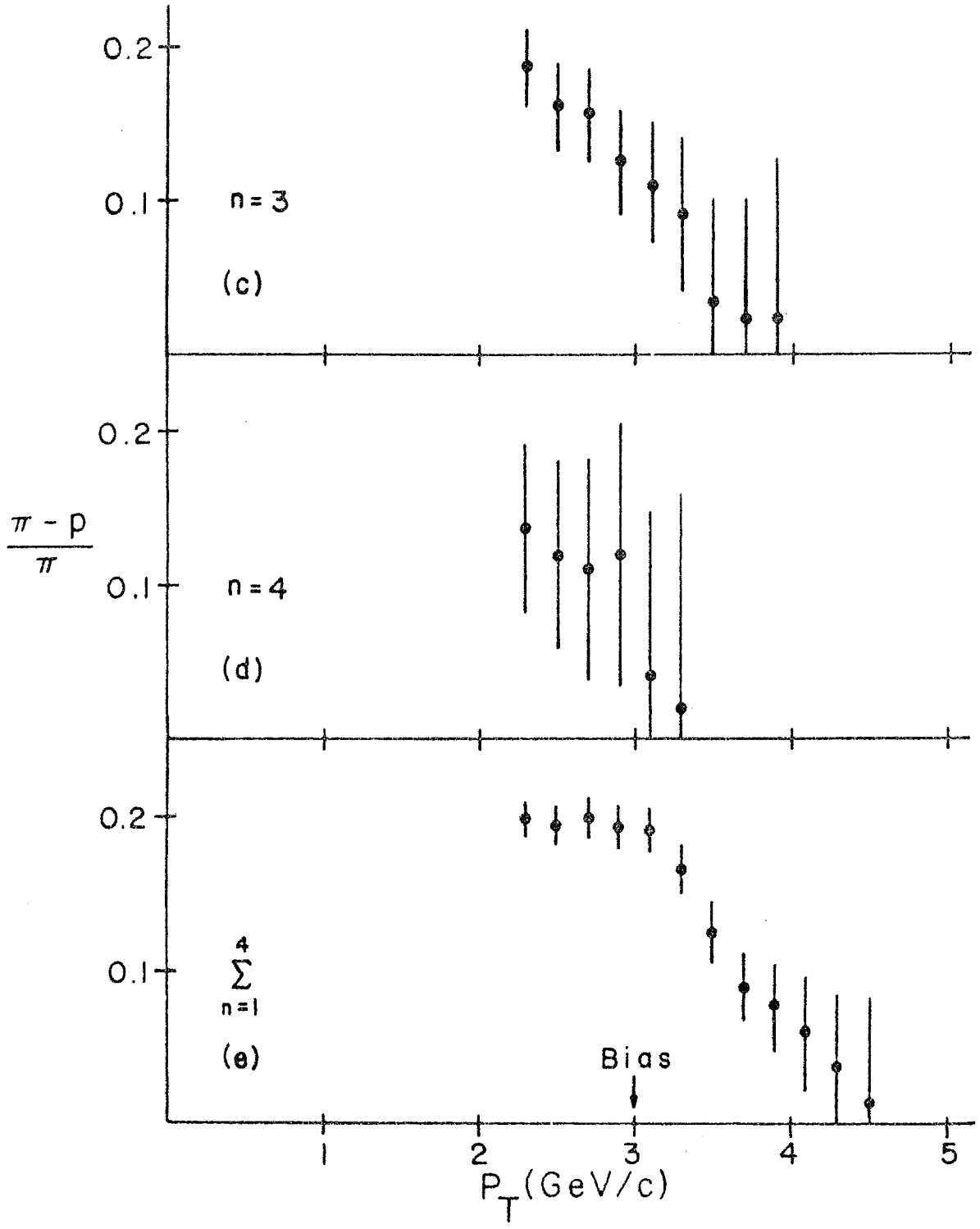
0.2
0.1
n = 3
(c)
0.2
0.1
n = 4
(d)
$\frac{\pi - p}{\pi}$
0.2
0.1
$\sum_{n=1}^{4}$
(e)
Bias
1
2
3
4
5
P_T (GeV/c)

may not know the true hadronic multiplicity because of missed tracks and neutrals. However, one should be aware of the fact that heavy particles trigger less efficiently than π's.

3.4 Cerenkov Counter Photoelectrons and Gains

The efficiency and gain of each mirror-phototube system was found by using cases where only one fast particle was incident into a mirror with its Cerenkov light cone fully contained in the cell. The fastness cut was made by requiring that the light produced by $\geq$ 67% the light of a $\beta = 1$ particle. The momentum requirement is found from

$$e(p) \equiv \frac{\text{Light}}{\text{Light}_{|\beta=1}} = \frac{D}{D_{max}} \left(1 - \frac{p^2_{th,\pi}}{p^2} \right) \qquad (3.9)$$

where $p_{th,\pi}$ is the π threshold momentum and D/D_{max} is the fraction of the maximum radiator length the particle traverses. Table 3.4 lists the various particle threshold momenta for air and the He mixture. Since particles above kaon threshold can be K's giving a small amount of Cerenkov light we also require particles to be below K threshold. This insures us that if any light is given it comes only from relatively fast π's. Assuming that the photoelectrons follow a Poisson distribution the average number of photoelectrons can be calculated using

$$\langle n_{\gamma e} \rangle = \left(\frac{\langle PH \rangle}{\sigma} \right)^2 \qquad (3.10)$$

where $n_{\gamma e}$ is the number of photoelectrons producing a pulse height PH with a standard deviation of σ. The average cell efficiency is then given by

$$\varepsilon = 1 - e^{-\langle n_{\gamma e} \rangle} \qquad (3.11)$$

We must point out that Eq. 3.10 may not necessarily be the correct

Particle	Air Threshold (GeV/c)	He Threshold (GeV/c)
π	5.77	8.93
K	20.40	31.61
P	38.76	60.07

Table 3.4 Cerenkov threshold momenta for air and the mixture of 2/3 He and 1/3 air.

method of determining the photoelectron yield. There are at least two reasons: (i) if the phototubes have a very high voltage then space-charge effects limit the number of electrons produced at the anode (saturation), or (ii) the number of photoelectrons may be the RMS sum of the Cerenkov photons plus the effective number of photons reflected into the photocathode. Case (i) may indeed by satisfied with the large amount of photoelectrons expected with air. Alternate methods of calculating the photoelectron yield can include fits of Poisson distributions or comparing the average pulse height to the pulse height for one photoelectron. Knowing the momentum distribution of particles into a given cell we can calculate the average effective pions contributed to that cell. If $f_n(p)$ is the momentum spectrum of particles into cell n, then the average effective pions is

$$\langle e \rangle = \frac{\int_M f_n(p)\, e(p)\, dp}{\int_M f_n(p)\, dp} \tag{3.12}$$

where the integral ranges over momentum region M defined above, i.e., $1.73 \leq P/p_{th,\pi} \leq 3.46$. The corresponding number of photoelectrons from $\beta = 1$ particles will be

$$\langle n_{\gamma e} \rangle_{\beta=1} = \frac{\langle n_{\gamma e} \rangle_M}{\langle e \rangle} \tag{3.13}$$

where $\langle n_{\gamma e} \rangle_M$ is the number of photoelectrons determined from the raw pulse heights in the momentum region M. The gains for each cell were determined by requiring $\beta = 1$ particles to be in pulse height channel 400. Table 3.5 lists the photoelectrons for each cell of C1 for both $\beta = 1$ particles and particles in region M.

The edges of the mirrors were investigated next by using a normalized pulse height for the struck mirrors. Let a particle striking cell n also contribute light to adjacent mirrors. We define the nor-

AIR

CELL	$1.73 \leq p/p_{th,\pi} \leq 3.46$			$\beta = 1$		
	<PH>	σ	$\langle n_{\gamma e} \rangle$	$\langle n_{\gamma e} \rangle_{\beta=1}$ RAW PH	NPH-CENTER	NPH-EDGE
1						
2	100.6	42.8	5.5	7.1	4.5	4.9
3	312.6	126.1	6.1	7.7	6.7	7.0
4	311.8	99.0	9.9	12.5	10.2	4.7
5	320.2	109.4	8.6	10.7	9.1	7.9
6	325.2	155.1	4.4	5.4	4.3	3.8
7	324.0	112.4	8.3	10.3	9.1	7.0
8	313.6	137.8	5.2	6.5	5.6	5.6
9	321.6	102.4	9.9	12.3	10.5	8.9
10	268.6	106.0	6.4	8.3	7.2	4.6
11						
12						
13	175.6	75.5	5.4	6.9	5.3	2.8
14	318.2	120.2	7.0	8.7	7.7	6.0
15	312.4	120.8	6.7	8.4	7.2	3.8
16	323.3	98.3	10.8	13.6	11.9	9.1
17	328.6	162.3	4.1	5.0	4.3	4.2
18	328.0	127.8	6.6	8.2	7.0	5.3
19	321.2	174.2	3.4	4.3	3.8	2.4
20	324.0	121.7	7.1	8.9	7.1	5.0
21						
22						

Table 3.5a Cl photoelectron yield calculated from the raw pulse heights and the normalized pulse heights. Cl filling is air.

HELIUM

CELL	$1.73 \leq p/p_{th,\pi} \leq 3.46$			$\beta = 1$		
	<PH>	σ	$\langle n_{\gamma e} \rangle$	$\langle n_{\gamma e} \rangle_{\beta=1}$ RAW PH	NPH-CENTER	NPH-EDGE
1						
2						
3	334.3	170.1	3.9	5.0	4.5	4.9
4	301.8	121.7	6.1	7.7	6.2	4.8
5	315.4	140.4	5.0	6.4	5.5	5.5
6	335.0	170.4	3.9	4.7	3.4	2.8
7	316.9	131.9	5.8	7.3	6.5	5.0
8	323.7	163.1	3.9	4.9	4.2	5.3
9	320.4	132.7	5.8	7.5	6.2	5.5
10						
11						
12						
13						
14	285.0	143.5	3.9	5.1	4.2	3.6
15	285.1	143.0	4.0	5.0	4.2	2.9
16	356.0	134.2	7.0	9.0	7.9	5.4
17	306.8	183.0	2.8	3.5	3.0	3.0
18	303.8	143.9	4.5	5.7	4.6	3.9
19	335.3	197.9	2.9	3.6	3.1	2.8
20	302.0	135.4	5.0	6.4	5.0	3.7
21						
22						

Table 3.5b C1 photoelectron yield for the He filling.

malized pulse height for the struck cell n, NPH_n, as the sum of the ratios of pulse height to effective pions for all the cells to which the particle contributes light:

$$NPH_n = \sum_i \frac{PH_i}{e_i} \qquad (3.14)$$

where e_i is the fraction of e that shines into cell i. A cell n having a particle incident with its light fully contained in it has its average number of photoelectrons calculated using Eq. 3.10 but with NPH replacing PH. Again particles are required to be in the momentum region M. Since we normalize by the effective pions the number of photoelectrons found by this method corresponds directly to $\beta = 1$ particles. We find, however, that the photoelectrons found in this case are always about 15% lower than $\langle n_{\gamma e} \rangle_{\beta = 1}$ found with the raw pulse height. This is due to the fact that sometimes a smal e will correspond to a large PH which then makes the calculated σ large. The two methods agree if we instead leave out the very high values of the normalized pulse heights. We now calculate, using NPH the number of photoelectrons for particles striking cell n that shar the Cerenkov light in neighboring cells and compare to the non-overlapping calculation. Table 3.5 also shows the photoelectron yield calculated from the normalized pulse height for both the contained a overlapping light. Finally $\langle n_{\gamma e} \rangle_{\beta = 1}$ for the edges is found and is listed in Table 3.5.

Neglecting mirrors 6 and 17 in the beam region we find that the average photoelectron yield for C1, $\overline{\langle n_{\gamma e} \rangle}$, for $\beta = 1$ particles is

$$\overline{\langle n_{\gamma e} \rangle}_{Air} = 9.0 \pm 2.5$$

$$\overline{\langle n_{\gamma e} \rangle}_{He} = 6.1 \pm 1.5$$

Comparing this result to the calculated expectation found in Section 2.2f, we find that the photoelectron yield agrees with the He calculation but is low for the air calculation. If the phototubes are at a high gain then we expect to see effects of tube saturation with a large number of photons as calculated for air. A quantitative measure of the saturation effect would indeed be nice to confirm our conjecture, but the writer finds it difficult at this time to do so. But it may just be fortuity that the photoelectron yield agrees in He with our calculated value in which case it would be difficult to explain a lack of agreement in the air case and not the helium.

Recall that the quality factor characterizing our Cerenkov counter, A, was defined in Section 2.2f by $N_{\gamma e} = A l \sin^2\theta$. We found that, under ideal conditions, A was about 70 cm^{-1}. In actual operation, we find

$$A \simeq 38 \pm 10 \text{ cm}^{-1} \text{ for air,}$$

and

$$A \simeq 61 \pm 15 \text{ cm}^{-1} \text{ for helium-air}$$

The variations in the number of photoelectrons for cell to cell is about ±25%. This variation is probably due to the reflectivity of the mirrors which may have had some surface imperfections. Multiple reflections in the light cones, through the phototube windows and into the phototubes can reduce the number of photons onto the photocathode.

3.5 Particle Identification

We will be interested in categorizing the secondary hadrons according to whether the cells in C1 the particles strike are in an ON or OFF state. ON will be defined as a corrected pulse height ≥ 5 and OFF less than 5. Because of the high multiplicities[20] and large physical size of the mirrors we can often expect there to be more

than one particle contributing light to a given cell. Table 3.6 shc the average number of extra particles contributing light to differen cells in the HIPT trigger. Included here are particles that are directly incident or fast particles whose Cerenkov light cone overlaps several mirrors. In Table 3.6 the minimum number of effective pions per contribution is 0.05. Especially in the center cells - 5, 6, 7, 16, 17, 18 - we see that there is a good chance to have another particle to confuse identification. Therefore the software has to be such as to disentangle as many particles as possible. In trying to identify a particle which may contribute light to one or more struck cells of C1, we proceed to classify the following identification categories:

1. No other particles can contribute light to struck cells. The cells may by ON or OFF.
2. The struck cells are OFF even if $\geq$ 2 particles can contribute light.
3. The Cerenkov light cone is fully contained in one cell and this cell has $\geq$ 2 contributions. We are able to subtract the other contributions by checking neighboring cells.
4. The Cerenkov light overlaps into a neighboring cell that has no other contributions.
5. Ambiguous because the particle misses C1 or is below pion threshold.
6. Ambiguous because $\geq$ 2 particles are entirely contained in one cell.
7. Ambiguous because the Cerenkov light cones of other particles overlap the particle of interest making the identification difficult.

CELL	HIPT		INT BEAM	
	% Time ≥ 2 Contr	<Contr>	% Time ≥ 2 Contr	<Contr>
1	2.1 ± 2.1	1.02	-	-
2	3.1 ± .6	1.03	2.5 ± 2.0	1.02
3	7.8 ± .6	1.08	2.5 ± 1.1	1.03
4	13.5 ± .6	1.16	6.8 ± 1.2	1.07
5	34.8 ± .5	1.46	32.3 ± .9	1.41
6	70.5 ± .4	2.37	72.3 ± .6	2.42
7	36.7 ± .5	1.49	32.4 ± .9	1.41
8	15.1 ± .6	1.17	7.8 ± 1.2	1.08
9	8.6 ± .6	1.09	4.3 ± 1.4	1.05
10	1.9 ± .5	1.02	0	1.0
11	0	1.00	-	-
12	0	1.0	-	-
13	2.7 ± .5	1.03	0	1.0
14	9.2 ± .6	1.10	3.7 ± 1.4	1.04
15	14.3 ± .6	1.16	4.9 ± 1.0	1.05
16	35.2 ± .5	1.47	30.1 ± .9	1.39
17	72.6 ± .4	2.44	74.9 ± .6	2.52
18	35.4 ± .5	1.48	33.0 ± .9	1.42
19	15.8 ± .6	1.18	8.1 ± 1.2	1.09
20	7.8 ± .5	1.08	4.9 ± 1.5	1.06
21	2.5 ± .5	1.03	1.7 ± 1.7	1.02
22	0	1.0	-	-

Table 3.6 The average number of particles contributing Cerenkov light to a cell. Also given is the percent of time that there are ≥ 2 contributing particles. The HIPT trigger and interacting beam trigger are shown for comparison.

8. Ambiguous because insufficient Cerenkov light may be produced.

These ID classes will be further discussed after we define particle types and discuss ID class 8 below.

Of major importance in this work will be the identification of the trigger particle(s). Therefore we are most interested in the pa ticles that hit the calorimeters and the Cerenkov mirrors that overlap them - cells 3, 4, 8, 9, 14, 15, 19 and 20. Figure 3.5 shows th expected efficiency of these cells in C1 for air or He as a function of momentum. The number of $\beta = 1$ photoelectrons is obtained from Tab 3.5 and we use $\overline{\langle n_{\gamma e} \rangle}_{Air} = 8.6$ and $\overline{\langle n_{\gamma e} \rangle}_{He} = 5.6$ in constructing Figure 3.5. For ID classes 1 - 4 above the identification of the secon daries proceeded in two modes. In the threshold mode, knowing the momentum of a particle from the spectrometer enabled us to use the ON/OFF state of C1 to do rough categorization. Neglecting inefficie cy for the moment, if C1 if ON/OFF we therefore identify the secondaries as π/Kp in region (I) of Figure 3.5, a πK/p in region (II), and in region (III) as πKp/?. Definite identification exists in the threshold mode only for π's between about 6 GeV/c and 30 GeV/c and for protons between 20 GeV/c and 60 GeV/c combining both the air and He fillings in C1.

For a cell that is OFF, a possible K or p, we have to consider whether or not sufficient Cerenkov light is produced so as to be certain we are not seeing C1 inefficiency. For example, just above pion threshold π's may be, on the average, 80% efficient in turning a cell ON. Therefore, 20% of the π's will masquerade as a Kp and we must decide to what level π contamination is acceptable. In pp inelastic collisions the π-Kp ratio for positive particles is about

Figure 3.5 The expected average efficiency of the C1 mirrors in front of the calorimeters. The efficiency for both air and helium is shown and the respective particle thresholds are indicated.

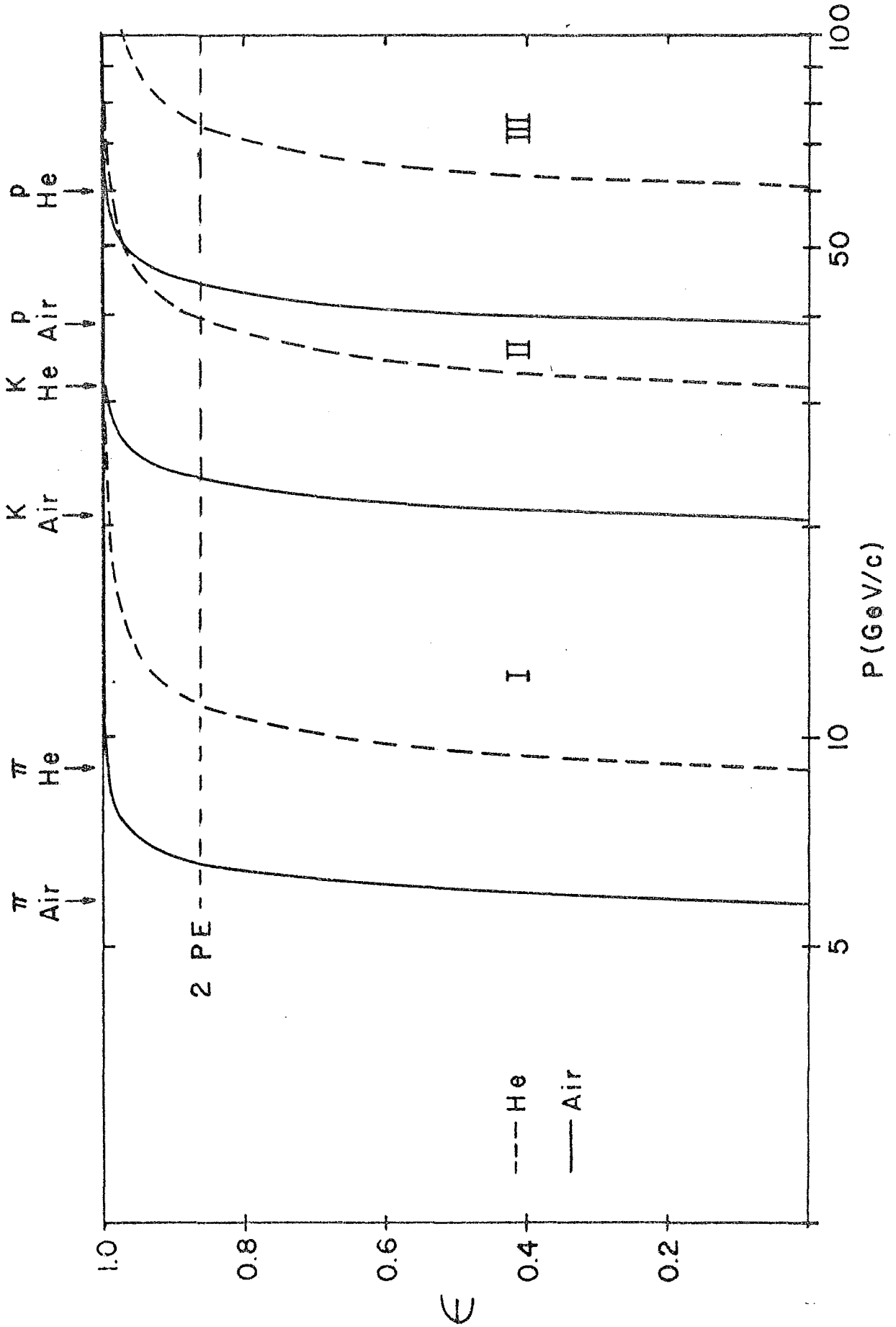
π Air
π He
K Air
K He
p Air
p He
2 PE
I
II
III
He
Air
ε
1.0
0.8
0.6
0.4
0.2
5
10
50
100
P(GeV/c)

2 and for negatives is about 11[36]. An 80% detection efficiency implies that the number of measured Kp^-'s is three times larger than the real number and the number of Kp^+'s is 40% larger. The π background is troublesome for efficiencies that are not close to 99%. However we can correct for π contamination knowing the detection efficiency. But if we want to be certain that a Kp is not a pion, w have to accept only a small contamination. A π into the trigger cel will fake a Kp or p $\lesssim$ 1% of the time if its momentum is $\geq$ 9 GeV/c in air or $\geq$ 20 GeV/c in He. A K will fake a p less than 1% of the time if its momentum is $\geq$ 30 GeV/c in air or $\geq$ 70 GeV/c in He.

Looking at the ON signals, Figure 3.6 shows the effective numbe of photoelectrons, $e\langle n_{\gamma e}\rangle_{\beta=1}$, for the π and πK tags. We average ov all cells and the air and He runs. A π is well defined at around 1 photoelectron and a πK becomes established at about 2 photoelectrons A 2-photoelectron minimum requirement for C1 to define an OFF signal means that C1 will be at least 87% efficient. The Kp and p tagged particles will be required to contribute at least 2 photoelectrons t the cells that identify them. An OFF signal not satisfying this requirement will be placed in ID class 8 above. Figure 3.7 shows the effective number of photoelectrons for the Kp tagged particles and the effective number of photoelectrons for the class 8 particles.

One other effect may give rise to C1 OFF signals. As noted in Section 2.2f, the ac coupling of the phototubes to the ADC's will result in a possible "1" in the pulse height thus faking an OFF signal. Table 3.7 gives the percentages of "1" compared to real ON signals. This effect is predominant in the center cells, 6 and 17, where most of the diffractive-type particles scatter. However, for this analysis it was found that no apparent effect was seen whether

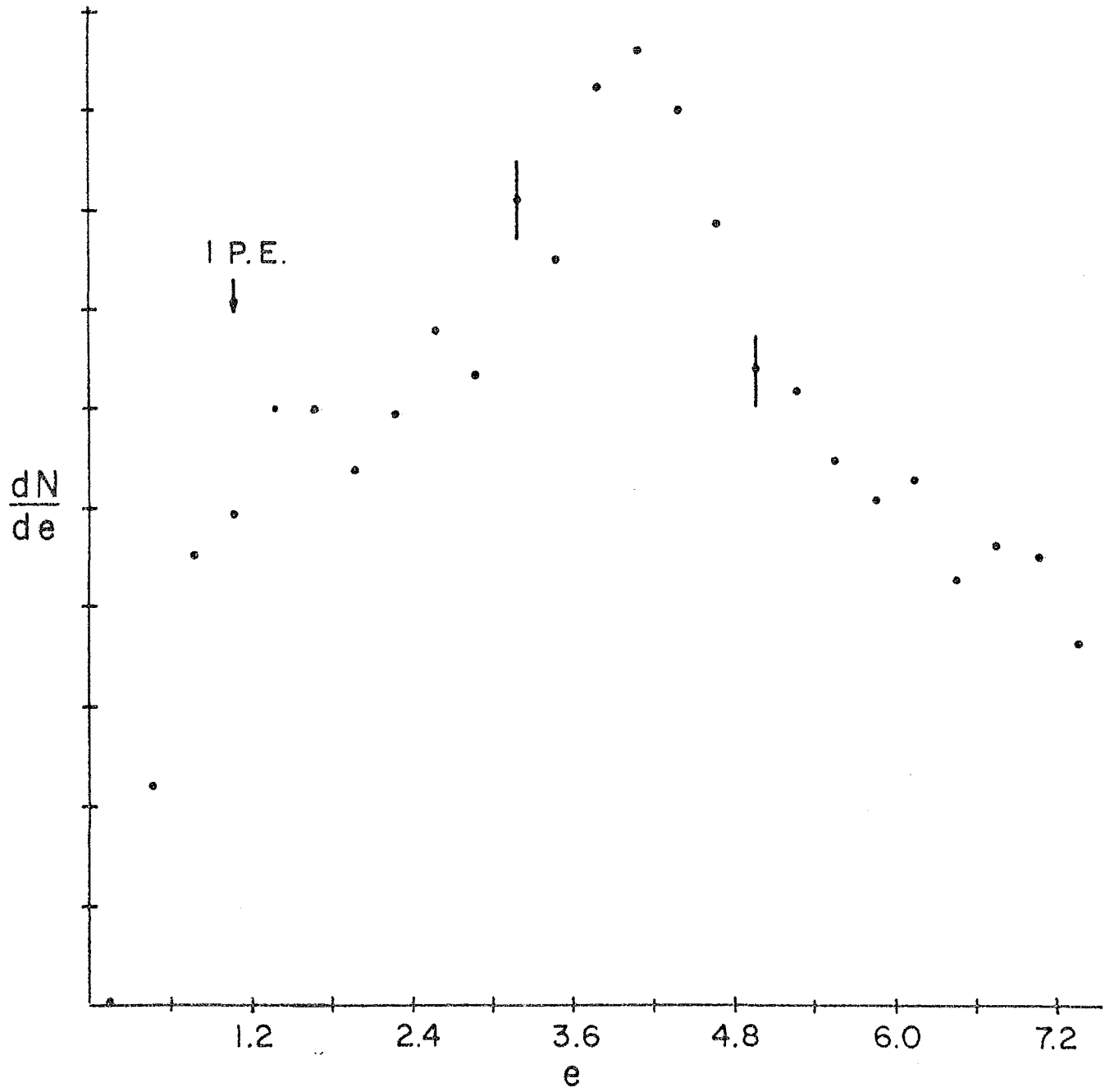

Figure 3.6a The number of effective photoelectrons for a π tag. We average our air and He data as well as Cl mirrors.

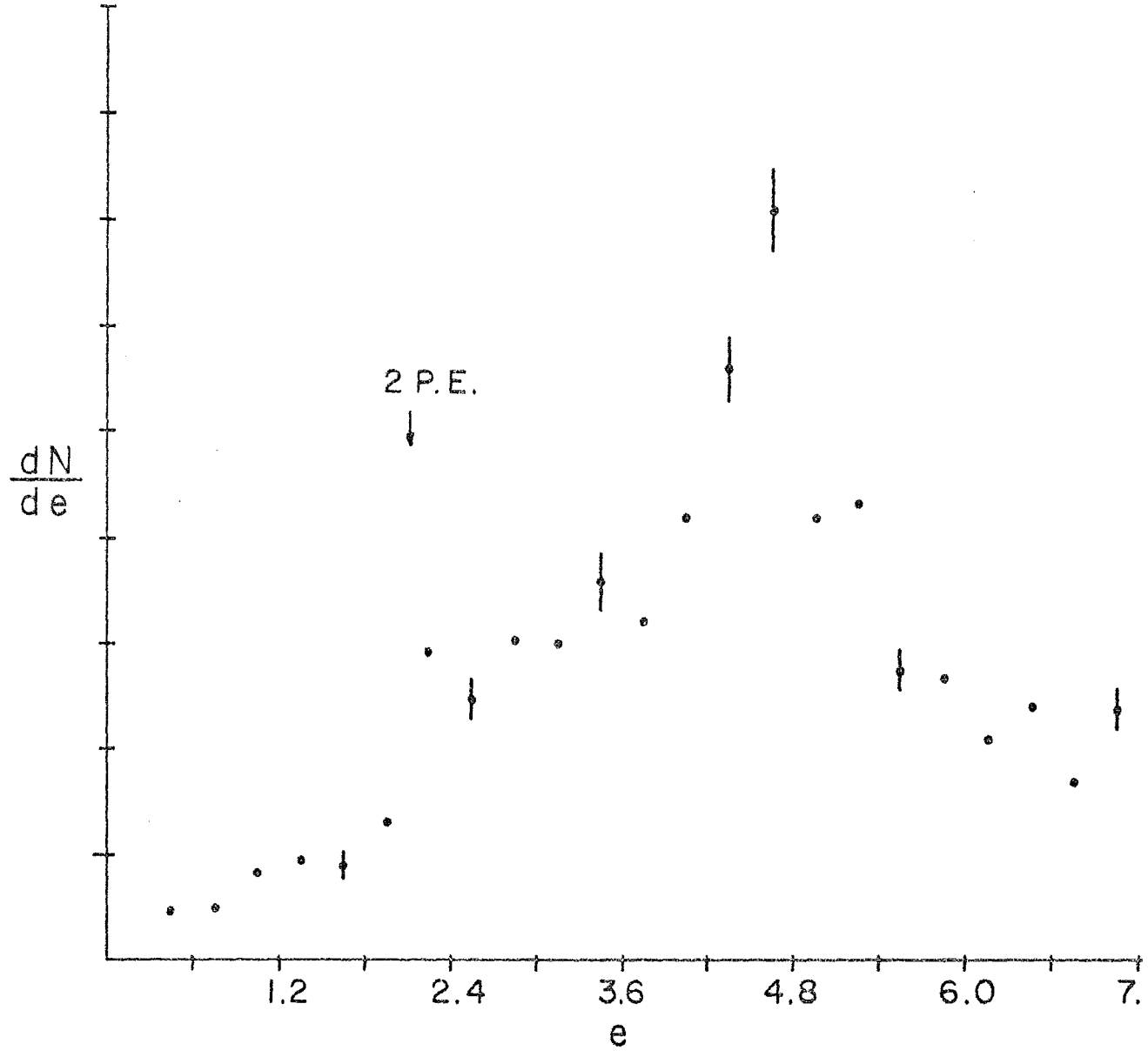

Figure 3.6b The number of effective photoelectrons for a πK tag.

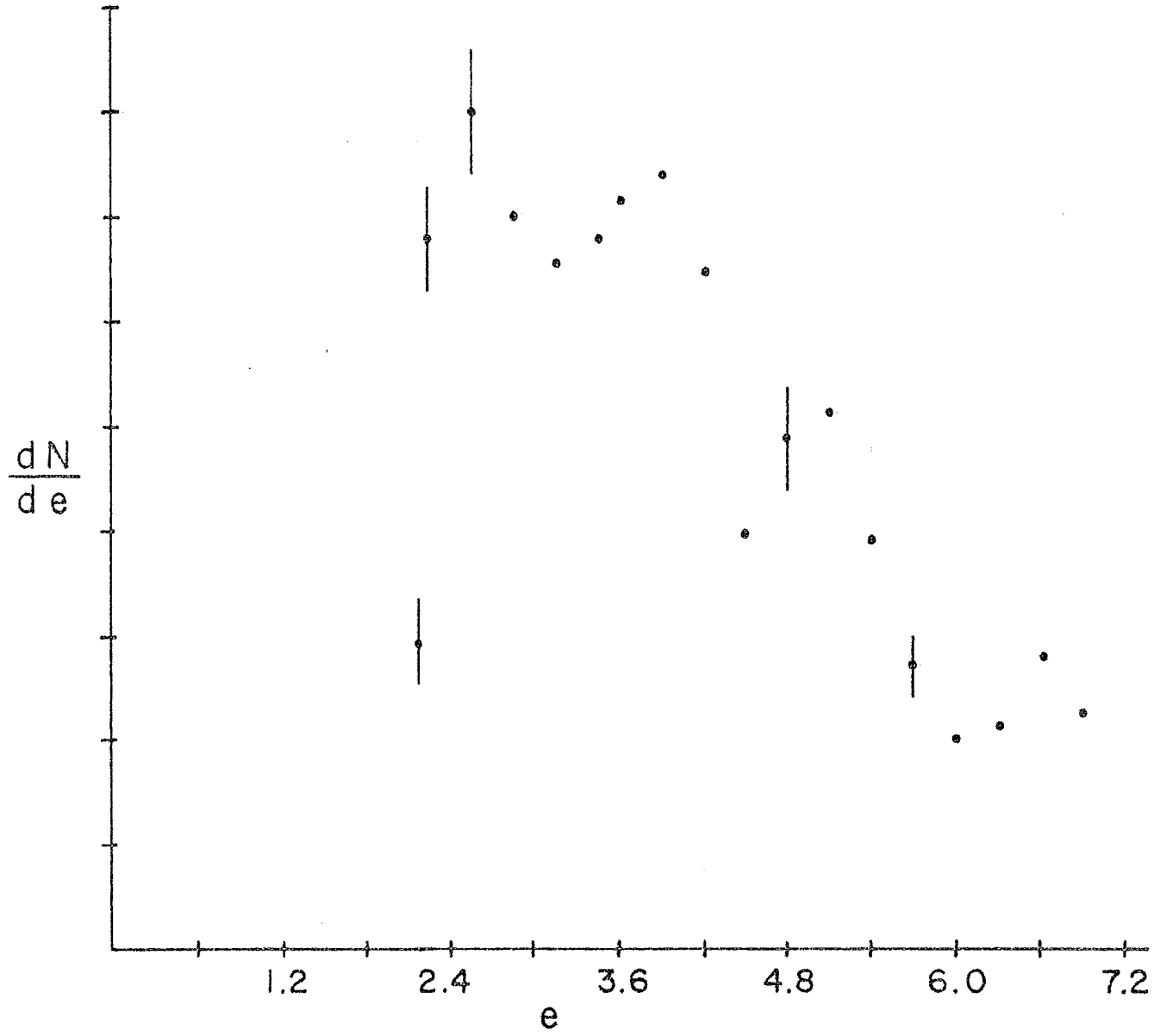

Figure 3.7a The number of effective photoelectrons for a Kp tag. We average our air and He data as well as Cl mirrors.

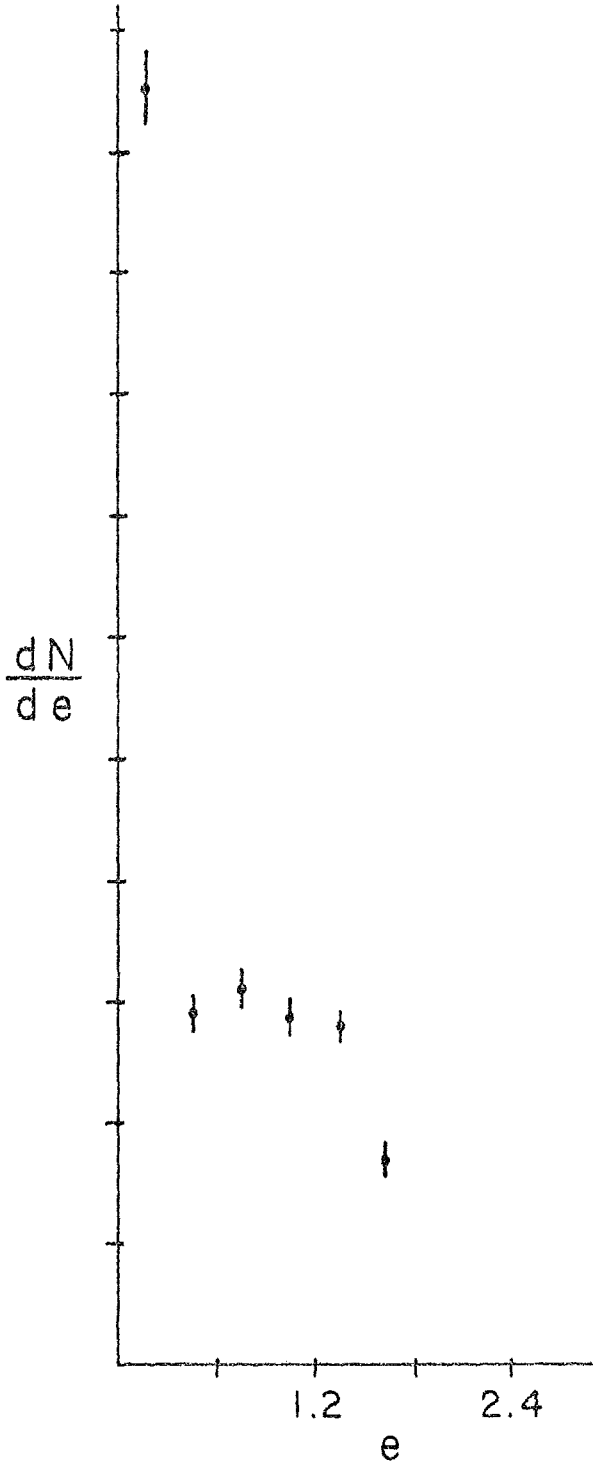

Figure 3.7b The number of effective photoelectrons for particles judged too close to threshold.

CELL	"1"/ON
1	-
2	-
3	0.14
4	0.11
5	0.18
6	0.58
7	0.14
8	.06
9	0.15
10	-
11	-
12	-
13	-
14	.03
15	.04
16	.20
17	.40
18	.07
19	.08
20	.06
21	-
22	-

Table 3.7 Fraction of cell ON signals that are pulse height of "1".

we considered the "1" to be OFF or ON.

Turning to the Cerenkov ON signals, we need to know what contri bution δ-rays or, perhaps, missed tracks have. Remember that our analysis uses only primary vertex associated tracks so that if we find an ON cell with only one track incident above pion threshold, t track may really be a π or may be a K or p with δ-rays or decay particles from neutral V's firing the counter. We can estimate the mis track contribution by asking how often a cell is ON with no particle incident. Since the number of δ-rays produced by a particle moving with velocity β is proportional to β^{-2}, the δ-ray contribution to th ON state can well be estimated by seeing how often a cell is ON with an incident particle below π threshold. Cells are ON with either no tracks incident or incident tracks below pion threshold about 5 - 10% of the time. This becomes about a factor of two worse in the center cells, 6 and 17, and it is constant in the cells in front of the calorimeters.

As a further refinement of the threshold mode, a second mode of identification uses the pulse height information from the cells the particle strikes. Here the ON state of the counter is investigated when the threshold mode tagging indicates we have a πK or a πKp. If we calculate the amount of expected Cerenkov light, on the average, a kaon or proton will yield, then we can ask whether the correspondi pulse height is most probably due to a π well above its threshold or a K or p slightly above their thresholds. If a particle is tagged a πK, then analagous to Eq. 3.9 we calculate for a K the effective kaons, e_K, and compare to the effective pions, e. We can relate the amount of light particle type i contributes compared to a pion of th same momentum;

$$e_i = e\left(\frac{m_i}{m_\pi}\right)^2 - \frac{D}{D_{max}}\left(\left(\frac{m_i}{m_\pi}\right)^2 - 1\right) \tag{3.15}$$

where m_i is the mass of particle type i. Since we know the average number of photoelectrons a $\beta = 1$ particle contributes to any given cell, we calculate the average number of photoelectrons particle type i yields,

$$\langle n_{\gamma e}\rangle_i = e_i \langle n_{\gamma e}\rangle_{\beta = 1} \tag{3.16}$$

where i denotes π, K or p. Now from the pulse height in the struck cell we ask how many photoelectrons gave this pulse height. Since the gains are adjusted so that a $\beta = 1$ particle gives a pulse height of 400, a pulse height for cell j, PH_j, will be produced by n_s photoelectrons. We have

$$n_s = \langle n_{\gamma e}\rangle_{\beta = 1, j} \frac{PH_j}{400} \tag{3.17}$$

where $\langle n_{\gamma e}\rangle_{\beta = 1, j}$ is the average number of $\beta = 1$ photoelectrons for cell j. We therefore know how many photoelectrons are produced by this particle and what the average photoelectron yield would be if it were a π, K, or p. Assuming again that the photoelectrons produced follow a Poisson distribution, we calculate the probability that a π, K or p produces n_s photoelectrons. The probability that a particle of type i produces n_s photoelectrons is

$$P_i(n_s) = \frac{e^{-\langle n_{\gamma e}\rangle_i} \langle n_{\gamma e}\rangle_i^{n_s}}{n_s!} \tag{3.18}$$

We construct W_i which is the probability that the ambiguously tagged πK or πKp is a particle of type i.

$$W_i = \frac{P_i(n_s)}{P_\pi(n_s) + P_K(n_s) + P_p(n_s)} \tag{3.19}$$

Using W we now have to decide at what level to accept the particles as

a π, K or p. This of course depends on how much contamination of th other particle species we will tolerate. It is also obvious that as one gets further above K threshold there will be an equal probabilit of classifying a πK as either a π or as a K. In Figure 3.8 we show P_π versus P_K for a πK into the trigger cells. Again we average over the air and He runs. There is no clear-cut place where to simply define a π or K so we will define a π if $W_\pi \geq 0.6$ and a K if $W_\pi \geq 0$. Similarly, for a πKp signal, a Kp is defined if $W_K + W_\pi \geq 0.9$. Figure 3.9 shows how the πK's separate into π's, K's and still unresolv πK's for $W_\pi \geq 0.6$ and $W_\pi \geq 0.5$. Notice that there is a small fracti of K's that are found by this method. The K contamination to the π sample, $C_K(\pi)$, can be calculated if we know the π-K ratio, $R(\frac{\pi}{K})$. We find

$$C_K(\pi) = \frac{1 - W_\pi}{R(\frac{\pi}{K})} \tag{3.20}$$

and the π contamination to the K's $C_\pi(K)$ is

$$C_\pi(K) = (1 - W_K) R(\frac{\pi}{K}) \tag{3.21}$$

As worst-case examples using W_K and W_π as above, the π contamination to the K's is 150% if $R(\frac{\pi}{K}) = 15$ and the K contamination to the π's i 25% if $R(\frac{\pi}{K}) = 2$. The π's from this method are fairly certain of bei real pions and not kaons, but there can be a large π contamination t the K's derived from this method. This is true for both K^+'s and K^-'s since the π-K ratio is large in both cases. But there is anoth method of positively identifying a kaon for particles close to K thre hold. Figure 3.10a shows the typical normalized pulse height distri bution for the momentum range 20 GeV/c $\leq$ p < 30 GeV/c. The small amount of photoelectrons contributed by K's just above their thresho

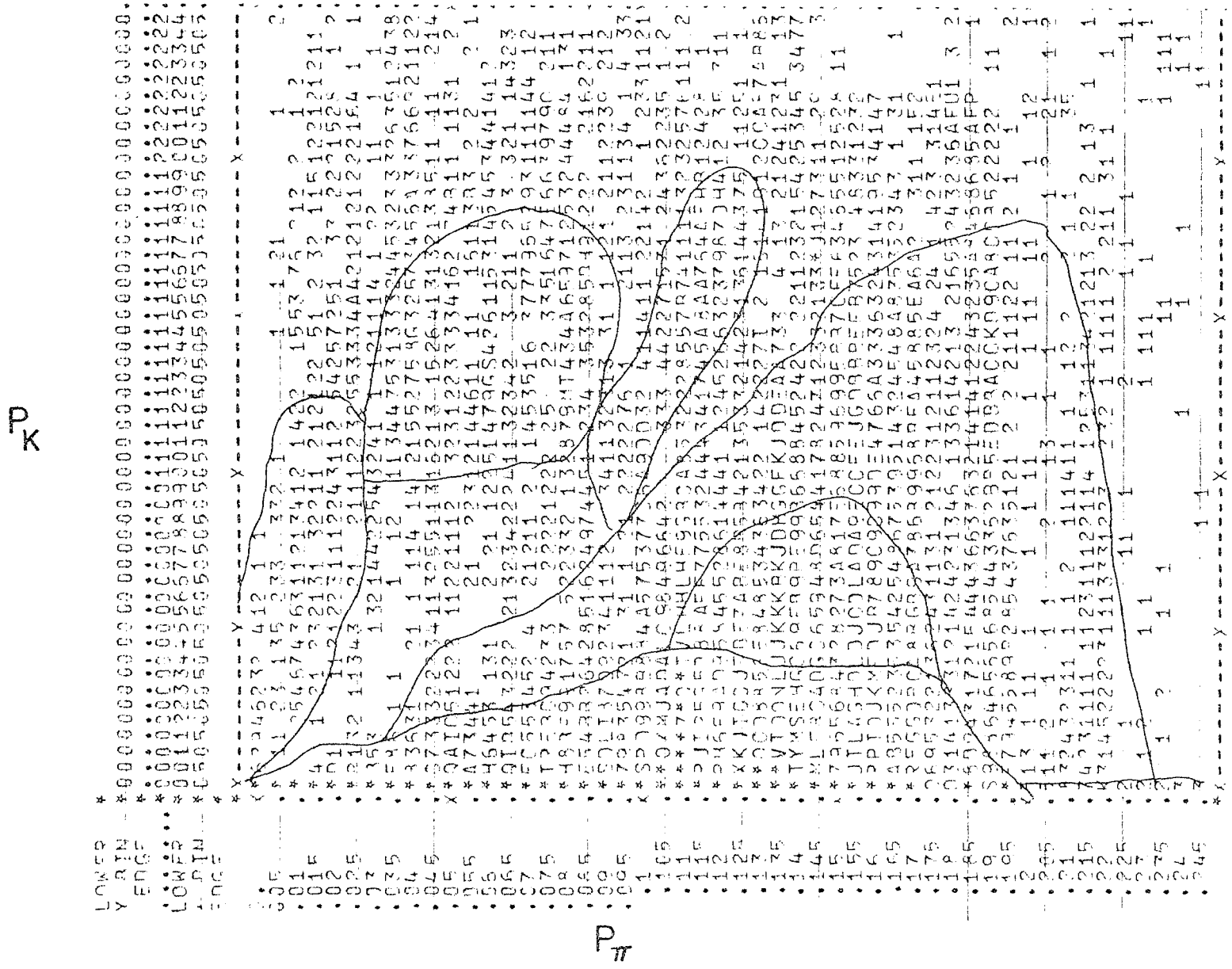

Figure 3.8 A plot of the probability that a πK could be a π vs. the probability that it could be a K from pulse height analysis. Contours are hand drawn to guide the eye.

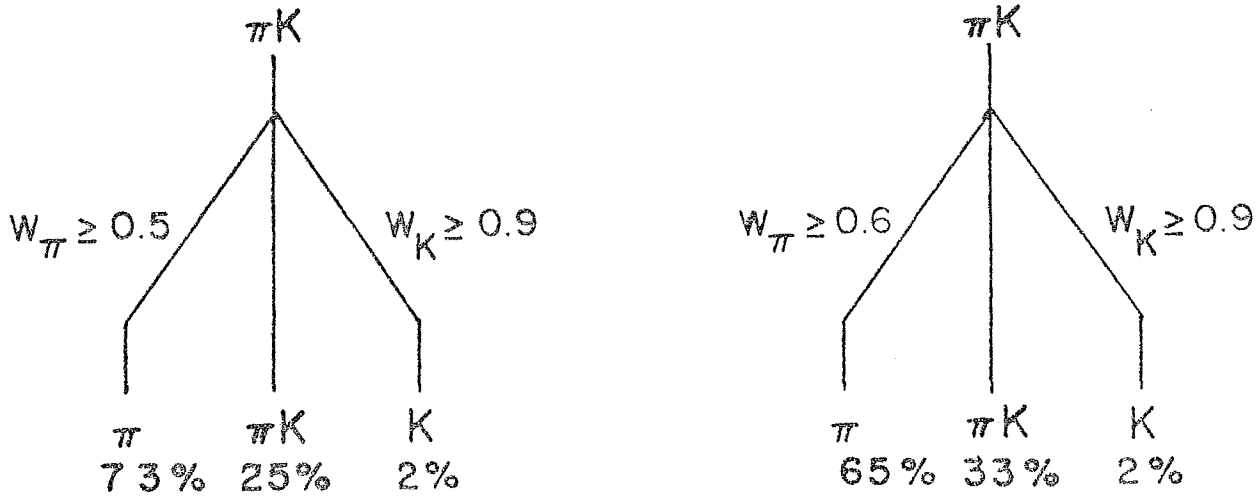

Figure 3.9 Schematic of the reclassification of πK's into π's and K's from pulse height analysis.

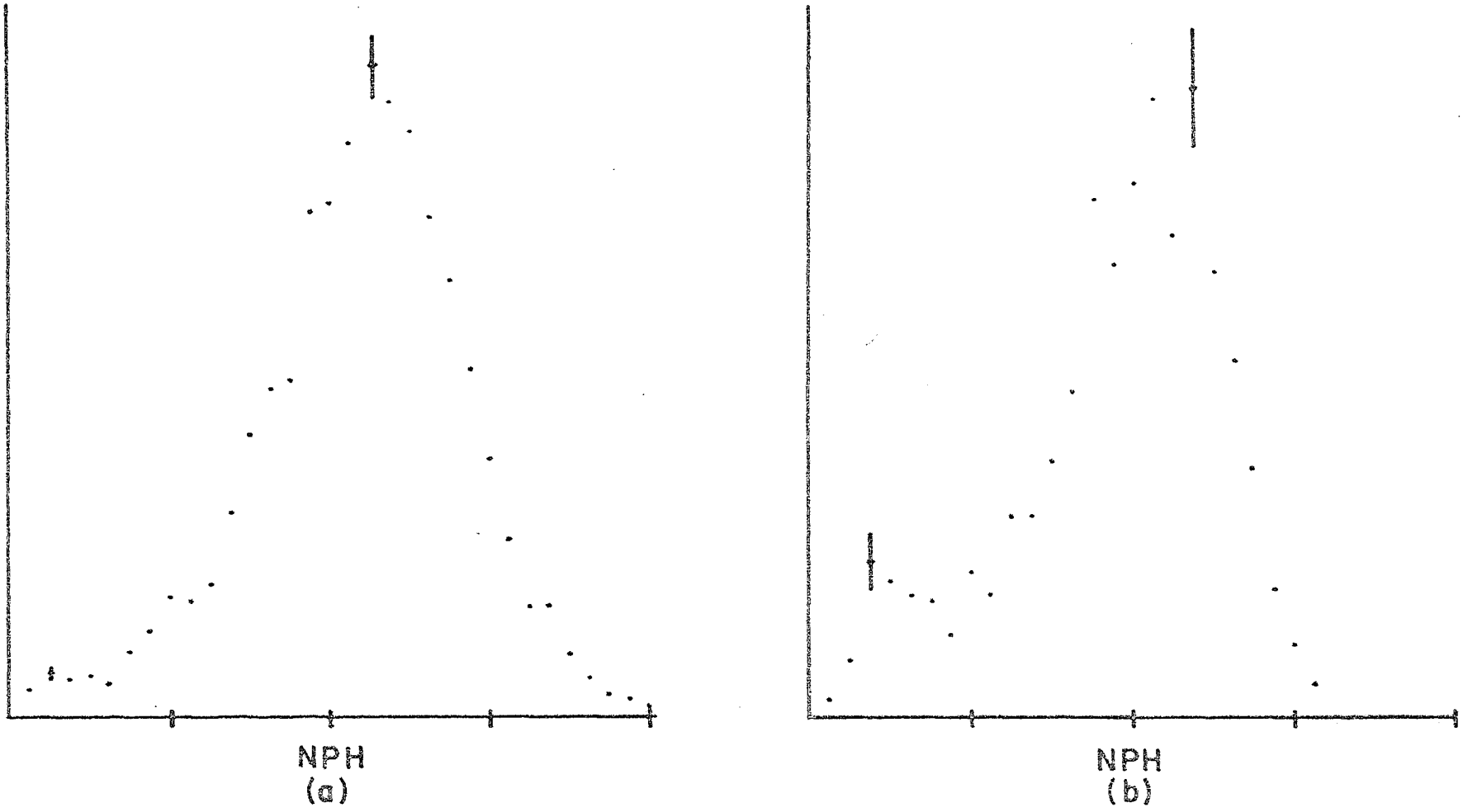

Figure 3.10 Normalized pulse height distribution for cell no. 4 with the air filling. (a) The momentum of incident particles is between 10 and 20 GeV/c. (b) The incident momentum is between 20 and 30 GeV/c. The bump at low pulse height in (b) is the onset of kaons giving Cerenkov light.

can be clearly seen. If we have a πK that gives a pulse height mor that 2σ down from the average pulse height that a pion of that mome tum would give, we classify that particle a definite K. Again that is only a small amount not worth worrying about.

To summarize the results of the particle identification, we tal ulate certain aspects of the particle types. Table 3.8 lists the pa ticle type versus its ID class. Table 3.9 lists the fraction of par ticle types found in each cell for ID class 1 only. Finally in Tabl 3.10 we show the number of cells the Cerenkov light shines on for di ferent particle types.

3.6 Single Particle Trigger

Along with obtaining physics results, the single-particle trigg with incident protons is important to study in order that comparison of cross sections can be made with other experiments. If these comparisons agree, it gives us confidence that our apparatus and data r duction techniques are working properly, and can then be used to mea sure cross sections with other incident particles. In particular, w need to know how well we can identify the secondary particles and wh corrections have to be made for efficiencies, calorimeter response, etc. The recent Chicago-Princeton experiment contains cross section and ratios of cross sections for 200 GeV pp collisions producing hig p_T $\pi^{\pm}$, $K^{\pm}$, p and $\bar{p}$ trigger particles. Instead of calculating cross sections for our single particle trigger, acceptances and some efficiencies will cancel if we compare the ratios of cross sections.

The trigger particle was found by selecting events with the HIP tagbit on and the trigger module having a $p_{Tmod} \geq 3.2$ GeV/c for run numbers less than 484 and for run numbers greater than 484 we require the trigger module to have its $p_{Tmod} \geq 3.0$ GeV/c. About 10% of the events with the tabgit on satisfied had the trigger p_{Tmod} below this

	FRACTION IN ID CLASS						
Cl TAG	1	2	3	4	5	6	7
π[1]	.75		.12	.13			
πK	.76		.06	.17			
πKP	.59		.10	.31			
KP	.63	.25	.06	.05			
P	.56	.29	.06	.09			
K[1]	.68		.10	.22			
Ambiguous[2]						.25	.75

[1] Not from πK reclassification.

[2] Other than those that are classed too close to threshold.

Table 3.8 Fraction of Cl tagged particles that are in the various ID classes defined in the text.

	FRACTION FOUND IN CELLS 1 - 11										
C1 TAG	1	2	3	4	5	6	7	8	9	10	11
π			.07	.08	.10	.03	.10	.09	.06		
πK			.03	.10	.07	.09	.08	.13	.02		
πKp			.01	.03	.06	.34	.07	.03	.0		
Kp			.08	.08	.06	.03	.06	.09	.06		
p			.03	.11	.05	.07	.08	.13	.02		

	FRACTION FOUND IN CELLS 12 - 22										
C1 TAG	12	13	14	15	16	17	18	19	20	21	22
π			.07	.08	.09	.04	.09	.08	.04		
πK			.03	.11	.05	.10	.07	.11	.02		
πKp			.0	.03	.03	.32	.05	.02	.0		
Kp			.08	.11	.06	.02	.06	.11	.06		
p			.04	.12	.06	.08	.07	.13	.03		

Table 3.9 Fraction of the particular C1 tagged particles found in the different cells of C1. The tags here only have ID class 1.

C1 TAG	NO. OF CELLS 1	2	3	4
π[1]	.74	.25	.01	.0
πK	.55	.39	.03	.02
πKp	.39	.53	.05	.03
Kp	.74	.24	.01	.01
p	.47	.46	.05	.03
K[1]	.57	.38	.03	.02
Amb.[2]	.62	.36	.01	.0

[1] Not from πK reclassification.

[2] Other than those that are classed too close to threshold.

Table 3.10 Fraction of the C1 tagged particles that contribute Cerenkov light to a given number of mirrors.

bias. We will refer to this trigger as the HIPT trigger. Similarly for the low bias trigger mode, for proper normalization and to obtai triggers unbiased by the JET or HIPT triggers, the LOPT tagbit is re quired to be on with no other tagbits on. The p_{Tmod} in the trigger module was required to be 1.0 GeV/c less than the corresponding HIPT requirements. This will be referred to as the LOPT trigger. Once the trigger module was found all particles entering it were looked a Figure 3.11 shows the number of all particles entering a trigger modu for the HIPT trigger. The trigger particle with momentum p was re- quired to have $\geq$ 50% of the module's energy. Therefore, a particle into the trigger module was chosen as a trigger particle if $E_{mod}/p \leq$ This cut was hopefully lenient enough to take care of leakage from neighboring modules, accompanying neutrals, the lack of total absorp tion and the upward swing of the calorimeter resolution but stringen enough to exclude multiple particle triggers. The point here is tha we want to have events that have only one charged particle into the trigger. Otherwise, comparison with other single-particle experimen may not yield the same results because the experiments may in fact b of a different nature with several particles constituting the trigge Furthermore, a bad-y cut was made throwing out all events in which t trigger module had a bad-y in either the electron or hadron part of the module. This was a frequent occurence and was caused by seconda particles hitting the source calibration scintillators glued to the light pipes close to the phototubes at the top and bottom. Approxi- mately 45% of the trigger modules had bad-y's. However, for trigger particles with $p_T \geq 2$ GeV/c and $E_{mod}/p \leq 2$, we lose less than 6% of our good single-particle events by throwing the bad-y events away. With $E_{mod}/p \leq 3$, 4% of the HIPT events have $\geq$ 2 trigger particles an

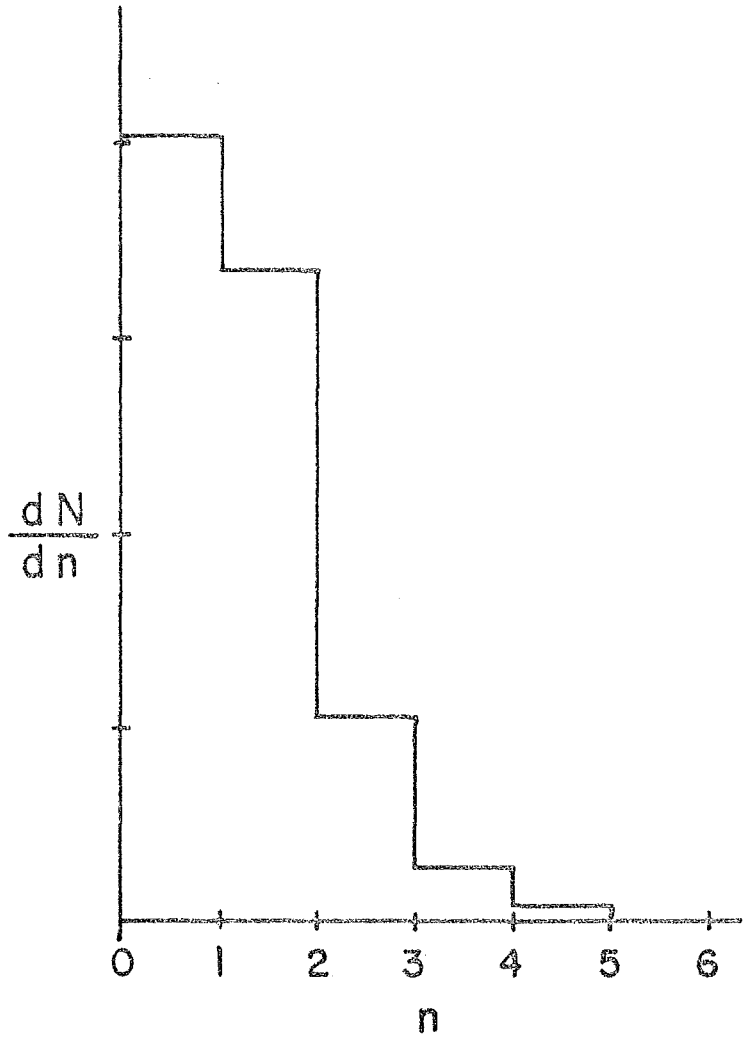

Figure 3.11 The number of particles entering the trigger module with the HIPT trigger.

with $E_{mod}/p \leq 2$, less than 2% of the events have two trigger particl
In both cases about 75% of the HIPT triggers have no trigger particl
according to the above requirements. Figure 3.12 shows an E_{mod}/p pl
versus p_T for all particles into the trigger modules for the HIPT tr
ger. Events with bad-y's are shown as well as those without. It is
evident that the bad-y events can be rejected without a loss of good
events. Figure 3.13 shows a rapidity plot of all particles entering
the trigger modules. By recalling the transformation of the rapidit
y, to the CMS angle,

$$\theta^* = 2 \arctan(e^{-y}) \qquad (3.22)$$

the rapidity plot just reflects the triggering efficiency of the cal
orimeter across its face. We select particles in the rapidity range
$-0.3 \leq y \leq 0.5$. A p_T distribution of particles satisfying the above
criterion is shown in Figure 3.14a for the HIPT trigger and in Figur
3.14b for the LOPT trigger. We can see that the calorimeter respons
does not appreciably affect the trigger particle spectrum if we sele
trigger particles with $p_T \geq 2.0$ GeV/c in the HIPT trigger and $p_T \geq 1$
GeV/c in the LOPT trigger. After the LH_2 vertex requirement, the ab
trigger definitions and the requirement for an identifiable beam par
ticle, this analysis contains 16,000 events from the HIPT trigger an
8,000 events from the LOPT trigger.

Although we have just a handful of select single-particle trig-
gers obtained over many weeks of running, we can be certain that the
are clean triggers. We base this on the following criteria:

1. All events are associated with an interaction in the target. A vertex cut ensures us that all tracks come from the LH_2.

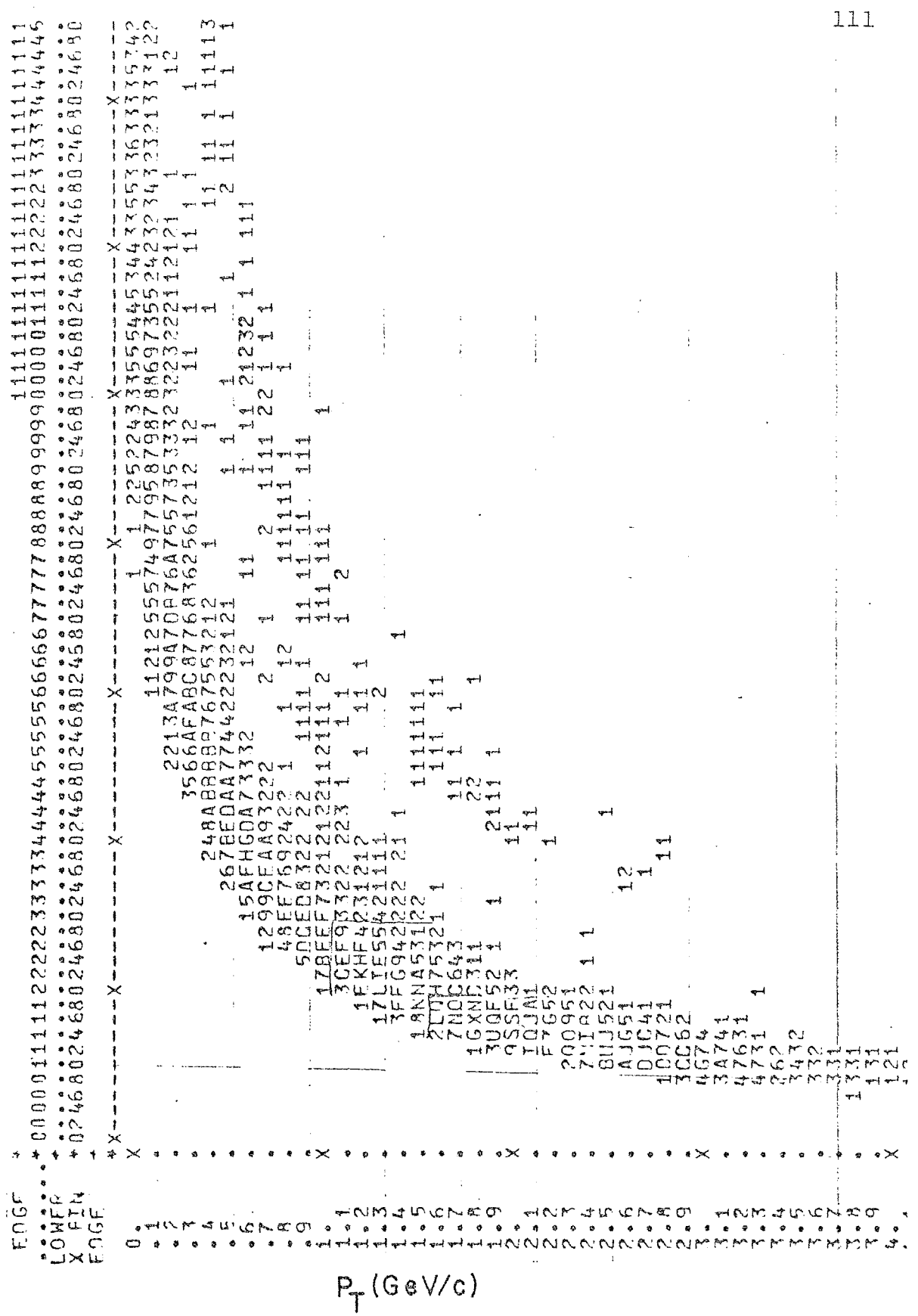

Figure 3.12 A plot of E_{mod}/p vs. p_T for all particles entering the trigger module.

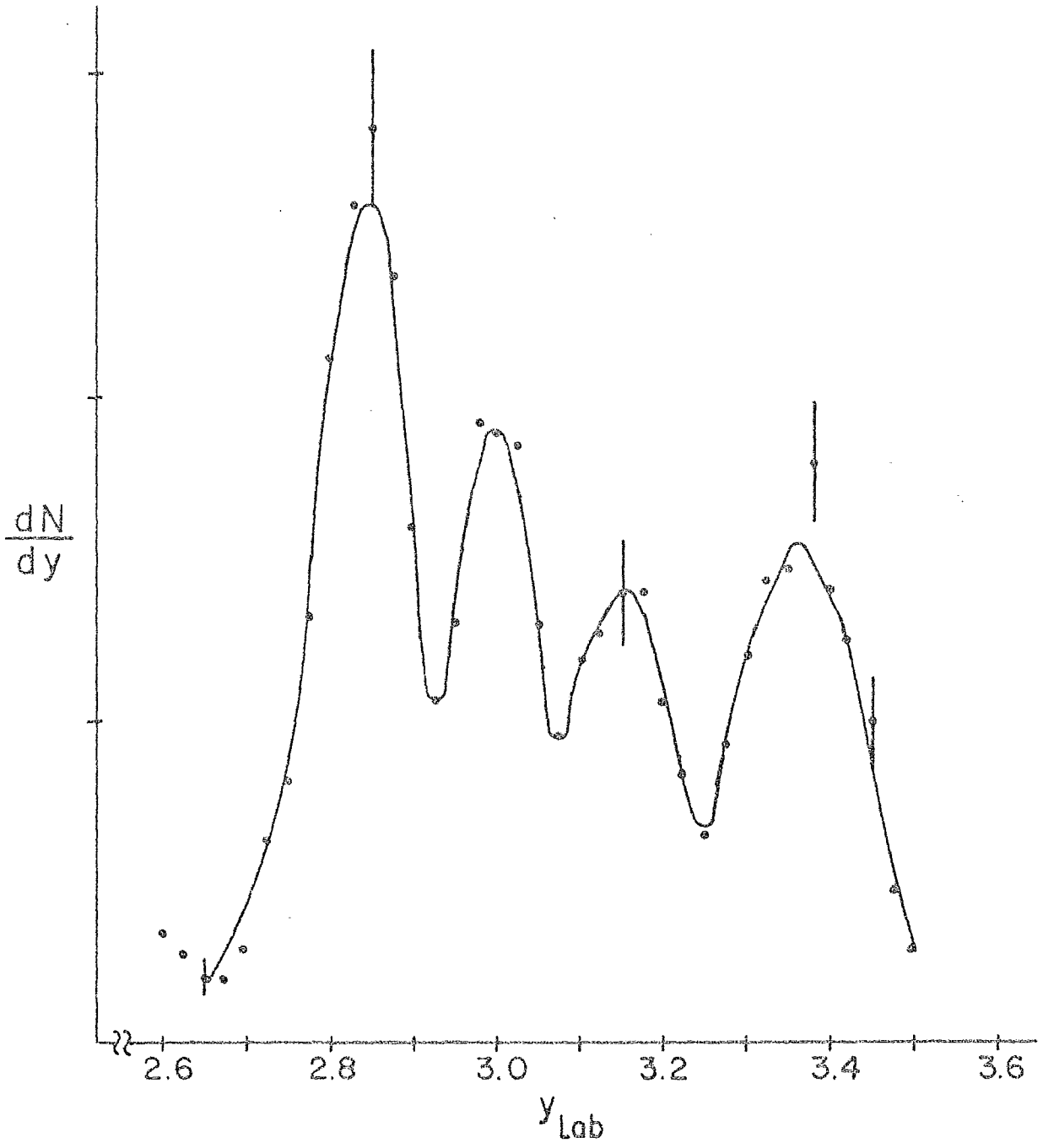

Figure 3.13 Rapidity distribution of particles into the trigger module which have $2.0 \leq p_T < 3.0$ GeV/c.

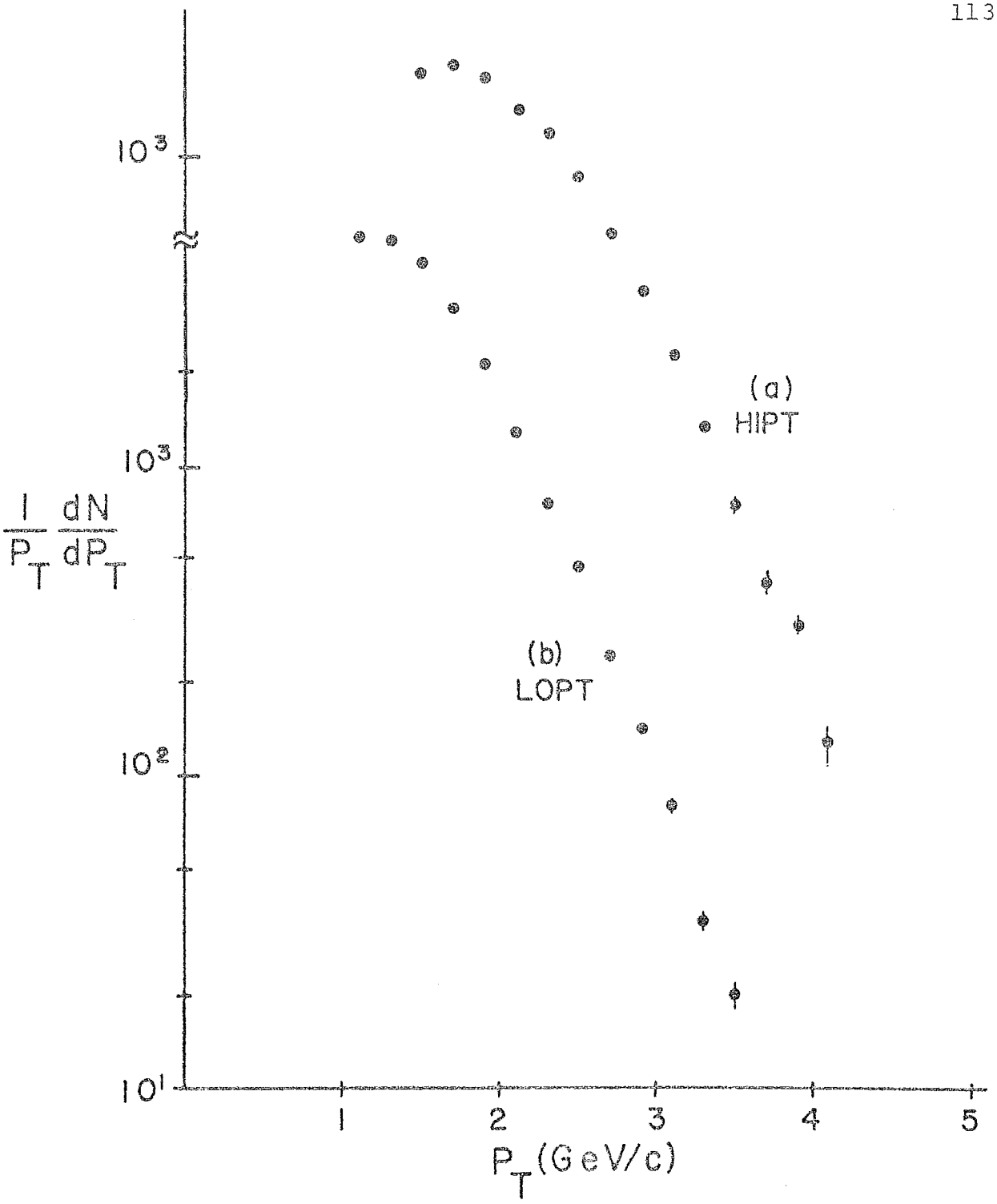

Figure 3.14 Transverse momentum distributions for particles chosen according to the (a) HIPT and (b) LOPT triggers.

2. A single-particle trigger is selected by requiring that the trigger module have a signal in both the top and bottom phototubes. Events with bad-y's are discarded.

3. We select the high p_T, single-particle track by requiring it to enter the trigger module and further requiring it to deposit at least 50% of its energy in the module.

Thus, halo particles or non-beam associated particles giving a large signal in the calorimeter are definitely excluded. We have, for the most part, events which are one-particle triggers produced by an interaction in the hydrogen target.

3.7 Corrections to the Trigger Particle

For beam particle a and different charged secondaries, h and h' produced with high transverse momenta, we will be interested in finding the ratios of the production rates - $\frac{d\sigma}{dp_T}$ (ap → hX)/ $\frac{d\sigma}{dp_T}$ (ap → h'X In defining the trigger particle type and measuring its rate we must consider corrections to the measured rate due to the following effec

- Beam Cerenkov counter efficiency
- Attenuation in the target
- Acceptances
- Track finding efficiency
- Calorimeter response
- Cerenkov counter (Cl efficiency)
- π - K contaminations
- δ-rays, V's

Many of these corrections will be applied in identical fashion to the cross section for h and the cross section for h' resulting in cancel

lation when the ratio is taken. As shown in Section A.1 of Appendix A, we can write the cross section for beam particle a producing hadron h at high p_T as

$$\frac{d\sigma}{dp_T}(ap \to hX) = \sum_{i=runs} B_i \frac{dN_i(a \to h)}{dp_T} \frac{1}{\varepsilon_{Ci}^a} \frac{1}{\varepsilon_{dhi}(p_T)} \frac{(1 - C_i)}{A_i(p_T)} e^{\bar{z}/L} \qquad (3.23)$$

where B_i is the appropriate normalization, A_i is the geometric acceptance of the detector, ε_{Ci}^a is the efficiency for detecting beam particle a and $\varepsilon_{dhi}(p_T)$ is the efficiency for detecting, or triggering on, hadron h with high p_T. C_i is a contamination factor due to misidentification of h. $\bar{z}$ is the average amount of LH_2 the high p_T particles traverse and L is the liquid hydrogen absorbtion length. Finally $\frac{dN_i(a \to h)}{dp_T}$ is the measured number of particles of type h produced by beam a at a transverse momentum p_T. In the analysis we update $N_i(a \to h)$ every time we identify a beam particle as type a and a secondary as type h. In general, all the above variables can change from run to run depending on operating conditions. Before proceeding further it may be useful to clarify what the normalization term represents.

The normalization term, B, is discussed in detail in Section A.1 of the Appendix. From Figure 2.13 we see that the cross section for producing a TRIGLOG is proportional to TRIGLOG/EFFBEAM where EFFBEAM is the effective amount of beam taken when the PDP 11 is in the ready mode and the trigger electronics is not taking in an event. Note that this ratio is independent of spark chamber dead time. When we fire the spark chambers and obtain a TRIG, we sample a random fraction of the TRIGLOG's. The true cross section is then proportional to the number of good triggers found, $N(a \to h)$, divided by the triggers written onto tape. Thus

$$B = \frac{\text{TRIGLOG}}{\text{TRIG} \cdot \text{EFFBEAM}}$$

a. Beam Cerenkov Efficiency

Section A.2b of Appendix A shows the calculations for the beam Cerenkov counter efficiencies and the corrections to them due to different beam particle contamination. This results in the efficiency for detecting beam particle a, ε_C^a. We see from Figure 2.2 that these efficiencies may be very run dependent. We therefore do not assume any "average" beam type efficiency, but instead normalize our counting rate per run by ε_C^a.

b. Target Attenuation

If we average the events over all the 12" of hydrogen target length there will be about a 2% correction to the cross section made for all types of secondary particles. We assume this a constant throughout the experiment.

c. Acceptance

For trigger particles, the acceptance, $A(p_T)$, is just the fraction of 4π steradians which the calorimeters subtend. In general, A will depend on the triggering efficiency as seen in Figure 3.13 where the geometric acceptance should be flat for $-0.3 \leq y \leq 0.5$, our fiducial region in y. Similarly, the azimuthal acceptance should also be flat across the face of the calorimeter. Therefore the acceptance has to include multiplicative factors which will correct the observed rapidity and azimuthal distributions to the flat distributions expected for a uniformly efficient detector.

Figure 3.15 shows an azimuthal (ϕ) distribution of the trigger particles. For $p_T \geq 1.5$ GeV/c the ϕ distribution just reflects the triggering efficiency of the calorimeter coupled with the sharp transverse momentum spectrum resulting in a preferential trigger at the center of the calorimeter, or $\phi = \pm 90^\circ$ (ϕ measured from y axis). The acceptance of the trigger particles can be written

$$A(p_T) = \frac{\Delta\phi}{2\pi} \frac{\Delta y}{2Y_{max}} f_y(p_T) f_\phi(p_T) \quad (3.24)$$

where Y_{max} is the maximum attainable rapidity for the system ap → hX. $f_y(p_T)$ and $f_\phi(p_T)$ are the factors which correct the observed rapidity and ϕ distributions into the distributions expected from a uniformly efficient calorimeter. We will select trigger particles within $\pm 45^\circ$ azimuth of $\phi = 90^\circ$. Δy is chosen to be 0.8 units. We assume that the p_T corrections to the rapidity and distributions are constant[26] so that

$$A(p_T) = \text{constant} \quad (3.25)$$

d. Track Finding Efficiency

An average track finding efficiency of 95% will be assumed with no production of spurious high p_T tracks. We assume the track finding to be independent of both p_T and particle type.

e. Calorimeter Response

Besides the efficiencies noted under "Acceptance" above we also need to discuss the response of the calorimeter to π's, K's and p's. This effect will be included in the detection efficiency, $\varepsilon_{dhi}(p_T)$.

We will assume the response of the calorimeter to be dependent on particle mass and not on charge. i.e.,

$$\varepsilon_{dh^+}(p_T) = \varepsilon_{dh^-}(p_T) \neq \varepsilon_{dh'}(p_T) \quad (3.26)$$

Especially in the case of p and $\bar{p}$ this is not necessarily true. In the case of $\bar{p}$ triggers where no baryons have to be produced, $\bar{p}p$ annihilation results in an extra 2 GeV in energy over p triggers. This results in the extra energy helping $\bar{p}$'s below the threshold to trigger more readily than p's of the same momentum.

Another assumption that we make is that the difference in trig-

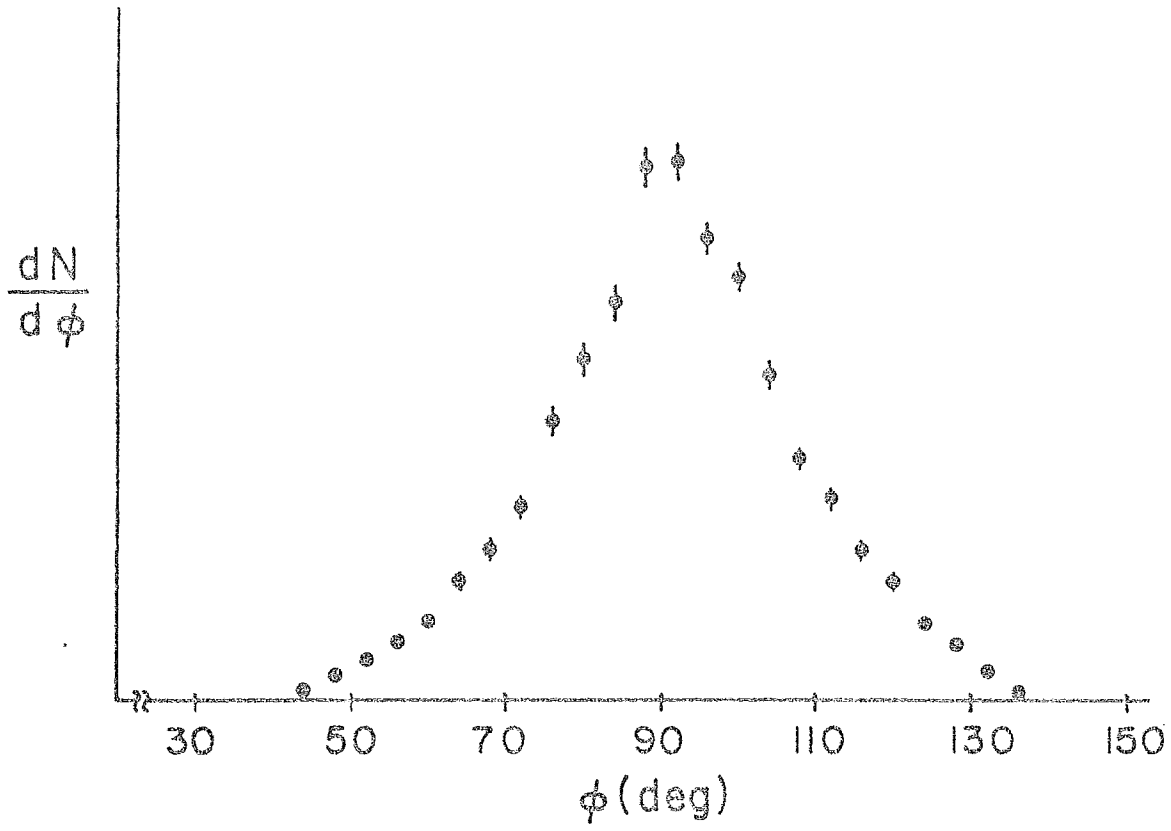

Fig. 3.15 Azimuthal angle (ϕ) distribution of trigger particles.

gering rates, according to Figure 3.4e, is $1 - \frac{\varepsilon_{dp}(p_T)}{\varepsilon_{d\pi}(p_T)}$ for either positive or negative trigger particles. Therefore the measured production ratio of π's to p's will have to be increased by ~20% below bias according to Figure 3.4e. Furthermore, if the calorimeter responds to identical kinetic energies and not momenta, then for particles that are produced according to a spectrum e^{-bp_T}, the ratio of π trigger rates to p trigger rates, $\frac{R_\pi(p_T)}{R_p(p_T)}$, can be shown to be

$$\frac{R_\pi(p_T)}{R_p(p_T)} = e^{\alpha b(m_p - m_\pi)} = \frac{\varepsilon_{d\pi}(p_T)}{\varepsilon_{dp}(p_T)} \tag{3.27}$$

with m_p and m_π the p and π masses respectively. α is the sine of the laboratory angle where the particles are detected. The K detection efficiency is given by

$$\frac{\varepsilon_{d\pi}(p_T)}{\varepsilon_{dK}(p_T)} = \exp\left\{ \ln\left(\frac{R_\pi}{R_p}\right)\left(\frac{m_k - m_\pi}{m_p - m_\pi}\right)\right\}$$

$$= \left(\frac{\varepsilon_{d\pi}(p_T)}{\varepsilon_{dp}(p_T)}\right)^{0.44} \tag{3.28}$$

The K to p detection efficiency will therefore by

$$\frac{\varepsilon_{dK}(p_T)}{\varepsilon_{dp}(p_T)} = \left(\frac{\varepsilon_{d\pi}(p_T)}{\varepsilon_{dp}(p_T)}\right)^{0.56} \tag{3.29}$$

Since we cannot always differentiate K's and p's in our analysis, we will be taking production ratios of $\pi^\pm$ to $Kp^\pm$ and Kp^+ to Kp^-. Since the above efficiency corrections are very approximate in the first place because of the unknown real response the calorimeter has to π's, K's and p's, and since we don't know the K/p production ratio for other than p beams from the CP group, we make the approximation for the Kp efficiency

$$\varepsilon_{dKp^+}(p_T) \simeq \tfrac{1}{2}\varepsilon_{dK^+}(p_T) + \tfrac{1}{2}\varepsilon_{dp}(p_T) \tag{3.30a}$$

$$\varepsilon_{dKp^-}(p_T) \simeq \varepsilon_{dK^-}(p_T) \qquad (3.30b)$$

The calorimeter response corrections, Eq. 3.26 through 3.30, will be applied to the appropriate ratios.

Another charge-dependent efficiency exists for the two classes of particles - "bend-ins" and "bend-outs". As shown in Figure 3.16, the bend-ins are particles that bend into the center of the spectrometer, the magnet subtracting a p_T kick from their transverse momenti The magnet adds a p_T kick to the bend-outs. Because of this added p_T the bend-outs with transverse momentum below bias will preferentially trigger the calorimeter. Therefore we expect two different efficiencies for bend-ins and bend-outs, the bend-in efficiency less than the bend-out efficiency. Because of this difference, bend-ins comprise only about 12% of the trigger. We will use only bend-out triggers in our analysis.

f. C1 Efficiency, π-K Contamination, δ-Rays

Although we have a minimum efficiency of 87% for the OFF signals in C1, this efficiency varies as a function of both runs - air and He fillings - and momentum of the trigger particle. For particles close to K threshold, the π/Kp ratio can be corrected by up to 15% because of the minimum acceptable efficiency. We can keep track of the number of effective photoelectrons the trigger particle yields and then calculate its efficiency for firing C1.

Let π_{MI} and Kp_{MI} be the number of π's and Kp's that are actually recorded in region I of Figure 3.5. Recall that region I is the momentum region between pion threshold and kaon threshold. Region II is between kaon threshold and proton threshold and region III is above proton threshold. We let π_{RI} and Kp_{RI} be the real number of π's and Kp's that should have been recorded in region I. Similarly for regic

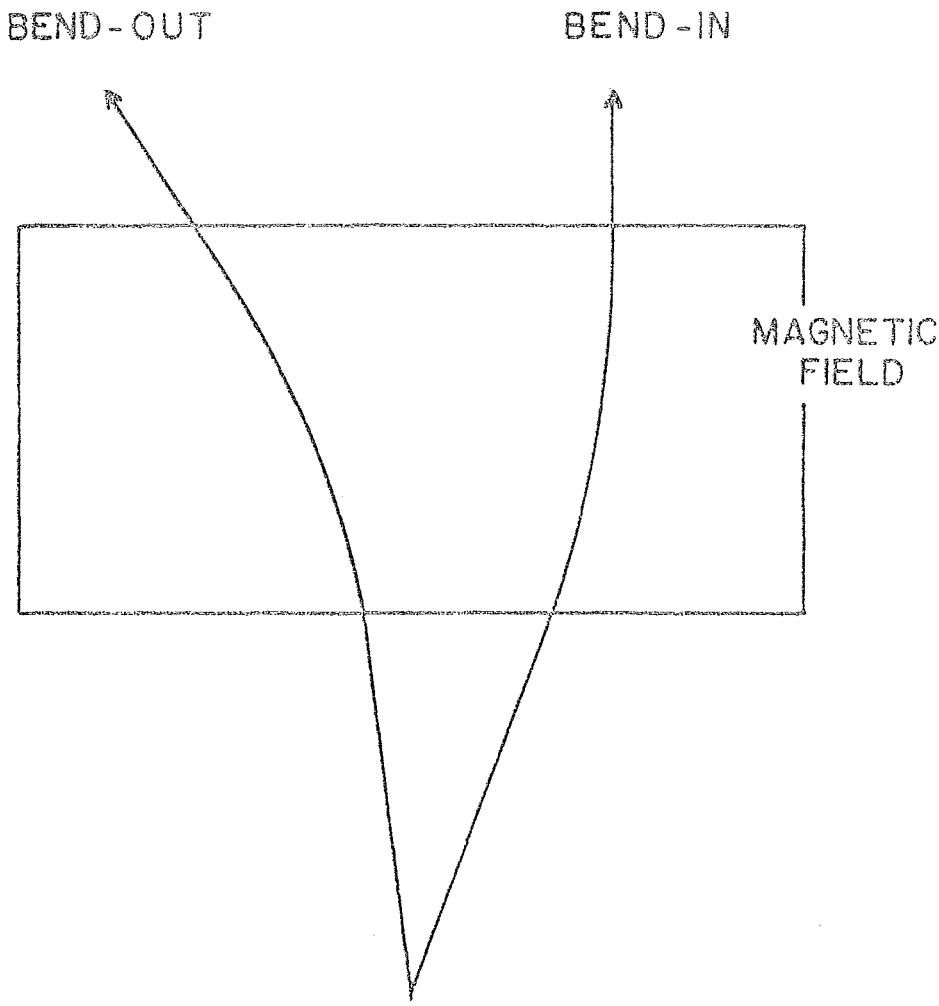

Figure 3.16 Sketch of bend-in particles and bend-out particles.

II, πK_{MII} and p_{MII} are the measured number of πK's and p's. πK_{RII} and p_{RII} are the real number that exist. In region I we detect π's with an efficiency $\varepsilon_{\pi I}$ and in region II with an efficiency $\varepsilon_{\pi II}$. K's are detected in region II with efficiency ε_{KII}. We neglect region III since there are only a small number of particles at this high momentum. It is also necessary to point out that the ε's are functions of the transverse momenta of the π's and K's as are the number of particles measured and their corresponding real distributions. δ is the fraction of ON signals in C1 due to δ-rays produced by particles below their respective thresholds. From Section 3.5 we estimate δ from ON signals with incident particles below threshold and take it to be constant and approximately equal to 0.05. We can therefore write

$$\pi_{MI}(p_T) = \varepsilon_{\pi I}(p_T)\pi_{RI}(p_T) + Kp_{RI}(p_T) \quad (3.31$$

$$Kp_{MI}(p_T) = Kp_{RI}(p_T) + (1 - \varepsilon_{\pi I}(p_T))\pi_{RI}(p_T) \quad (3.31$$

$$\pi K_{MII}(p_T) = \varepsilon_{\pi II}(p_T)\pi_{RII}(p_T) + \varepsilon_{KII}(p_T)K_{RII}(p_T) + \delta p_{RII}(p_T) \quad (3.31$$

$$p_{MII}(p_T) = p_{RII}(p_T) + (1 - \varepsilon_{\pi II}(p_T))\pi_{RII} + (1 - \varepsilon_{KII}(p_T))K_{RII}(p_T) \quad (3.31$$

Table 3.11 shows, at a given p_T, the number of photoelectrons produced by a pion in air or helium and in the momentum regions I and I While keeping track of the particle's momentum, we calculate the ave age number of photoelectrons that would be produced if the particle were a kaon and not a pion. From these results we calculate and tabulate $\varepsilon_{\pi I}$, $\varepsilon_{\pi II}$ and ε_{KII}. Remember that we will select only trig gers with $p_T \geq 1.5$ GeV/c so that ε_π will always be $\geq 95\%$ in either air or He so that only a correction of about 5% has to be made to th measured π's. But even for 99% efficient π's, the possibly large π^- K^- ratio will imply about a 10% correction to the Kp^- spectrum. For

	AIR						HE					
	I			II			I			II		
p_T	$n_{\gamma e}$	ε_π	ε_K	$n_{\gamma e}$	ε_π	ε_K	$n_{\gamma e}$	ε_π	ε_K	$n_{\gamma e}$	ε_π	ε_K
1.0-1.2	4.9	.99	0.				2.5	.92	0.			
1.2-1.4	5.5	1.0	0.	6.6	1.0	0.	2.9	.95	0.			
1.4-1.6	6.0	1.0	0.	6.8	1.0	.87	3.2	.96	0.			
1.6-1.8	6.4	1.0	0.	6.8	1.0	.90	3.5	.97	0.			
1.8-2.0	6.8	1.0	0.	6.9	1.0	.94	3.7	.98	0.			
2.0-2.2	6.5	1.0	0.	6.9	1.0	.96	3.9	.98	0.	4.4	.99	0.
2.2-2.4	6.5	1.0	0.	6.6	1.0	.97	4.1	.98	0.	4.6	1.0	0.
2.4-2.6				6.8	1.0	.98	4.4	.99	0.	4.6	1.0	0.
2.6-2.8				6.6	1.0	.98	4.7	.99	0.	4.7	1.0	.87
2.8-3.0				6.8	1.0	.99	4.6	.99	0.	4.6	1.0	.87
3.0-3.2				6.8	1.0	.99				4.8	1.0	.89
3.2-3.4				6.6	1.0	.99						

Table 3.11 The average photoelectron yield for trigger pions as a function of their p_T and momentum regions as defined in the text. From these is calculated the expected kaon detection efficiency.

detecting p's, the efficiency for K's in region II can be close to th minimum acceptable for p_T's $\geq$ 1.5 GeV/c. A large correction can exis for the $\bar{p}$ sample if the $K^-/\bar{p}$ ratio is large.

The corrections to region I - π and Kp - are straightforward. W will correct the measured distributions according to Eq. 3.34 for Cl inefficiency using the π efficiency in Table 3.11. 70% of the air efficiency and 30% of the He efficiency will be weighted for the aver age efficiency used. For region II we try to separate the π's from the πK sample and then neglect the unseparable class. However, this can readily be done only when the πK's are not too far above the kaon threshold. This means that $\varepsilon_{KII} << 1$. Corrections to the proton dis tribution are hard because we have to know the real distribution of π's or K's. However, $\varepsilon_{\pi II} \simeq 1$ and there is only a loss in detecting the true kaons which will then fake a proton. Equations 3.31 can be solved for the real distributions and we find the corrections as follows.

$$\pi_{RI} \simeq \pi_{MI} \frac{1 - \delta \frac{Kp_{MI}}{\pi_{MI}}}{\varepsilon_{\pi I}} \tag{3.32a}$$

$$Kp_{RI} \simeq Kp_{MI}\left[1 - \frac{1 - \varepsilon_{\pi I}}{\varepsilon_{\pi I}} \left(\frac{\pi_{MI}}{Kp_{MI}} - \delta\right)\right] \tag{3.32b}$$

$$\pi_{RII} = \frac{\pi K_{MII}}{\varepsilon_{\pi II}}\left[1 - \varepsilon_{KII} \frac{K_{RII}}{\pi K_{MII}} - \delta \frac{p_{RII}}{\pi K_{MII}}\right]$$

$$\simeq \pi K_{MII} \frac{\left(1 - \delta \frac{p_{RII}}{\pi K_{MII}}\right)}{\varepsilon_{\pi II}} \tag{3.32c}$$

$$p_{RII} \simeq p_{MII}\left[1 - \frac{\pi K_{MII}}{p_{MII}} \left(\frac{1}{\varepsilon_{KII}} - 1\right) + \frac{\pi_{RII}}{p_{MII}} \left(\frac{\varepsilon_{\pi II}}{\varepsilon_{KII}} - 1\right)\right]$$

$$\simeq p_{MII}\left[1 - f \frac{\pi K_{MII}}{p_{MII}} \left(\frac{1}{\varepsilon_{KII}} - 1\right)\right] \tag{3.32d}$$

where $f = 1 - \frac{\pi_{RII}}{\pi K_{MII}}$ and lies somewhere between 0 and 1 and is a function of p_T. Since we don't know what the fraction of K's is in our

πK sample f remains unknown. If the π/K ratio is about 10, then f = 0.1 and if the π/K ratio is 1, then f = 0.5. The biggest correction to p_{MII} occurs when $\pi K_{MII}/p_{MII}$ is large. Depending on what this ratio is and what the kaon efficiency is, the error in choosing f is proportional to this factor. To avoid very large corrections in the $\bar{p}$ case we choose f = 0.1.

These Cerenkov corrections will be applied to various distributions in the following section and in the next chapter. The efficiencies from Table 3.11 will be used.

3.8 The Ratio $\frac{d\sigma}{dp_T}(pp \to h^+X)/\frac{d\sigma}{dp_T}(pp \to h^-X)$

In order to check the reliability of our trigger selection before proceeding to Cerenkov analyzing the final hadrons, we will look at the ratio of cross sections for pp collisions producing charged hadrons, h^+ and h^-, at high p_T. Of course we could calculate an absolute cross section for all charged particles as we have previously done[26,44], and show excellent agreement with CP. But in taking ratios many details of the acceptance factors will cancel at all p_T. As mentioned before this will then be compared to the 200 GeV pp collisions by the CP group. The efficiency of triggering on either-side calorimeter will be shown as well as the matching of the low bias data to the high bias data. Assuming all corrections are done properly any systematic differences can be ascribed to normalization errors.

In computing how many positive trigger particles are produced versus the number of negative trigger particles, it is not good enough to simply count them over the entire experiment. Because of the p_T kick of the magnet, trigger particles which bend out in the magnetic field will preferentially fire the calorimeters over those that bend in which are neglected here anyway. So for any particular magnet

setting - up or down - positive particles will trigger one side calorimeter and negative particles will trigger the opposite side. If one side is more efficient than the other there will be a depletion of one kind of charge. Of course, if the magnetic field is changed frequently enough so that the same amount of beam is on target for u as well as down fields, then efficiency effects will cancel and we can then simply count charges. But when we normalize correctly, as shown in Section A.2c of Appendix A, we actually perform two separat experiments. Comparing these two experiments provides an important check. Because of magnet polarity changes, we measure, at different points in time, the number of positive and negative hadrons triggeri the left calorimeter. The same is done with the right calorimeter. Neglecting charge-dependent efficiencies in the same calorimeter thes two results should agree. Figure 3.17 shows the ratio $\frac{d\sigma}{dp_T}(pp \rightarrow h^+X)$, $\frac{d\sigma}{dp_T}(pp \rightarrow h^-X)$ for the left side triggers and right side triggers for both the high bias and low bias data. Figure 3.17 uses just the raw data with no efficiency corrections. Since we have no a priori way of knowing how many of the charged hadrons are heavy particles, we cannot correct for the kinetic energy effect. Although the left side trigger is systematically higher than the right side for the HIPT trigger, overall left-right agreement is good as is the merging of th low bias data onto the high bias data. The discrepancy of the points below threshold of the HIPT trigger may be due to a difference of charge dependent efficiencies of the left and right sides.

However another method of determining the cross section ratio, referred to as method HGB, uses the number of positive hadrons in one calorimeter and the number of negative particles in the other calorimeter during the same run. This eliminates the need for a run to run

normalization. According to Eq. A.18 in Appendix Section A.2d, the ratio of the number of positive trigger particles to negative trigger particles for all magnetic field up runs, $\Sigma Outs^{+}_{\uparrow} / \Sigma Outs^{-}_{\uparrow}$, is equal to

$$\frac{\Sigma Outs^{+}_{\uparrow}}{\Sigma Outs^{-}_{\uparrow}} = \frac{\frac{d\sigma}{dp_T}(pp \to h^{+}X)}{\frac{d\sigma}{dp_T}(pp \to h^{-}X)} \cdot \frac{\varepsilon^{+}_{\uparrow}}{\varepsilon^{-}_{\uparrow}} \tag{3.33}$$

Similarly for the field down runs,

$$\frac{\Sigma Outs^{+}_{\downarrow}}{\Sigma Outs^{-}_{\downarrow}} = \frac{\frac{d\sigma}{dp_T}(pp \to h^{+}X)}{\frac{d\sigma}{dp_T}(pp \to h^{-}X)} \cdot \frac{\varepsilon^{+}_{\downarrow}}{\varepsilon^{-}_{\downarrow}} \tag{3.34}$$

where $\varepsilon^{\pm}_{d}$ is the calorimeter average trigger efficiency for $\pm$ charged particles when the magnetic field is in direction d. It then follows,

$$\frac{\frac{d\sigma}{dp_T}(pp \to h^{+}X)}{\frac{d\sigma}{dp_T}(pp \to h^{-}X)} = \sqrt{\frac{\Sigma Outs^{+}_{\uparrow}}{\Sigma Outs^{-}_{\uparrow}} \cdot \frac{\Sigma Outs^{+}_{\uparrow}}{\Sigma Outs^{-}_{\uparrow}}} \cdot \sqrt{\frac{\varepsilon^{-}_{\downarrow} \cdot \varepsilon^{-}_{\uparrow}}{\varepsilon^{+}_{\uparrow} \cdot \varepsilon^{+}_{\downarrow}}}$$

$$\simeq \sqrt{\frac{\Sigma Outs^{+}_{\downarrow}}{\Sigma Outs^{-}_{\downarrow}} \cdot \frac{\Sigma Outs^{+}_{\uparrow}}{\Sigma Outs^{-}_{\uparrow}}} \tag{3.35}$$

The HGB method is independent of the normalization but depends on the left-right trigger efficiency. The approximation in Eq. 3.35 is made assuming that the left or right calorimeters trigger about the same on either positive or negative particles and that this efficiency remains constant in time. This is not true as we know but Eq. 3.35 should hold to a first approximation. The method in Figure 3.17 is independent of time-varying efficiency but still will include effects of charge dependent efficiencies and normalization uncertainties. Table 3.12 contains the positive to negative charge production ratios for methods HGB, the average of left and right triggers, and the weighted average of left and right triggers. Outside of normalization uncer-

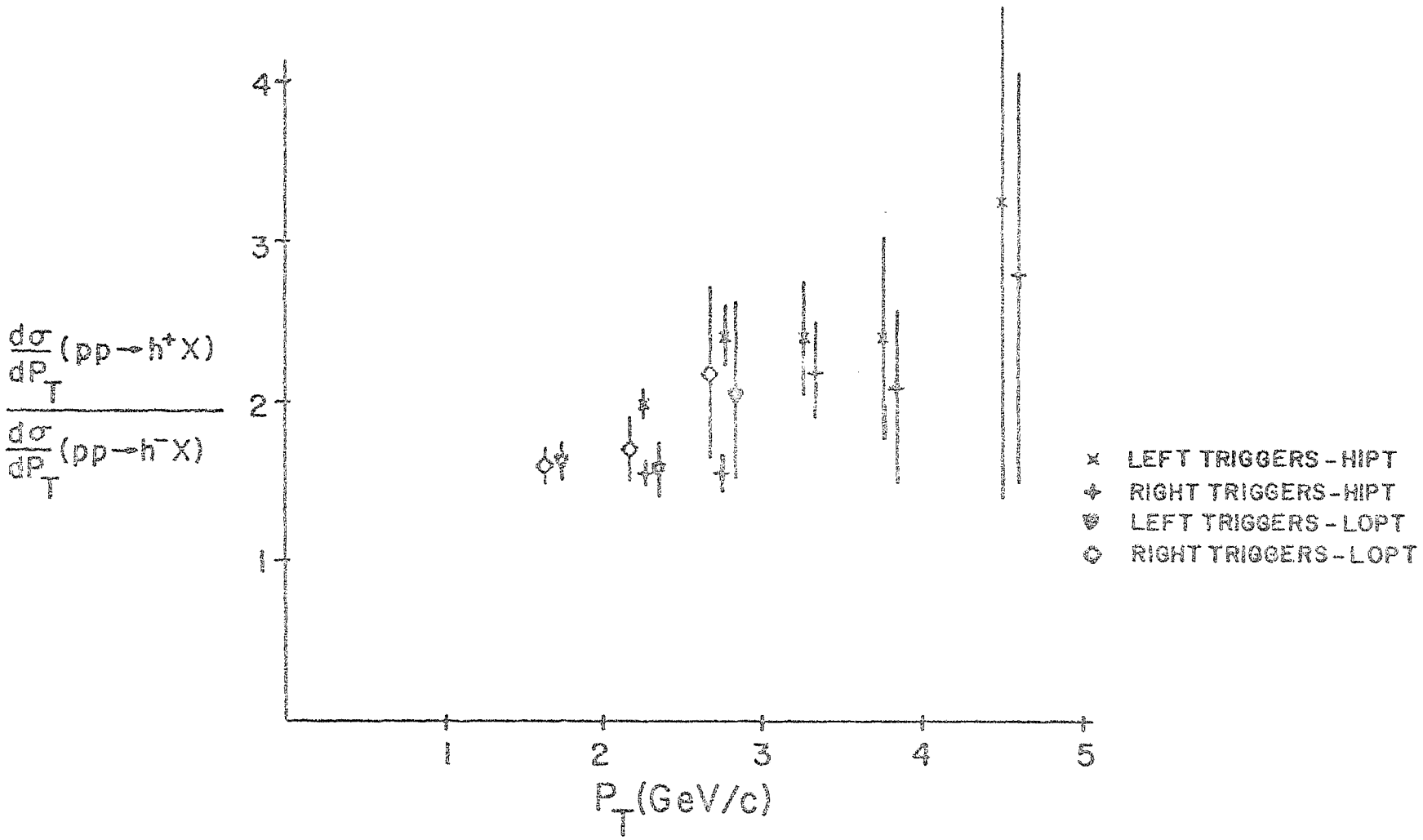

Figure 3.17 Ratios of the positive charge to negative charge production cross sections for pp collisions. Shown separately are left and right side triggers for both the LOPT and HIPT triggers.

p_T (GeV/c)	CHARGE PRODUCTION RATIO USING LEFT-RIGHT COMBINATION METHOD - LOPT TRIGGER		
	HGB	AVERAGE	WTD AVERAGE
1.5 - 2.0	1.65 ± 0.08	1.62 ± 0.05	1.62 ± 0.07
2.0 - 2.5	1.67 ± 0.13	1.64 ± 0.18	1.64 ± 0.13
2.5 - 3.0	2.12 ± 0.39	2.11 ± 0.55	2.12 ± 0.39

(a)

p_T (GeV/c)	CHARGE PRODUCTION RATIO USING LEFT-RIGHT COMBINATION METHOD - HIPT TRIGGER		
	HGB	AVERAGE	WTD AVERAGE
2.0 - 2.5	1.76 ± 0.07	1.77 ± 0.11	1.71 ± 0.07
2.5 - 3.0	1.93 ± 0.12	1.98 ± 0.17	1.81 ± 0.11
3.0 - 3.5	2.29 ± 0.24	2.30 ± 0.35	2.28 ± 0.24
3.5 - 4.0	2.23 ± 0.46	2.24 ± 0.64	2.23 ± 0.45
4.0 - 5.0	3.0 ± 1.12	3.01 ± 1.59	2.93 ± 1.24

(b)

Table 3.12 Ratios of the positive charge to negative charge production cross sections for pp collisions calculated by the three method for combining left and right triggers. The LOPT trigger (a) and HIPT trigger (b) are shown separately. We will use the weighted average method in the rest of this analysis.

tainty the weighted average of the left and right triggers is the most correct since it statistically weights the left and right data with their respective errors and has only a charge dependent unknown Since there is not a great disagreement between different methods, w choose to use the weighted average of left and right triggers to pro duce final data.

Figure 3.18 show the charge production ratio of our experiment compared with the data from CP. Within statistical errors both expe ments agree very well. If we assume the CP ratios of heavy particle to pions, then our data in Figure 3.18 below p_T = 3.0 GeV/c can be corrected upwards by about 5% under the mass dependent efficiency assumption of Section 3.7e. We should point out that in both Fig- ures 3.17 and 3.18 we are limited to p_T's $\lesssim$ 5 GeV/c by statistics. In any case we satisfy ourselves that the method for trigger particl determination is good and that our systematic errors are of the orde of 20%.

3.9 Cl Identified Trigger Particle Ratios in pp Collisions

To check the Cerenkov tagging of the trigger particles we will now take the cross section ratio defined in Section 3.8 with h^+ and now a π or Kp according to our Cerenkov classification schemes. We therefore can investigate four ratios - π^+/π^-, π^+/Kp^+, π^-/Kp^-, Kp^+/K

Following the same procedure presented in Section 3.8, using be outs, normalizing according to Appendix A, and taking a weighted ave age of left and right triggers, Figures 3.19a through 3.19d show the cross section ratio, $\frac{d\sigma}{dp_T}(pp \to hX)/\frac{d\sigma}{dp_T}(pp \to h'X)$, for $h/h' = \pi^+/\pi^-$, π^+/Kp^+, π^-/Kp^-, Kp^+/Kp^- respectively. The triangular points on the figures are the corresponding CP data. The data are uncorrected for Cl inefficiency or calorimeter response. Both the LOPT trigger and

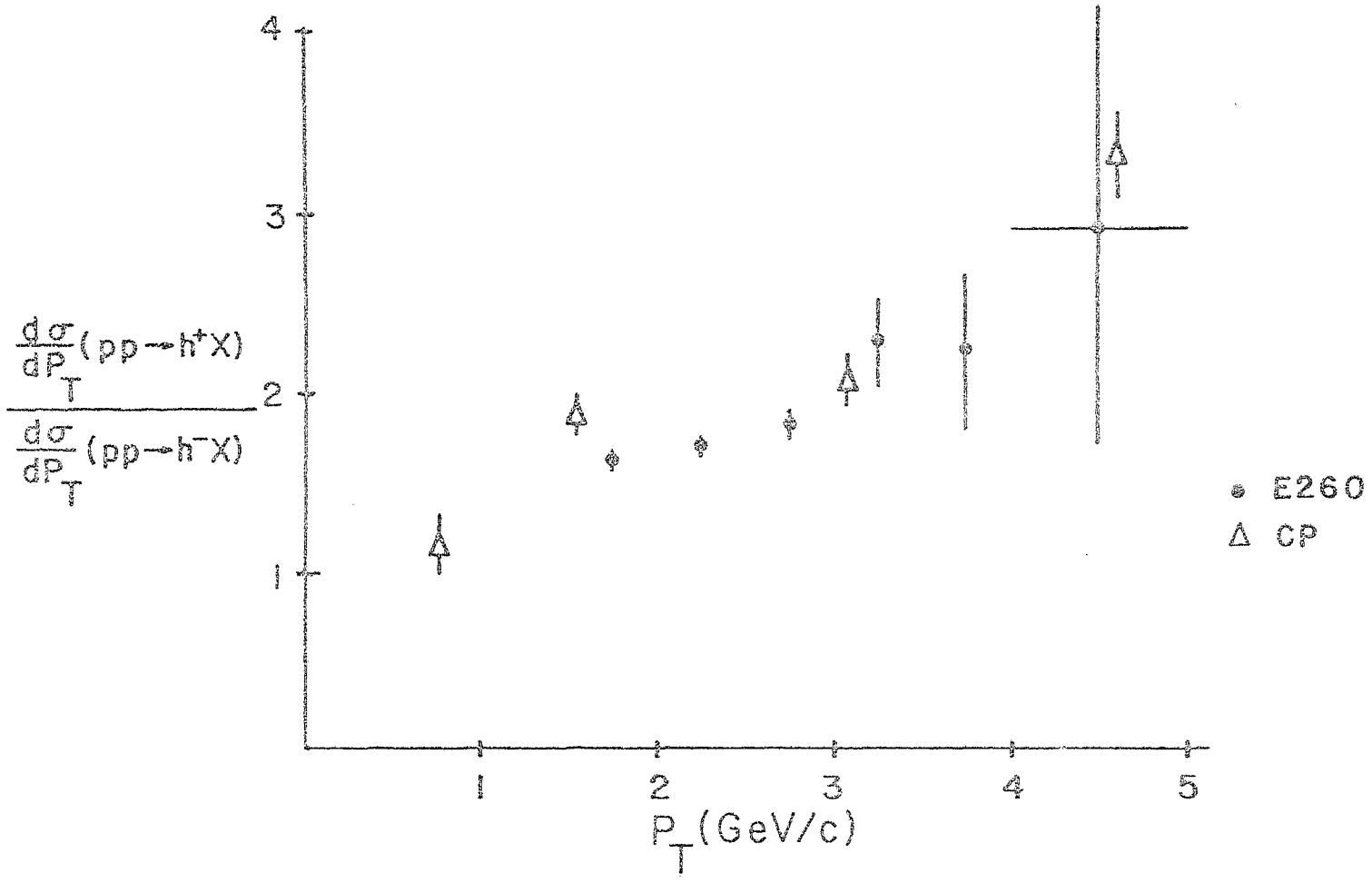

Figure 3.18 E260 charge production ratios from pp collisions compared to the data from Chicago-Princeton. No corrections to the data have been made.

the HIPT trigger are shown. However, the data that include Kp trigg particles obviously have to be corrected for either Cl efficiency or calorimeter response.

Figures 3.20a through 3.20d show the combined data (LOPT + HIPT from the previous four figures corrected as described in Sections 3. and 3.8f. There is less than a 2% Cerenkov efficiency correction an no calorimeter correction to the π^+/π^- ratio of Figure 3.19a. The K signals at $p_T \simeq 2$ GeV/c and at $p_T \simeq 3$ GeV/c may arise from a thresho inefficiency in air for the former and in He for the latter. These efficiencies result in an upward correction of 10 - 20% for the π^+/K ratio but because of the large π^-/K^- and $K^-/\bar{p}$ ratios, the Cl corrections to the π^-/Kp^- and Kp^+/Kp^- ratios are between 75 - 175% at the high p_T end. Calorimeter corrections are small in comparison and te to lower the π/Kp ratios by about 5 - 15% and raise the Kp^+/Kp^- rati by only 5%.

The agreement with CP seen in Figure 3.20a for π^+/π^- is good throughout the entire p_T region. But the 30% or so disagreement wit CP for ratios involving Kp's probably means that we do not understan well enough how the calorimeter responds to heavy particles. Notice that the direction in which the data must be corrected can only be explained by the calorimeter and not by Cl inefficiency.

Figure 3.19 The ratios of $\frac{d\sigma}{dp_T}(pp \rightarrow hX)/\frac{d\sigma}{dp_T}(pp \rightarrow h'X)$ for h/h' as the following: (a) π^+/π^-, (b) π^+/Kp^+, (c) π^-/Kp^-, and (d) Kp^+/Kp^-. The data are uncorrected for Cl efficiency or the calorimeter response. Also shown for comparison are the data from the Chicago-Princeton group.

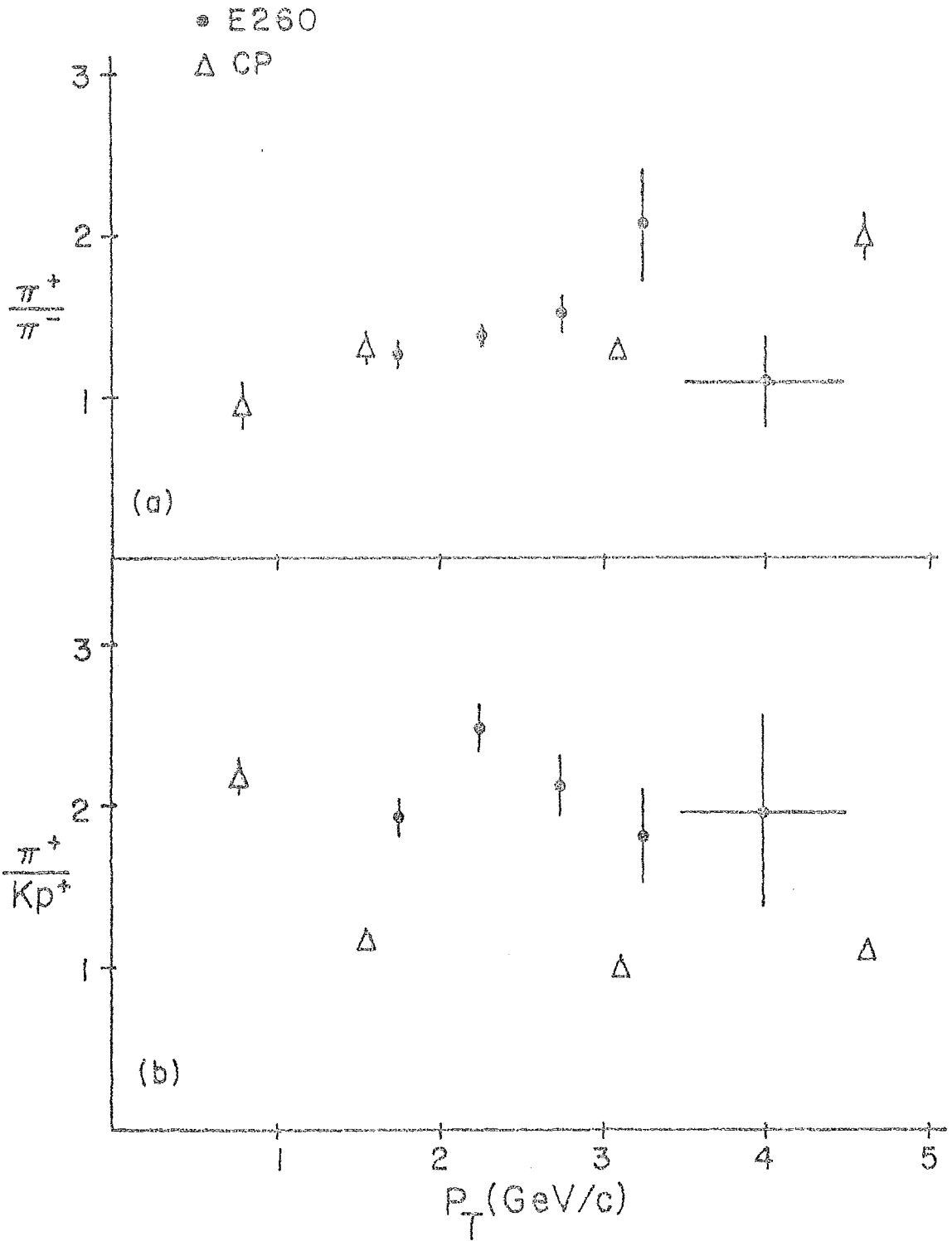
• E260
Δ CP
3
2
1
$\frac{\pi^+}{\pi^-}$
(a)
3
2
1
$\frac{\pi^+}{Kp^+}$
(b)
1
2
3
4
5
P_T (GeV/c)

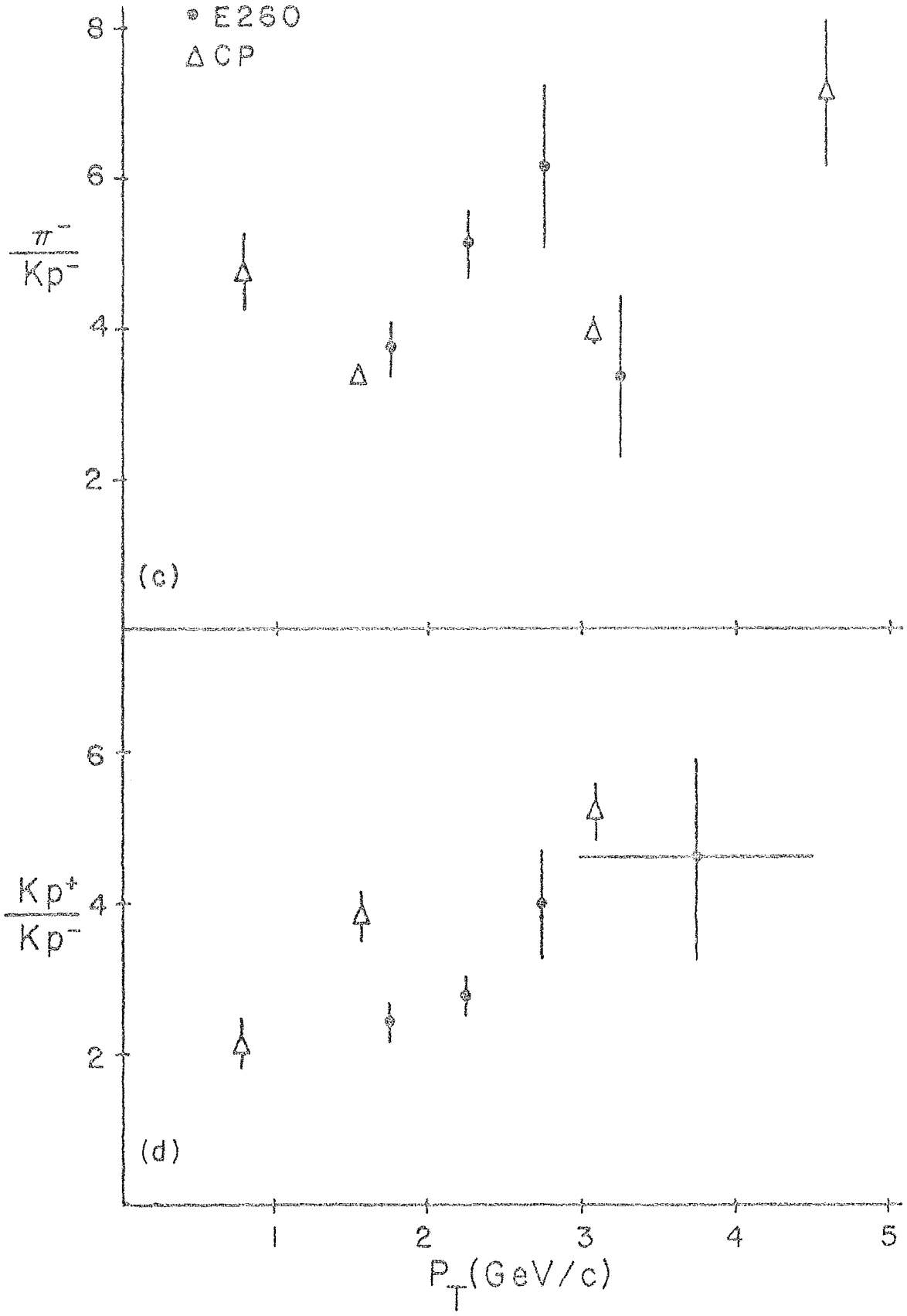
• E260
Δ CP
8
6
4
2
$\frac{\pi^-}{Kp^-}$
(c)
6
4
2
$\frac{Kp^+}{Kp^-}$
(d)
1
2
3
4
5
P_T (GeV/c)

Figure 3.20 The ratios of $\frac{d\sigma}{dp_T}(pp \to hX)/\frac{d\sigma}{dp_T}(pp \to h'X)$ for h/h' as the following: (a) π^+/π^-, (b) π^+/Kp^+, (c) π^-/Kp^-, and (d) Kp^+/Kp^-. The data have been corrected for Cerenkov counter efficiency and calorimeter response. The direction of the disagreement between E260 and CP for (b) through (d) indicate that the calorimeter corrections have to require that p's be much less efficient than we assume in this analysis. Also note that Cl inefficiency implies corrections which are in the opposite direction than the calorimeter corrections.

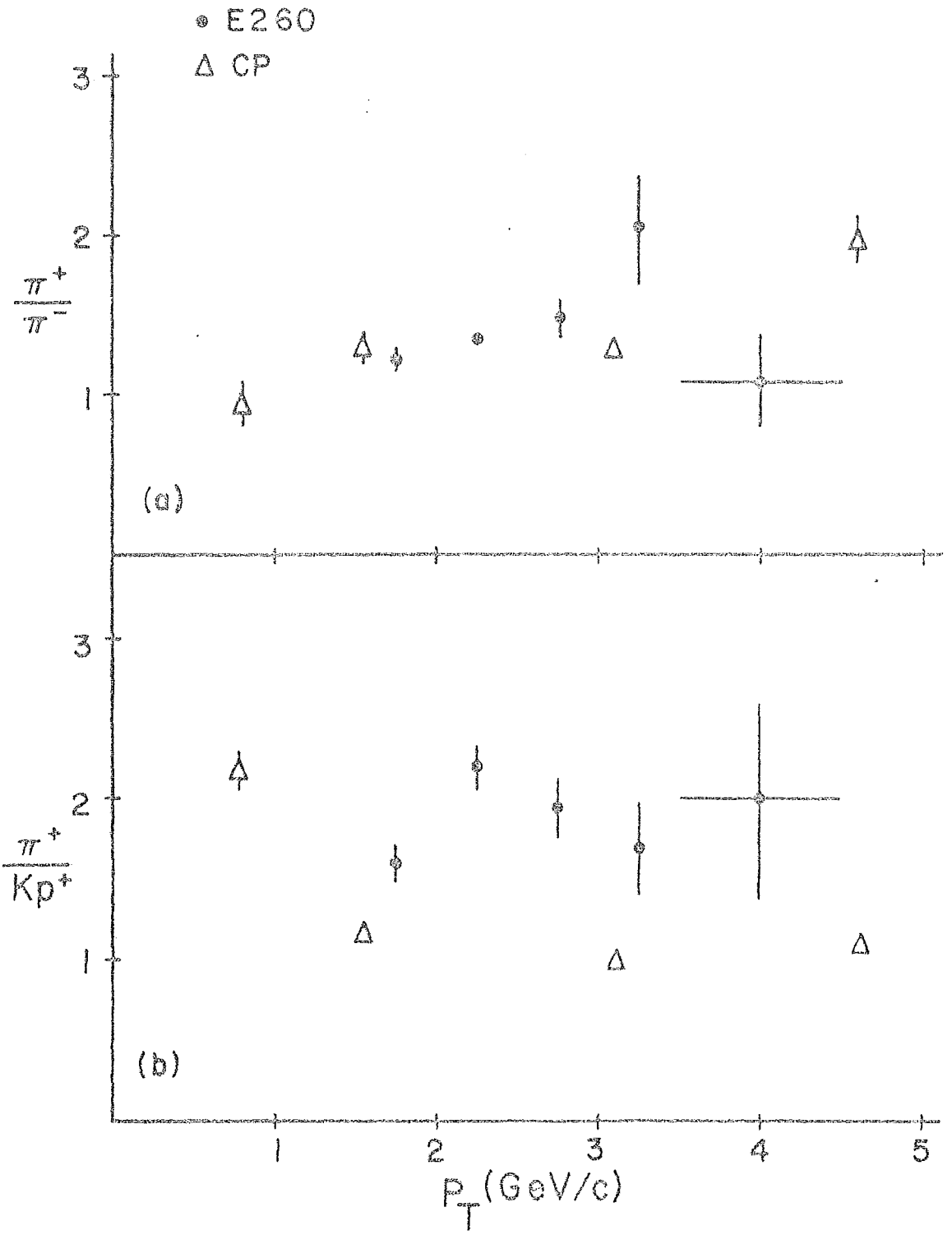
• E260
Δ CP
3
2
1
$\frac{\pi^+}{\pi^-}$
(a)
3
2
1
$\frac{\pi^+}{Kp^+}$
(b)
1
2
3
4
5
P_T (GeV/c)

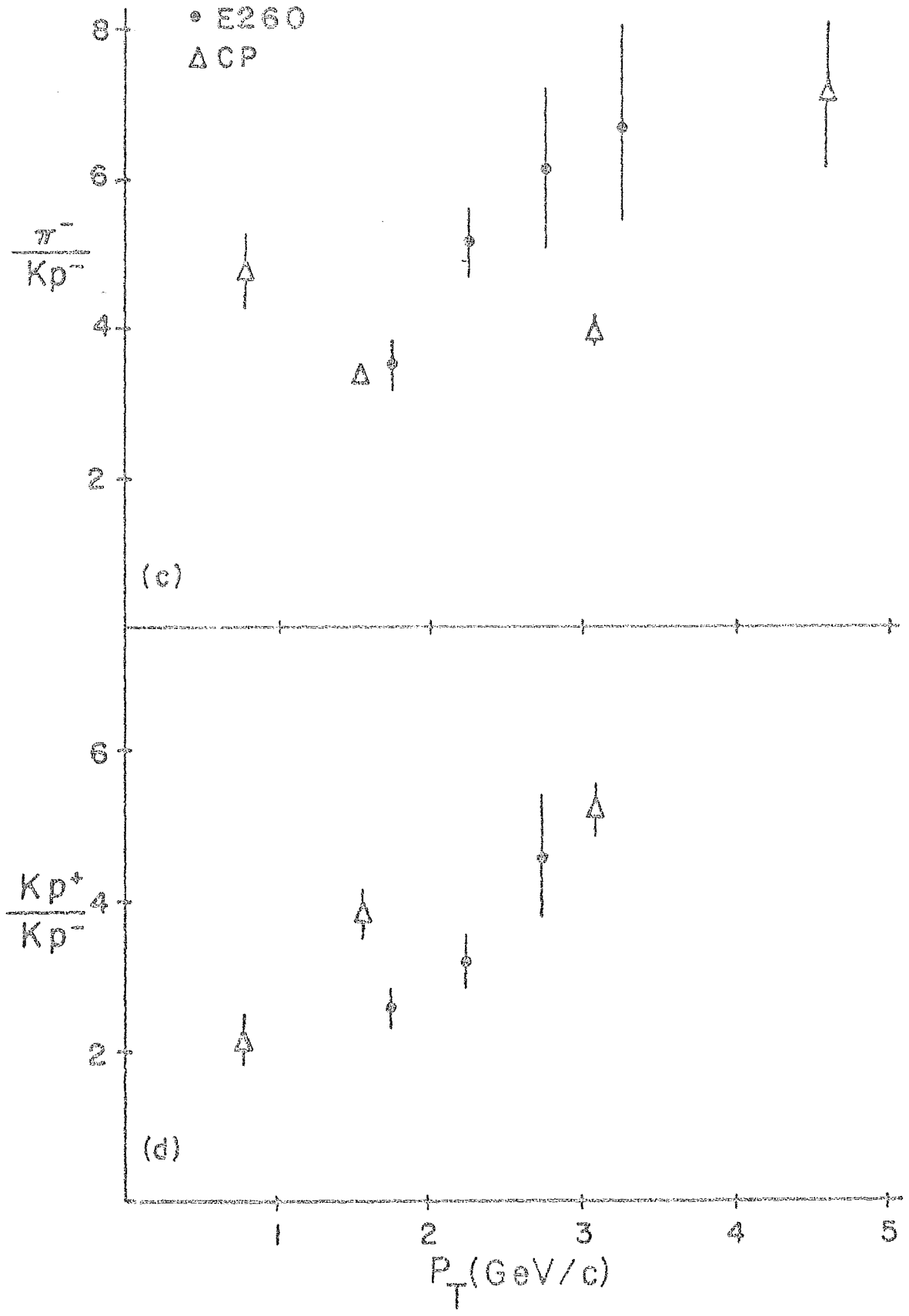
• E260
Δ CP
8
6
4
2
$\frac{\pi^-}{Kp^-}$
(c)
6
4
2
$\frac{Kp^+}{Kp^-}$
(d)
1
2
3
4
5
P_T (GeV/c)

CHAPTER IV

DATA ANALYSIS RESULTS

With the results of Chapter III showing how to make the appropriate corrections to the data we consider π^+, π^- and K^- beams and determine ratios analogous to those in Figures 3.18 and 3.20. The same corrections and methods will be used as those discussed in obtaining the p induced triggers. Since this is the first data obtained from meson beams, we will present the data and then later discuss theoretical expectations in the next chapter. For the pion and proton beams we will also investigate the multiplicity of "away" side charged hadrons as we vary the trigger particle.

4.1 Cross Section Ratios for $\pi^{\pm}$ and K^- Beams

Figures 4.1a through 4.1c show the ratio $\frac{d\sigma}{dp_T}(ap \to h^+X)/\frac{d\sigma}{dp_T}(ap \to h^-X)$ for beam particle a as a π^+, π^- and K^- respectively. There are no calorimeter corrections made to these figures and the method of obtaining this data is identical to that in Section 3.8. The most striking features of these figures are the similarity between π^+ and p induced charge ratios - positive triggers are produced about twice as often as negative triggers - and the similarity between K^- and π^- induced ratios - positive triggers are about as likely as negative triggers.

Because statistics are lacking for K^- and π^+ beams, we show in Figures 4.2a through 4.2d only the cross section ratios $\frac{d\sigma}{dp_T}(\pi^-p \to hX)/\frac{d\sigma}{dp_T}(\pi^-p \to h'X)$ for $h/h' = \pi^+/\pi^-$, π^+/Kp^+, π^-/Kp^- and Kp^+/Kp^- respectively. The data are corrected for Cl efficiency. A π^- is able to produce a π^+ or π^- with about the same rate up to $p_T \tilde{} 4.5$ GeV/c. However, the production of Kp trigger particles is strongly suppressed at high transverse momenta. At p_T's $\lesssim$ 2 GeV/c, Kp^+'s are as likely

Figure 4.1 Ratios of the positive charge to negative charge production cross sections for (a) π^+p, (b) π^-p and (c) K^-p collisions. Also sketched in (a) is a hand-drawn curve showing where the data for pp collisions lie.

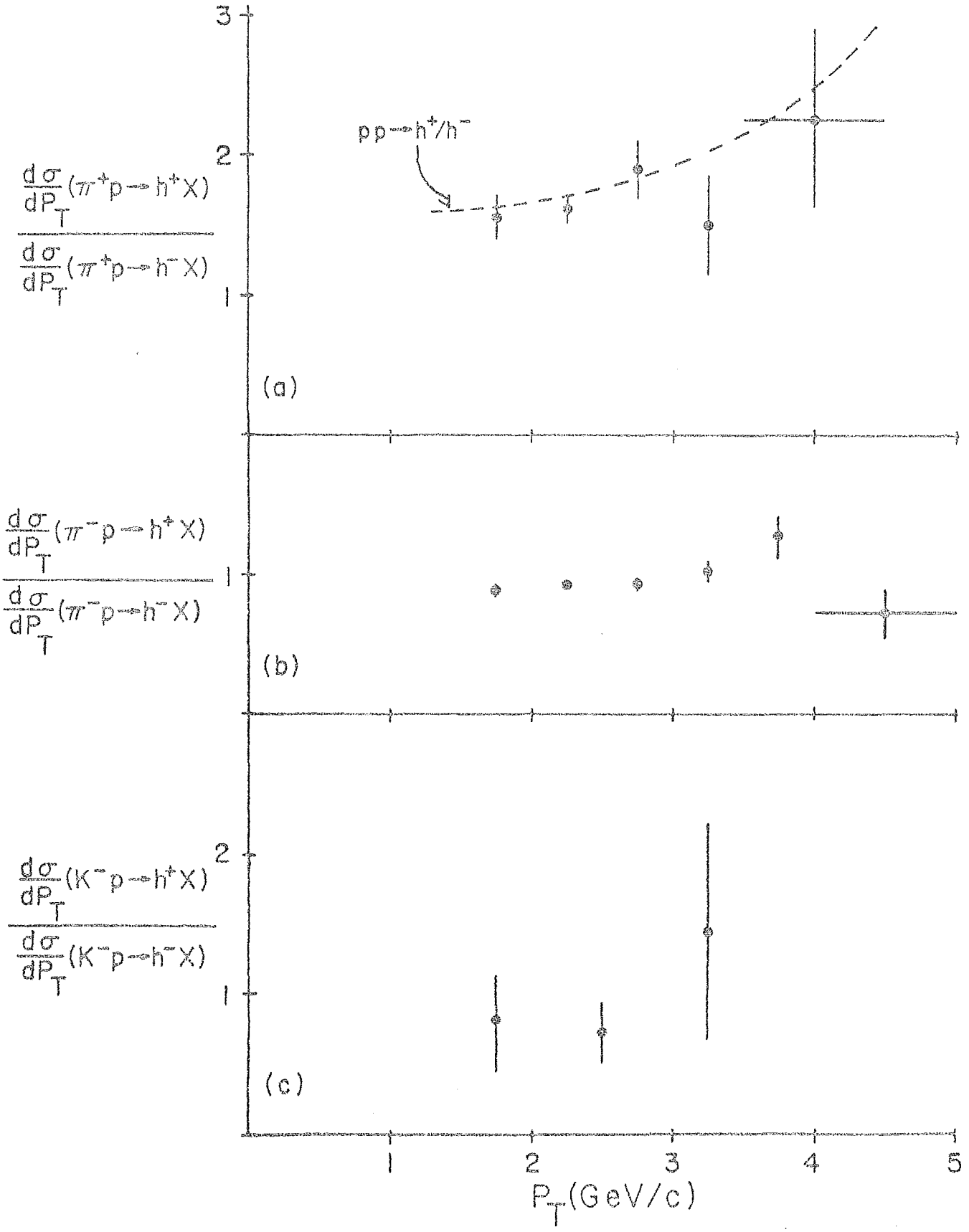
$\frac{d\sigma}{dP_T}(\pi^+p \to h^+X)$
$\frac{d\sigma}{dP_T}(\pi^+p \to h^-X)$
pp → h⁺/h⁻
(a)
$\frac{d\sigma}{dP_T}(\pi^-p \to h^+X)$
$\frac{d\sigma}{dP_T}(\pi^-p \to h^-X)$
(b)
$\frac{d\sigma}{dP_T}(K^-p \to h^+X)$
$\frac{d\sigma}{dP_T}(K^-p \to h^-X)$
(c)
3
2
1
2
1
1
2
3
4
5
P_T(GeV/c)

Figure 4.2 The ratios $\frac{d\sigma}{dp_T}(\pi^- p \to hX)/\frac{d\sigma}{dp_T}(\pi^- p \to h'X)$ for h/h' as the following: (a) π^+/π^-, (b) π^+/Kp^+, (c) π^-/Kp^-, and (d) Kp^+/Kp^-. The data have been corrected for the efficiency of the Cerenkov counter.

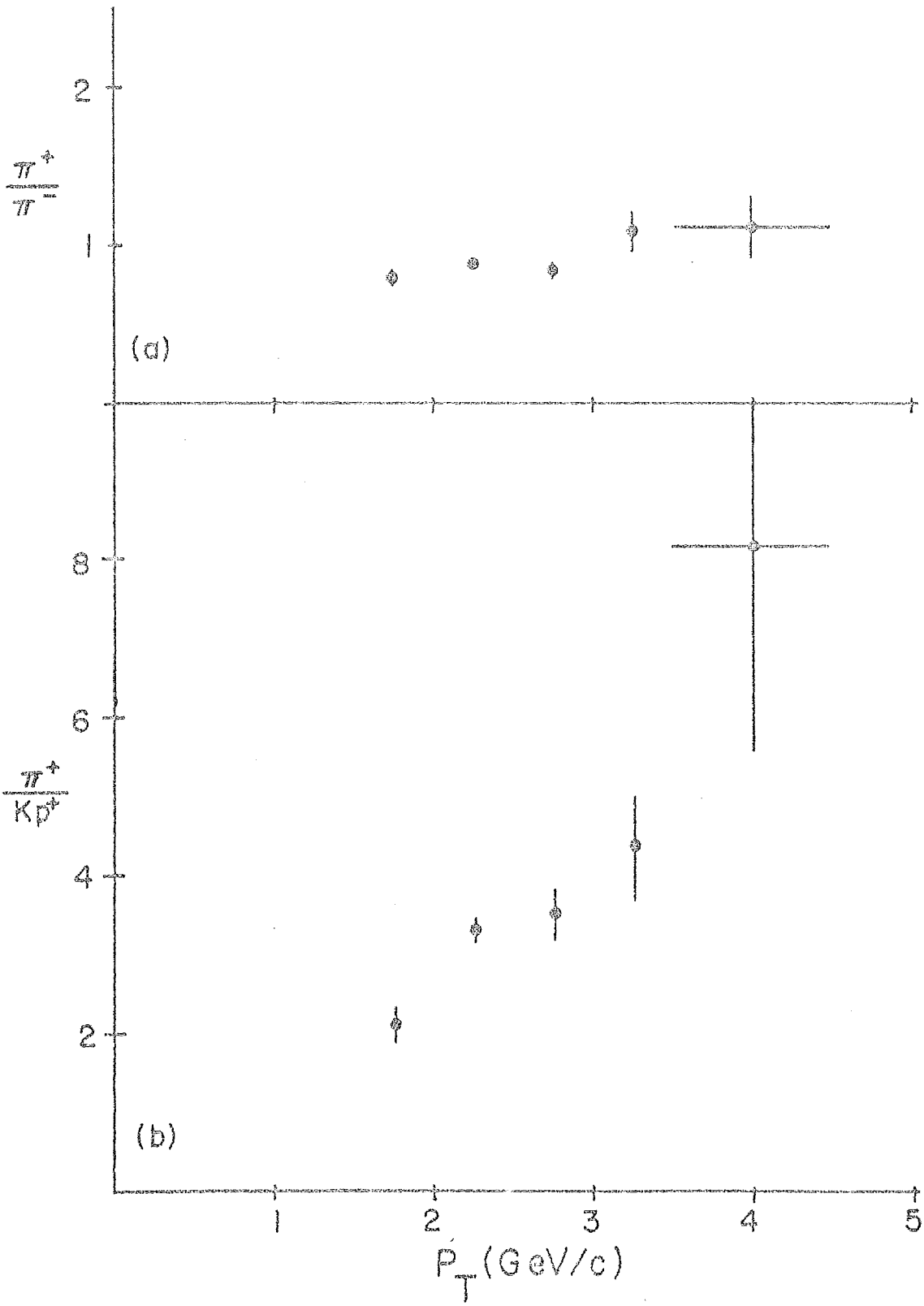
$\frac{\pi^+}{\pi^-}$
2
1
(a)
8
6
$\frac{\pi^+}{Kp^+}$
4
2
(b)
1
2
3
4
5
P_T (GeV/c)

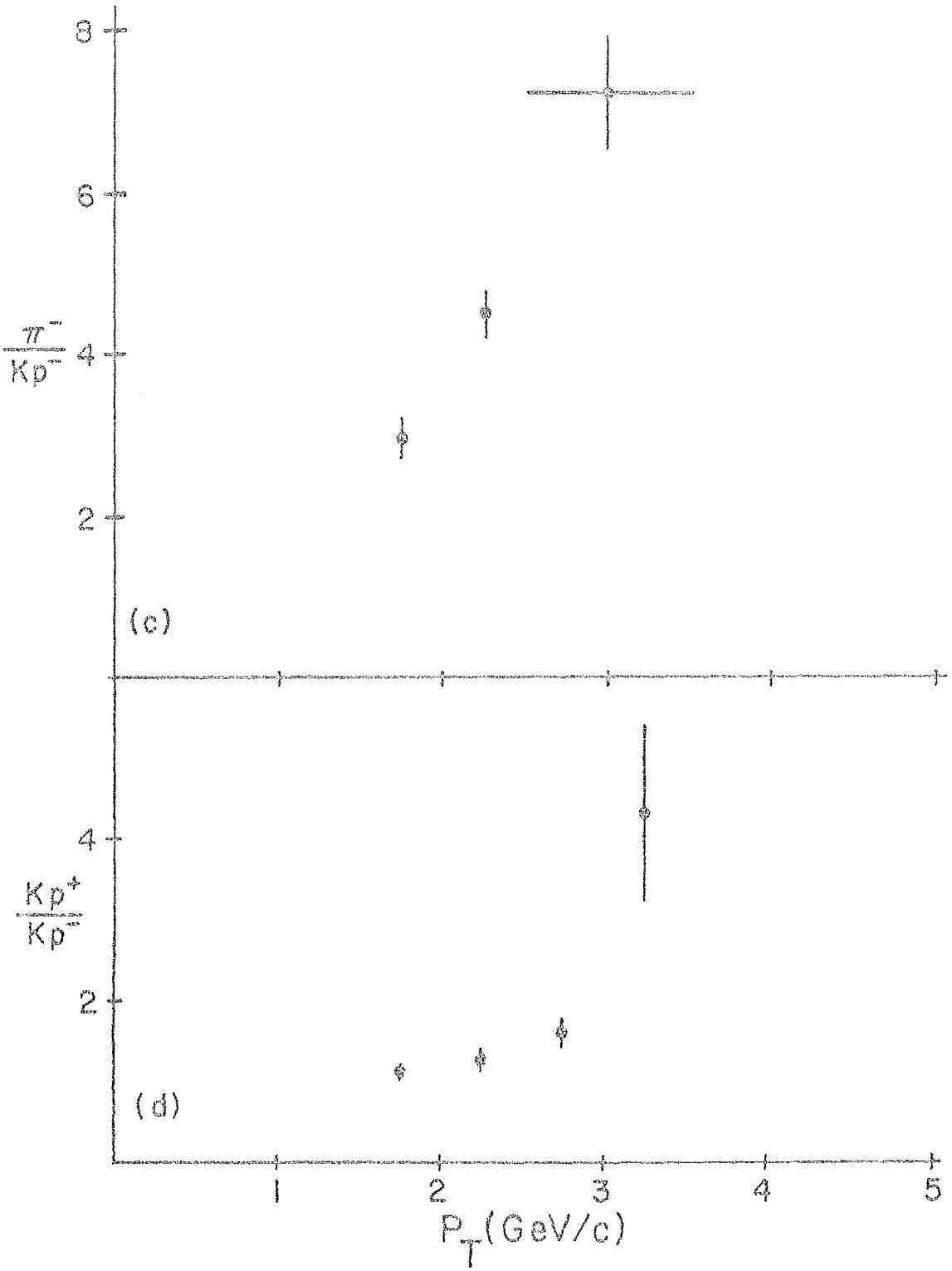
8
6
4
2
$\frac{\pi^-}{Kp^-}$
(c)
4
2
$\frac{Kp^+}{Kp^-}$
(d)
1
2
3
4
5
P_T(GeV/c)

to be produced as Kp^-'s, but as the p_T increases, so does the probability that the Kp trigger will be positive. Figures 4.2b and 4.2c show that π's definitely are predominant over both positive and negative Kp's. But in comparing Figure 4.2 with Figure 3.20 for the p beam, we note that the ratios of π^- to Kp^- are not all that different in π^- and p induced reactions. Since $\bar{p}$ production is low in pp collisions, it may also be that in π^-p collisions the $\frac{K^-}{\bar{p}}$ ratio is also large and therefore the $\frac{\pi^-}{K^-}$ ratio is about the same magnitude. As for the $\frac{\pi^+}{Kp^+}$ ratios, the π^- beam ratio is slightly higher than that for a proton beam. About 25% of the positive triggers are p's in the proton beam. Because we don't have to create as many baryons with the π^- beam we can naively expect that p production will be lower than that of the p beam. Thus, if the π^+ to K^+ ratio is about the same for both beams we expect the $\frac{\pi^+}{Kp^+}$ ratio for π^- beams to be larger than that for p beams. Chapter V will contain further theoretical discussion with references to hard scattering models and the relationship that initial state quarks have on the trigger particle production rates.

4.2 Away Side Acceptances

In measuring the away side multiplicity that accompanies a high p_T particle we have to allow for the acceptance of our apparatus. In general, the acceptance is a function of the charge and the transverse momentum of the particles. If $A^{\pm}(p_T)$ is the acceptance of a charged particle with transverse momentum p_T, then the true charged multiplicity, $n^{\pm}(p_T)$, is related to the observed multiplicity, $n_o^{\pm}(p_T)$ by

$$n_o^{\pm}(p_T) = n^{\pm}(p_T)A^{\pm}(p_T) \qquad (4.1)$$

$A^{\pm}(p_T)$ can be determined by Monte Carlo studies but here we will

not follow that procedure and instead determine where $A^{\pm}(p_T)$ is independent of charge and transverse momentum.

Because the wire chambers are large enough to measure the trajectories of wide angle tracks that exit the magnet, the acceptance of the spectrometer is limited for the most part by the aperture of the magnet. Figure 4.3a is a sketch of the magnet aperture as we look downstream. We can qualitatively predict what our acceptance for charged particles should look like. If we accept all particles with an azimuthal range of $\pm\phi_0$, then we expect, according to Figure 4.3a, the acceptance to be constant until particles with polar angles θ_1 are measured. We lose a certain fraction of particles that don't ma it through the aperture as shown by the shaded regions in Figure 4.3 For $\phi_0 = 45^{\circ}$, θ_1 is approximately 110° in the CMS. As θ increases t acceptance will slowly decrease until finally no particles exit the magnet at polar angle θ_2. This occurs at roughly $\theta_2 = 130^{\circ}$. Toward small values of θ, the forward direction, two effects will diminish the number of observed particles. First, no real particles can hit the 2 x 2 veto counter otherwise there will not be a trigger. Secon ly, the forward direction is expected to contain many sparks caused by particles produced by a previous interaction, not necessarily a trigger, or from old beam tracks which then may produce junk tracks. With so many extra sparks at small θ, the track finding routines wil not be as reliable in the forward direction. We therefore expect th acceptance to behave as shown in Figure 4.3b. Region A is depleted because of track finding inefficiency and Region C is depleted becau of a loss of particles into the magnet. Region B has roughly consta acceptance and, since $p_T = p\sin\theta$, the measurement of the number of particles in this θ range will be independent of their p_T's. i.e.,

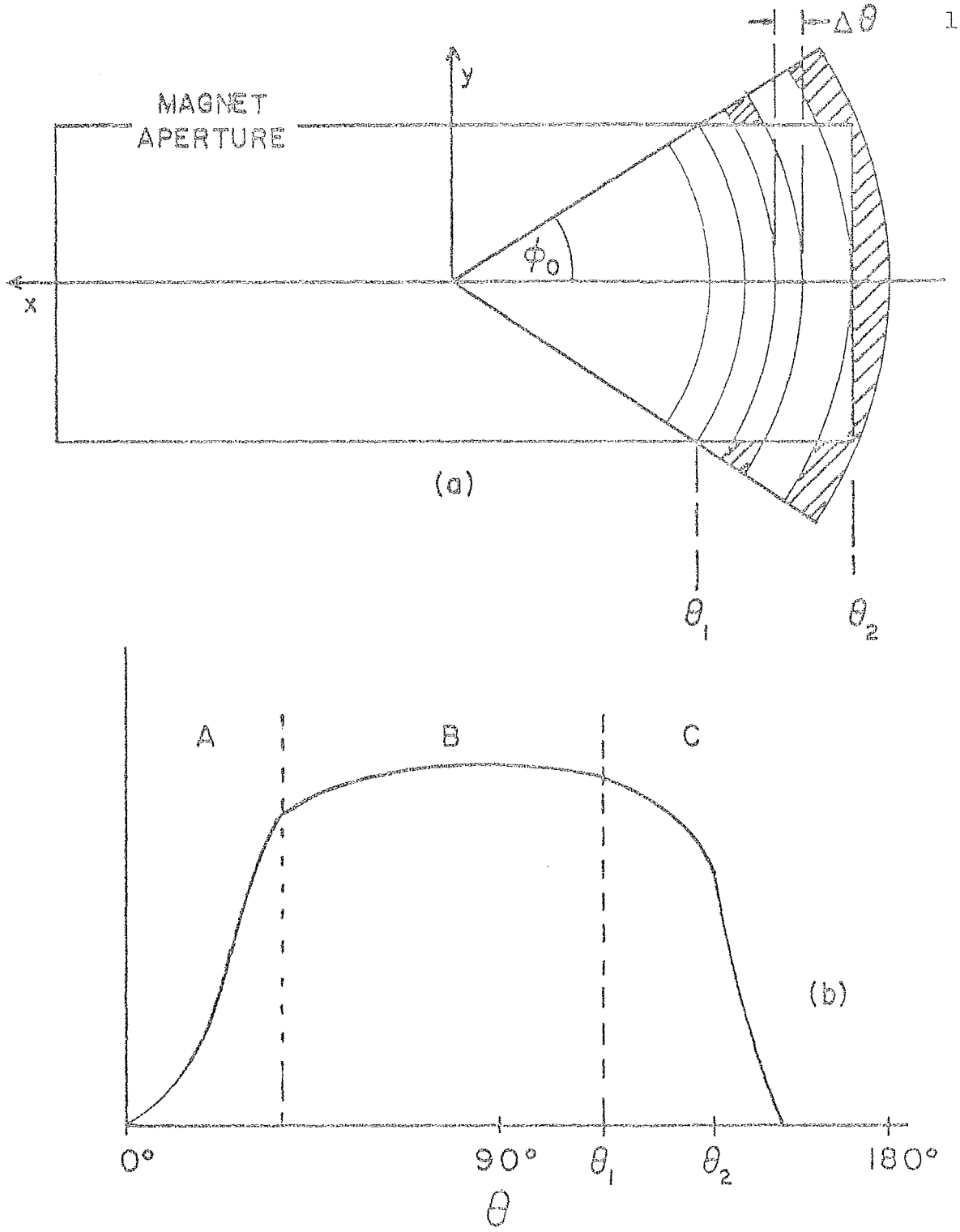

Figure 4.3 (a) A sketch of the effect of the magnet aperture on the acceptance. For fixed ϕ_0, the acceptance, proportional to $\Delta\theta\phi_0$, is constant until θ_1 and then slowly decreases to zero at θ_2; (b) a qualitative expectation of the acceptance as a function of θ. Region A is depleted due to track funding losses, B is roughly constant and C is depleted due to losses through the magnet.

in Region B,

$$A^{\pm}(p_T) = A^{\pm}, \qquad (4.2)$$

From Figure 4.4 we see that the acceptance will be charge dependent the high-θ end because bend-outs will hit the side of the magnet so(than will bend-ins. Of course this is most evident at small values of p_T where particles are bent through large angles. Figure 4.5a i: a plot of $\frac{1}{N}\frac{dN}{d\theta}$ for the away side particles that have $0.3 \leq p_T < 1.0$ GeV/c and Figure 4.5b shows $\frac{1}{N}\frac{dN}{d\theta}$ for away particles with $p_T > 1.0$ GeV/c. The trigger particle in either case has a $p_T \geq 1.5$ GeV/c. T away side as defined here is essentially all particles within $\pm 45^{\circ}$ c the trigger particle azimuth. The expected effects of the acceptance are seen in these figures. The track finding routines apparently are unr liable for $\theta \lesssim 25^{\circ}$. θ_1 occurs at about $90^{\circ} - 100^{\circ}$ and the acceptance totally cuts off at about 120°. Note that these figures are an aver age of bend-ins and bend-outs. The away spectra seem to be relative unaffected by the p_T change for particles with $\theta \gtrsim 35^{\circ}$. The peaking in the forward direction of the low transverse momentum particles (Figure 4.5a) may be due to diffractive-type particles which disappe (Figure 4.5b) as one asks for faster away side particles.[6,9,10] For particles with $0.3 \leq p_T < 1.0$ GeV/c, Figures 4.6a and 4.6b show $\frac{1}{N}\frac{dN}{d\theta}$ for bend-ins and bend-outs respectively. Bend-outs start to become lost into the magnet at $\theta \simeq 95^{\circ}$. Therefore for a uniform acceptance $A^{\pm}(p_T)$ = constant, we have to choose, for this ϕ_0, a θ region betwee ~35° and ~95°. But we know from the ISR experiments[6,9,10] that a jet of particles opposite a high p_T trigger is uniformly distributed in the range $45^{\circ} \lesssim \theta \lesssim 135^{\circ}$. Correlations of this jet with the trigger are important so we should therefore restrict ourself to θ's inside this region. This won't assure us of measuring only jet-associated

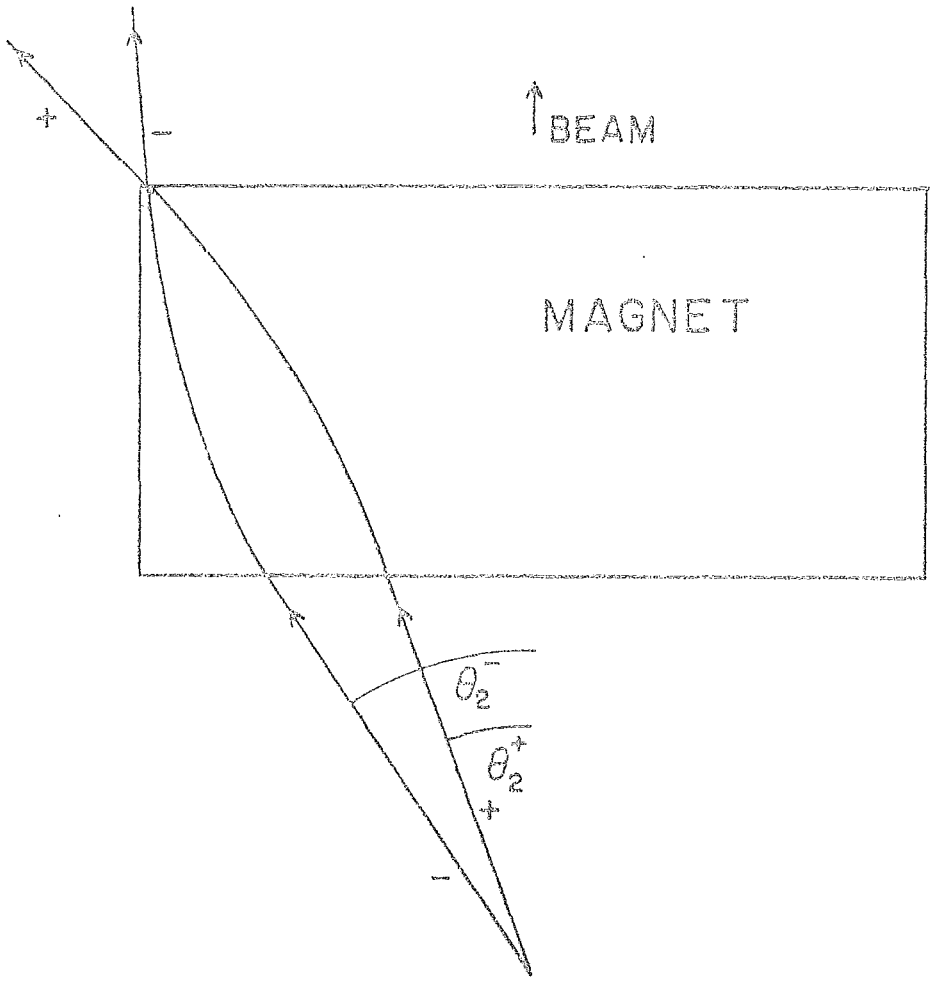

Figure 4.4 Two particles with the same momentum but opposite charges have different limiting angles, θ_2. Bend-ins get through the magnet aperture at larger θ than do bend-outs.

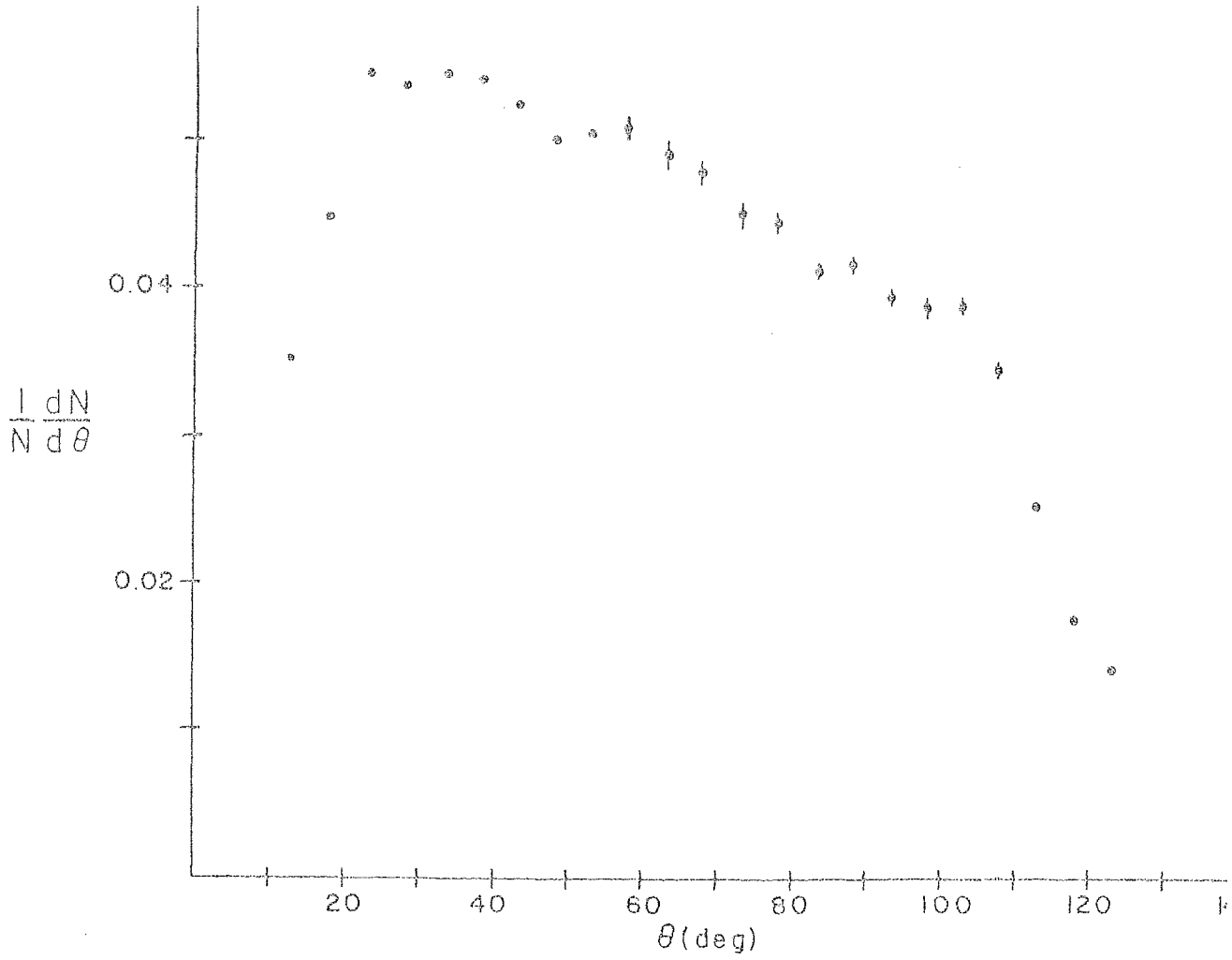

Figure 4.5a The distribution in θ of particles in a $\pm 45^{o}$ azimuthal wedge directly opposite a trigger particle having $p_T \geq 1.5$ GeV/c. These away particles are in the range $0.3 \leq p_T < 1.0$ GeV/c and the distribution in the figure is normalized to one.

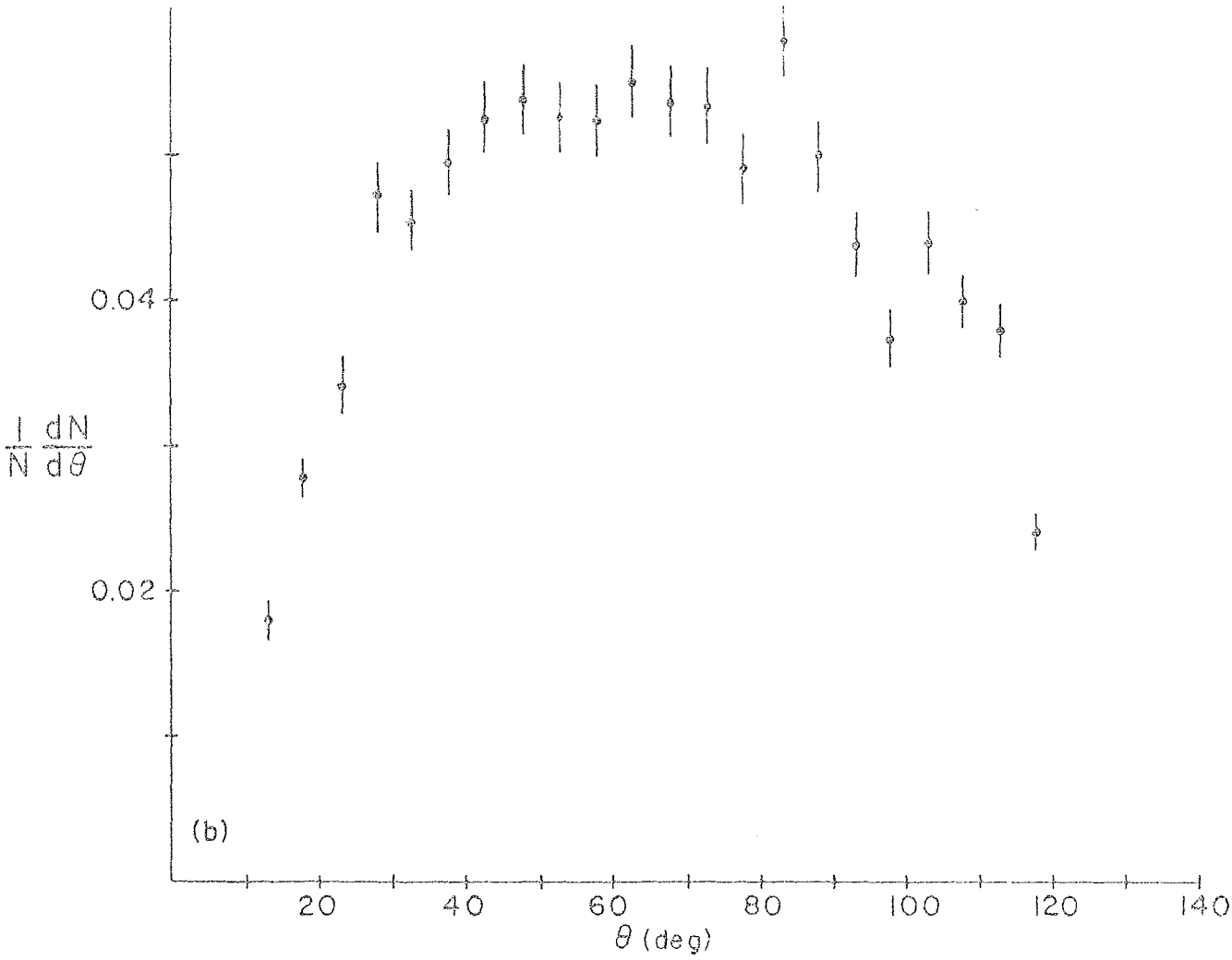

Figure 4.5b The same as (a) but the away particles are in the range $1.0 \leq p_T < 2.0$ GeV/c.

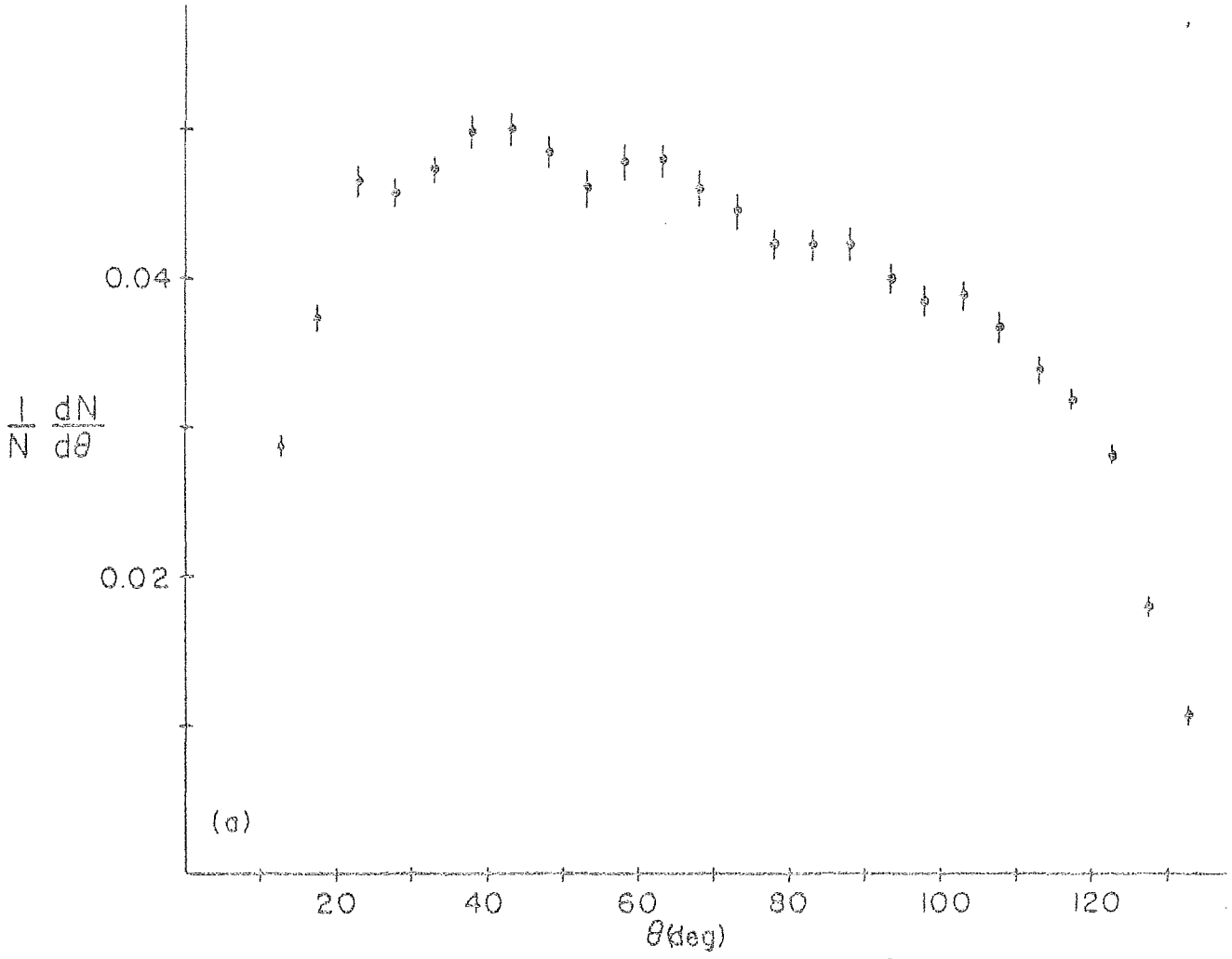

Figure 4.6a The distribution in θ of bend-in particles opposite a trigger particle having $p_T \geq 1.5$ GeV/c. These away particles are in an azimuthal wedge of $\pm 45^\circ$ directly opposite the trigger particle and have $p_T \geq 0.3$ GeV/c.

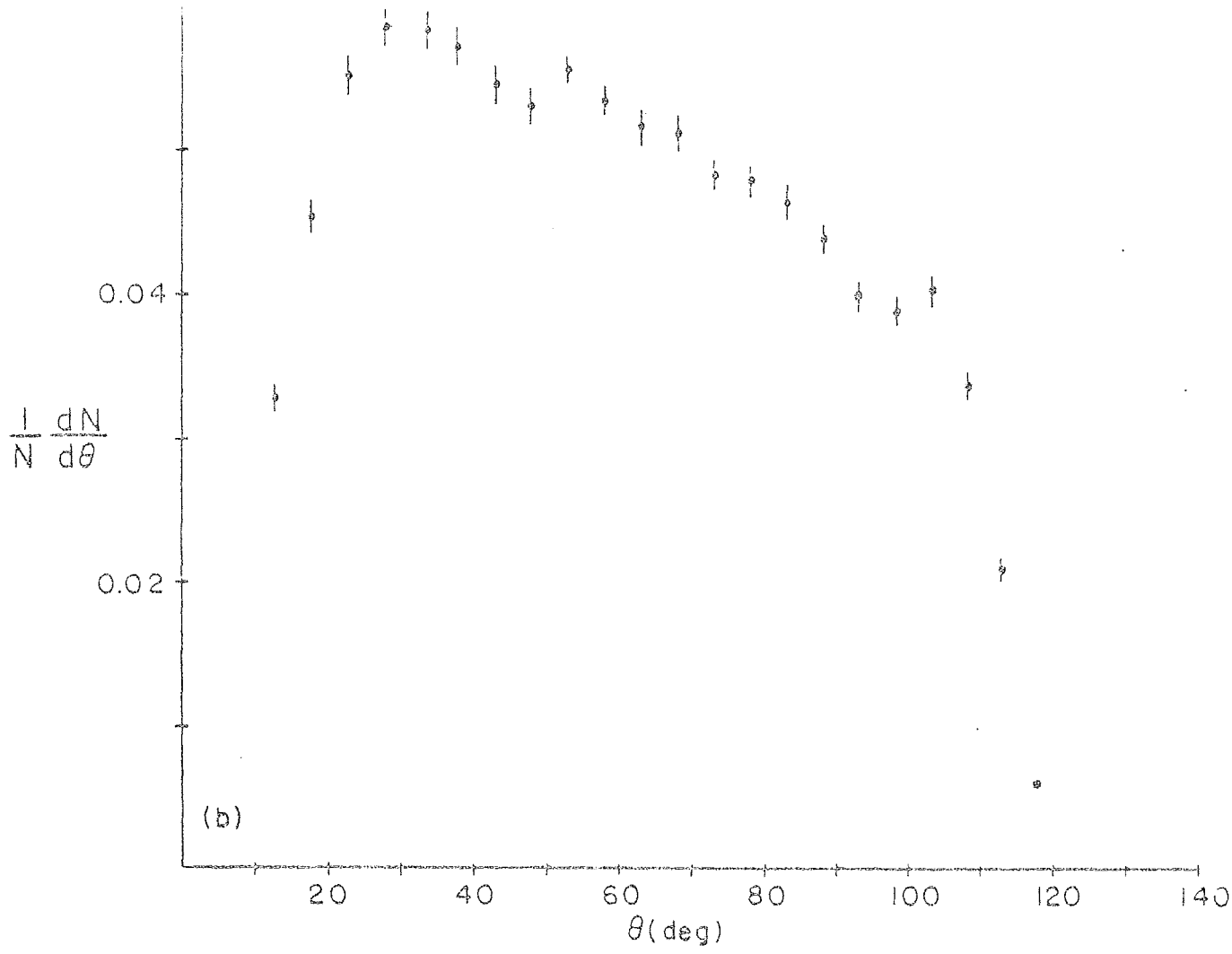

Figure 4.6b The same as (a) but for away side bend-outs.

particles but should restrict the background to few low p_T particles We choose the minimum away θ to be 45^o. Partially motivated by symmetry and Figure 4.6b, the high-θ cutoff is chosen to be 90^o. Table 4.1 summarizes the kinematic regions accepted for particles on the away side and lists the corresponding trigger particle cuts.

4.3 Away Side - Trigger Particle Correlations

With the away side parameters firmly established we now investigate how the away jet, for the sake of discussion here assumed to be produced by the decay of a quark, is correlated to the type of trigg particle. We will do this by measuring the charged multiplicity on the away side opposite various trigger particles that have $p_T \geq 1.5$ GeV In particular, with beam particle a opposite a trigger of type h, th ratio of the number of positive particles to negative particles, $R_a($ is related to the average charge of the away side, $\langle Q_a(h)\rangle$,

$$\langle Q_a(h)\rangle = \frac{n_a^+(p_T) - n_a^-(p_T)}{n_a^+(p_T) + n_a^-(p_T)} = \frac{R_a(h) - 1}{R_a(h) + 1} \qquad (4.3)$$

This, we will see further in the next chapter, can be related to the charge of the decaying quark. Obviously, if a quark of charge Q deca into charged hadrons and we count only these hadrons, then, after ma such events, Eq. 4.3 closely specifies the exact charge Q. We need not worry about acceptance corrections since we take the ratio of ob served multiplicities and for uniform acceptances, according to Eq. 4.1, the acceptance factors cancel. But since there is a background from beam and target fragmentation particles with low p_T, the charge measurement is contaminated by non-jet hadrons. To avoid much of th background the away particles will be chosen to have fairly high p_T. If the fragmentation background follows the usual $\exp(-6p_T)$ spectrum then Figure 4.7 shows the fraction of this background that remains

	TRIGGER PARTICLE	AWAY SIDE PARTICLES
Rapidity Range	$2.55 \leq y_{lab} \leq 3.55$	$0 \leq y_{lab} \leq 8.0$
Polar angle (θ) range	$25^{o} \leq \theta \leq 180^{o}$	$45^{o} \leq \theta \leq 90^{o}$
Azimuthal angle (ϕ) range	$0^{o} \leq \phi_T \leq 180$	$225^{o}-\phi_T \leq \phi \leq 135^{o}-\phi_T$
p_T range	$p_T \geq 1.5$ GeV/c	$p_T \geq 0.3$ GeV/c

Table 4.1 A summary of the kinematic regions explored in this analysis. Both the trigger side and away side cuts are listed. Note that the away side rapidity is limited by the choice of polar angle and not by the rapidity cut used.

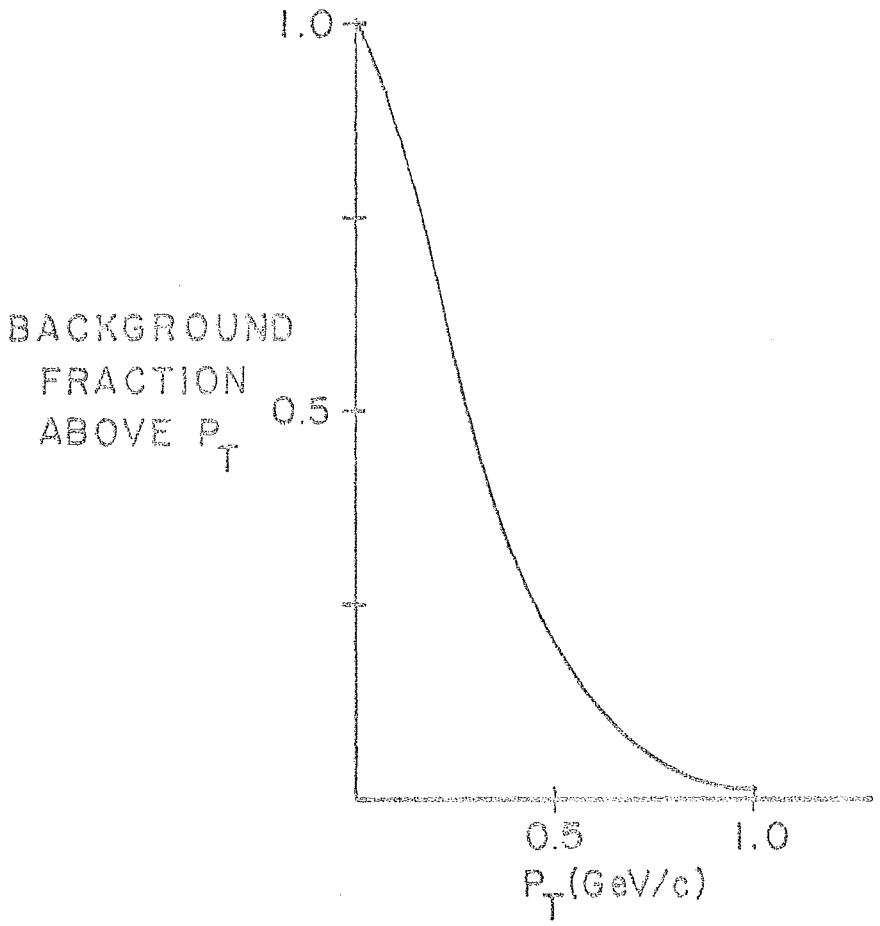

Figure 4.7 Fractional amount of background of the type $\exp(-6p_T)$ existing above any value of p_T.

above a given p_T. Even for p_T's $\geq$ 0.5 GeV/c 20% of the background remains. Besides the background problem there are theoretical prejudices that state that the faster (higher p_T) away jet members should tend to reflect the flavor of the decaying quark more than the lower p_T jet members.[37] As a measure of the fastness of the away particles relative to the trigger we will use a variable that is essentially the ratio of the away transverse momentum for particle i, p_T^i, to that of the trigger. In the transverse plane, this variable, x_e, is defined as

$$x_e = - \frac{\vec{p}_T^{\,i} \cdot \vec{p}_T}{|\vec{p}_T|^2} \qquad (4.4)$$

with $\vec{p}_T$ the transverse momentum vector of the trigger particle.

It is important to realize that the distribution of the away side hadrons is seen in a totally unbiased way. Of course we are limited by acceptance but the away side is independent of calorimeter response or triggering efficiency. Given an event with a high p_T trigger selected in any fashion, the away side particles will depend only on the beam particle and the type of trigger and its transverse momentum. Especially when using a relative variable such as x_e, it is important that the trigger p_T spectrum be shown when presenting away side distributions which are averaged over the trigger p_T. For p and π^- beams the actual p_T spectra for charged, π^+ and Kp^+ trigger particles are shown in Figure 4.8. The minimum trigger p_T is 1.5 GeV/c while the average p_T is about 2.2 GeV/c. The structure observed in these figures occurs because we combine both LOPT and HIPT triggers. A very similar spectrum is seen for the π^+ beam.

As mentioned in Chapter I we will try to resolve the question of how the away charged multiplicity depends on the nature of the trigger particle. We first look at $R(h^+)$ and $R(h^-)$ as a function

Figure 4.8 The p_T spectra of the trigger particles, $\frac{1}{N_j}\frac{dN_j}{dp_T}$, used in the analysis of the away side distributions. These curves are normalized to one and are plotted for the reactions $ap \rightarrow jX$ for (a) $pp \rightarrow h^+X$ and $pp \rightarrow h^-X$, (b) $\pi^-p \rightarrow h^+X$ and $\pi^-p \rightarrow h^-X$, (c) $pp \rightarrow Kp^+X$ and $pp \rightarrow \pi^+X$, (d) $\pi^-p \rightarrow Kp^+X$ and $\pi^-p \rightarrow \pi^+X$.

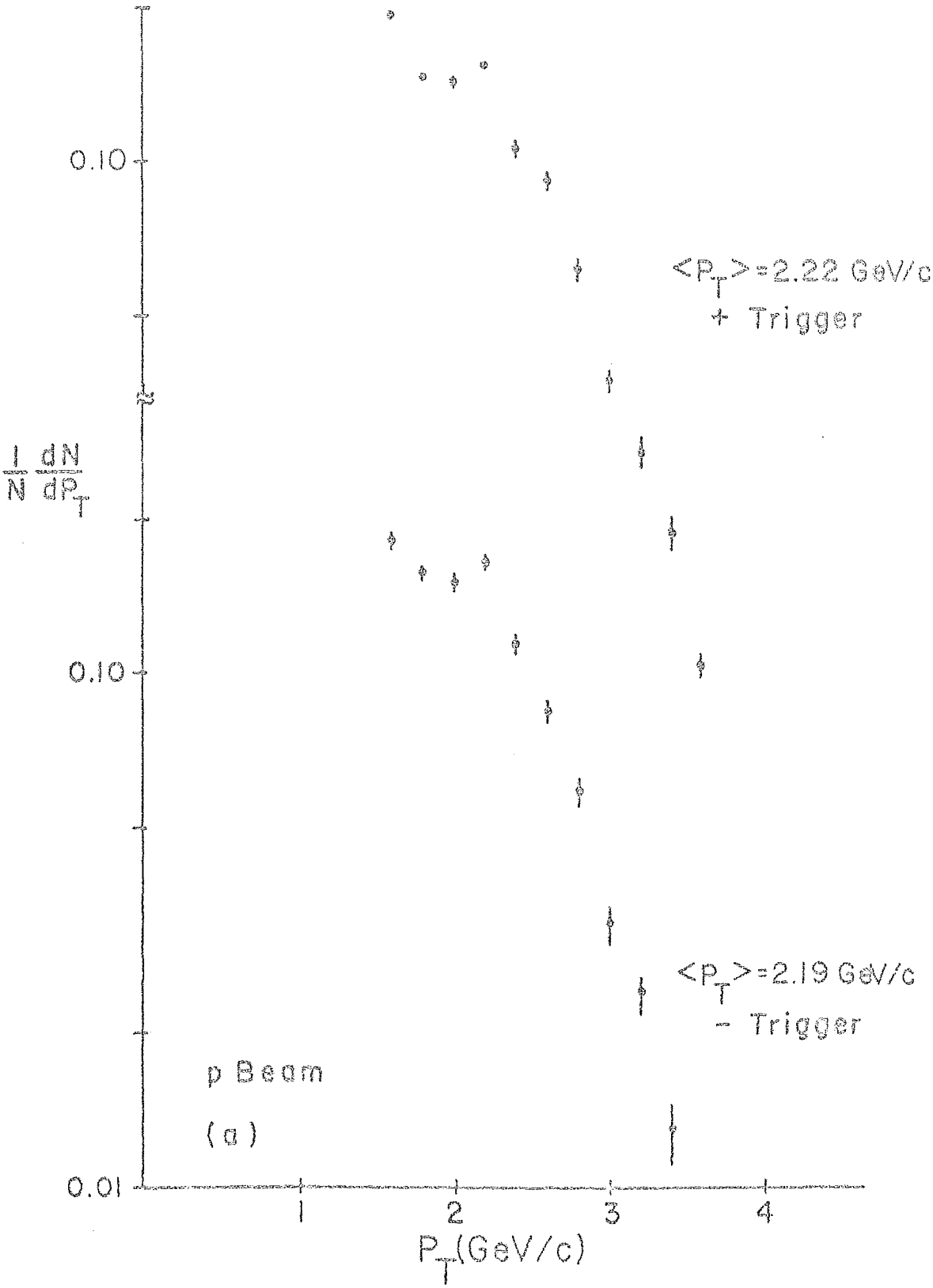
0.10
0.10
0.01
$\frac{1}{N}\frac{dN}{dP_T}$
$\langle P_T \rangle$ = 2.22 GeV/c
+ Trigger
$\langle P_T \rangle$ = 2.19 GeV/c
- Trigger
p Beam
(a)
1
2
3
4
P_T (GeV/c)

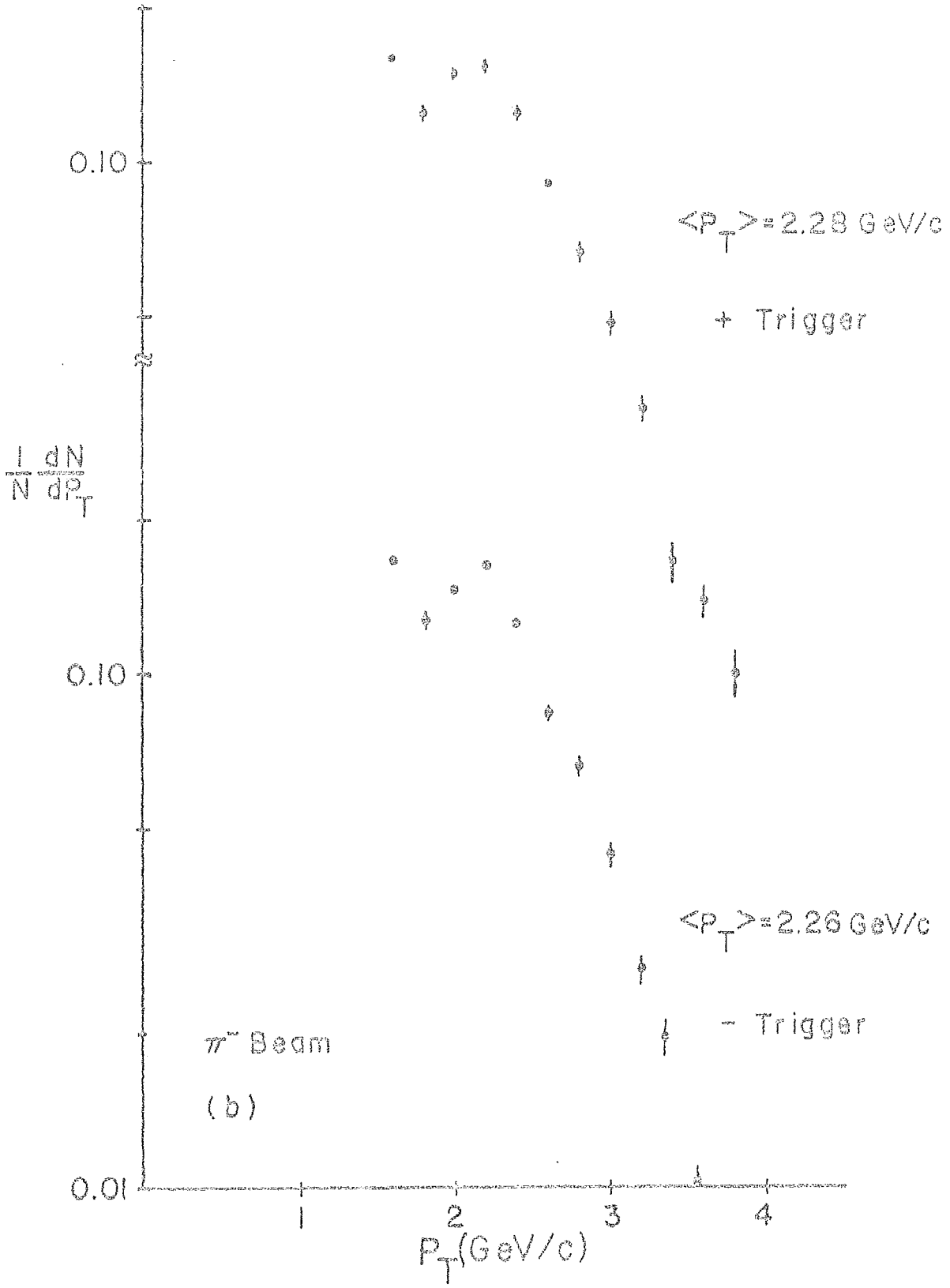
0.10
0.10
0.01
$\frac{1}{N}\frac{dN}{dP_T}$
$\langle P_T \rangle = 2.28$ GeV/c
+ Trigger
$\langle P_T \rangle = 2.26$ GeV/c
- Trigger
π^- Beam
(b)
1
2
3
4
P_T(GeV/c)

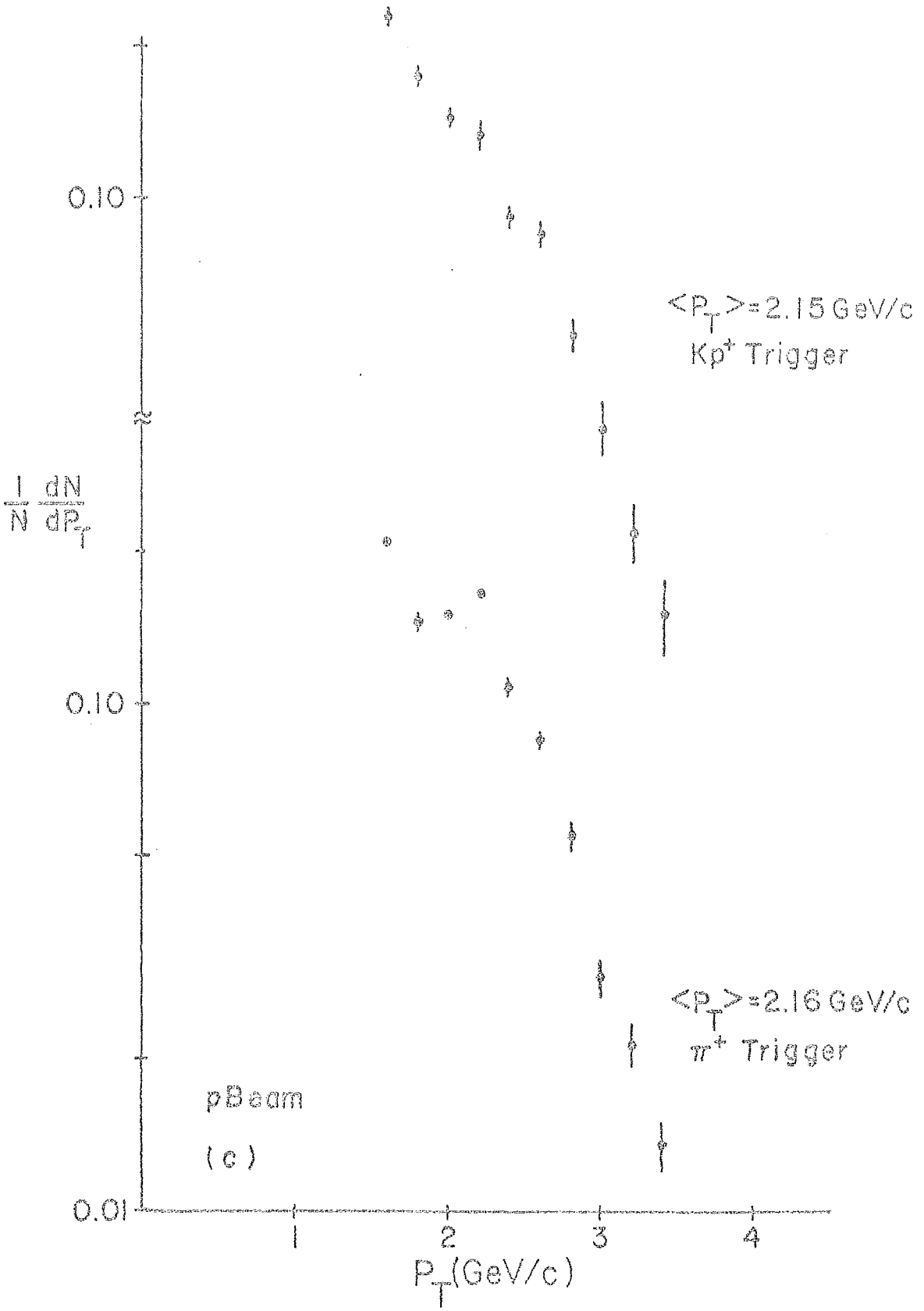
0.10
0.10
0.01
$\frac{1}{N}\frac{dN}{dP_T}$
$\langle P_T \rangle = 2.15$ GeV/c
Kp^+ Trigger
$\langle P_T \rangle = 2.16$ GeV/c
π^+ Trigger
pBeam
(c)
1
2
3
4
P_T(GeV/c)

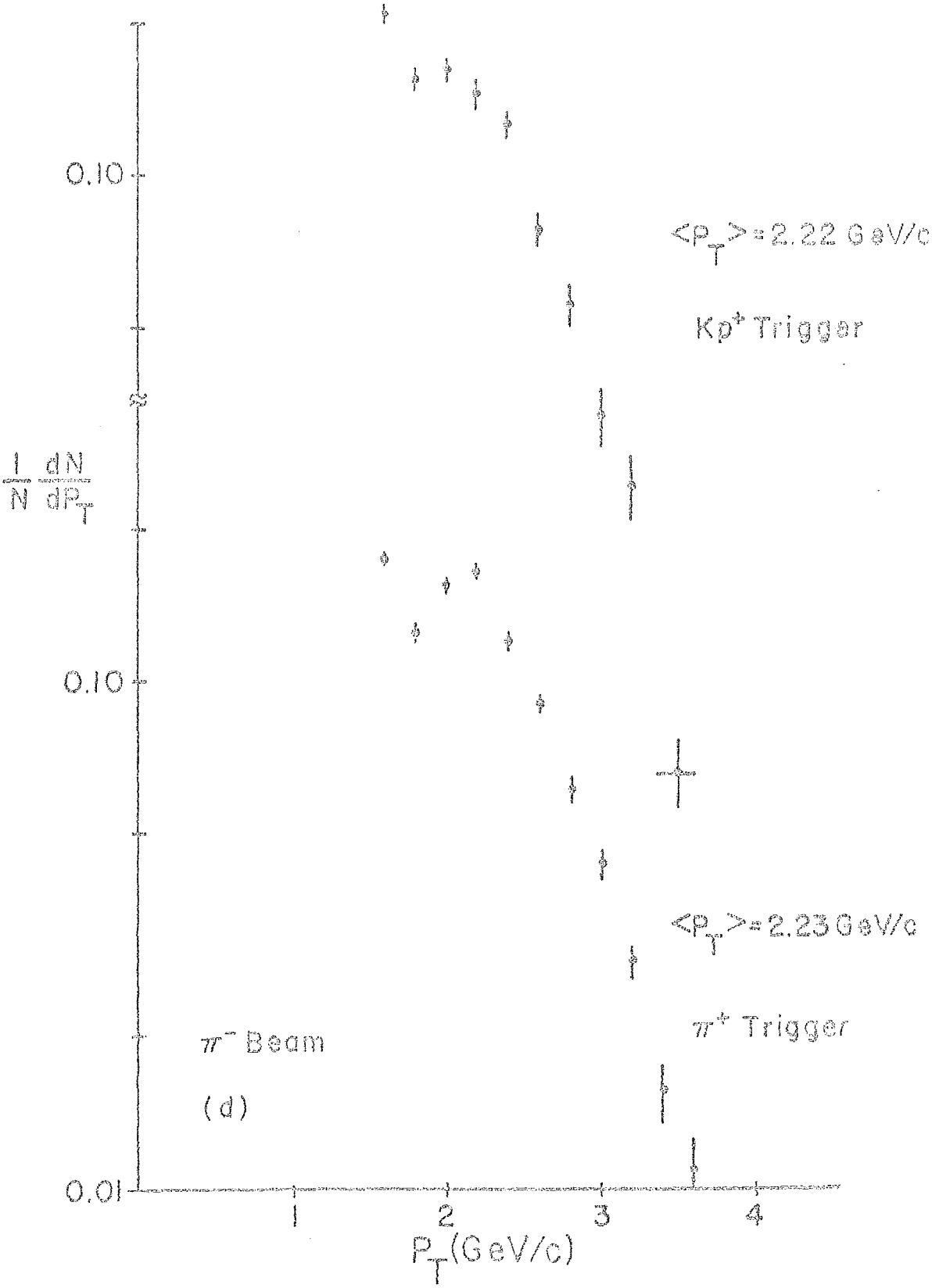
0.10
0.10
0.01
$\frac{1}{N}\frac{dN}{dP_T}$
$\langle P_T \rangle = 2.22$ GeV/c
Kp^+ Trigger
$\langle P_T \rangle = 2.23$ GeV/c
π^+ Trigger
π^- Beam
(d)
1
2
3
4
P_T(GeV/c)

of x_{eMIN} as shown in Figure 4.9 for π^+, p and π^- beams. R and x_{eMIN} are defined by

$$R_a(h) = \frac{\sum_{runs} \sum_{x_e \geq x_{eMIN}} n^+_{a\to h}(x_e)}{\sum_{runs} \sum_{x_e \geq x_{eMIN}} n^-_{a\to h}(x_e)} \qquad (4.5)$$

where $n^+_{a\to h}(x_e)$ is the number of charged hadrons with fraction x_e of the trigger's momentum produced in the reaction $ap \to hX$. For equal amounts of positives and negatives $R(h) = 1$. From the figures we see that for all beams there is a noticeable charge dependent effect - triggering on a negative particle enhances the probability of finding a positive particle opposite to it. With the positive trigger both the π^+ and p beams show about twice as many positives as negatives at high x_e while for the π^- beam there are about the same number of positives as negatives. With a negative trigger $R(h^-)$ does not have as strong an x_e dependence as does $R(h^+)$. For both the positive beams the away positives are only about 20 - 40% greater than the negative away hadrons whereas the negatives dominate the positives by 20 - 40% in the π^- beam. Clearly the away side with a π^- beam is different from either π^+ or p beam. But there is also a difference between the p and π^+ beams. For either trigger charge there seems to be a systematic trend showing $R_{\pi^+}(h) < R_p(h)$, i.e., there are always more positive particles around than negatives for the p beam compared to the π^+ beam. Since the average inelastic multiplicity for either beam is roughly the same[38] a simple charge conservation argument for some of these effects may possibly be ruled out.

If we can take the liberty of comparing experiments which investigate different kinematic regions, particularly s and x_T, we will compare our data for $R_p(h^+)$ and $R_p(h^-)$ with that of CCHK, BFS, and E494. A summary of the results from these groups is contained in

Figure 4.9 The away side ratio of positive hadrons to negative hadrons opposite a charged trigger particle produced by beam a, $R_a(h^{\pm})$, as a function of x_{eMIN}; (a) $R_{\pi^+}(h^+)$, (b) $R_{\pi^+}(h^-)$, (c) $R_p(h^+)$, (d) $R_p(h^-)$, (e) $R_{\pi^-}(h^+)$, and (f) $R_{\pi^-}(h^-)$. The arrows shown indicate the values of R that the simple charge conservation model discussed in the text predicts.

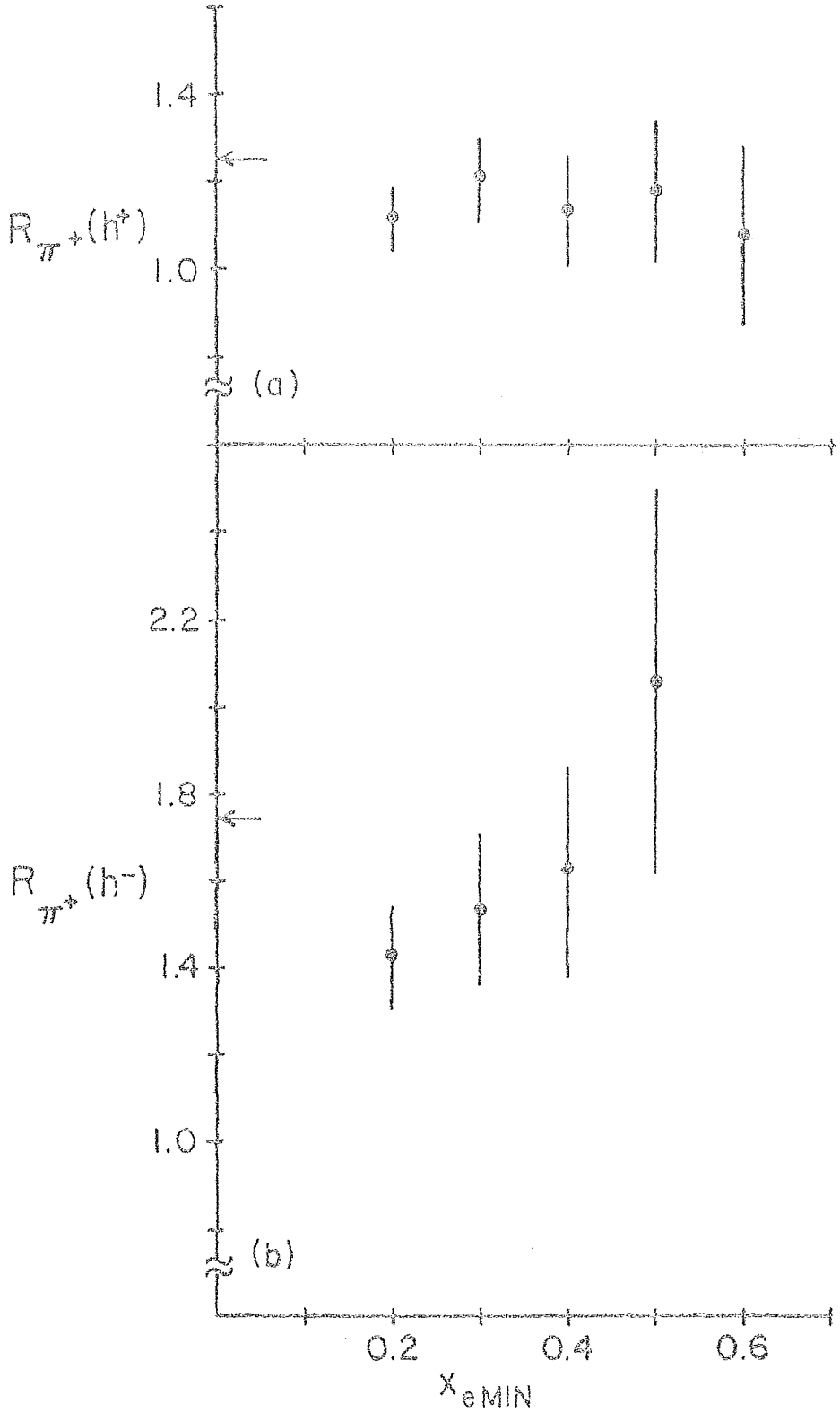
1.4
1.0
$R_{\pi^+}(h^+)$
(a)
2.2
1.8
1.4
1.0
$R_{\pi^+}(h^-)$
(b)
0.2
0.4
0.6
x_{eMIN}

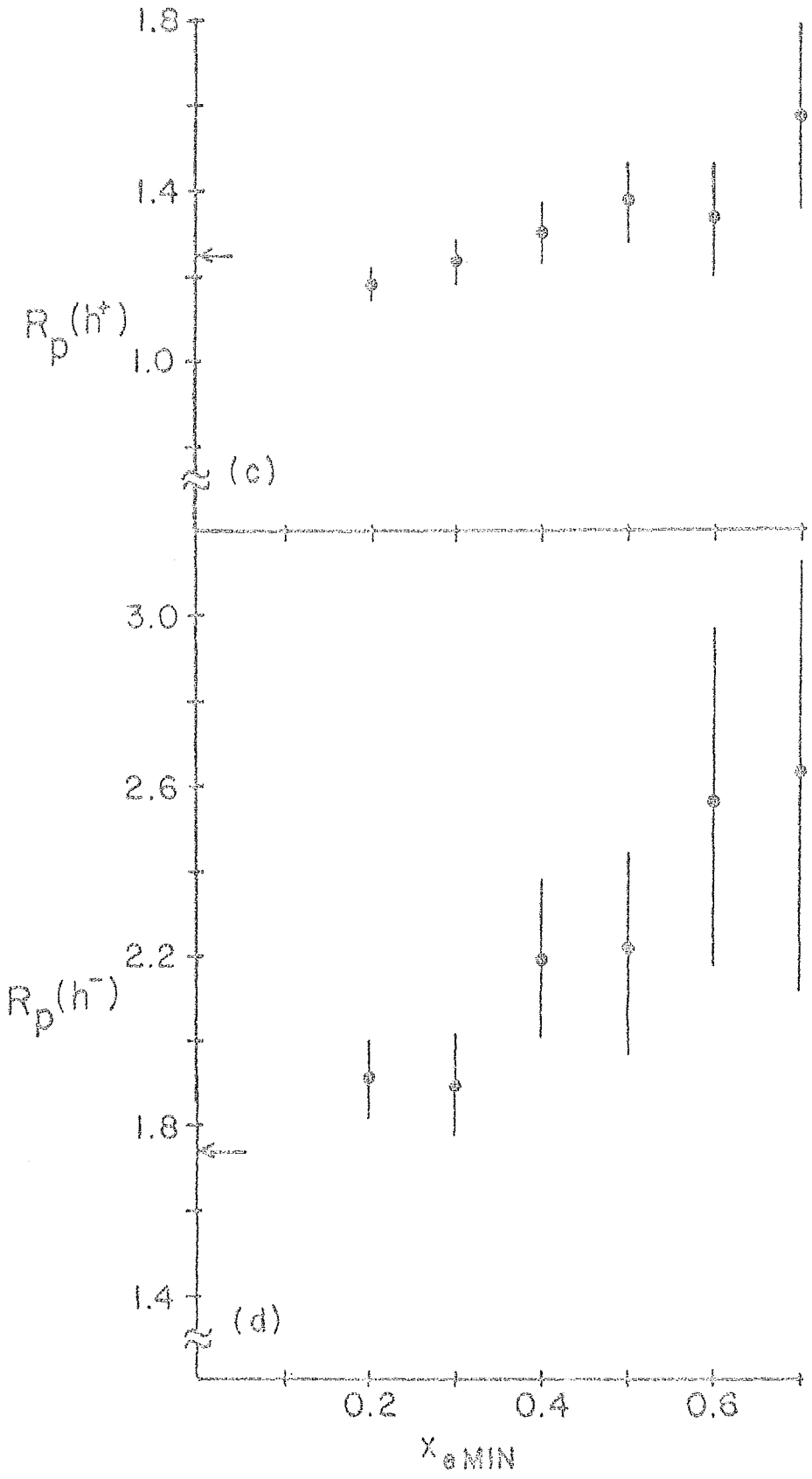
1.8
1.4
1.0
$R_p(h^+)$
(c)
3.0
2.6
2.2
1.8
1.4
$R_p(h^-)$
(d)
0.2
0.4
0.6
$X_{\theta MIN}$

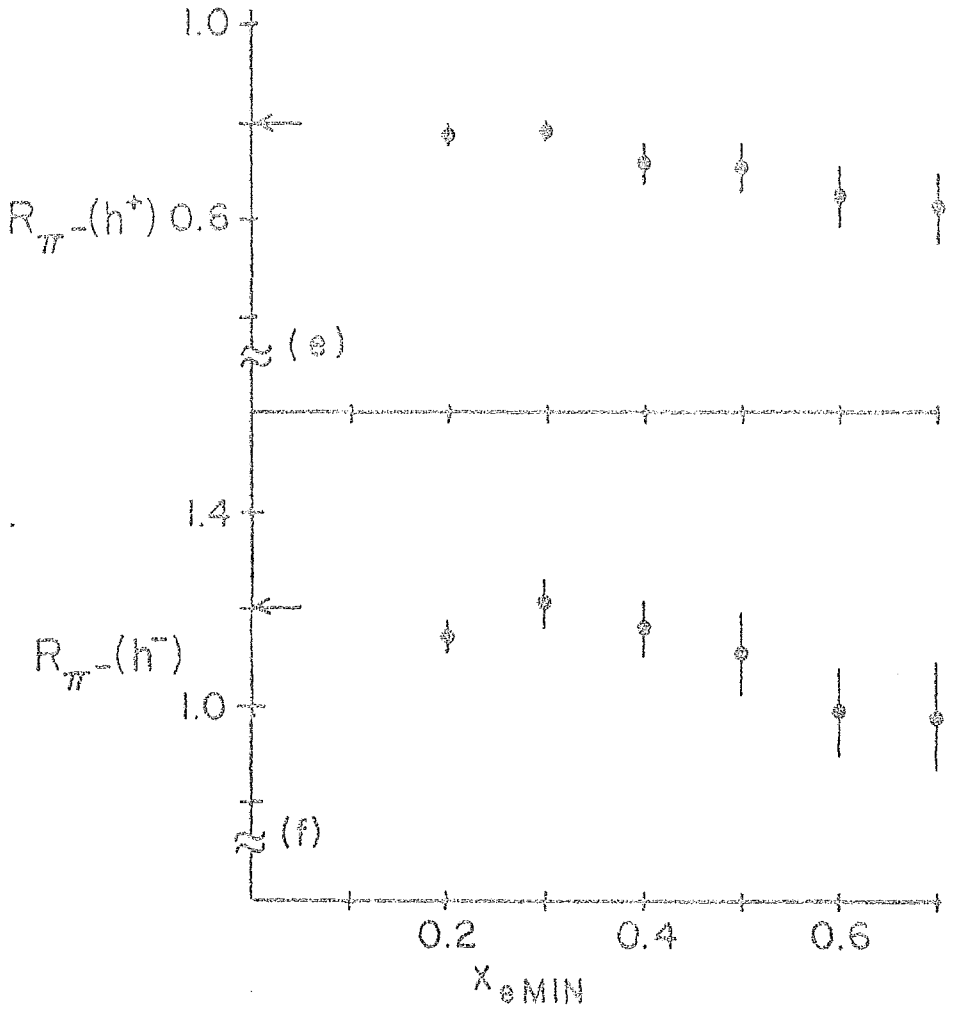
1.0
$R_{\pi^-}(h^+)$ 0.6
(e)
1.4
$R_{\pi^-}(h^-)$
1.0
(f)
0.2
0.4
0.6
$X_{e\,MIN}$

Chapter I while Table 1.1 lists the various kinematic regions explo
Shown on Figure 4.10 is $R_p(h)$ versus x_{eMIN} for the various groups.
For E260 and CCHK h is a charged hadron while for BFS and E494 h is
pion only.

From the figure we see that, for the positive trigger, there i
excellent agreement throughout the x_e range between our data and th
other experiments. However, it seems that our data for $R_p(h^-)$ is
considerably higher than that from BFS and E494. But the E494 data
is from pBe collisions and it is not inconceivable that the proton
scattering from the Be neutrons will tend to produce fewer positive
particles. Therefore we may expect the E494 data to be lower than
data from pp collisions. The later BFS data agree to within 15% of
our value of $R_p(h^-)$ but the earlier BFS data for $R_p(\pi^-)$ is about
twice as low as our data. $R_p(Kp^-)$ from early BFS is only 20% highe
than our data so that, considering the differences in away-side def
nitions, we will be bold and say that we are consistent with all pr
vious experiments except the earlier BFS and we believe, in the lig
of their later analysis, that the earlier result may have been wron

A charge conservation argument can be applied to the result th
the positive to negative charge ratio on the away side increases if
we trigger on a negative particle as discussed above. Let us first
consider the total charge in the event. Let i be the total initial
charge. For a positive beam i = 2 and for a negative beam i = 0. In
any event the number of positive and negative particles, n_+ and n_-
are related by

$$n_+ - n_- = i \qquad (4.6)$$

but if we now selectively remove one of the positive particles - th
trigger particle - and ask what is the relation between the rest of

Figure 4.10 The away side charge ratios for p induced triggers; (a) $R_p(h^+)$, and (b) $R_p(h^-)$. Shown is the E260 and CCHK data for h a charged hadron and the BFS and E494 data for h as a pion. Recall that E494 used a Be target while the other experiments used p targets.

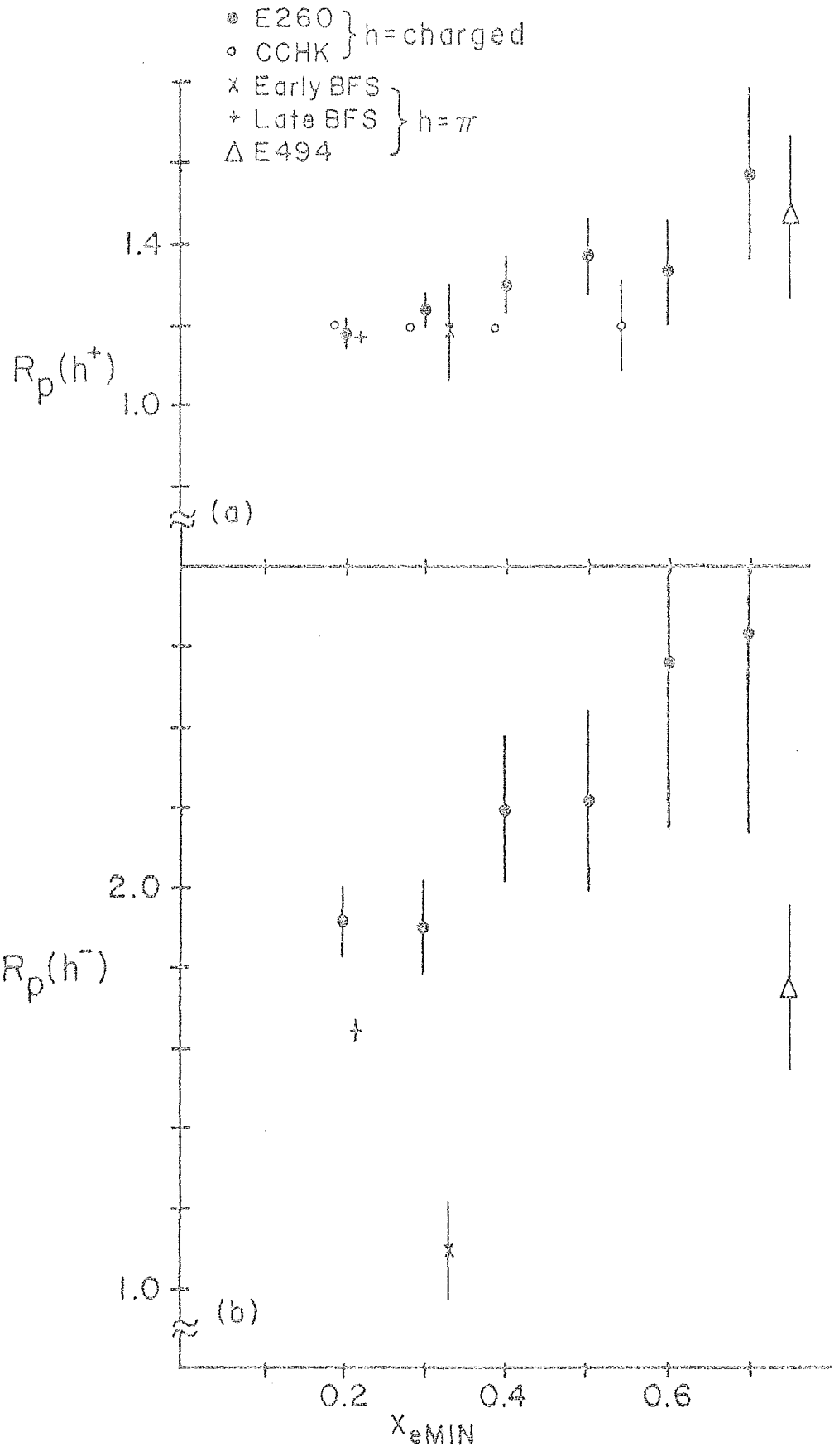
E260
CCHK
h = charged
Early BFS
Late BFS
h = π
Δ E494
$R_p(h^+)$
$R_p(h^-)$
1.4
1.0
2.0
1.0
(a)
(b)
0.2
0.4
0.6
X_{eMIN}

particles, we can write

$$\left.\frac{n_+}{n_-}\right|_{+trig} = 1 + \frac{i-1}{n_-} \qquad (4.7)$$

Similarly for a negative trigger particle

$$\left.\frac{n_+}{n_-}\right|_{-trig} = 1 + \frac{i+1}{n_-} \qquad (4.8)$$

For a charged multiplicity of 10^{26}, for a positive beam we find

$$\left.\frac{n_+}{n_-}\right|_{+trig} = 1.25$$

$$\left.\frac{n_+}{n_-}\right|_{-trig} = 1.75$$

and for a negative beam

$$\left.\frac{n_+}{n_-}\right|_{+trig} = 0.8$$

$$\left.\frac{n_+}{n_-}\right|_{-trig} = 1.2$$

If we argue that the ratio of positive to negative hadrons of the a
side is indicative of the charged multiplicity everywhere, then the
ratios in Figure 4.9 should correspond to those calculated above. T
ratios in Figure 4.9 seem to approach these values at low x_e where
fact we expect to be sampling the total charged multiplicity. But a
$x_e \to 1$ the data are inconsistent with the charge conservation model
although the qualitative difference between a positive and negative
trigger is predicted. It should be kept in mind that some of these

effects that we see may in fact be charge conservation and a detailed Monte Carlo may shed light on this aspect. But we will show in the next chapter how the values of R(h) may be connected to quark models and the effect the initial quark states have on it. However, it may be necessary to look at very high values of x_e to unambiguously determine quark effects. Unfortunately, we are limited by statistics beyond x_e about 0.6.

A trade-off between reasonable statistics and high x_e prompts us to choose $x_{eMIN} = 0.4$. According to Figure 4.9, within statistical errors, R(h) is not drastically varying for $x_e \geq 0.4$. Furthermore, for $x_e \geq 0.4$ the remaining diffractive background for p_T's $\geq$ 0.4 x 1.5 GeV/c is < 15%. Figures 4.11a through 4.11c show $R_{\pi^+}(h)$, $R_p(h)$ and $R_{\pi^-}(h)$ respectively and the trigger particle h is further classified as $\pi^{\pm}$ and $Kp^{\pm}$. The trigger particle identification is as described in Section 3.5; however the corrections described in Section 3.7, especially Cl efficiency and π-K contamination, cannot be applied. These corrections will not affect the quality of the away side data but merely the quantity. They are important in determining relative amounts of different trigger particles but in any given event we cannot tell whether we have Kp or inefficient π as the trigger. Therefore, in looking at the away side as a function of a specific type of trigger particle we have to understand that there is a certain π contamination to the Kp sample according to how the specific cuts were made. These are all discussed in Chapter III. From Figure 4.11 we see that for both pion beams the away side shows no dependence on the trigger particle outside of the charge dependence already mentioned above. Both π and Kp triggers yield the same away side charge ratios as long as both trigger species have the same charge. For p induced events, Figure 4.11c shows that

Figure 4.11 The away side charge ratios opposite a trigger identified as $\pi^{\pm}$ or $Kp^{\pm}$; (a) $R_{\pi^+}(h)$, (b) $R_p(h)$, and (c) $R_{\pi^-}(h)$. The away side particles all have $x_e \geq 0.4$.

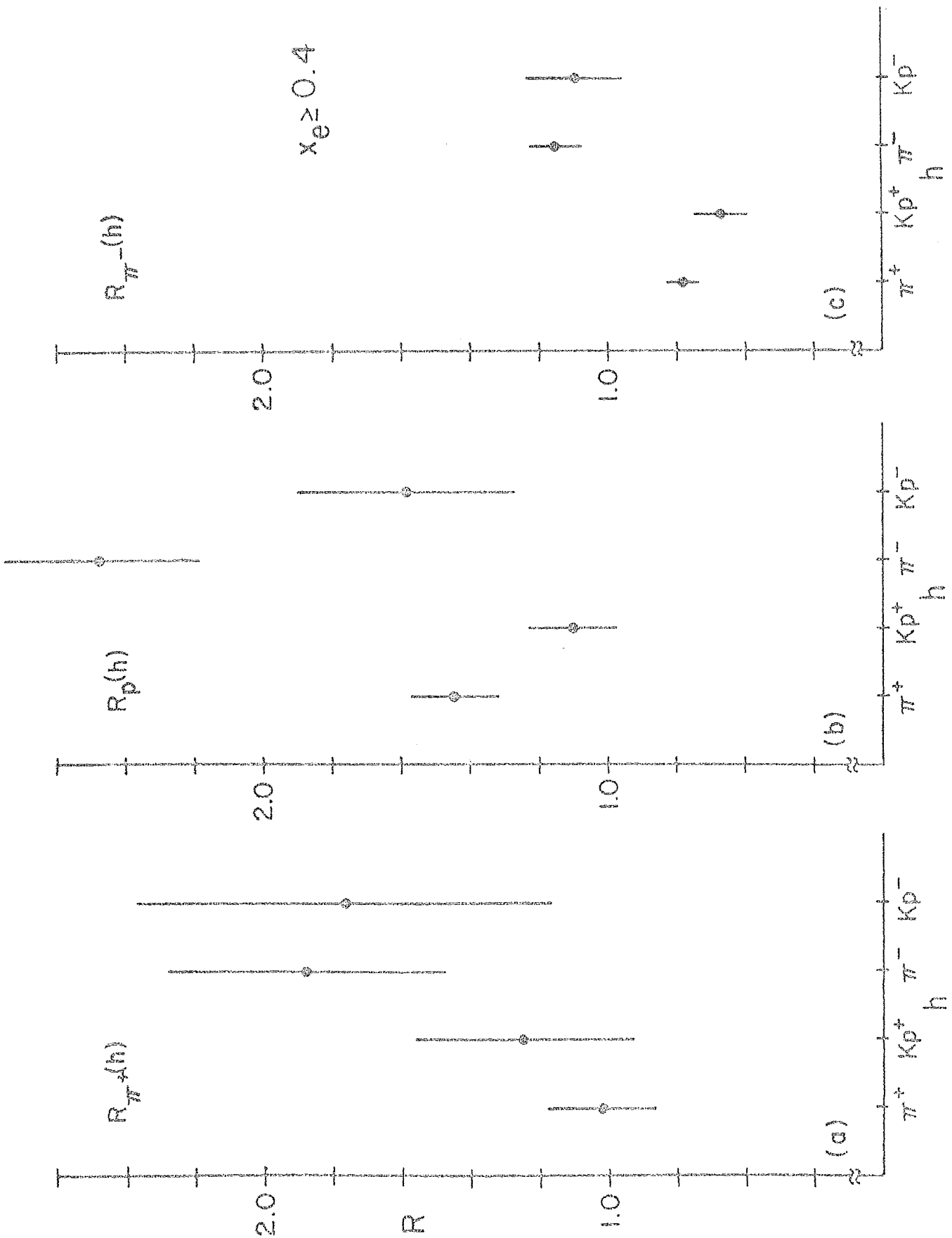
$R_{\pi^+}(h)$
$R_p(h)$
$R_{\pi^-}(h)$
$x_e \geq 0.4$
2.0
1.0
R
(a)
(b)
(c)
π^+ Kp^+ π^- Kp^-
h

$R_p(\pi)$ is unusually large compared with $R_p(Kp^-)$ and $R_p(\pi^+)$ is larger than $R_p(Kp^+)$. We point out that both of these effects differ from each other by roughly two standard deviations. The statistical sig nificance of the data can still be questioned. But in comparing our data to the BFS group mentioned in Chapter I, the excess positive charge (or depletion of negative charge) opposite a Kp^- is not seen We must remember that, according to Table 1.1, both experiments ove lap different kinematic regions and comparisons of data may not be meaningful.

CHAPTER V

CONCLUSIONS

In this concluding chapter we will compare the data to the various hard scattering models that predict the behavior of the events with a high p_T particle. Features of the Quantum Chromodynamics (QCD) models of Feynman, Field and Fox[18] and the Constituent Interchange Model (CIM) of Brodsky, Blankenbecler and Gunion[39] will be discussed. Trigger particle ratios for various beams and triggers will be looked at for both models. The away side spectra, again as a function of trigger and beam, will also be investigated in these theories. The correlation data that we have presented in Chapter IV is unique input to these models due to the fact that, one, beams other than p beams are used and, two, the data is in a different kinematic region not yet investigated at the ISR or at Fermilab.

It will not be our intention here to dwell on the fine points of either the QCD model or the CIM model. Many fine review articles exist for the CIM model[40,42] and the reader is referred to the original Field - Feynman paper for quark scattering[5] and an earlier paper by Ellis and Kislinger[4] for an excellent introduction to the QCD approach. We will strive to point out salient features that are necessary to develop an understanding of how the basic constituents in the initial and final state will influence the structure of the event. Most elements of both theories involve complicated Monte Carlo programs to facilitate the evaluation of integrals. Therefore, except for a few specific cases, only qualitative predictions can be made. Because of this, theoretical predictions have been made for only a few specific reactions which may not overlap our data. Therefore, comparisons to our data may be very crude. For example, we may have

to use predictions for a π^0 trigger instead of a $\pi^{\pm}$ or a trigger wi p_T = 4 GeV/c instead of 2 GeV/c. For much of the data we present, the theories are practically untested so that, in many cases, compa sons will indicate only general trends or model differences and not specific predictions.

5.1 High p_T Scattering and the QCD Model

The pioneering work of Bjorken and Paschos[2] on deep inelastic lepton scattering, ep → eX at large momentum transfers, showed that the proton can be interpreted to a very good approximation as consisting of a large number of pointlike entities - partons - each carrying a fraction of the proton's momentum. If the scattered lepton is detected at a fixed CMS angle, θ^*, the Bjorken parton model predicts the cross section to vary as

$$\frac{d\sigma}{dp_T^2} \sim p_T^{-4} F(x_T) \qquad (5.1)$$

where x_T, we recall, is $2p_T/\sqrt{s}$. The generalization of this results from the parton model to high p_T hadron-hadron scattering[3] and the subsequent discovery at the ISR[1] that the high p_T π^0 cross section varied as $p_T^{-N} f(x_T, \theta^*)$ argues persuasively for a constituent picture of the proton and that the dynamics of high p_T scattering should follow the laws of the parton model.

The parton model, or after later refinements the QCD model, is typified in Figure 5.1. For the hadron reaction AB → CX, constituen a and b from the initial hadrons A and B scatter elastically with an amplitude $\frac{d\hat{\sigma}}{dt}(ab \to cd)$ into constituents c and d. Constituents c the decays into the observed high p_T hadron C. In the CMS c and d have transverse momentum $x_b \frac{\sqrt{s}}{2}$ and $x_a \frac{\sqrt{s}}{2}$ respectively, so that when constituent c has $x_T \to 1$, x_a or x_b also approaches 1. The constituents in the QCD model may either be valence quarks, sea quarks or gluons

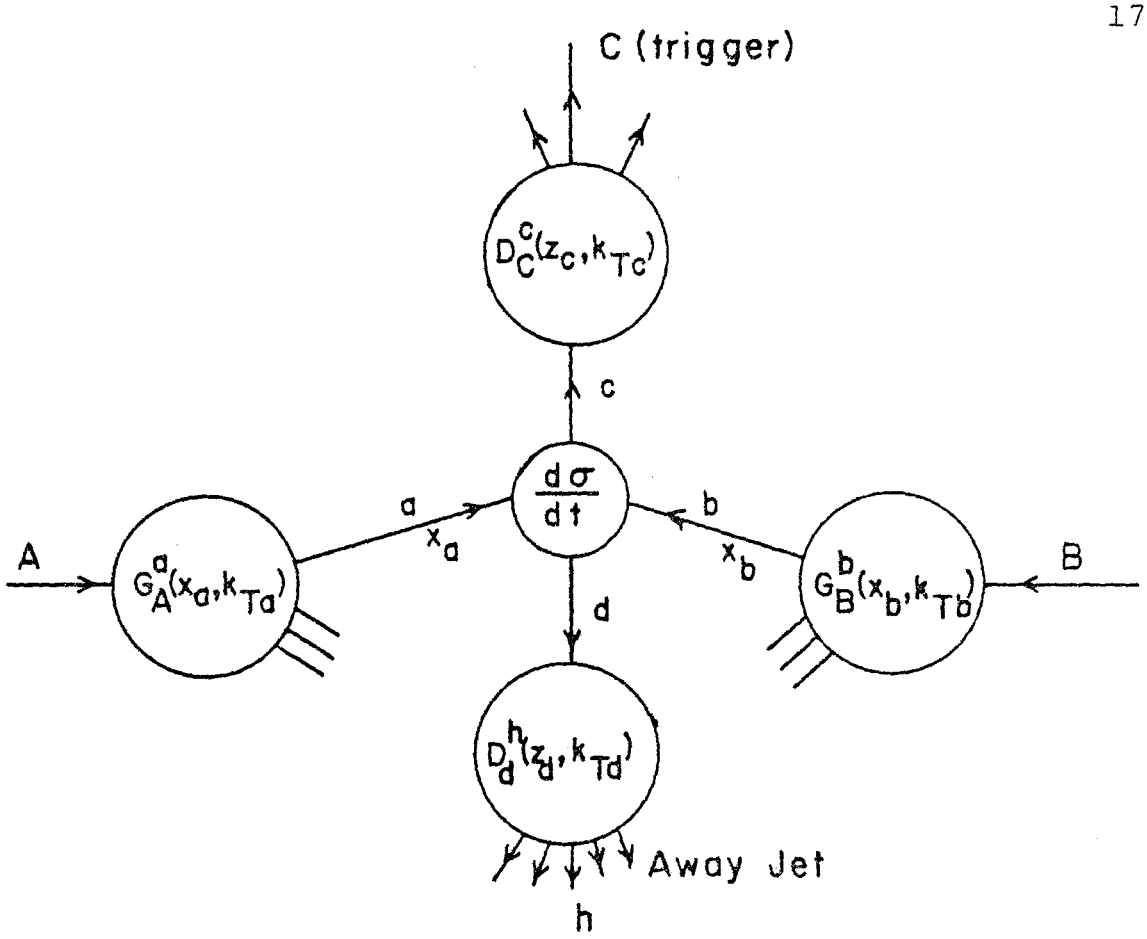

Figure 5.1 Schematic of the underlying structure of high p_T scattering for AB → CX. The high p_T trigger, C, results from the large angle scattering of the constituents (ab → cd), followed by the decay of constituent c into the trigger hadron and some associated hadrons. Constituent d fragments into the away side hadrons. x_a and x_b are the fraction of the incoming hadrons A and B momentum while k_{Ta} and k_{Tb} are the transverse momentum of constituents a and b. z_c and z_d are the fraction of the constituents c and d momentum carried by the hadrons C and h.

and may possess an intrinsic internal transverse momentum k_T. The production rate for particle C is governed by the constituent scattering amplitude, $\frac{d\hat{\sigma}}{dt}(ab \to cd)$, and by the probabilities that A will fragment into a with fraction of A's momentum x_a, $G_A^a(x_a)$, B will fragment into b with fraction of B's momentum x_b, $G_B^b(x_b)$, and that constituent c will have a particle C as one of its decay hadrons whose momentum is a fraction z_c of the constituents c's, $D_c^C(z_c)$. Since we do not select x_a and x_b, a convolution integral of these four terms over x_a and x_b is done to finally obtain the cross secti

$$E\frac{d^3\sigma}{dp^3}(AB \to CX) = \int d^2k_{Ta} d^2k_{Tb} d^2k_{Tc} \int dx_a dx_b G_A^a(x_a,k_{Ta}) G_B^b(x_b,k_{Tb}) \cdot$$

$$\frac{1}{\pi z_c} \frac{d\hat{\sigma}}{dt}(ab \to cd)\ D_c^C(z_c,k_{Tc}) \qquad (5.2)$$

We have indicated in the G and D functions an explicit k_T dependence of the constituents inside the hadrons. Again, since we do not choo the particular k_T's, an integral over them is performed in Eq. 5.2 t obtain the cross section.

Finally, an important aspect of the QCD model is that constitue d opposite the trigger particle will decay into hadrons essentially independently of how C was created. The catch work here - essentiall means that the particle C may be preferentially created by a certair combination of the types of a + b in the initial state. For example in $K^+p \to K^+X$, the high p_T K^+ may be preferentially formed by the scattering of a u quark from the proton with an $\bar{s}$ from the initial K which subsequently fragments into the trigger. Thus the constituent fragmenting into the away hadrons is less likely to be an $\bar{s}$ than in, say, $K^+p \to \pi^+X$ where the π^+ is likely to be produced from a fragment u quark from either K^+ or the p. This, as we will indicate, is the

only source of trigger side-away side quantum correlations in the QCD model.

Much debate has gone into what the underlying scattering amplitude is. Analagous to single photon exchange at the abcd vertex in Figure 5.1, the simple parton model with a single gluon exchange predicts a p_T^{-4} behavior of the cross section whereas p_T^{-8} is observed. Instead of disregarding the parton model completely at this stage, Field and Feynman (FF) in an early parameterization of the QCD model[5] took the point of view that the amplitude was an unknown and therefore an ad hoc choice for $\frac{d\hat{\sigma}}{d\hat{t}}$ to fit the p_T spectrum was devised. Quarks were assumed to be the constituents and the G and D functions discussed above were derived from deep inelastic scattering from neutrons and protons. With these functions determined, the parton model with the FF quark scattering amplitude successfully predicted cross sections and particle ratios. Although a later refinement of this model[17] recognized the importance of internal transverse momentum of the quarks, the away side multiplicities were incorrectly predicted. The possibility now exists that QCD field theory, coupled with gluons also as scattering constituents, provide the full explanation of all high energy p_T experimental results. We refer the reader to the literature for further details[18,43]. We just note here that quarks - valence and sea - and gluons are assumed to be the underlying constituents in the scattering mechanism and that the internal transverse momentum of the constituents is relatively high - $\langle k_T \rangle \simeq 850$ MeV/c. Baryon production in these theories has not yet been developed. Also to be pointed out is the fact that although QCD predicts results that are in closer agreement with the observed data, the original FF theories do not do a very bad job in most cases.

In the QCD model a constituent from hadron A scatters off a con-

stituent of hadron B, which in our case is always a proton. One of these constituents then fragments into the trigger particle and the other into the away side particles. We want to ask how the trigger and away side are correlated with each other and with hadron A. Table 5.1 lists the valence quark content of various initial states. For later reference we also list the average quark charge of the initial states, <Q>, and the positive to negative charge ratio of integrally charged hadrons, R, needed to construct this average char R can be written

$$R = \frac{1 + \langle Q \rangle}{1 - \langle Q \rangle} \tag{5.3}$$

Which of the initial state quarks listed in Table 5.1 will enter int the scattering process is determined by the $G_A^q(x_T)$ and $G_p^q(x_T)$ functions. Using the existing data on deep inelastic scattering, electron-positron annihilation and high p_T hadron collisions, FF have determined the quark distributions inside nucleons and pions; these are shown in Figures 5.2a and 5.2b respectively. The gluon distributions are determined from later QCD calculations. We will not go into detail here but will only summarize the pertinent results. (1) Valence quarks dominate over sea quarks especially at $x \gtrsim 0.2$. For $x \gtrsim 0.2$, gluons and valence quarks have about equal probability for entering the scattering. (2) At large x the u quarks dominate over the d quarks in the proton. The ratio $G_p^d(x)/G_p^u(x)$ behaves as (1-x). (3) At all x, it is equally likely that either valence quark in the pion will enter into the scattering. The probability for finding a quark at high x in a pion is approximately constant as opposed to the $(1-x)^n$ behavior in a nucleon. Thus, at high p_T, π induced cross sections are larger than p induced[26,44]. (4) Gluon distributions are not well known yet but are peaked at low x and become increasing

Initial State	Quark Content	<Q>	R
pp	uud + uud	1/3	2
$\pi^- p$	$\bar{u}d$ + uud	0	1
$\pi^+ p$	$u\bar{d}$ + uud	2/5	2.3
$K^- p$	$\bar{u}s$ + uud	0	1
$K^+ p$	$u\bar{s}$ + uud	2/5	2.3

Table 5.1 The valence quark content of various initial states. Also listed is the average initial state quark charge, <Q>, and the ratio of positive to negative hadrons, R, needed to form this average charge.

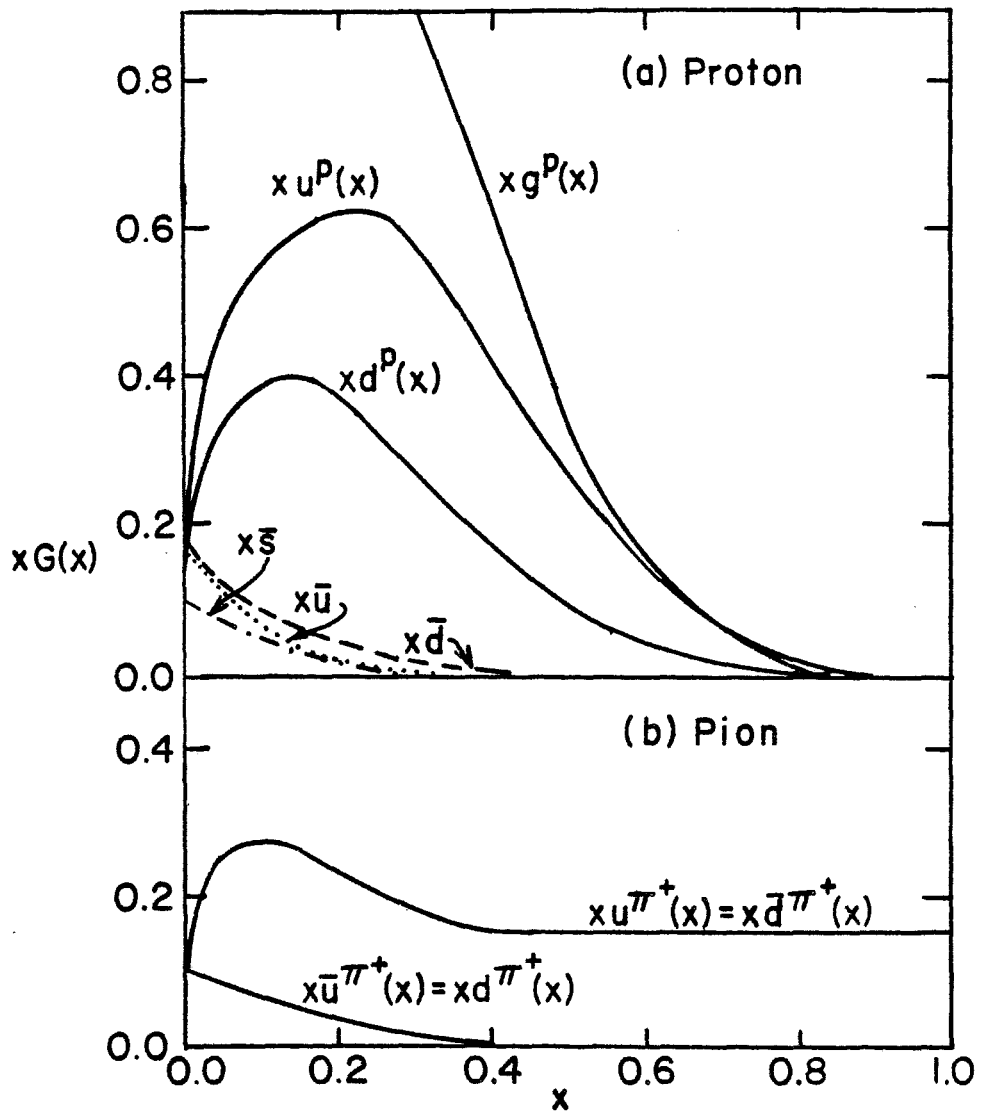

Figure 5.2 (a) Quark distributions within the proton. The distribution functions, $G_p^q(x)$, are labelled here as $q^p(x)$. At low x, sea quarks are non-negligible while at high x, the u quark dominates over the d quark. (b) Quark distributions within the pion. $G_{\pi^+}^q(x)$ is denoted as $q^{\pi^+}(x)$. The probability of seeing a valence quark at large x is non-zero.

important at very high p_T's and very high s.[18] We expect that gluons may noticeably enter into the scattering at $x_T \lesssim 0.4$ and may be non-negligible even for $x_T \lesssim 0.8$.

The fragmentation of the two constituents into the trigger particle and away particles is governed by $D_i^h(z)$ where i is a quark or gluon. Figure 5.3 shows the FF results for various quarks decaying into mesons and the QCD results for gluons decaying into a π^0. The most evident feature of these curves is that the constituents tend to fragment into several hadrons with low z. How then do we get one trigger particle? To understand the qualitative reasons let us refer to the FF approximation. According to Eq. 5.2 the single particle cross section is a function of $D(z)\cdot\frac{d\hat{\sigma}}{d\hat{t}}$. The falling spectrum of D(z) together with the rising spectrum (in z) of $\frac{d\hat{\sigma}}{d\hat{t}}$ results in the trigger particle having, on the average, 80 - 90% of the quark momentum. One of the constituents therefore decays into the trigger particle which has a high z. With the help of this basic information we can proceed to summarize the implications of the decay functions, $D_i^h(z)$. (1) Since $D_q^h(z)$ approaches a constant as $z \to 1$ and $D_g^h(z)$ approaches 0, trigger particles are produced more abundantly by quarks than by gluons. (2) Opposite the trigger particle there will be several low-z hadrons whose essence is determined by the initial state constituents. (3) u-quarks decay more readily into positive mesons than negative and into π's more readily than K's. Similarly, d-quarks decay preferentially into negative hadrons. A positive trigger is most likely to come from a u, $\bar{d}$, or $\bar{s}$ quark and a negative trigger from a d, s, or $\bar{u}$. Gluons produce an equal number of positive and negative hadrons.

With the properties of the probability functions qualitatively understood we will, in Section 5.3, turn to specific QCD predictions

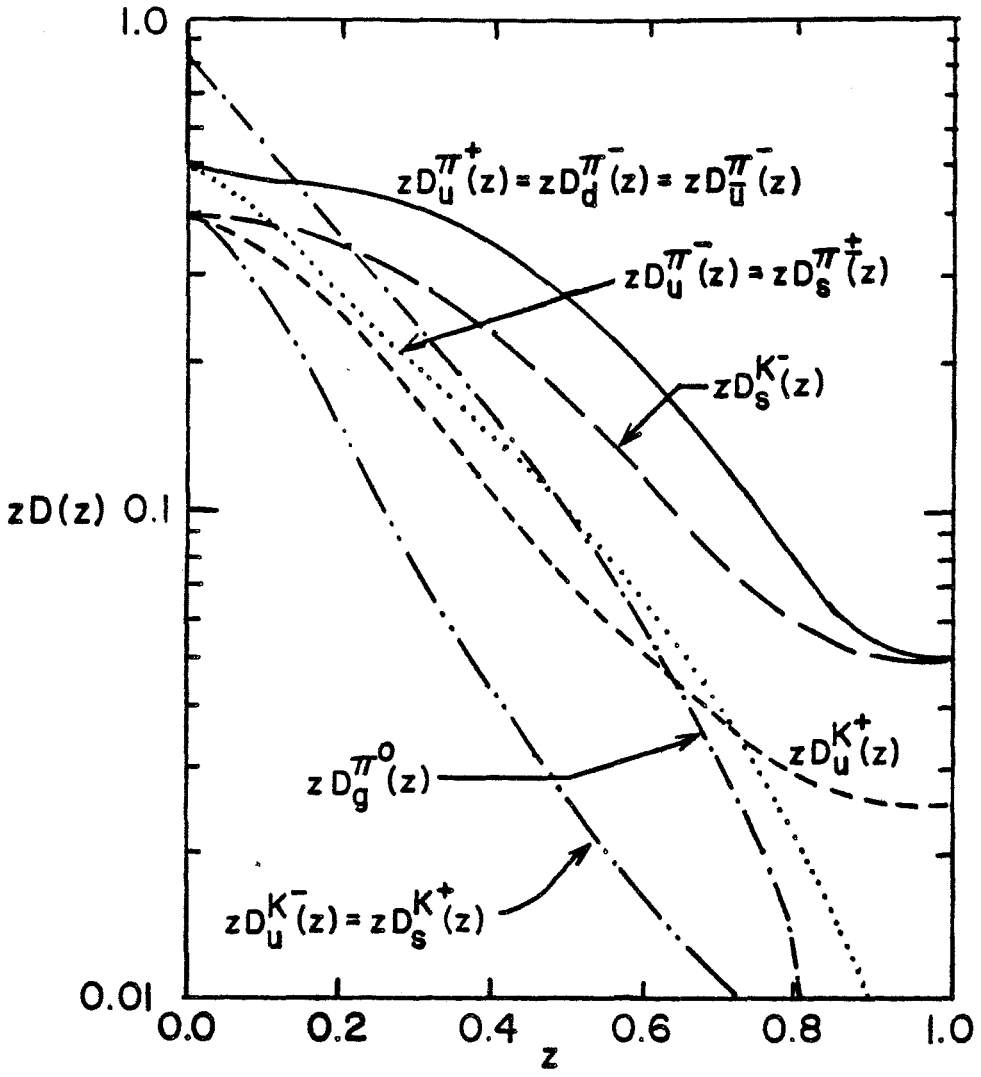

Figure 5.3 Decay functions for quarks into mesons and for gluons into π^0's. Mesons with high z are likely to come from quarks while at low z, mesons can come from decaying gluons as well as quarks. (The data for the gluon decay function is taken from Ref. 18 with Q^2 = 4 Gev^2.)

of the trigger and away side. We have not discussed the consequences of the large Fermi motion of the quarks inside the hadrons which result in a large quark internal transverse momentum. These effects will be specifically pointed out as we discuss the trigger and away sides. Before proceeding to the specific predictions we will discuss the general features of the CIM models.

5.2 High p_T Scattering and the CIM Models

The motivation for CIM is simple. Because the pion and kaon single particle cross sections vary as p_T^{-8}, dimensional counting rules[40] imply that there are six elementary fields participating in the underlying scattering process. Furthermore, the peripheral nature of $\frac{d\sigma}{d\hat{t}}$ ($\sim \hat{t}^{-3}$) arises in one-particle exchange models with the exchanged particle a spin-½ entity and not 0 or 1. Therefore quarks and not gluons must be exchanged. The possible exchanges that one can construct with quarks, anti-quarks, di-quarks and mesons are shown in Figure 5.4. Notice that the true CIM term is $qM \to qM$ as seen in Figure 5.4c but we will collectively refer to the models which exchange quarks as the CIM. These models have the nice feature that they predict reasonably well the p_T and x_T dependence of the cross sections. However there are problems with each individual scattering process in Figure 5.4[42,45] and, since each type of process is expected to exist at some level, we refer to the work of Chase and Stirling[45] (CS) who determine the various contributions of CIM, QF, and DQ terms by best fits of these processes to the existing cross sections and particle ratios.

The distribution of valence and sea quarks in protons and mesons used by CS are not the same distributions found by Field and Feynman although they are very similar. The distribution of mesons inside hadrons are taken as either bound $q\bar{q}$ pairs from the sea or a sea

quark bound with a valence quark. Excluded from the CS analysis are meson constituents which are formed from the two valence quarks within a pion or kaon. Thus the extra contribution from the direct scattering of π's from a proton quark in πp collisions, which does not exist in pp collisions, is neglected here.

Since the coupling of a quark to an anti-quark in QF (Figure 5.4a) is probably as large as the coupling of a quark to a quark in DQ (Figure 5.4b), a combination of DQ and QF diagrams can naturally be expected to coexists. Similarly, by crossing symmetry, the CIM term and the QF term have the same scattering amplitude. We expect that the CIM and QF terms also coexist. However, if the number of mesons in a hadron is negligible, then DQ + QF is expected to dominat and if the DQ mechanism is negligible in producing a meson of a particular type, then CIM + QF should be the dominant scattering mechanism. CS find "best" fits to each of these combinations and arrive at two combinations of the cross sections, referred to as $\frac{1}{3}$DQ + QF and $\frac{1}{2}$CIM + QF, either of which reasonably fit the existing particle ratios. In comparing the CS predictions to our data we will always use the $\frac{1}{2}$CIM + QF fit. It should be kept in mind that, as mentioned above, no one of the diagrams in Figure 5.4 will fit all the data.

With the specific of these theories understood we can now turn to the predictions these models make for the trigger side and away side correlations.

5.3 Model Predictions

a. QCD and the Trigger Side

We consider the ratios $\frac{d\sigma}{dp_T}(bp \to h^+X)/\frac{d\sigma}{dp_T}(bp \to h^-X)$, referred to as the h production ratio, with b as a pion, kaon, or proton and h as a charged, π or Kp trigger particle. We can understand the QCD mechanisms if we think simply in terms of the quark model and then

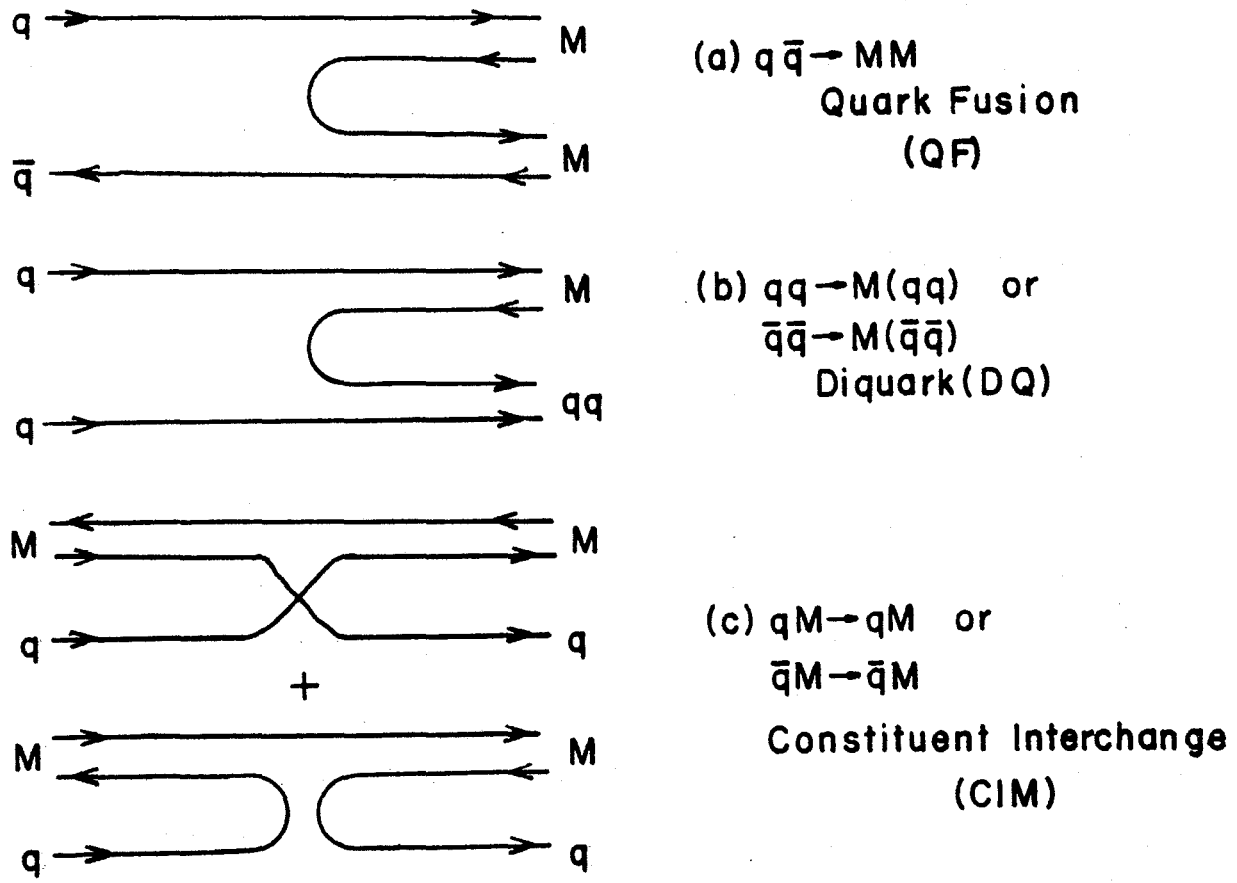

Figure 5.4 The elementary CIM subprocesses for (a) quark fusion, (b) diquark, and (c) constituent interchange.

refine our observations with the knowledge of the G and D functions discussed above. Table 5.1 lists the values of the average charge, <Q>, and the resulting ratio of positive to negative triggers, R, if we naively assumed that each quark in the initial state scattered and decayed with equal probability into the trigger. For the p beam the charged production ratio will then be expected to be around 2. But as $x_T \to 1$ the u quarks dominate in the proton and the positive to negative ratio should then become very large. Similarly, for $x_T \lesssim 0.3$, the ratio of u to d quark in the proton decreases somewhat and the charge production ratio should fall below 2. In comparing the data to the actual QCD predictions we have to be careful and remember that the theory does not include baryons. Definite predictions are made only for mesons. The inclusion of gluons as scattering constituents will lower the ratio predictions made without gluon because gluons produce positive and negative triggers equally. Figure 5.5 shows the results of the QCD calculations for the π production ratio compared to our pion data and our charged data. Within statistics the QCD predictions represent our data very well. It is also interesting to note that the naive expectations are seen in the charged data of Figure 5.5. At low x_T the production ratio for charged triggers is about 1.7, at $x_T \simeq 0.3$ it is 2 and increases as $x_T \to 1$. The charged production ratio is higher than the π productio ratio and seems to increase more rapidly than the pion ratio. This can also be understood in QCD by noting that K^- triggers are produce less frequently than π^- triggers by a u quark as seen in Figure 5.3. Therefore the K production ratio should be larger than, and increase more rapidly than, the π ratio. Thus, the charged production ratio, if assumed to measure only mesons and not baryons, should exhibit th increase over the π ratio as does our data. Notice also that a gluo

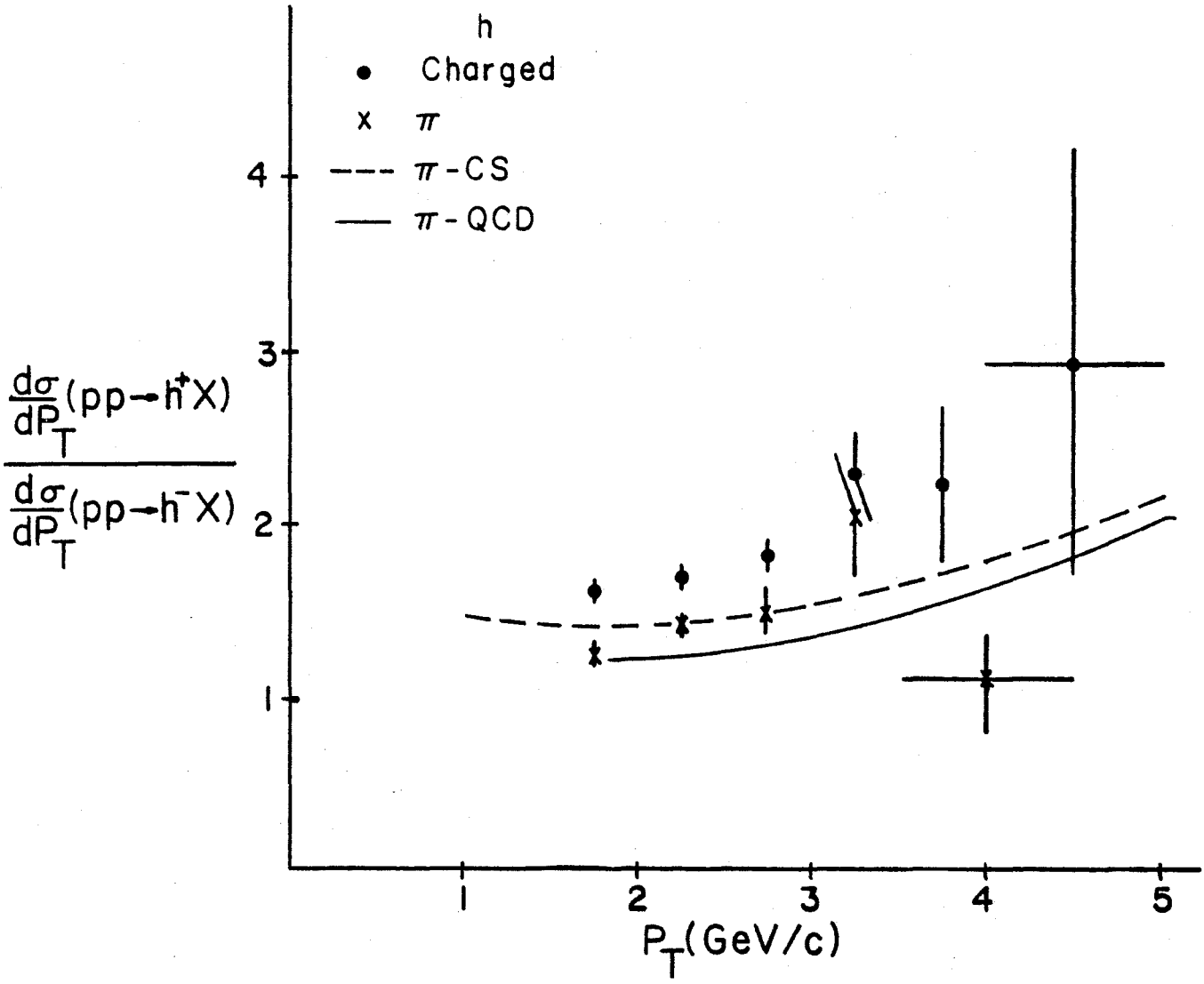

Figure 5.5 The pion and charged production ratios reproduced from Figures 3.18 and 3.20a. The predictions for π production are shown for the QCD model (solid line) and for the CS parameterization of the CIM models.

contribution at low x_T will result in a charge production ratio tha has a value less than the naive prediction of 2.

At 90^o both the beam and target play an equal role in determin the flavor of the quark fragmenting into the trigger. For both π^+ and π^- beams the valence quarks in the beam have an equal probabili of entering into the scattering. Thus, at low x_T where u quarks in the proton are about twice as abundant as d quarks, we naively expect the charged production ratio to be around 1 for a π^- beam and 2 for a π^+ beam. At higher x_T the d quark in the proton become a spectator and the production ratio should slowly increase for bot beams. No information on the quark distributions within kaons is known and we can only assume that the distribution in a K^- is analogous to the quarks in a π^- and that K^+ distributions are similar to π^+. Also, at this time there exists only the FF aproximation to th particle ratios for pion beams and not the full-blown QCD results. Figure 5.6a compares the FF π production ratio for a π^- beam with our results. Included on the figure for comparison is our data for the charged production ratio. Figure 5.6b compares our charged rat only for a π^+ beam with the slightly different π^+/π^- prediction of FF. The FF approximation does not include gluons so that QCD, with their inclusion, will predict a higher ratio for the π^- beam for $x_T \lesssim 0.3$ and a lower ratio than FF for the π^+ beam. In any case th QCD predictions agree with our π beam data very well and the data correspond nicely to what one would naively expect from the quark-parton model. Due to the fact that there are so many unknowns in this theory we cannot say in more detail what the particular influence of gluons, sea quarks, etc. may mean to the data. We leave a more precise theory and a better explanation of the data to the theorists.

Figure 5.6 (a) The ratio $\frac{d\sigma}{dp_T}(\pi^- p \to h^+ X)/\frac{d\sigma}{dp_T}(\pi^- p \to h^- X)$ for h a pion or a charge hadron. The data are compared to the QCD approximation of Field and Feynman and the CIM parameterization by Chase and Sterling.
(b) The ratio $\frac{d\sigma}{dp_T}(\pi^+ p \to h^+ X)/\frac{d\sigma}{dp_T}(\pi^+ p \to h^- X)$ for h a charged hadron. The FF and CS predictions for h as a pion are shown. The CS predictions are clearly in disagreement with the data while the FF model fits nicely.

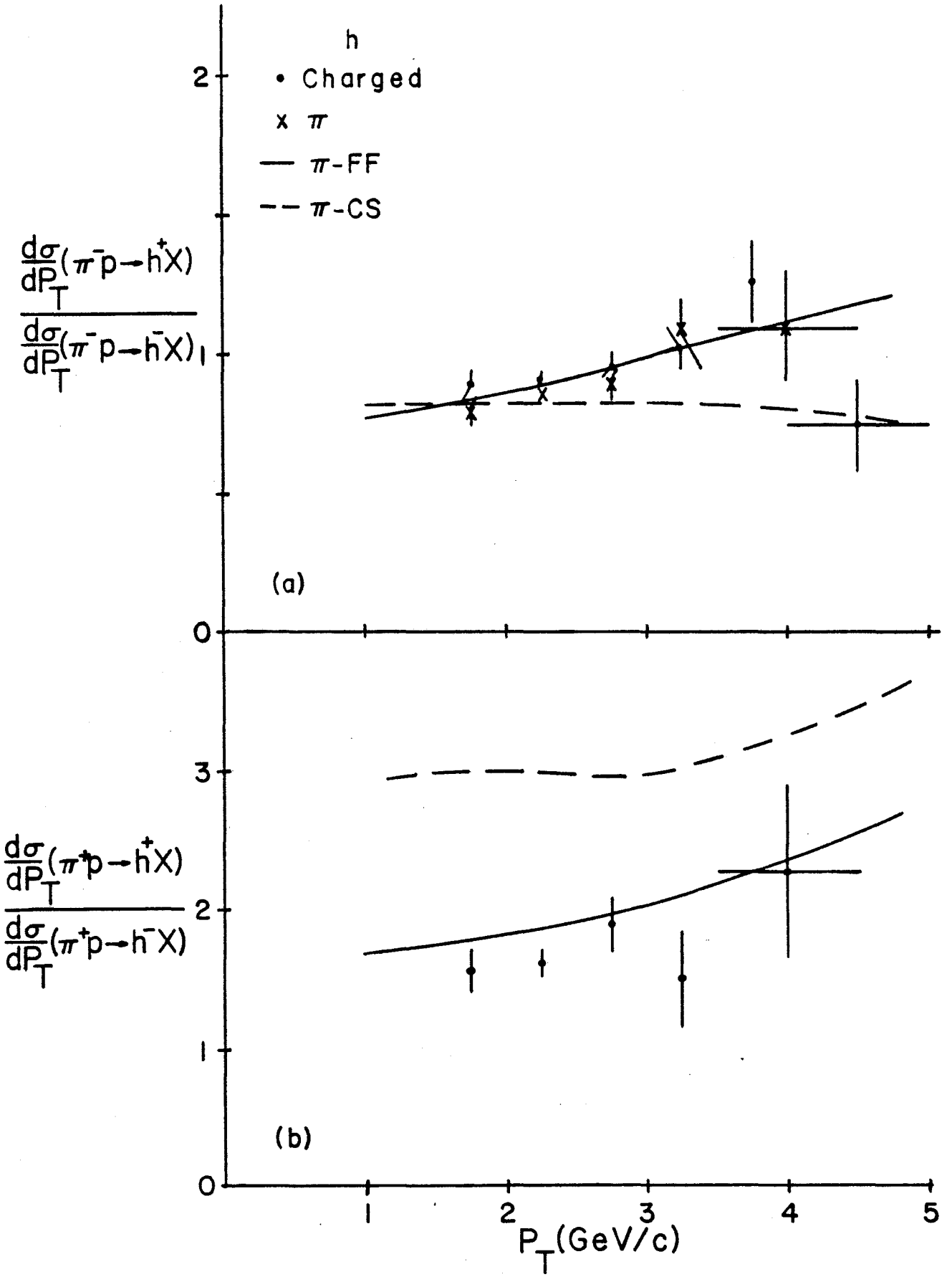
h
• Charged
x π
— π-FF
-- π-CS
$\frac{d\sigma}{dP_T}(\pi^- p \to h^+ X)$
$\frac{d\sigma}{dP_T}(\pi^- p \to h^- X)$
(a)
$\frac{d\sigma}{dP_T}(\pi^+ p \to h^+ X)$
$\frac{d\sigma}{dP_T}(\pi^+ p \to h^- X)$
(b)
0
1
2
3
4
5
P_T(GeV/c)

b. CIM and the Trigger Side

Because the fits for the CS parameterization of the CIM models was done using the existing particle ratios for pp collisions, we can expect that the CS predictions will fit our p beam data well. This is indeed the case as seen in Figure 5.5 where the CS prediction for $\frac{d\sigma}{dp_T}(pp \rightarrow \pi^+X)/\frac{d\sigma}{dp_T}(pp \rightarrow \pi^-X)$ is compared to our data and the QCD prediction. As we discuss the reasons why different terms of the CS parameterization work or do not work in explaining the data, it will be useful to refer to Figure 5.7 which shows the various subprocesses of QF and CIM for pp and πp collisions producing specific triggers.

The dominant contribution to CIM and DQ is valence quark-valence quark scattering with the trigger pion taking one of its valence quarks from the proton. See Figure 5.7a. Since $\pi^+ = u\bar{d}$ and $\pi^- = \bar{u}d$ the π^+/π^- ratio is proportional to the u/d ratio available in the protons. This varies as $(1-x)^{-1}$ and the π^+/π^- ratio for DQ and CIM rapidly rises as $x_T \rightarrow 1$. Since the proton has no valence anti-quark QF is dominated by valence quark-sea quark scattering. Selecting the antiquark of the trigger from the proton sea results in QF predicting the π production ratio to be ~1 throughout the entire x_T range. QF agrees with only the lowest p_T's of our data.

For pion beams, DQ has valence quark-valence quark scattering as the dominant contribution. A π^- beam can produce a π^+ trigger with the proton's two u quarks and a π^- trigger with either a proton d quark or the beam's d quark. Therefore π^- production is a little larger than π^+ production at low x_T but these become roughly equal at high x_T. The π^+ beam can produce a π^- trigger only by scattering the proton's d quark but can produce a π^+ trigger by scattering either the beam's u quark or the proton's u quarks. Therefore the π produc

Figure 5.7 (a) The lowest order QF and CIM subprocesses for pp collisions producing $\pi^{\pm}$ or $K^{\pm}$ triggers. These diagrams represent the constituent scattering cross sections and are the same as in Figure 5.4 but redrawn so that the trigger particle emerges at the top and the away side quarks or particles emerge at the bottom. Dashed lines represent sea quarks and solid lines represent valence quarks or exchanged quarks. The same diagrams are drawn in (b) for $\pi^{-}p$ collisions and in (c) for $\pi^{+}p$ collisions.

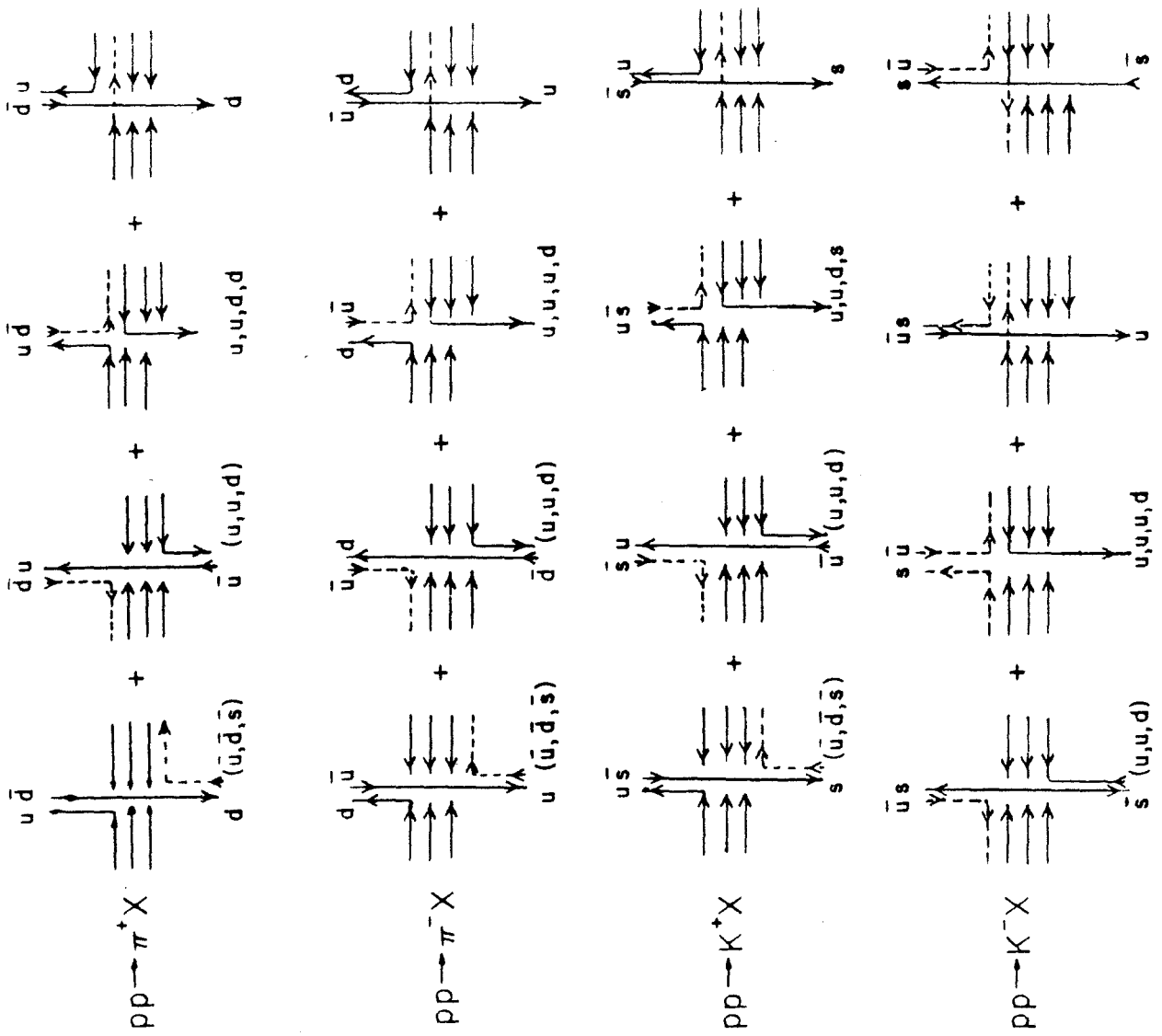
pp→π⁺X
pp→π⁻X
pp→K⁺X
pp→K⁻X
(a)

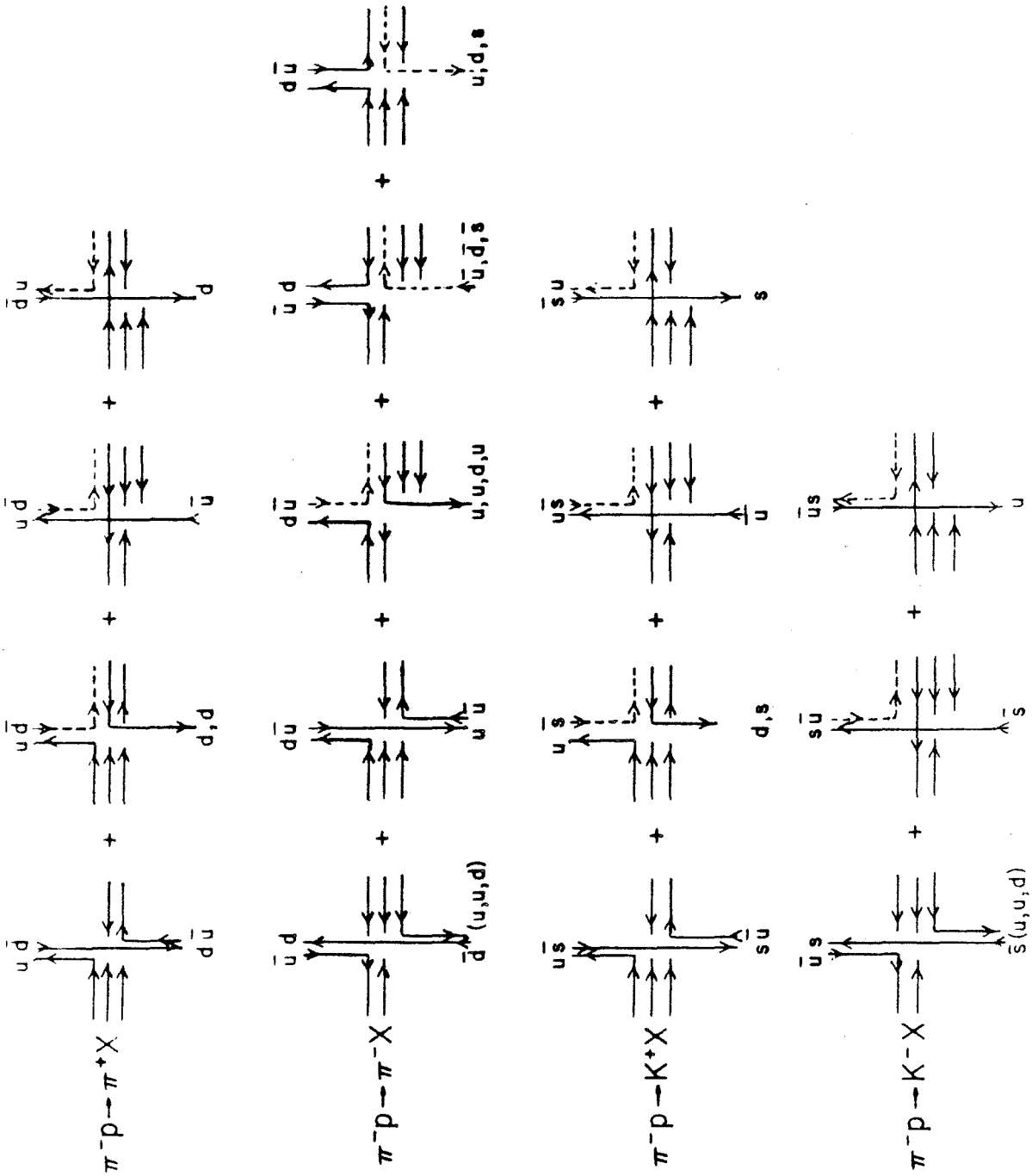
π⁻p → π⁺X
π⁻p → π⁻X
π⁻p → K⁺X
π⁻p → K⁻X
(b)

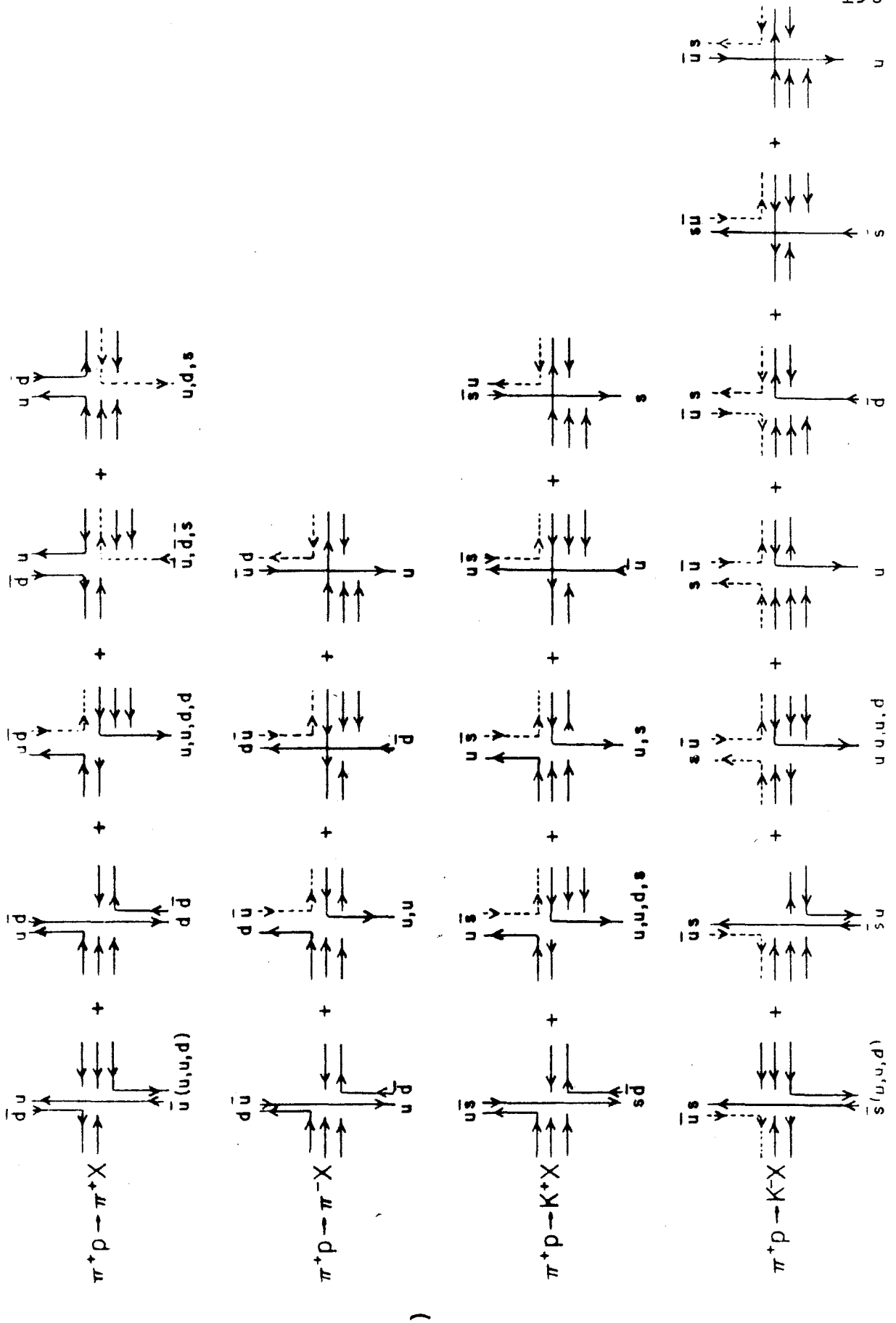

(c)

tion ratio in DQ rapidly increases as $x_T \to 1$. Similarly, QF has valence antiquark-valence quark scattering as dominant as seen in Figure 5.7b and Figure 5.7c. π^- beams will produce a π^+ about as often as a π^-. But a π^+ beam, because the $\bar{d}$ from the pion must scatter from two u's or a d, preferentially produces π^+ triggers.

The dominant CIM contribution in πp collisions is valence quarks from the proton scattering from either sea or valence quarks from the pion. From Figure 5.7b we see that π^- beams preferentially produce π^- triggers rather than π^+ triggers since the proton's d and either a valence $\bar{u}$ or a sea $\bar{u}$ from the beam can form the π^- trigger while the proton's u can only form a π^+ with a $\bar{d}$ from the beam's sea. Similarly, as seen in Figure 5.7c, a π^+ beam produces a π^+ trigger by combining a proton u quark with a $\bar{d}$ from the beam's valence or sea quarks while a π^- trigger is produced from the proton d quark and the beam's $\bar{u}$ quark. Thus CIM predicts that both $\frac{d\sigma}{dp_T}(\pi^- p \to \pi^- X)$, $\frac{d\sigma}{dp_T}(\pi^- p \to \pi^+ X)$ and $\frac{d\sigma}{dp_T}(\pi^+ p \to \pi^+ X)/\frac{d\sigma}{dp_T}(\pi^+ p \to \pi^- X)$ will rapidly rise as $x_T \to 1$ and that the latter ratio will increase more rapidly than the former because the d quark in the proton interacts in the $\pi^+ p \to \pi^- X$ reaction.

The CS predictions for the π production ratio with ½CIM+QF are shown in Figure 5.6a for the π^- beam and in Figure 5.6b for the π^+ beam. The π^- beam prediction is in reasonable agreement with the data and not very much different than the FF model. Our data cannot provide enough information here to rule out one model or the other. Data is needed at higher x_T where the two models show an appreciable difference. The CS prediction for the π^+ beam, however, is clearly in disagreement with the data. Adding more QF would certainly improve this fit. For both pion beams, as is the case with the p

beam, neither QF, DQ or CIM alone satisfactorily explain all the data and the combinations of DQ+QF or QF+CIM must be used. Recall that CS do not include the pion directly scattered from a quark in the proton. If this were included in the analysis the π^+/π^- ratios predicted in Figures 5.6a and 5.6b would rise even faster[42].

The particle ratios that we present certainly favor the QCD model over the CIM models in that QCD can fit all the data reasonably well over the p_T region we cover. But only the π^+ beam data is badly represented by the CIM models and perhaps a readjustment of parameters will bring this model in as good agreement as QCD.

c. QCD and the Away Side

We have already shown that at very low x_e the ratio of positive to negative hadrons opposite a given charged trigger may be accounted for by simple charge conservation. We would now like to see whether QCD can account for the spectrum of high-x_e hadrons. Given a constituent of type i with momentum P, the multiplicity of charged hadrons resulting from the decay of the parent constituent that have momentum greater than z_0P, $n^{\pm}(z_0)$, is given by

$$n^{\pm}(z_0) = \sum_h \int_{z_0}^{1} D_i^{h^{\pm}}(z)dz \qquad (5.3)$$

Although x_e is not the correct variable to use for multiplicity calculations it is related to the correct variable, z, although the relationship between x_e and the away side z is not so simple. In Figure 5.8a the constituent scattering process of ab → cd is viewed in the cd center of mass system where constituent a has momentum $x_a\frac{\sqrt{s}}{2}$ and constituent b has momentum $x_b\frac{\sqrt{s}}{2}$. c then fragments into the trigger, C, having a fraction z_c of the constituent c's momentum.

z_c we know is about 0.9. Constituent d, to balance momentum,

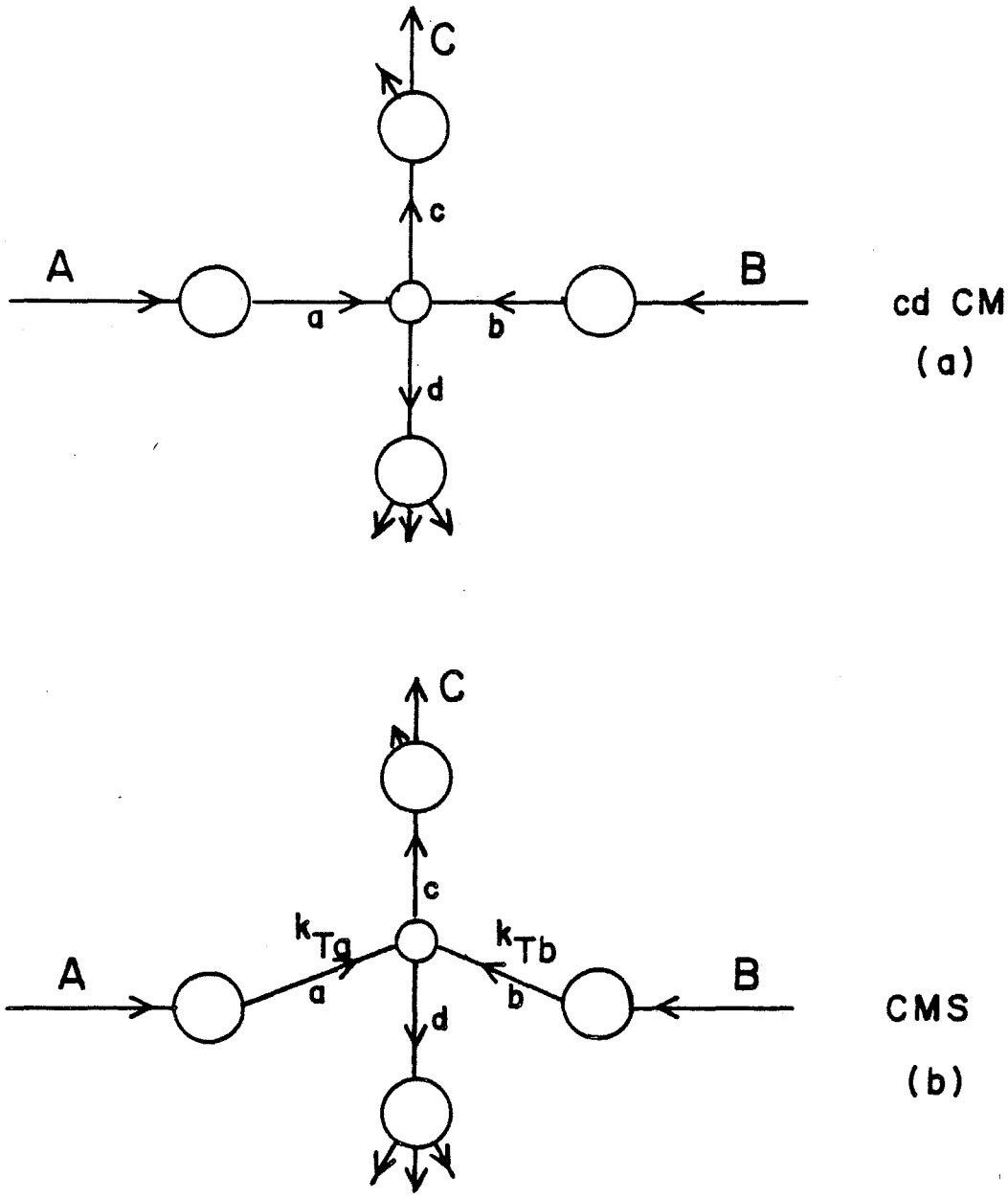

Figure 5.8 The underlying scattering for AB → CX in (a) the cd constituent center of mass and (b) in the actual CMS where the constituents have transverse momenta, k_T, in the direction of the trigger.

has momentum $x_a \frac{\sqrt{s}}{2}$ and it decays into hadrons that each have momenta $z_i x_a \frac{\sqrt{s}}{2}$. x_e is now simply $\frac{x_a}{x_b} \frac{z_i}{z_c}$. But because the constituents a and b have transverse momenta inside the hadrons and because $\frac{d\hat{\sigma}}{d\hat{t}}$ is sharply falling in $\hat{t}$, the initial constituents will tend to line up in the direction of the trigger and select events satisfying the trigger but produced preferentially at lower $\hat{t}$. This is illustrated in Figure 5.6b. A Lorentz transformation from the actual CMS to the cd center of mass results in x_e for the away hadrons as

$$x_e \simeq z_i \cdot \frac{x_a}{x_T} \sqrt{\frac{1-\beta}{1+\beta}} \tag{5.4}$$

where β is the velocity of the cd constituent system in the CMS.

In comparing our data to other experiments Eqs. 5.3 and 5.4 indicate that it is not sufficient to simply choose similar values of x_e. The multiplicity depends on z_i which in turn depends on at least four variables: (1) x_e which we can choose, (2) x_T which can be variable between ISR and Fermilab energies, (3) the quark internal transverse momentum which also varies with incident energy and with the trigger p_T[17], and (4) the fraction of the initial hadrons' momenta the scattering constituents have. We can see from Eq. 5.4 that two effects can occur when we choose x_e very large: (1) we will start to select events that have x_a and z_i approaching 1, and (2) events having the initial internal transverse momenta small in the direction of the trigger will be selected. Only as $x_e \gtrsim 1$ can meaningful comparisons of the ISR and Fermilab data be made. It is also important to remember that when one increases x_T of the trigger particle, x_a of the recoiling constituent increases. Therefore an increase of x_T increases the x-region from where the away side quark comes. This can change the probability of obtaining a particular flavor quark on the away side.

Assuming large x_e so that z_i can be assumed to be fairly close to 1, the away side charged multiplicities can now be predicted by asking what kind of constituent scatters opposite the constituent producing a given trigger type. For a proton beam we assume that all the constituents can be considered mainly as u quarks, d quarks and gluons and that they can interact as shown in Figure 5.9a. Gluons fragment equally into positives and negatives, u's fragment predominantly into positives and d's predominantly into negatives. We imagine a model that has each diagram in Figure 5.9a contributing equally. In this equal interaction model (EIM) where positive triggers arise only from gluons (½ the time), u's and $\bar{d}$'s and negative triggers only from gluons (½ the time), d's and $\bar{u}$'s, the ratio of positive to negative hadrons on the away side, $R_p(h)$, is calculated from the average away charge. If the gluons in the proton enters the scattering with the same probability as either of the u quarks to form the away side as shown in diagrams (a), (c), (e), and (f) of Figure 5.9a, we find the average charge opposite a positive trigger as

$$\langle Q \rangle = \frac{\frac{1}{4}\cdot\frac{1}{3} + \frac{1}{4}\cdot 0 + \frac{1}{2}\cdot\frac{1}{4}\cdot\frac{1}{3} + \frac{1}{2}\cdot\frac{1}{4}\cdot 0}{\frac{1}{4} + \frac{1}{4} + \frac{1}{8} + \frac{1}{8}} = \frac{1}{6}$$

Similarly, diagrams (b), (d), (e) and (f) imply $\langle Q \rangle = \frac{1}{6}$ for a negative trigger. Therefore, EIM predicts $R_p(h^+) = R_p(h^-) = 1.4$. $R_p(h$ will become even larger as x_e increases since the away quark will not as often be a d. Notice that this ratio is lower than naively predicted in Table 5.1 because of the introduction of gluons.

QCD calculations show that for a π^0 trigger with p_T = 3 GeV/c $R_p(\pi^0)$ = 1.21 implying that gluons have a sizeable contribution to the away side[18]. This same analysis also shows that if we look

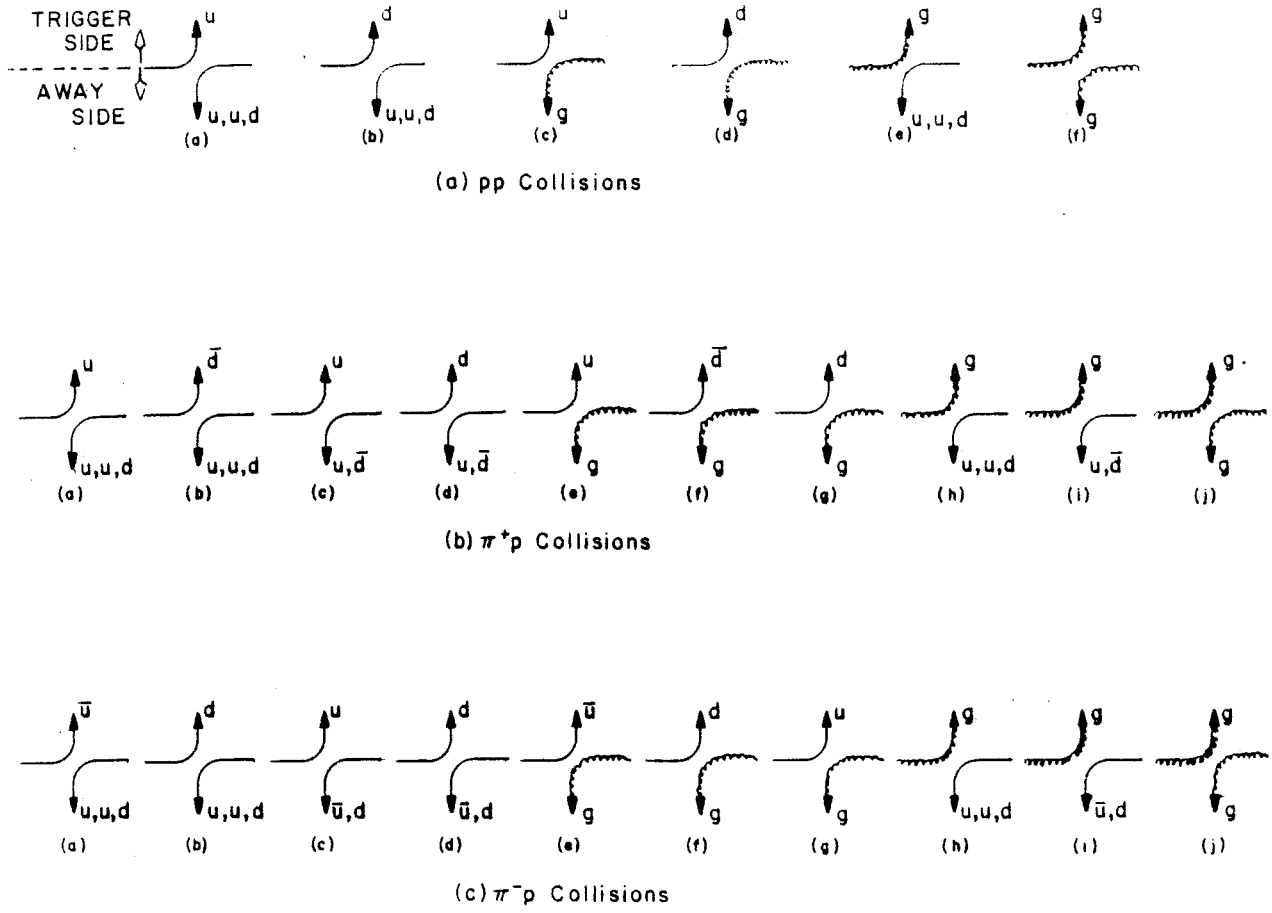

Figure 5.9 The possible scattering diagrams in QCD for (a) pp, (b) $\pi^+ p$ and (c) $\pi^- p$ collisions.

opposite a u, d or gluon decaying into the π^0, we see no difference in the ratio of away side positive to negative hadrons. $R_p(h)$ is largely independent of both the charge of h and its nature as shown in Figures 5.10a and 5.10b where specific QCD calculations are compared to the E494 away side data and the early BFS data. Note that the QCD calculations cannot explain the anomalous behavior opposite the K^- trigger seen by BFS.

Since detailed calculations for pion beams are presently lackir in QCD, we will have to rely on our EIM for rough predictions. Usir the possible constituent interactions shown in Figure 5.9b for π^+p collisions we calculate $R_{\pi^+}(h^+) = 1.64$ and $R_{\pi^+}(h^-) = 1.84$. We see from the figure that the negative trigger is produced by a gluon or d quark from the proton which scatters off the π^+ constituents. Thu the away side here will be the recoil u's, $\bar{d}$'s and gluons from the π^+. The positive trigger comes from either gluons, the pion quarks which scatter from the proton quarks, or the proton u scattering from the pion quarks. The away side is the recoil proton quarks or the pion quarks and gluons. Therefore the result that $R_{\pi^+}(h^-) \gtrsim R_{\pi^+}(h^+)$ emerges naturally.

Similarly we can calculate the away ratio for a π^- beam assumin equal contributions from each diagram in Figure 5.9c. We again find a natural difference between positive and negative triggers where th former arise from the fragmentation of gluons and u quarks from the proton that scatter off of the π^- constituents which result in $\bar{u}$'s, d's and gluons on the away side. The negative triggers are formed from the decay of gluons, π^- quarks scattering from the proton quark or the proton d quark scattering from the pion quarks. Here the awa side will be gluons, recoil proton constituents or recoil π^- constituents. We calculate $R_{\pi^-}(h^+) = 0.71$ and $R_{\pi^-}(h^-) = 1.0$ For both

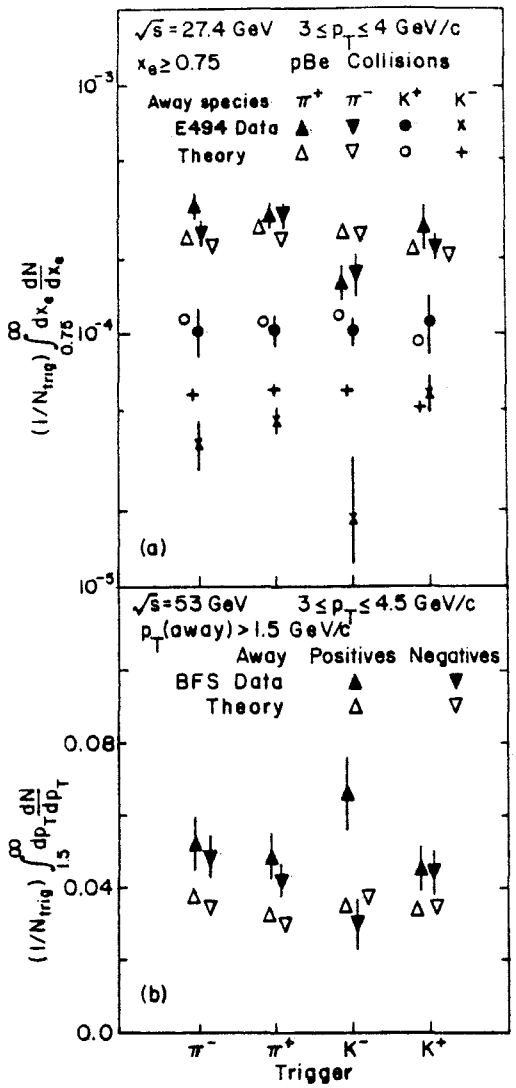

Figure 5.10 Specific QCD predictions for the away side data of (a) E494 and (b) BFS. Note that QCD does not explain the positive excess of hadrons opposite a K^- trigger. QCD agrees well with the E494 data.

	AWAY SIDE POSITIVE/NEGATIVE RATIO		
REACTION	EIM	NO GLUONS	E260 DATA
$pp \rightarrow h^+X$	1.4	2.0	1.30 ± 0.07
$pp \rightarrow h^-X$	1.4	2.0	2.20 ± 0.18
$\pi^+p \rightarrow h^+X$	1.64	2.27	1.14 ± 0.12
$\pi^+p \rightarrow h^-X$	1.84	3.0	1.63 ± 0.25
$\pi^-p \rightarrow h^+X$	0.71	0.33	0.71 ± 0.04
$\pi^-p \rightarrow h^-X$	1.0	1.12	1.15 ± 0.05

Table 5.2 The naive QCD predictions for the away side ratio of positive to negative hadrons and our corresponding data. Model EIM assumes gluons and quarks scattering on an equal basis as shown in Figure 5.9. Also listed is the resulting ratio if we assume only valence quarks interacting and no gluons. The naive model with gluons comes reasonably close to our data except for $pp \rightarrow h^-X$, where our data lies about 50% higher.

beams d in the proton may become unimportant as an away side quark and all these ratios will therefore increase due to a lessening of negative producing constituents. Table 5.2 lists the EIM predictions for the three beams producing charged triggers assuming that the away quarks that scatter out of the proton are u's 2/3 of the time and d's 1/3 of the time. Included in the table for comparison is our away side data with $x_e \geq 0.4$ and the results of the naive quark model which neglects gluons as constituents and only uses the valence quarks. EIM nicely predicts our data except for the negative trigger in pp collisions and the positive trigger in $\pi^+ p$ collisions. Our data certainly requires the addition of gluons as scattering constituents and not only valence quarks. However, the ratios which we measure can all approach 1 if there is a sizeable background (equal positives and negatives) contribution at $x_e \geq 0.4$. It is, at this x_e, difficult to say whether or not gluons are responsible for the shift away from the valence-quark-only ratios. Since K triggers come mainly from strange sea quarks, gluons and u quarks, the away side ratios are expected to be independent, or only slightly dependent, on the nature of the trigger.

Reproduced in Figure 5.11 is our away side data for $x_e \geq 0.4$ previously introduced in Figure 4.11. Also shown on our p beam data are the away side ratios found by E494 and by the BFS group. Although these experiments cover different x_e and x_T regions, it is nonetheless interesting to compare them. Several features of the figure should be pointed out.

(a) Within statistical errors, the data for $R_{\pi^+}(h)$ and $R_{\pi^-}(h)$ are independent of the nature of h but not its charge. There appears to be a dependence on

trigger type as well as charge for the proton beam. For either charge trigger, $R_p(Kp)/R_p(\pi) < 1$. This is seen for positive triggers by the other experiments whereas only E494 sees this for the negative trigger.

(b) The large value of $R_p(Kp^-)/R_p(\pi)$ reported in the early BFS analysis is not seen in our data, the data of E494 or even the later BFS analysis.

(c) Comparison of our data for the three beams with the QCD predictions in Table 5.2 shows that the simple interpretation of QCD (model EIM) gives correct approximate predictions for our data. The predictions for $R_{\pi^+}(h^+)$, however, does not agree well with either the π^+ or the Kp^+ trigger. The naive model without gluons is a much poorer fit to the data.

Certainly much more detailed QCD calculations have to be made in order to determine the validity of QCD on the away side. Certainly the gluon distributions in the proton should be refined and the gluon distributions in the pion should be attempted in order that the pion data be explained. We can say that the rough models we hav used that incorporate gluons as constituents are not totally absurd in their predictions.

d. CIM and the Away Side

In Figure 5.7a we write the dominant QF + CIM diagrams for π an K production by a proton beam. The solid lines are valence quarks and the dashed lines are sea quarks. As in our QCD estimates, we ca simply count the average charge on the away side to see what predic-

Figure 5.11 The away side positive to negative charge ratios for (a) π^-p, (b) π^+p and (c) pp collisions opposite specific triggers. This data was previously introduced in Figure 4.11. The proton data is compared to the BFS and E494 data.

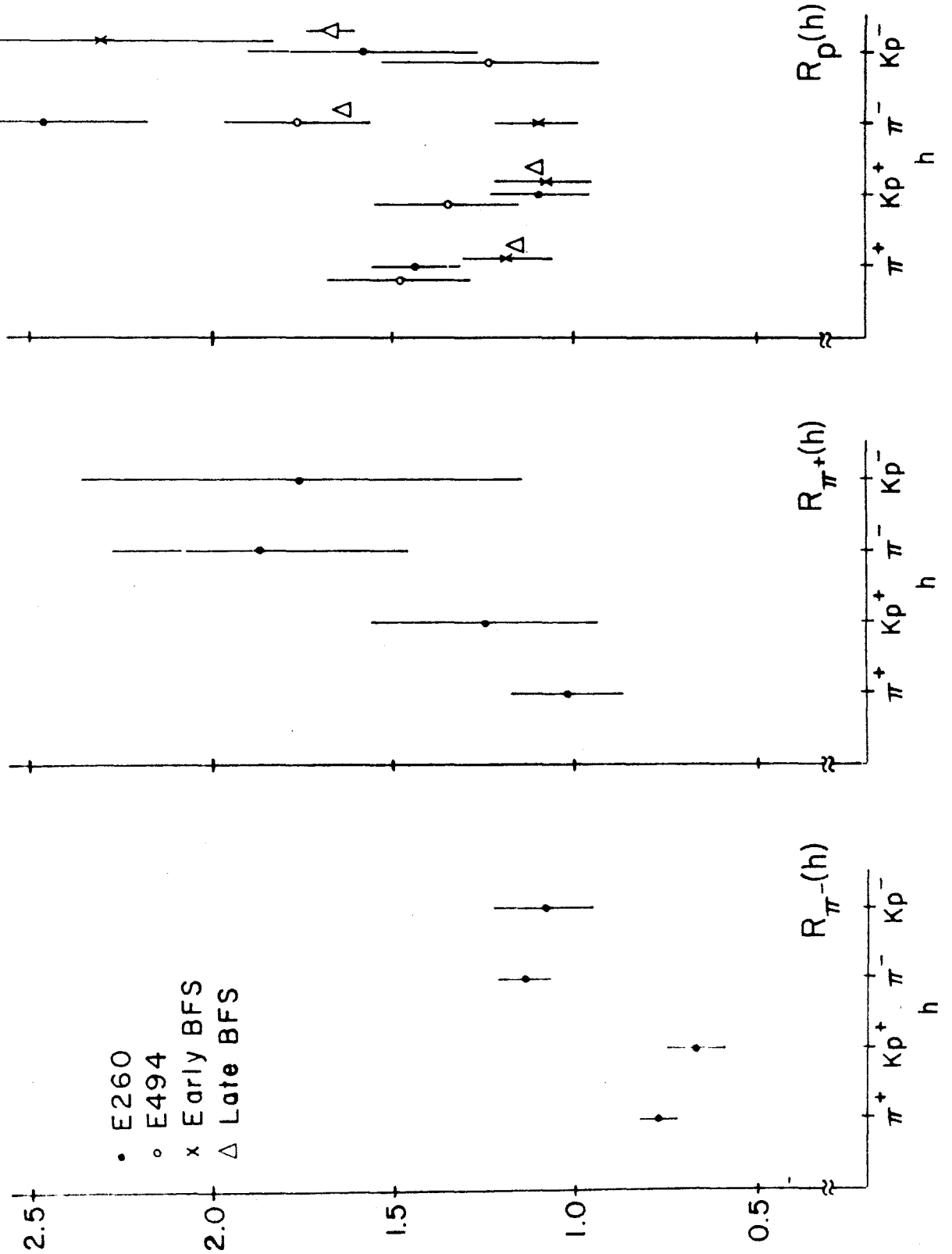
• E260
∘ E494
× Early BFS
△ Late BFS
2.5
2.0
1.5
1.0
0.5
$R_{\pi^-}(h)$
$R_{\pi^+}(h)$
$R_p(h)$
π^+ Kp^+ π^- Kp^-
h

tions QF and CIM make for R. Assuming each diagram in Figure 5.7 to contribute equally we construct Table 5.3 which lists the away side average charge, $\langle Q_a \rangle$, and the corresponding ratio of away positive hadrons to negative hadrons for each trigger particle. Notice from the table that both CIM and QF predict the away side to be more positive opposite a negative trigger. Any combination of these models can correctly predict the observed charge structure for all beams - $R_i(h^-) > R_i(h^+)$.

Specific beam predictions will probably add confusion to which of the underlying scattering mechanisms is at work. For a proton beam, QF and CIM both predict $R_p(\pi^+) = R_p(K^+)$ and $R_p(\pi^-) = R_p(K^-)$. Compared to our data the QF prediction is too low and the CIM ratio is approximately correct. But we know that for K^- production, CIM involves valence quark-sea quark scattering thus making QF dominant for K^- triggers. These effects result in $R_p(K^-) > R_p(\pi^-)$ as seen by the early BFS analysis. Although not shown in Figure 4.7, the same arguments lead to the result $R_p(\bar{p}) > R_p(\pi^-)$. This positive excess reported by the BFS group certainly added evidence for the existence of CIM as a viable hard scattering model. But our data, the E494 data and the recent BFS data do not show this positive excess. Thus the manner in which the CIM models is thought to act will have to be re-explained. Perhaps we can say that if CIM + QF is a component of the scattering in pp collisions, the QF term is certainly not dominant at our x_T but in fact may be important at the ISR.

Conclusions from pion beam data are not so concise. In $\pi^+ p$ collisions QF predicts a very large amount of positive hadrons opposite a π^- or K^- where in the latter trigger, QF is expected to dominate CIM. But CIM also predicts a large number of positives for the

ap → hX	QF		CIM		
	$\langle Q_a \rangle$	$R_a(h)$	$\langle Q_a \rangle$	$R_a(h)$	E260 $R_a(h)$ [1]
$pp \to \pi^+X$	-1/3	.67	1/15	1.1	1.44 ± 0.12
$pp \to K^+X$	-1/3	.67	1/15	1.1	1.10 ± 0.13
$pp \to \pi^-X$	2/3	5.0	7/15	2.8	2.46 ± 0.28
$pp \to K^-X$	2/3	5.0	4/9	2.6	1.58 ± 0.32
$\pi^+p \to \pi^+X$	-1/4	.6	1/15	1.1	1.03 ± 0.15
$\pi^+p \to K^+X$	0	1.0	0	1.0	1.25 ± 0.32
$\pi^+p \to \pi^-X$	1	∞	7/12	3.8	1.87 ± 0.41
$\pi^+p \to K^-X$	3/4	7.0	11/24	2.7	1.76 ± 0.60
$\pi^-p \to \pi^+X$	-1	0	-5/12	.4	0.78 ± 0.05
$\pi^-p \to K^+X$	-1	0	-5/12	.4	0.67 ± 0.08
$\pi^-p \to \pi^-X$	1/2	3.0	5/30	1.4	1.14 ± 0.08
$\pi^-p \to K^-X$	2/3	5.0	1/2	3.0	1.09 ± 0.14

[1] "K" triggers here are Kp triggers.

Table 5.3 The average away side charge, $\langle Q_a \rangle$, and the resulting away side ratio of positive to negative hadrons opposite a specified trigger in πp and pp collisions calculated for the basic subprocesses in QF and CIM. The diagrams used in Figure 5.7 are used to determine what kind of quarks are on the away side.

triggers also. Both QF and CIM are in disagreement with the data fc the negative triggers but are approximately correct for positive triggers. For π^- beams QF seems to be definitely out. It predicts too low a ratio for positive triggers and too high a ratio for negative triggers. CIM, although also low for positive triggers and hi for negatives, comes closer than QF in predicting our observed ratic QF and CIM show a large positive excess opposite the K^- trigger whic is not seen. Thus CIM appears to be more prominent, or just fortuitous, in πp collisions although the relative degree with which different quarks scatter has to be considered.

Further evidence for components of CIM in the scattering is see if we follow the trend of the away ratios as the beam changes. Both QF and CIM terms say that $R_p(h^+) \simeq R_\pi+(h^+)$, $R_p(h^-) \lesssim R_\pi+(h^-)$ and $R_\pi-(h^+) < R_\pi+(h^+)$. This is true within statistical errors. But QF predicts that $R_\pi-(h^-) \simeq R_p(h^-)$ which disagrees with the data. CIM, on the other hand, correctly shows $R_\pi-(h^-)$ as approximately the smallest of the three ratios.

5.4 Summary

We have measured the production rate of mesons and baryons in high transverse momentum collisions for π^+, π^-, and p beams. The structure opposite these triggers also was studied. We have presented here results on the production ratios of these triggers and on the ratios of the away side positive to negative hadrons.

The charged and pion production ratios in pp collisions have been found to slowly increase as x_T approaches 1. A similar spectrum is found for a π^+ beam, but the pion production ratio for a π^- beam is seen to be $\simeq 1$ throughout our x_T region. These high p_T particles may be produced by quarks or gluons elastically scatterin

on other quarks or gluons[5,18], the fusion of a quark and anti-quark or the scattering of a quark with a ($q\bar{q}$) system[39-42,45]. For all three beam particle types a QCD model can correctly predict most of the features of the production ratios. QF or CIM alone cannot explain these ratios for any beam. QF and CIM acting together, however, provide an explanation for pp and $\pi^- p$ collisions but not for $\pi^+ p$ collisions. Large differences between these underlying mechanisms are not evident in the p_T region covered by our experiment. Significant differences arise as $x_T \to 1$.

The ratio of away positive to negative hadrons may provide more useful information for determining the underlying scattering mechnism. We have found that measuring "slow" particles may just reflect simple charge conservation. For any beam, no variation of the away side ratios is seen when the trigger is a π or Kp of the same sign charge and $x_e \geq 0.4$. Positives dominate when the trigger is negative which can imply that we may still see evidence of charge conservation instead of underlying dynamics. The away ratios for all beams can probably be explained by a QCD model with gluons further developed for pion beams. QF is seen to be negligible in our regions of x_T and x_e. CIM, after developing the important scattering diagrams, may make reasonable predictions for π and p beams. Large values of x_e are needed to be sure that the dynamics of the constituents are seen.

As for the theoretical models, it may be that all of the cross section down to p_T around 2 GeV/c may be due to scattering of quarks and gluons. On the other hand, a non-leading constituent process such as CIM or QF may make contributions in the range of $1.5 \lesssim p_T \lesssim 4$ GeV/c with QCD dominating at higher p_T's.

REFERENCES

1. F. W. Busser et. al., Phys. Lett. 46B, 471 (1973).
2. J. D. Bjorken and E. A. Paschos, Phys. Rev. 184, 1975 (1969); Phys. Rev. D1, 3151 (1970).
3. S. M. Berman, J. D. Bjorken and J. B. Kogut, Phys. Rev. D4, 3388 (1971).
4. S. D. Ellis and M. B. Kislinger, Phys. Rev. D9, 2027 (1974).
5. R. D. Field and R. P. Feynman, Phys. Rev. D15, 2590 (1977).
6. G. Ginochiaro et. al., Phys. Lett. 50B, 396 (1974); R. Kephart et. al., Phys. Rev. D14, 2909 (1976).
7. K. Eggert et. al., Nucl. PHys. B98, 49 and 73 (1975).
8. F. W. Busser et. al., Phys. Lett. 51B, 306 and 311 (1974).
9. F. W. Busser et. al., Phys. Lett. 56B, 482 (1975); Nucl. Phys. B106, 1 (1976).
10. M. Della Negra et. al., Phys. Lett. 59B, 401 and 481 (1975); Nucl. Phys. B104, 365 (1976) and B127, 1 (1977).
11. P. Darriulat et. al., Nucl. Phys. B107, 429 (1976) and B110, 365 (1976).
12. B. Alper et. al., Nucl. Phys. B114, 1 (1976).
13. M. Jacob, "Large Transverse Momentum Phenomena", summary of ISR discussion meeting between theorists and experimentalists, 21 (1977).
14. H. Boggild, (BFS Collaboration), in Proceedings of the Eighth International Symposium on Multiparticle Dynamics, Kavsersberg, France, 1977, edited by R. Arnold, J. B. Gerber and P. Schubeli (Centre National de la Recherche Scientifique, Strasbourg, France, 1977); R. Moller, invited talk at the Moriond Conferenc (1977); H. Boggild and K. Hansen, University of Bielefeld Repor No. BI-TP 77/39, November, 1977; H. Boggild, Niels Bohr Institute preprint NBI-HE-77-9.
15. M. G. Albrow et. al., "Studies of Proton-Proton Collisions at the CERN ISR with an Identified Charged Hadron of High Transverse Momentum at 90°," CERN preprint, 1977.
16. R. J. Fisk et. al., Phys. Rev. Lett. 40, 984 (1978).
17. R. P. Feynman, R. D. Field and G. C. Fox, Nucl. Phys. B128, 1 (1977).

REFERENCES (Continued)

18. R. P. Feynman, R. D. Field and G. C. Fox, Phys. Rev. D18, 3320 (1978); G. C. Fox, Caltech preprint CALT-68-643 (1978); R. D. Field, Phys. Rev. Lett. 40, 977 (1978).
19. R. F. Schwitters, "Hadron Production at SPEAR," International Symposium on Lepton and Photon Interactions, Stanford (1975); J. C. VanderVelde, "Neutrino-Proton Interations in the 15-foot Bubble Chamber and Properties of Hadron Jets," IVth International Winter Meeting on Fundamental Physics, Salardu, Spain (1976); J. T. Dakin et. al., Phys. Rev. D10, 1401 (1974); G. Hanson et. al., Phys. Rev. Lett. 35, 1609 (1975).
20. C. Bromberg et. al., Phys. Rev. Lett. 38, 1447 (1977); Nucl. Phys. B134, 189 (1978); Phys. Rev. Lett. 43, 1202 (1979); "Jet Production in 200 GeV/c Hadron-Proton Collisions" (to be published).
21. Contributions to the Multiparticle Spectrometer Workshop at Fermilab, March 4-5, 1977, include: "Multiparticle Spectrometer at Fermilab," A. Dzierba, E. Malamud and D. McLeod, unpublished (1977); "The M6 Beam Line," E. Malamud, unpublished, (1977).
22. K. B. Burns et. al., Nucl. Instr. Meth. 106, 171 (1973).
23. Epon 815 Resin manufactured by Shell, and Epicure 874 hardener manufactured by Celanese was used in all epoxy applications except for the casting of the wire-winding drum. Because excess heat would be generated with 815, Thiokol EM308 was used here.
24. B. Bertoluzzi, SLAC-PUB-1177, unpublished (1972).
25. K. J. Foley et. al., Nucl. Inst. Meth. 108, 33 (1973).
26. C. Bromberg et. al., in Proceedings of the Eighth International Symposium on Multiparticle Dynamics, Kaysersberg, France, 1977, edited by R. Arnold, J. B. Gerber and P. Schubelin (Centre National de la Recherche Scientifique, Strasbourg, France, 1977).
27. H. Haggerty, "Multiparticle Spectrometer Calorimeters," in Proceedings of the Calorimeter Workshop, 251, Fermilab (1975).
28. H. Hinterberger and R. Winston, Rev. Si. Instr. 37, 1094 (1966).

REFERENCES (Continued)

29. A. Brenner and R. Martin, "CAMAC Lam Latch Module," BISON HN-5, unpublished, Fermilab (1972).
30. A. Brenner and R. Martin, "Bison Interrupt and Gate Controls," BISON HN-3, unpublished, Fermilab (1972).
31. F. Bartlett, Caltech, designed for use in E111 at Fermilab.
32. D. Antreasyan et. al., Phys. Rev. Lett. 38, 112, 115 (1977); Phys. Rev. D19, 764 (1979).
33. K. Yung, Ph.D. thesis, Caltech (unpublished).
34. D. Horn and F. Zachariasen, Hadron Physics at Very High Energie (Benjamin, Mass. 1973).
35. F. J. Sciulli, "Photon-Collecting Hadron Calorimeters," in Proceedings of the Calorimeter Workshop, 79, Fermilab (1975).
36. M. Antinucci et. al., Let. Nuovo Cimento, 6, 121 (1973).
37. R. D. Field and R. P. Feynman, Nucl. Phys. B136, 1 (1978).
38. J. Whitmore, Phys. Reports, 10C, 275 (1974).
39. R. Blankenbecler, S. J. Brodsky, and J. F. Gunion, Phys. Lett. B39, 649 (1972); B42, 461 (1973); Phys. Rev. D12, 3469 (1975).
40. S. J. Brodsky, SLAC Report No. SLAC-PUB-1575 (unpublished).
41. S. J. Brodsky, SLAC Report No. SLAC-PUB-2009 (unpublished).
42. R. Blankenbecler, S. J. Brodsky, and J. F. Gunion, Phys. Rev. D18, 900 (1978).
43. B. L. Combridge, J. Kripfganz, and J. Ranft, Phys. Lett. 70B, 234 (1977); R. Cutler and D. Sivers, Phys. Rev. D16, 679 (1977) and D17, 1966 (1978); D. Jones and J. F. Gunion, Phys. Rev. D19 867 (1979).
44. G. Donaldson et. al., Phys. Rev. Lett. 36, 1110 (1976); C. Bromberg et. al., Phys. Rev. Lett. 43, 561 (1979).
45. M. K. Chase and W. J. Stirling, Nucl. Phys. B133, 157 (1978).

APPENDIX A

NORMALIZATION

As a check of our data with other experiments it will be necessary to calculate a cross section, or at least find terms that are proportional to the cross section and are time dependent. These, of course, are such things as detection efficiency, Cerenkov counter efficiencies, beam flux, etc. Scaler information obtained after each run tells us how much of the beam has satisfied our various trigger logical requirements. We must decide how many of these logical triggers are good events.

We will first write down how we can arrive at the cross section and then proceed to develop ways to measure, or bypass, various efficiencies of the spectrometer.

A.1 Cross Section Derivation

For a particular polarity beam, the number of triggers written onto the tape, TRIG, is given by

$$TRIG = BEAM \cdot (\sigma_{good} t_{good} + \sigma_{bad} t_{bad}) \cdot LT \cdot \varepsilon_d \cdot \Delta A \qquad (A.1)$$

where

BEAM = total number of incident beam particles

$\sigma_{good} t_{good}$ = cross section x target thickness for good events

$\sigma_{bad} t_{bad}$ = cross section x target thickness for bad events

LT = live time for the experiment

ΔA = acceptance

ε_d = triggering efficiency

The live time is just the product of the spark chamber live time and the PDP11 live time. From Figure 2.13 we can see

$$LT = \frac{\text{EFFECTIVE BEAM}}{\text{BEAM}} \cdot \frac{\text{TRIGGERS}}{\text{TRIGLOGICS}} \qquad (A.2)$$

However, all triggers have an equal probability of getting written onto tape. Therefore,

$$\frac{\text{TRIGGERS}}{\text{TRIGLOGICS}} = \frac{HPT}{HPL} = \frac{JETT}{JETL} = \frac{LPTDIVT}{LPTDIVL} = \frac{LJETDIVT}{LJETDIVL} \qquad (A.3)$$

where

HPT,L = high bias single particle triggers, logics

JETT,L = jet triggers, logics

LPTDIVT,L = divided low bias single particle triggers, logics

LJETDIVT,L = divided low jet triggers, logics

The logics are known from the scaler readings after each run and th triggers are known from counting them on the tape.

The high bias triggers are straightforward. Any event with either the single particle tagbit ON or the jet tagbit ON is a prospective trigger. But for proper normalization, the low bias trigger are found by requiring that only the low bias tagbit be on. For the low bias single particle trigger, this meant we look for events that have only the LOPT tag ON and the others OFF. This constitutes LPTDIVT above. The number of triggers can then be written

$$TRIG = EBM \cdot \frac{HPT}{HPL} \cdot (\sigma_{good} t_{good} + \sigma_{bad} t_{bad}) \cdot \varepsilon_d \cdot \Delta A \qquad (A.4)$$

where EBM is the effective beam on target. For the sake of discussion we will refer to only the high bias single particle trigger. The result is applicable to any trigger correctly chosen.

After analysis we find only good events from the tape; we throw out fake triggers, non-vertex events, etc. and are left with a fraction of the original triggers that were on tape. For a given run,

then, the number of good high bias events found, N, is

$$N = EBM \cdot \frac{HPT}{HPL} \cdot \sigma_{good} t_{good} \cdot \varepsilon_d \cdot \varepsilon_r \cdot \Delta A \qquad (A.5)$$

where ε_r is the event reconstruction efficiency. Eq. A.5 is valid for all beam particles only because EBM is scaled independently of the beam composition. For a particular beam particle, we can write

$$N = EBM \cdot \frac{HPT}{HPL} \cdot t \cdot (f_\pi \sigma_\pi + f_K \sigma_K + f_p \sigma_p) \varepsilon_d \varepsilon_r \Delta A \qquad (A.6)$$

where f_j is the true fraction of particle j of the beam. But if we have a selection criteria for a π, K, or p, then we identify a beam particle j with efficiency ε_C^j and the number of good triggers is

$$N = EBM \cdot \frac{HPT}{HPL} \cdot t \cdot (f_\pi \sigma_\pi \varepsilon_C^\pi + f_K \sigma_K \varepsilon_C^K + f_p \sigma_p \varepsilon_C^p + rest) \varepsilon_d \varepsilon_r \Delta A \qquad (A.7)$$

where "rest" is unidentifiable beam particles times their respective cross section. The cross section for beam particle a producing a high p_T event is then

$$\frac{d\sigma}{dp_T}(ap \rightarrow HIPT) = \frac{dN(a)}{dp_T} \left(EBM \frac{HPT}{HPL} t \, \varepsilon_d \varepsilon_r \varepsilon_C^a f_a \Delta A\right)^{-1} \qquad (A.8)$$

$\frac{dN(a)}{dp_T}$ is the p_T spectrum of good events found after the analysis. This requires choosing the trigger correctly and having defined the beam particle as a that produced the event.

For the low bias triggers Eq. A.8 is still valid except that N(a) must reflect the unbiased trigger and be scaled up by its appropriate division number. A low bias trigger must be chosen as mentioned above, so that only either the LOPT tagbit or the LOJET tagbit is ON.

A.2 Efficiencies

a. Event Reconstruction, ε_r

The reconstruction efficiency is a product of vertex finding

efficiency and track finding efficiency combined with the efficiency for writing the events on tape and reading them back (parity errors). We estimate the efficiency for the combined reconstruction to be better than 90%. For a complete discussion see the work of Kar Yung[33]. In any case we assume that this reconstruction process is fairly constant in time. When taking ratios, errors here will become negligible.

b. Beam Identification Efficiency, ε_C^a

For beam particle identification we need to know what the overall efficiency is for tagging a particle as π, K or p. In principle this can be obtained by knowing the beam Cerenkov counter efficiencies and how often each will fire on a different particle. But this is only measurable for CO and PRUSS because, since both are set for pions, we can check one counter against the other. But for BDIFF and DISC we cannot rely on other counters to also verify the beam particle. Since the beam Cerenkov counter efficiencies may vary fro run to run it is important to include the beam identification efficiency in Eq. A.8 as a variable.

We define our beam particles to be used in the analysis as

$$\begin{aligned} \pi &= (CO+PRUSS)\cdot\overline{BDIFF}\cdot\overline{(D6+D8)} \\ K &= (D6+D8)\cdot\overline{(CO+PRUSS)}\cdot\overline{BDIFF} \\ p &= BDIFF\cdot\overline{(CO+PRUSS)}\cdot\overline{(D6+D8)} \end{aligned} \qquad (A.9)$$

where + means a logical OR and $\cdot$ means a logical AND. D6 and D8 are the six-fold and eight-fold coincidences of the DISC counter. The efficiency for tagging a beam particle i, ε_C^i, is given for a π, K and p as

$$\varepsilon_C^{\pi} = (1 - (1 - \varepsilon_{CO}(\pi))(1 - \varepsilon_{PR}(\pi)))(1 - \varepsilon_{BD}(\pi))(1 - \varepsilon_{DI}(\pi)) \quad \text{(A.10a)}$$

$$\varepsilon_C^{K} = \varepsilon_{DI}(K)(1 - \varepsilon_{CO+PR}(K))(1 - \varepsilon_{BD}(K)) \quad \text{(A.10b)}$$

$$\varepsilon_C^{p} = \varepsilon_{BD}(p)(1 - \varepsilon_{DI}(p))(1 - \varepsilon_{CO+PR}(p)) \quad \text{(A.10c)}$$

where we define the following efficiencies:

$\varepsilon_{CO}(\pi)$ = efficiency for CO to fire on π's

$\varepsilon_{PR}(\pi)$ = efficiency for PRUSS to fire on π's

$\varepsilon_{CO+PR}(K/p)$ = efficiency for either CO or PRUSS to fire on a K/p

$\varepsilon_{DI}(\pi/K/p)$ = efficiency for either D6 or D8 to fire on a π/K/p

$\varepsilon_{BD}(\pi/K/p)$ = efficiency for BDIFF to fire on a π/K/p

The problem now remains to determine the above efficiencies. We define the following variables and, for each run, we record the indicated quantities.

NCO = number of times CO=ON

NCOAPR = number of times CO=ON and PRUSS=ON

NPR = number of times PRUSS=ON

N10X = number of times (CO+PRUSS)=ON and DISC=OFF

N101 = number of times BDIFF=ON AND (CO+PRUSS)=ON AND DISC=OFF

N1X0 = number of times (CO+PRUSS)=ON AND BDIFF=OFF

N110 = number of times DISC=ON AND (CO+PRUSS)=ON AND BDIFF=OFF

The efficiencies for the various counters on pions can now be found:

$$\varepsilon_{CO}(\pi) = \text{NCOAPR/NPR}$$

$$\varepsilon_{PR}(\pi) = \text{NCOAPR/NCO}$$

$$\varepsilon_{BD}(\pi) = \text{N101/N10X}$$

$$\varepsilon_{DI}(\pi) = \text{N110/N1X0} \quad \text{(A.11)}$$

Similarly for the kaon and proton efficiency calculations,

NKAONS = number of kaons found by Eq. A.9

NPROTS = number of protons found by Eq. A.9

NX10 = number of times DISC=ON AND BDIFF=OFF

N01X = number of times (CO+PRUSS)=OFF AND DISC=ON

N011 = number of times (CO+PRUSS)=OFF AND DISC=ON AND BDIFF=ON

N0X1 = number of times (CO+PRUSS)=OFF AND BDIFF=ON

NX01 = number of times DISC=OFF AND BDIFF=ON

The following efficiencies are straightforward:

$$\begin{aligned} \varepsilon_{CO+PR}(K) &= N110/NX10 \\ \varepsilon_{BD}(K) &= N011/N01X \\ \varepsilon_{DI}(p) &= N011/N0X1 \\ \varepsilon_{CO+PR}(p) &= N101/NX01 \end{aligned} \qquad (A.12)$$

For a typical run with negative beam (runs 689 - 700 in particular) we find

$$\begin{aligned} \varepsilon_{CO}(\pi) &\geq 70\% \\ \varepsilon_{PR}(\pi) &\geq 62\% \\ \varepsilon_{DI}(\pi) &\leq 1\% \\ \varepsilon_{BD}(\pi) &\leq 1\% \\ \varepsilon_{CO+PR}(K) &\leq 15\% \\ \varepsilon_{BD}(K) &\leq 1\% \\ \varepsilon_{CO+PR}(p) &\leq 4\% \\ \varepsilon_{DI}(p) &\leq 1\% \end{aligned}$$

Of course these efficiencies will reflect the fact that particular counters may have been incorrectly set for their proper beam particle For example, if DISC was slowly losing pressure and had drifted near the pion peak, then our analysis above will have used real pions in calculating the response of CO to kaons. Thus in this case $\varepsilon_{CO+PR}(K)$ will be artificially high while DISC may have a low overall efficien

resulting in $\varepsilon_{DI}(\pi)$ small. However by requiring an OFF in PRUSS and CO for a K definition, we reduce the π contamination to our sample but may not be efficient in tagging a kaon if the DISC counter is near the pion peak. Similar arguments can be made for BDIFF but compared to the DISC counter this was a fairly reliable counter for counting protons.

To find the DISC efficiency on K's and the BDIFF efficiency on p's for a given run, we use the fraction of K's and the fraction of p's that are in the beam - f_K and f_p. We can write

$$NKAONS = f_k \cdot TRIG \cdot \varepsilon_C^K \tag{A.13a}$$

$$NPROTS = f_p \cdot TRIG \cdot \varepsilon_C^p \tag{A.13b}$$

where TRIG is the number of triggers taken in the run. Eq. A.13 is not completely correct since one type of beam particle may be more efficient than another in creating a trigger. However we will neglect this effect and calculate the DISC and BDIFF efficiencies from Eq. A.10.

$$\varepsilon_{DI}(K) = \frac{NKAONS}{TRIG}(f_K(1 - \varepsilon_{CO+PR}(K))(1 - \varepsilon_{BD}(K)))^{-1} \tag{A.14}$$

$$\varepsilon_{BD}(p) = \frac{NPROTS}{TRIG}(f_p(1 - \varepsilon_{CO+PR}(p))(1 - \varepsilon_{DI}(p)))^{-1} \tag{A.15}$$

But since nature is not an invariant we do not know the beam composition at any one time. We have an accurate determination of pion tagging efficiency, ε_C^π, and we measure the number of pions, NPIONS, by our definition in Eq. A.9. The fraction of pions in the beam, f_π, is then, to a good approximation, given by

$$f_\pi = \frac{NPIONS}{TRIG} \cdot \frac{1}{\varepsilon_C^\pi} \tag{A.16}$$

Since $f_p + f_K = 1 - f_\pi$ we are left with choosing either f_p or f_K. The error in the efficiency is proportional to f_i^{-1} so that the

smaller f_i is the larger the error. This is good since we would like to minimize the errors on the higher percentage particles in the beam. We therefore choose from Table 2.3 the smaller of f_p and f_K. That is, for positive 200 GeV beam, $f_{K^+} = 0.026$ and $f_p = 0.974 - f_{\pi^+}$. For negative beam, $f_{\bar{p}} = 0.01$ and $f_{K^-} = 0.99 - f_{\pi^-}$

Using these results we plot in Figure 2.2 the efficiencies for tagging a π, K and p in the beam.

c. Detection Efficiency, ε_d

The detection or triggering efficiency is, for the most part, a function of the magnet polarity, the particles' charge and the calorimeter response. This means that the left-side trigger may be different than the right-side trigger if the calorimeters are not identical. We want to see how to combine all our runs with differen magnet settings and different thresholds to minimize our apparatus dependence.

Consider M different runs, each run having incident BEAM B_i, live time L_i and N_i good triggers. The magnet can be either up ($\uparrow$) or down ($\downarrow$) resulting in a detection efficiency $\varepsilon_{\uparrow i}$ or $\varepsilon_{\downarrow i}$. The number of good triggers in the runs can be written

Run	Magnet	Number of Good Triggers
1	$\uparrow$	$N_1 = B_1 \sigma t L_1 \varepsilon_{\uparrow 1} \Delta A$
2	$\downarrow$	$N_2 = B_2 \sigma t L_2 \varepsilon_{\downarrow 2} \Delta A$
3	$\downarrow$	$N_3 = B_3 \sigma t L_e \varepsilon_{\downarrow e} \Delta A$
.	.	.
.	.	.
M	$\uparrow$	$N_M = B_M \sigma t L_M \varepsilon_{\uparrow M} \Delta A$

Assuming a single particle trigger produced by beam particle a, the cross section for measuring a particle of type c, $\sigma(ap \to cX)$, can be

written

$$\sigma(ap \to cX) = \frac{\text{all}\,\Sigma_{\text{runs}}\, N_i^c(a)}{t\Delta A\ \text{all}\,\Sigma_{\text{runs}} f_a \varepsilon_C^a B_i L_i \varepsilon_i^c} \tag{A.17}$$

where $N_i^c(a)$ is the number of triggers in the run containing particle c produced by beam a and $\varepsilon_{\updownarrow}^c$ is the efficiency for triggering on c. If $\varepsilon_{\updownarrow}^c$ is a constant, then when we take ratios of cross sections we need only be concerned with the amount of beam onto the target and not the detection efficiency of the particles. But this may not be the case if, for example, c is charge. Then for ↑ magnet, positive particles bend into the right calorimeter and negatives bend into the left calorimeter. There will also be a difference in detection efficiency for bend-ins and bend-outs because of the magnet p_T kick.

We subdivide our runs into ↑ magnet and ↓ magnet and select only bend-in triggers. Then

$$\sigma(ap \to cX) = \frac{\Sigma_{\uparrow}\, N_i^c(a)}{t\Delta A\ \Sigma_{\uparrow}\, f_a \varepsilon_C^a B_i L_i \varepsilon_{\uparrow}^c} \tag{A.18a}$$

and

$$\sigma(ap \to cX) = \frac{\Sigma_{\downarrow}\, N_i^c(a)}{t\Delta A\ \Sigma_{\downarrow}\, f_a \varepsilon_C^a B_i L_i \varepsilon_{\downarrow}^c} \tag{A.18b}$$

If we assume only charge dependent efficiencies, i.e., $\varepsilon_{\updownarrow}^{c^{\pm}} = \varepsilon_{\updownarrow}^{\pm}$, we are left with four efficiencies to determine:

$\varepsilon_{\uparrow}^{+}$ = detection efficiency of positives by RHS calorimeter
$\varepsilon_{\downarrow}^{+}$ = detection efficiency of positives by LHS calorimeter
$\varepsilon_{\downarrow}^{-}$ = detection efficiency of negatives by RHS calorimeter
$\varepsilon_{\uparrow}^{-}$ = detection efficiency of negatives by LHS calorimeter

With the assumption that the either-side calorimeter response be independent of the charge, we can now take ratios like $\sigma(ap \to h^+X)/\sigma(ap \to h^-X)$ and be largely independent of triggering efficiency by looking separately at $\uparrow$ magnet runs and $\downarrow$ magnet runs. For example, using only right-side triggers,

$$\frac{\sigma(ap \to h^+X)}{\sigma(ap \to h^-X)} = \frac{\sum\limits_{\uparrow} N_i^+(a)}{\sum\limits_{\downarrow} N_i^-(a)} \frac{\sum\limits_{\downarrow} f_a \varepsilon_C^a B_i L_i}{\sum\limits_{\uparrow} f_a \varepsilon_C^a B_i L_i} \tag{A.19a}$$

And for left-side triggers,

$$\frac{\sigma(ap \to h^+X)}{\sigma(ap \to h^-X)} = \frac{\sum\limits_{\downarrow} N_i^+(a)}{\sum\limits_{\uparrow} N_i^-(a)} \frac{\sum\limits_{\uparrow} f_a \varepsilon_C^a B_i L_i}{\sum\limits_{\downarrow} f_a \varepsilon_C^a B_i L_i} \tag{A.19b}$$

We note that Eqs. A.19 rely on having approximately constant triggering efficiencies over the range of runs in the summations. As long as our triggers are far enough bias or if there were no large threshold variations we should be safe. The triggers for each magnet setting are weighted by the amount of beam taken on the target, $\Sigma f_a \varepsilon_C^a EBM_i \frac{HPT_i}{HPL_i}$.

VITA

Robert Walter Stanek [redacted] he attended the University of Illinois at Chicago Circle. In 1970 he received a B.S. in Physics and entered the graduate college at the University of Illinois at Chicago Circle. He received his M.S., also in Physics, in 1971.